UNIVERSITY OF CALIFORNIA,
IRVINE

Multiscale Modeling for Tissue Patterning: Growth and Stochasticity

DISSERTATION

submitted in partial satisfaction of the requirements
for the degree of

DOCTOR OF PHILOSOPHY

in Mathematics

by

Yuchi Qiu

Dissertation Committee:
Professor Qing Nie, Chair
Professor Long Chen
Professor Xiaohui Xie

2020

DEDICATION

To my girlfriend, Yutong Sha.
To my mother, Shenru Chen.
To my father, Jianxian Qiu.

TABLE OF CONTENTS

LIST OF FIGURES

LIST OF TABLES

List of Algorithms

ACKNOWLEDGMENTS

It is my fortune to have many people generously helping me out all the time. It is impossible to complete my doctor of philosophy degree without their help and supports.

I would like to thank my advisor and my committee chair, Dr. Qing Nie, for being a tremendous mentor for me. His visionary insights and enthusiasm for research inspire me to continue my academic path. With his encouragement and guidance, I have learned how to be an independent researcher. Without his support, I would not finish this thesis.

I would like to express my appreciation to Lander's lab: Dr. Arthur Lander and Dr. Yilun Zhu. Together, we published a fantastic paper for *Drosophila* imaginal wing disc patterning. Most importantly, the knowledge, creativity, and persistence I have learned from them are a precious treasure to me.

I am thankful to Schilling's lab: Dr. Thomas Schilling and Lianna Fung. I learned so much biological knowledge from them. The valuable discussions are critical to the success of our interdisciplinary work. I also appreciate Lianna's efforts for collecting experimental data.

I would like to express my gratitude to my committe members, Dr. Long Chen and Dr. Xiaohui Xie, for their insightful comments and encouragement. I would like to thank the Department of Mathematics, Center for Complex Biological System and Center for Multiscale Cell Fate Research for their help and cares for my lives and studies. Especially, many thanks to Karen Martin, Naomi Carreon, Donna McConnell, Aubrey Rudd and Clare Cheng.

I would like to thank all my former and current members of Nie lab: Qixuan Wang, Tian Hong, Chunhe Li, Adam Maclean, Lina Meinecke, Christian Guerrero-Juarez, Axel Almet, Honglei Ren, Emmanuel Dollinger, Floyd Maseda, Matt Karikomi, Kevin Johnston, Daniel Bergman, Lei Zhang, Jiajun Zhang, Chris Rackauckas, Seth Figueroa, Catherine Ta. Especially, many thanks to Weitao Chen for her generous help and it was awesome to publish many nice papers with her. I appreciate the suggestions and support from many people for helping me go through the tough time: Zixuan Cang, Peijie Zhou, Yangyang Wang, Shuxiong Wang, Suoqin Jin and Lihua Zhang, Yutong Sha, Tao Peng and Huijing Du.

CURRICULUM VITAE

Yuchi Qiu

EDUCATION

Doctor of Philosophy in Mathematics **2020**
University of Califronia, Irvine *Irvine, California, USA*

Master of Science in Mathematics **2016**
University of Califronia, Irvine *Irvine, California, USA*

Bachelor of Science in Mathematics **2014**
Nanjing University *Nanjing, China*

EXPERIENCE

Teaching Assistant **2014–2020**
University of Califronia, Irvine *Irvine, California*

Research Assistant **2015–2020**
University of Califronia, Irvine *Irvine, California*

Awards

Center for multiscale cell fate research (CMCF) interdisciplinary opportunity award *2019*

PUBLICATIONS

published

- Yuchi Qiu, Weitao Chen, and Qing Nie. A hybrid method for stiff reaction-diffusion equations. *Discrete & Continuous Dynamical Systems-B*, pages 28-34, 2019
- Yangyang Wang, Christian F Guerrero-Juarez, Yuchi Qiu, Huijing Du, Weitao Chen, Seth Figueroa, Maksim V Plikus, and Qing Nie. A multiscale hybrid mathematical model of epidermal-dermal interactions during skin wound healing. *Experimental dermatology*, 28(4): 493502, 2019
- Yuchi Qiu, Weitao Chen, and Qing Nie. Stochastic dynamics of cell lineage in tissue homeostasis. *Discrete & Continuous Dynamical Systems-B*, pages 853865, 2019
- Qing Nie, Lingxia Qiao, Yuchi Qiu, Lei Zhang and Wei Zhao. Noise control and utility: from gene regulatory network to spatial patterning. *Science China Mathematics*, 1-16, 2020

- Yilun Zhu, Yuchi Qiu, Weitao Chen, Qing Nie, and Arthur D Lander. Scaling a morphogen gradient through feedback control of receptors and co-receptors. *Developmental Cell*, 2020

in preparation

- Yuchi Qiu, Lianna Fung, Thomas Schilling and Qing Nie. Dissection of multiple morphogens and morphogenesis in zebrafish hindbrain pattern formation.

ABSTRACT OF THE DISSERTATION

Multiscale Modeling for Tissue Patterning: Growth and Stochasticity

By

Yuchi Qiu

Doctor of Philosophy in Mathematics

University of California, Irvine, 2020

Professor Qing Nie, Chair

The spatial organization of tissues is often determined by long-range signals, morphogens, through the concentration-dependent manner. The morphogen-mediated patterning is a great foundation, but inadequate to explain the effects of tissue growth and stochasticity, the two prevalent phenomena, in pattern formation. In this thesis, we use multi-scale models to study those questions. In Chapter 2, we study how pattern scales to tissue size in *Drosophila* wing disc and find the scaling is through the feedback control on receptors and co-receptors of the morphogen. In Chapter 3, we study how different types of noise affect the dynamics of spatial pattern in the epithelium and we find the balanced levels of different types of noise is essential to the tissue homeostasis. In Chapter 4, we discuss both effects of growth and noise in the zebrafish hindbrain pattern. Despite the noise causes variability, growth improves the precision of the pattern. In Chapter 5, we develop a numerical method for solving stiff reaction-diffusion equations which provides a necessary tool for solving modeling problems.

Chapter 1

Introduction

In biology, the robust and precise spatial organization of tissues is critical to multi-cellular organisms to execute their specific functions. It is challenging to understand how microscopic intercellular interactions lead to the macroscopic pattern formation ubiquitous. In this thesis, I will use the multi-scale modeling to tailor the mechanisms in molecular, cellular and tissue scales to study pattern formation. A diffusive chemical, morphogen, having non-uniform distribution in space, provides positional information, enabling cells to respond collectively to form precise domains of target gene expression [182, 173]. Utilizing the theory of the morphogen-mediated patterning, multi-scale modeling successfully mimicked the pattern formation in extensive biological systems including vertebrate neural tube [9], vertebrate hindbrain [190], vertebrate limb buds [136], the *Drosophila* embryo [70], the *Drosophila* wing disc [13], and skin [172, 35]

During development, the role of tissue growth in the patterning process has been recently highlighted [160]. One common phenomenon is scaling where the gradients expand as the tissue grows to keep relative boundary positions approximately stationary. The source-sink model noted that an absorbing sink boundary is able to adjust gradients as the tissue grows

[182]. But it fails to explain the scaling under the large size of the tissue. Recently, the Expansion-Repression (ER) model is identified where a morphogen represses the expression of a secreted expander which, by diffusing back toward the morphogen source, promotes morphogen spread [14, 12]. In Chapter 2, we reexamine the ER model proposed in the *Drosophila* imaginal wing disc [11] where the expander needs to spread in a nearly uniform manner over the morphogen field. Instead, Arthur Lander's lab finds the expander only acts locally which is against the assumption of the uniform expander. Through genetic experiment and mathematical modeling, we propose an alternative model, in which the morphogen mediated regulation on receptor and co-receptor to drive its scaling.

On the other hand, noise permeates in patterning systems on all levels, from molecular, cellular to tissues, organs, causing fluctuations and variability to alter the precision of the pattern. Usually, noise is believed to be detrimental to biological functions, but sometimes the noise is found to be pivotal. In Chapter 3, we discuss the effects of different types of noise in the stratified epithelium tissue. We find the interactions between intracellular and extracellular noise are critical to the robust spatial organization.

In Chapter 4, we focus on the effects of both growth and stochasticity during the zebrafish hindbrain pattern formation. By acting on both cell fate decisions and intercellular mechanical interactions, growth is found to be an essential strategy to reduce the variability of the pattern caused by noise. In addition, we find an additional morphogen is helpful for improving the robustness of the system.

In the pattern system, the morphogen gradients are modeled by a system of reaction-diffusion equations. The classic numerical solvers are inefficient to solve such a system, especially, when the system is stiff. A class of methods, semi-implicit integration factor (IIF) methods [120], was able to solve the stiff system efficiently. However, the IIF behaves reduced order of accuracy phenomenon in practice. In Chapter 5, we develop a hybrid method (hIFE) to improve the practical accuracy of the IIF method.

Chapter 2

Scaling a morphogen gradient through feedback control of receptors and co-receptors

This chapter is a reprint of the material as it appears in Developmental Cell [194]. The co-authors listed in this publication directed and supervised research which forms the basis for this chapter.

2.1 Background

Gradients of decapentaplegic (Dpp) pattern *Drosophila* wing imaginal discs, establishing gene expression boundaries at specific locations. As discs grow, Dpp gradients expand, keeping relative boundary positions approximately stationary. Such scaling fails in mutants for Pentagone (*pent*), a gene repressed by Dpp that encodes a diffusible protein that expands Dpp gradients. Although these properties fit a recent mathematical model of automatic

gradient scaling, that model requires an expander that spreads with minimal loss throughout a morphogen field. From our collaborators Arthur Lander's lab, they show that Pent's actions are confined to within just a few cell diameters of its site of synthesis, and can be phenocopied by manipulating non-diffusible Pent targets strictly within the Pent expression domain. Using genetic experiment and the mathematical modeling we develop an alternative model of scaling, driven by feedback down-regulation of Dpp receptors and co-receptors. Among the model's predictions is a size beyond which scaling failssomething we observe directly in wing discs.

2.2 Introduction

During development, gradients of secreted morphogens convey positional information, enabling cells to behave and differentiate according to their locations. Over a century of evidence suggests that positional information is often specified in relative coordinates, i.e. scaled to the territory being patterned [25, 29, 34, 66, 68, 157]. Fifty years ago, Wolpert argued that this implies that morphogen gradients adjust themselves to the fields on which they act [182], a phenomenon that was eventually observed directly [13, 53, 55, 157, 174].

Wolpert noted that one type of gradient—a linear diffusion gradient from a source to an absorbing sink—scales naturally, automatically readjusting its slope whenever the sink moves [182]. Over time, the idea that morphogens form simple source-sink gradients gave way to the view—supported by observations [39, 42, 54, 157]—that gradients are shaped by continual decay throughout the morphogen field. Gradients shaped in this way should not scale automatically, implying that other mechanisms must enable scaling. Progress toward identifying such mechanisms has been slow, but received a boost with the development of the Expansion-Repression (ER) model [11], in which a morphogen represses the expression of a secreted "expander" which, by diffusing back toward the morphogen source, promotes mor-

phogen spread. This mechanism is homeostatic—moving a distal field boundary away from a morphogen source increases production of the expander, which spreads the morphogen gradient toward the field boundary—and, if the expander is long-lived, approximates "integral negative feedback", a control strategy that achieves perfect compensation [11].

So far, the ER model has been used to explain how gradients of bone morphogenetic proteins (BMPs) scale in response to embryo manipulations [14] and during growth of larval wing imaginal discs [12]. In the latter case, the relevant BMP is decapentaplegic (Dpp), which is produced by a stripe of cells in the center of the disc and spreads bidirectionally through the columnar epithelium to create gradients in the anterior and posterior compartments. During the larval period, wing discs grow at least 60-fold in anteroposterior dimension, and the Dpp gradient scales with it [55, 174]. Support for the ER model in this setting was provided by the identification of a putative expander, the secreted protein Pentagone (Pent, also known as Magu). *Pent* expression is repressed by Dpp, restricting *pent* to the most lateral cells of the central wing pouch. Loss of *pent* dramatic shrinks the Dpp signaling gradient, and *pent* overexpression expands it [165]. Moreover, in the absence of *pent*, developmental scaling of the Dpp gradient is greatly impaired [12, 55]. Although Pent's mechanism of action is not fully understood, it binds heparan sulfate proteoglycans (HSPGs) and triggers their removal from the cell surface. The same HSPGs act as co-receptors for BMPs [83], including Dpp [44, 69], strongly suggesting that Pent expands Dpp gradients by inhibiting receptor-mediated Dpp uptake.

Here we re-examine the role of Pent in the *Drosophila* wing disc, focusing on an important requirement of the ER model, namely that the expander spread in a nearly uniform manner over the morphogen field. Spreading uniformly is not the same as merely being diffusible, as spread quantifies the balance between transport (e.g. diffusion) and decay, where decay means all processes that remove a substance from a diffusing pool (i.e. destruction, uptake, leakage out of the system). In a stable diffusion gradient, a common measure of spread is the

"apparent decay length", or λ_{app}, the distance over which concentration falls by a factor of $1/e$ [90]. In the ER model, if an expander's λ_{app} is not greater than the size of the morphogen field, the expander will affect the morphogen differently at different locations, and effective scaling will not occur.

From experiment, Arthur Lander's lab found λ_{app} for Pent to be very small, strongly suggesting that Dpp gradient scaling cannot rely on Pent to play the expander role required by the ER model. Through their genetic experiment and the mathematical modeling, we arrived at an alternative model, in which the feedback that drives scaling is not repression of an expander, but morphogen-mediated regulation of receptor (and co-receptor) function, a phenomenon that is fairly common in patterning systems (e.g. [20, 45, 78, 94]). A key feature of this model is that it is dynamic, terminating scaling at a size that depends on the parameters of the system. In view of evidence that a growing Dpp gradient itself participates in driving disc growth [174], this feature suggests ways in which bi-directional coupling between patterning and growth could be achieved.

2.3 Quantifying morphogen gradient scaling

For discrete pattern elements, such as gene expression boundaries, one can define scaling as the preservation of these elements' relative positions. During development, however, sharp gene expression boundaries may emerge only late [30, 123], or read out morphogen signals in indirect (e.g. time-integrated) ways (e.g. [9, 31, 116]). To investigate developmental scaling directly, it is thus important to monitor morphogen gradients themselves, or gradients of immediate downstream signals (e.g. phosphorylated Mad [$pMad$], in the case of Dpp). As smooth gradients lack landmarks with which to assess relative position, this means tracking the locations of constant gradient amplitudes over time. It can be challenging, however, to measure absolute concentration in tissues. Furthermore, absolute morphogen or signaling

molecule concentration may not even be the best read-out of positional information across developmental time, because changing characteristics of cells likely influence how they decode morphogen signals. In wing discs, for example, changes in cell dimensions between first larval instar and the end of disc growth [178] imply that cell volumes increase by at least 7-fold.

For these reasons, morphogen gradient scaling is often evaluated in terms of preservation of relative gradient shape, typically quantified by the degree to which the apparent decay length (λ_{app}) of the morphogen (or its downstream signaling intermediates) changes proportionately with size of the morphogen field (e.g. [174]). For gradients of exponential shape, λ_{app} is simply the constant λ in the formula $C = C_0 e^{x/l}$ where C is concentration, x is distance from the morphogen source, and C_0 the value of C at $x = 0$. In practice, λ_{app} is often measured as the distance over which a gradient falls to $1/e$ of its starting value (or by extracting the length constant from a best-fit exponential curve). Here we follow others in using λ_{app} as a first-line metric for assessing scaling, but also take care to visually analyze absolute gradient shapes whenever possible. As we argue below, changes in both gradient amplitude and shape may play an important role in enabling certain kinds of scaling mechanisms.

2.4 Pent acts locally at the edges of the Dpp morphogen field on co-receptor

The ER model of scaling requires an expander to spread uniformly across a morphogen field, i.e. traverse it without much decrement in concentration. Although Pent can be detected at a distance from its site of synthesis [121, 165], and when overexpressed in the posterior half of the disc can influence gradient shapes in the adjacent anterior [165], such observations don't speak to how steeply Pent concentrations decline over distance. To address this, experimental results from Arthur Lander's lab show Pent act relatively locally, rather than

globally, undermining support for the ER model as an explanation for Dpp gradient scaling.

On the other hand, they show Pent does not need to spread by acting on co-receptor. Current consensus is that Pent acts by reducing levels (and thereby function) of HSPG co-receptors, in so doing decreasing Dpp uptake and increasing Dpp spread. Overexpressing Pent or knocking down co-recetpors at the edges of the Dpp morphogen field lead to similar expansion of Dpp gradient (pMad). But knocking down co-receptors throughout the entire disc results in the shrink of Dpp gradient. These results indicate Pent only acts on the edges of the disc by internalizing co-receptors.

2.5 Scaling of the Dpp signaling gradient is a transient phenomenon

Before investigating alternative explanations for scaling, Arthur Lander's lab more closely examined scaling dynamics. They collected many wild type wing discs, spanning a range of sizes, and calculated λ_{app} for pMad, using the same measurement approaches taken by other investigators, making an effort to avoid various pitfalls and artifacts (e.g. measuring too close to the dorsoventral boundary [55].

The observations (Figure S3, Figure 4-5 in [194]) confirm that λ_{app} grows roughly in proportion to disc size, but also show that it does so only up to the time (part-way through third larval instar) that posterior compartment sizes reach $\sim$50-60 μm—about a fourth to a third of their final size, or about two cell cycles (approximately one day) prior to the end of disc growth. After that, scaling seems to cease rather abruptly. Such behavior has not been noted previously, possibly because other groups have focused more on documenting the existence of scaling during most of disc growth, rather than on how it behaves during the very last stages of growth. What this behavior suggests is that whatever mechanism

accounts for scaling of the Dpp gradient, it is size- (or time-) limited, i.e. has a maximal distance or duration over which it functions. Thus, the challenge in explaining scaling in the wing disc is not only to understand how it happens, but why it stops when it does.

2.6 Feedback regulation of receptors and co-receptors is required for scaling

One reason that λ_{app} is widely used as a measure of morphogen gradient shape is that a simple model, the "uniform-decay" model, connects it to the biophysics of gradient formation: If morphogen decay is uniform in space, and the morphogen field sufficiently large (and sufficiently one-dimensional), then steady state gradient shape should have the form $e^{-x/\lambda}$, with $\lambda = \lambda_{app} = \sqrt{D/k}$, where D is the morphogen diffusion coefficient, and k is a rate constant of morphogen removal (e.g. uptake) [90].

In general, one cannot assume that morphogen decay is uniform in space, because morphogens may influence their own uptake or destruction. Some (e.g. Wingless and Hedgehog in *Drosophila* wing discs) upregulate their own removal; such "self-enhanced decay" characteristically alters gradient shape [39, 90]. In contrast, Dpp down-regulates both its receptor Tkv (through indirect effects on *tkv* transcription [94]), and the HSPG co-receptor Dally [45]. As Tkv appears to be the major determinant of Dpp uptake and, thereby removal [4, 94], and Dally likely boosts this function of Tkv, and may even mediate some uptake itself [45], we expect Dpp gradients to be shaped by "self-repressed decay".

Although the effects of self-enhanced and self-repressed decay on steady state gradient shape are fairly subtle [90], these processes can have large effects on how gradients respond to perturbations. For example, self-enhanced-decay gradients display increased robustness to changes in amplitude (i.e. threshold locations do not move nearly as much as they do in

uniform decay gradients [39]). Self-repressed-decay gradients, it turns out, display enhanced sensitivity to changes in the size of the morphogen field, a phenomenon that—as we will see shortly—can drive morphogen gradient scaling.

Before discussing the theory behind this assertion, Arthur Lander's lab presents experimental evidence in support of it: To test whether self-repression of decay is required for Dpp gradient scaling in the wing disc, it was necessary to disable the feedback loops that allow Dpp to down-regulate *tkv* and *dally*. For *tkv*, they used a transgenic allele in which a Ubiquitin promoter drives ubiquitous, unregulated expression of HA-tagged *tkv* [122]. When combined with null mutation of the endogenous *tkv* locus, viable flies are obtained, with late-third larval instar wing discs that do not differ significantly in pattern from wildtype, except for the fact that tkv expression is spatially uniform, rather than graded. We refer to this genotype as "Ubi-*tkv*". To disable feedback on dally, we used an *Act5C-Gal4* driver to drive a *UAS-dally* transgene in a uniform pattern in a *dally*-mutant background ($dally^{80}/dally^{80}$). We refer to this genotype as "Uniform-*dally*".

Figure 5 in [194] shows results for a large number of wildtype, *pent*, $pent^{+/-}$, Ubi-*tkv*, Uniform- *dally*; Ubi-*tkv*/Uniform-*dally*; and *pent*/Ubi-*tkv* and *pent*/Ubi-*tkv*/Uniform-*dally* discs of a broad range of sizes. λ_{app} was measured for pMad gradients and plotted against posterior compartment sizes.

The results show that scaling is significantly impaired when either *tkv* or *dally* regulation is bypassed, and nearly eliminated when both are bypassed. These differences emerge mainly after posterior compartments grow beyond 30 μm. Above that size, Ubi-*tkv* and Uniform-*dally* continue to scale, but much more slowly than wildtype gradients. Eventually, however, such gradients do "catch up" to wildtype gradients, as a result of the fact that wildtype gradients cease scaling sooner. In contrast, doubly-mutant Ubi-*tkv*/Uniform-*dally* gradients stop expanding altogether once posterior compartments grow beyond about 30 μm, reaching a final λ_{app} about half that of wildtype.

The defect in Ubi-*tkv*/Uniform-*dally* gradients is almost, but not quite, as severe as that in pent mutants, which cease scaling at a slightly earlier size. Interestingly, the phenotype of *pent*/Ubi-*tkv* and *pent*/Ubi-*tkv*/Uniform-*dally* discs was only slightly more severe than for *pent* alone. These results support the conclusion that both scaling, and the effect of Pent on scaling, depend upon feedback regulation of *tkv* and *dally* by Dpp.

2.7 Modeling the dynamics and endpoints of scaling

To explain the behaviors in Figure 5 in [194], we turned to mathematical modeling. Accounting for all the cell biological phenomena that affect Dpp gradient shape requires modeling a large number of molecular species and processes. As many of these processes are not quantitatively understood, they were represented as simply as possible, with model behaviors explored over parameter ranges that were wide but plausible (given available data). The goal was not so much to identify parameter values as to determine whether existing observations can be matched without invoking additional mechanisms. To the extent that inclusion of new mechanisms is not required, models such as these can help identify which processes potentially play the most important roles in morphogen gradient scaling.

2.7.1 The model with growing domain for the Dpp regulatory network

The molecular species represented in the model are Dpp, Tkv, "co-receptor" (to represent both Dally and Dlp), Pent, Dpp-coreceptor complexes, and two types of Dpp-receptor complexes (the more stable of which forms with the aid of coreceptor-mediated catalysis [83]), plus pMad and Brk. An additional transcription factor is included downstream of the transcriptional repressor Brk to enable it to activate Tkv and co-receptor synthesis indirectly

(the role of this factor in the model resembles that of *optomotor blind* [30]). Dpp and Pent are the only diffusing species, with Pent being assigned the same diffusivity as that measured empirically for Dpp [192].

The system of partial differential equations used to model the Dpp gradient on a growing wing disc is shown below as Eq. (2.1), and also diagrammed as a conceptual network (Figure 2.1). The modeled domain consists of the intercellular (basolateral) spaces of the posterior compartment of the wing disc, which is represented as a one-dimensional reaction-diffusion system. The one-dimensional approximation assumes that morphogen flux in the dorsoventral and apicobasal directions is negligible. This is probably a good assumption at large disc sizes, but, as described later (Section 2.9.5), and in [86], may be less so at small size. We model the basal rates of synthesis of gene products as constant in time and space, as modified by pMad or Brk, except in the following cases: we lower Tkv production and raise coreceptor production in the Dpp-production region, to capture known effects of Hedgehog signaling in that region [156]. In addition, we model the basal rate of Brk synthesis as continuously increasing during disc growth, in order to fit the data of [55], who show that peak Brk levels rise more than 10-fold over the course of wing disc development (because peak Brk expression occurs where Dpp signaling is essentially negligible, such changes cannot be attributed to an effect of Dpp). We model growth of wildtype discs to fit our own observations of disc growth rate (Figure S3 in [194]), which are similar to those published by [174]. For some genotypes, including homozygous *pent* mutants, we adjusted the growth rate (described further below) so that discs finish growing at a smaller size, in accordance with published data on *pent* discs [12, 165], and our own observations (Figure 5 and Figure S6 in [194]).

$$
\begin{aligned}
&\frac{\partial[Dpp]}{\partial t}+\frac{\partial\left(V[Dpp]\right)}{\partial x}=\frac{v_{dpp}}{1+\left(\frac{x}{prod(t)}\right)^{20}}+D_{dpp}\Delta[Dpp]-k_1[Dpp][Tkv]+k_{r1}[Dpp-Tkv]-k_2[Dpp][Cr]\\
&\qquad\qquad+k_{r2}[Dpp-Cr]-\frac{d_{dpp}}{1+\left(\frac{x}{prod(t)}\right)^{20}}[Dpp],\\
&\frac{\partial[Tkv]}{\partial t}+\frac{\partial\left(V[Tkv]\right)}{\partial x}=v_{tkv}-k_1[Dpp][Tkv]+k_{r1}[Dpp-Tkv]-k_4[Tkv][Dpp-Cr]+d_{dpptkv}[Dpp-Tkv]\\
&\qquad\qquad+d_{dpptkv*}[Dpp-Tkv*]-d_{tkv}[Tkv],\\
&\frac{\partial[Cr]}{\partial t}+\frac{\partial\left(V[Cr]\right)}{\partial x}=v_{cr}-k_2[Dpp][Cr]+k_{r2}[Dpp-Cr]+k_4[Tkv][Dpp-Cr]-k_3[Pent]_{in}[Cr]-d_{cr}[Cr],\\
&\frac{\partial[Dpp-Tkv]}{\partial t}+\frac{\partial\left(V[Dpp-Tkv]\right)}{\partial x}=k_1[Dpp][Tkv]-k_{r1}[Dpp-Tkv]-k_5[Cr][Dpp-Tkv]-d_{dpptkv}[Dpp-Tkv],\\
&\frac{\partial[Dpp-Tkv*]}{\partial t}+\frac{\partial\left(V[Dpp-Tkv*]\right)}{\partial x}=k_5[Cr][Dpp-Tkv]+k_4[Tkv][Dpp-Cr]-d_{dpptkv*}[Dpp-Tkv^*],\\
&\frac{\partial[Dpp-Cr]}{\partial t}+\frac{\partial\left(V[Dpp-Cr]\right)}{\partial x}=k_2[Dpp][Cr]-k_{r2}[Dpp-Cr]-k_4[Tkv][Dpp-Cr]-d_{dppcr}[Dpp-Cr],\\
&\frac{\partial[pMad]}{\partial t}+\frac{\partial\left(V[pMad]\right)}{\partial x}=v_{pmad}[Dpp-Tkv*]-d_{pmad}[pMad],\\
&\frac{\partial[brk]}{\partial t}+\frac{\partial\left(V[brk]\right)}{\partial x}=\frac{x_{\max}v_{brk}}{\left(1+\left(\frac{[pMad]}{EC_{brk}}\right)^2\right)}-d_{brk}[brk],\\
&\frac{\partial[TF]}{\partial t}+\frac{\partial\left(V[TF]\right)}{\partial x}=\frac{v_{tf}}{1+\left(\frac{[brk]}{EC_{TF}}\right)^2}-d_{tf}[TF],\\
&\frac{\partial[Pent]_{out}}{\partial t}+\frac{\partial\left(V[Pent]_{out}\right)}{\partial x}=\frac{v_{pent}}{1+\left(\frac{[pMad]}{EC_{pent}}\right)^2}+D_{pent}\Delta[Pent]_{out}-k_6[Pent]_{out},\\
&\frac{\partial[Pent]_{in}}{\partial t}+\frac{\partial\left(V[Pent]_{in}\right)}{\partial x}=k_6[Pent]_{out}-d_{pent}[Pent]_{in}.\\
&v_{tkv}=tkv1+\frac{tkv2}{1+\left(\frac{[TF]}{EC_{tkv}}\right)^2}+\frac{tkv3}{1+\left(\frac{x}{prod(t)}\right)^{-20}},\ v_{cr}=cr1+\frac{cr2}{1+\left(\frac{[TF]}{EC_{Cr}}\right)^2}+\frac{cr3}{1+\left(\frac{x}{prod(t)}\right)^{20}}.
\end{aligned}
\tag{2.1}
$$

In the above system of equations, $[P](x,t)$ denotes the concentration of species P at location x and at time t. To represent the likely fact that Pent must first bind cells to have effects on HSPGs, Pent has unbound and bound forms in the model, represented by $[Pent]_{out}$ and $[Pent]_{in}$, respectively. The spatial domain $[0, x_{\max}]$ represents the region of the posterior compartment. To represent disc growth, $x_{\max}$ increases according to: $x_{\max}(t) = x_0 e^{at\,{}_2F_1\left(1,\frac{1}{n},1+\frac{1}{n},-bt^n\right)}$ (see derivation below in Eq. (2.3)). Dpp and unbound Pent ($[Pent]_{out}$) are the only diffusive species in this model, and have diffusion coefficients D_{dpp} and D_{pent}, respectively. The term $\frac{\partial(V[P])}{\partial x}$ can be split into two terms $[P]\frac{\partial V}{\partial x}$ and $V\frac{\partial[P]}{\partial x}$ representing dilution and advection driven by disc growth, respectively. $V(x,t)$ is the disc

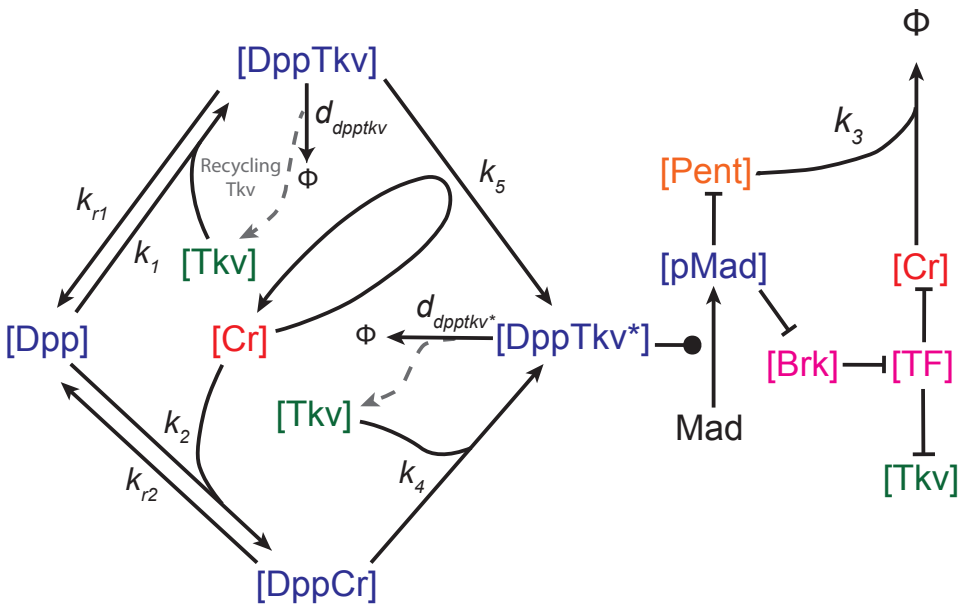

Figure 2.1: Conceptual model of the wing disc Dpp patterning system. Arrows depict biochemical interactions; lines ending in bars are regulatory inhibition, and lines ending in circles regulatory activation. Dpp binds with its receptor Tkv to form a complex DppTkv. DppTkv matures into a stabilized complex, DppTkv* (DppTkv* may be considered an analog of a heteromeric ligand-type I-type II receptor complex). DppTkv* may be formed either with catalytic assistance from co-receptors Dally and Dlp [83], or via Dpp first binding to co-receptor (Cr) (to form DppCr) and then transferring to receptors (regenerating Cr). DppTkv* induces phosphorylation of Mad to generate pMad. Dpp receptor complexes undergo first order decay with recycling of Tkv. pMad signaling inhibits the synthesis of both Pent and Brk. Brk inhibits one or more transcription factors (TF, e.g. optomotor blind) that inhibit of the synthesis of both Tkv and Cr. Pent also binds to Cr and drives its destruction.

growth velocity at location x and its value at $x_{\max}$ represents the growth rate of the entire posterior compartment: $V(x_{\max}, t) = \frac{dx_{\max}}{dt}$. We assume the disc grows homogeneously over the entire space, and $V(x,t)$ is a linear function of x:

$$V(x,t) = \frac{x}{x_{\max}(t)} V(x_{\max}, t). \tag{2.2}$$

For any species P and Q, $k_i[P][Q]$, $(i = 1, 2, 3, 4, 5)$, are association rates between P and Q, and $k_{ri}[PQ]$ $(i = 1, 2)$ are dissociation rates of the complex PQ formed by P and Q. For any species P, $d_P[P]$ represents a degradation rate for (free) P.

The rate constant k_6 describes first order association of $Pent_{out}$ with cells to produce the bound species $Pent_{in}$. We assume that Dpp is synthesized in a localized source (termed the production region), and the size of Dpp production region grows at the same rate as the rest of posterior compartment. Specifically, we take $prod(t) = px_{\max}(t)$, with $p = 0.12$. Dpp production is then modeled by $v_{dpp}/(1 + (x/prod(t))^{20})$. The high-exponent Hill function essentially approximates a step function. A Dpp degradation term is also added in the production region: $d_{dpp}/(1 + (x/prod(t))^{20})$.

The production rate of Tkv, v_{tkv}, contains three terms: $tkv1$ is a base production rate in the entire disc; $tkv2/(1 + ([TF]/EC_{tkv})^2)$ represents the production regulated by TF, which stands for downstream transcription factors repressed by Brinker (Brk); Tkv synthesis is low inside the Dpp production region due to the effect of Hedgehog [156] and $tkv3/(1 + (x/prod(t))^{-20})$ is used to model the additional Tkv production outside of the production region. Dally and Dlp are lumped together as "Co-receptor" (Cr) in this model. The production rate of co-receptor, v_{cr}, contains three terms: $cr1$ is base production rate; $cr2/(1+([TF]/EC_{Cr})^2)$ represents the production regulated by TF; and because co-receptor synthesis is high inside Dpp production region, due to effect of Hedgehog [156], $cr3/(1+(x/prod(t))^{20})$ is used to model the addition Cr production in the Dpp production region. To represent the fact that $Pent_{in}$ drives destruction of co-receptors, we introduce a decay term into the equation for Cr that is proportional to the level of $Pent_{in}$ with proportionality constant k_3.

To model the production of Brinker (Brk), which is repressed by pMad, we multiply a basal production rate by $1/(1 + [pMad]/EC_{brk})^2)$, however, because basal Brk production appears to increase markedly with disc size [55], we take the basal production rate to be a constant v_{brk} times $x_{\max}$ (disc diameter). To model the production of TF, we multiply a basal production rate v_{tf} by $1/(1 + [Brk]/EC_{TF})^2)$. To model the production of Pent, we multiply a basal production rate v_{Pent} by $1/(1 + [pMad]/EC_{Pent})^2)$.

The biochemical steps in the assembly of the active form of the Dpp receptor are modeled to

reflect that fact that TGF-beta family receptors assemble in a two-stage process which, for the BMP branch of the TGF-beta family, usually involves initial binding to type I receptors (e.g. Tkv) and subsequent recruitment of type II receptors. Thus, the species DppTkv may be construed to represent complexes that lack type II receptors while the species DppTkv* represents complexes containing both type I and II receptors.

We model co-receptor activity according to the results of [83], who showed that HSPGs catalyze the conversion of BMP-type I receptor complexes into BMP-type I receptor-type II receptor complexes. Rate constant k_5 captures this behavior. At the same time, because Dpp can bind HSPGs, we also model direct reversible binding, and allow for the possibility that Dpp initially bound to HSPGs can also recruit type I and type II receptors; this latter behavior is captured by k_4, but as described later, the value of k_4 may be set effectively to zero without having significant effect on the model output.

In solving system (2.1) over time and space it is necessary to specify initial conditions for all variables and boundary conditions for the diffusing species Dpp and Pent. The boundary conditions are no-flux at $x = 0$, i.e. $\left.\frac{d[P]}{dx}\right|_{x=0} = 0$, and absorbing at $x_{\max}$, i.e. $[P]|_{x=x_{\max}(t)} = 0$, where P stands for either Dpp or Pent. The no-flux condition is justified by the symmetry of the problem (anterior and posterior compartments are taken to be symmetric about the A-P boundary), and the absorbing condition creates a generalized sink at $x = x_{\max}$. The initial posterior compartment size is taken to be 0.1 μm—smaller than the actual size of discs—in order to provide sufficient simulation time for results to become independent of initial conditions. The initial conditions are then obtained by running the simulation in the fixed initial domain for 4 hours starting from zero values for all species. We verified that these conditions produced results that were independent of initial condition choices.

The total simulation time is 120 hours. We take time=0 to correspond to 24 hours after egg laying, which is consistent with the convention adopted by [174]. Because the rate at which discs grow is not constant, but slows as larval development proceeds, it was necessary

to use an empirically determined growth rate function in the model. To obtain this, we measured compartment sizes experimentally (Figure S3 in [194]). To fit those data to a simple equation we considered the following function which describes an arbitrary system that is growing exponentially but slowing according to a declining Hill function of time.

$$\begin{cases} \dfrac{dx_{\max}}{dt} = \dfrac{ax_{\max}}{1+bt^n} = f(x_{\max}, t) \\ x_{\max}(0) = x_0. \end{cases} \tag{2.3}$$

The general solution to Eq. (2.3) is $x_{\max}(t) = x_0 e^{at\,{}_2F_1\left(1,\frac{1}{n},1+\frac{1}{n},-bt^n\right)}$, where ${}_2F_1$ is the hypergeometric function:

$${}_2F_1(a,b;c;z) = \sum_{n=0}^{\infty} \frac{(a)_n (b)_n}{(c)_n} \frac{z^n}{n!}. \tag{2.4}$$

Here $(q)_n$ is the Pochhammer symbol, defined by:

$$(q)_n = \begin{cases} 1, & n = 0; \\ q(q+1)\cdots(q+n-1), & n > 0. \end{cases} \tag{2.5}$$

We used the built-in function *NonlinearModelFit* in Mathematica to fit the experimental data (Figure S3 in [194]) to the above function. By testing various integers n, the best fit was found to be given by $n = 3$. We then used this function to describe the growth of $x_{\max}$ over time in the model. Although the mathematical form is different from that proposed by [174] for the wing disc, the two functions are very similar in shape.

2.7.2 The model mimics scaling of gradient for multiple genotypes

Now, we use the model to examine the scaling for multiple genotypes. Summary results are shown in Figure 2.2A, with dietailed simulations in Figure 2.3. The behaviors of the geno-

types in Figure 5I from [194] are reasonably well replicated: Initially, all modeled genotypes scale well, until posterior compartment sizes reach $\sim$10 μm. Up to this time, Dpp and pMad gradient shapes produced by the model are essentially straight lines from source to the end of the morphogen field (Figure 2.3A).

Automatically-adjusting straight line gradients call to mind the "source-sink" scaling mechanism of [182], which exemplifies what mathematicians call a "boundary layer effect", whereby phenomena at a boundary influence gradient shape at a distance. For steady-state diffusion gradients, the approximate distance over which boundary layer effects occur is the *intrinsic decay length*, $\lambda_{intrinsic}$, defined as the square root of the ratio of the diffusion coefficient and the (effective) removal rate constant.

As previously noted, for uniform-decay gradients on a sufficiently large one-dimensional field, gradient shape is described by $e^{-x/\lambda}$, with $\lambda = \lambda_{app} = \sqrt{D/k}$; thus, for such gradients $\lambda_{app} = \lambda_{intrinsic}$. But "sufficiently large field" here turns out to mean large compared with $\lambda_{intrinsic}$. With fields smaller than $\lambda_{intrinsic}$, gradient shape becomes less exponential, and more linear; the more linear the gradient, the farther into it boundary-layer effects will occur. Wolpert's source-sink gradients are merely the limiting case of $\lambda_{intrinsic} = \infty$, (no decay within the morphogen field), yielding straight-line gradients that scale perfectly with boundary movement. As long as morphogen gradients operate in a regime of large $\lambda_{intrinsic}$ (compared with morphogen field size), they too will scale automatically (this is also true in higher dimensionssee section in Section 2.9.5). However, this can only go on for so long, as field size should eventually catch up with $\lambda_{intrinsic}$—at which point gradients will become more exponential and scaling will stop.

In the mathematical model, scaling initially displayed by all genotypes stops at different sizes (in agreement with experimental observations; Fig. 5I in [194]), for reasons that depend on the genotype. We consider first the wild type: In that situation, the initial value of $\lambda_{intrinsic}$ ($\sim$5 μm everywhere) suggests that scaling should fail sooner than it does but, as the disc

grows, the value of $\lambda_{intrinsic}$ near the morphogen source rises Figure 2.2, extending the period of scaling. The reason for the rise is that receptors and co-receptors become increasingly downregulated (since they are the primary means of morphogen removal, their loss drives $\lambda_{intrinsic}$ up). Interestingly, to prolong scaling it is not necessary for $\lambda_{intrinsic}$ to grow as fast as the disc itself. This is because once strongly non-uniform expression of receptors and co-receptors sets in—low near the morphogen source and high far away—the actual sink at the far end of the morphogen field becomes less and less important. Instead, the territory with high receptor/co-receptor expression itself acts like a sink, due to the high level of morphogen uptake there. We call this behavior "pseudo-source-sink" scaling, as it emulates a boundary-layer effect without the need for a true tissue boundary Figure 2.4AB.

The phenomenon that drives pseudo-source-sink scaling is, fundamentally, amplitude growth: In other words, it is because Dpp and pMad levels at the start of the gradient rise with disc growth that receptor and co-receptor expression become increasingly repressed, and at greater distance, over time. Whereas true source-sink scaling reflects a direct coupling of field size to gradient scale, pseudo-source sink scaling depends on indirect feedback: changes in field size first produce changes in gradient amplitude, and these then drive changes in gradient scale.

Why should changes in field size cause changes in amplitude? In the model, several processes contribute. The simplest is that the production region itself grows with the disc; as it does, it feeds more Dpp into the gradient (the magnitude of the effect depending on the level morphogen decay within the production region). A second reason arises from the laws of physics and the fact that the gradient has already been scaling: According to Fick's first law, net diffusive flux at any point is proportional to the slope of the diffusion gradient. So, whenever a gradient expands by becoming shallower, diffusive flux at the origin must decrease. That in turn leaves more molecules available to contribute to the local concentration of morphogen, raising free morphogen concentration.

Two other mechanisms can also contribute to amplitude growth, but have minor effects in the model: To the extent that Dpp molecules associated with or internalized within cells are very long-lived, the Dpp signal that cells receive will lag significantly behind the free Dpp concentration; this can cause pMad levels to rise even after Dpp levels have leveled off. And to the extent that disc growth is not purely exponential, but rather slows as time goes on [174], the loss of Dpp and pMad due to dilution will diminish, ultimately raising Dpp and pMad concentration.

Does amplitude growth, as seen in the model, actually happen in vivo? Monitoring Dpp and pMad amplitudes over time is challenging, not only because of individual variation among discs, but because discs change dramatically in thickness as they grow, necessitating corrections for systematic changes in the efficiency of immunostaining and/or imaging. Nonetheless, groups that have made such measurements consistently report amplitude growth in the wing disc Dpp gradient, although the degree to which they observe it varies [55, 174]. The model parameters used in Figure 2.3A predict an approximately 7-fold increase in Dpp and 12-fold increase in pMad over the time that posterior compartments lengthen ∼20-fold (from 10 to 195 μm), but the actual changes are likely less important than the degree to which they decrease Tkv and co-receptor expression.

To investigate the dynamics of that decrease in vivo, we monitored expression of a *tkv* enhancer trap line over a range of disc sizes. As shown in Figure S7F from [194], the pattern of *tkv* expression in early, small discs is much more uniform than it is later, strongly implying that Dpp-mediated repression is minimal early on and builds gradually. Similarly, Widmann and Dahmann [178] find that *brk* expression is also fairly uniform in early discs, only becoming strongly suppressed by Dpp later. We see much the same thing with *pent* which like *brk*, is a direct target of Dpp signaling: early expression in the center of the wing pouch, with the pattern of exclusively peripheral expression only emerging later (Fig. S7L in [194]). These results are all consistent with a Dpp signaling gradient that grows in amplitude

over time.

Given that feedback regulation of receptors and co-receptors plays an essential role in prolonging scaling in the mathematical model, it is not surprising that genotypes that eliminate both feedback loops stop scaling much earlier (at a posterior compartment size of $\sim$20 μm). In contrast, if only a single feedback loop is eliminated, gradients expand for a bit longer (posterior compartment size $\sim$30 μm), then very gradually catch up to a final λ_{app} almost equal to wild type (this agrees with experimental observations in Figure 5 from [194]). Examination of the model suggests an explanation for this behavior: because a single feedback loop capable of adjusting $\lambda_{intrinsic}$ remains, pseudo-source-sink scaling persists (Figure 2.2B), but the slower pace at which it happens means that one of the factors that contributes to amplitude growth (decreased diffusive flux due to shallower gradient slope) is less pronounced, leading to slower scaling.

In the model, scaling also fails for *pent* mutant discs, but the reasons are somewhat different. In the model, and as we observed experimentally (Figure S7 in [194]), *pent* is expressed throughout the wing pouch at early times. Since Pent removes co-receptors, Pent loss means increased co-receptor function, driving down $\lambda_{intrinsic}$ in most or all of the disc, and causing source-sink scaling to fail prematurely. Thus, whereas elimination of feedback control of receptors and co-receptors impedes scaling by interfering with the process of scaling itself, elimination of Pent further impedes scaling by changing the initial conditions of the disc. Consistent with this view are the results of RNAi up- and down-shift experiments (Figure 7 in [194]), which suggest that the effects of Pent on gradient scale are, to a fairly substantial degree, due to actions that occur during early disc growth (i.e. before mid-third instar).

In the model, the behaviors seen with other genotypes may be understood as combinations of the effects discussed above. Interestingly, the model captures the observed fact that *pent* mutant discs do not "catch up" after scaling slows, unlike Ubi-*tkv* and Uniform-*dally* discs. This difference only emerged in the model when we accounted for the fact that

basal Brinker (*brk*) expression increases dramatically during disc growth [55]; without this, modeled *pent* discs also displayed "catch-up" behavior. In effect, Brinker's rise seems to act as a countervailing force to pseudo-source-sink scaling, pushing thresholds back toward the Dpp source at the same time that increased Dpp signaling pushes them farther away. In [55], highest *brk* expression occurs where there is essentially no Dpp signaling, so Dpp itself cannot explain *brk*'s rise. In the model, we arbitrarily adjust *brk* amplitude to follow the findings from [55], however, it is intriguing to speculate that there could be some coupling between *brk* expression and disc size that would make such coupling automatic.

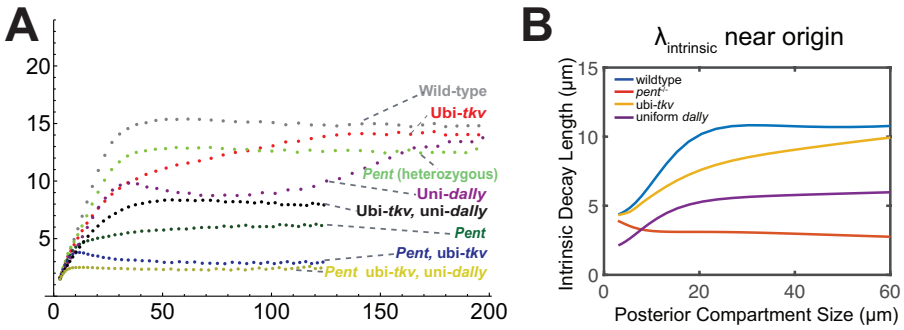

Figure 2.2: Mathematical simulations of Dpp gradient scaling.(A) pMad apparent decay lengths versus disc size for multiple genotypes including wildtype; $pent^{+/-}$; *pent*; ubi-*tkv*; uniform *dally*; ubi-*tkv*, unifrom *dally*; ubi-*tkv*, *pent*; and *pent*, ubi-*tkv*, uniform *dally*. (B) The source-adjacent Dpp intrinsic decay length ($\lambda_{intrinsic}$ averaged over locations from $x = 0$ to $x = 0.1x_{\max}$) for four genotypes (wildtype, $pent^{-/-}$, ubi-*tkv* and uniform-*dally*), was calculated and plotted as a function of compartment size ($x_{\max}$). $\lambda_{intrinsic}$ captures the distance over which boundary effects occur, so that source-adjacent $\lambda_{intrinsic}/x_{\max}$ provides a measure of the extent to which a gradient's shape near the morphogen source is strongly boundary-controlled. Transient rises in $\lambda_{intrinsic}$ demonstrate the effects of feedback downregulation of *tkv* and *dally*.

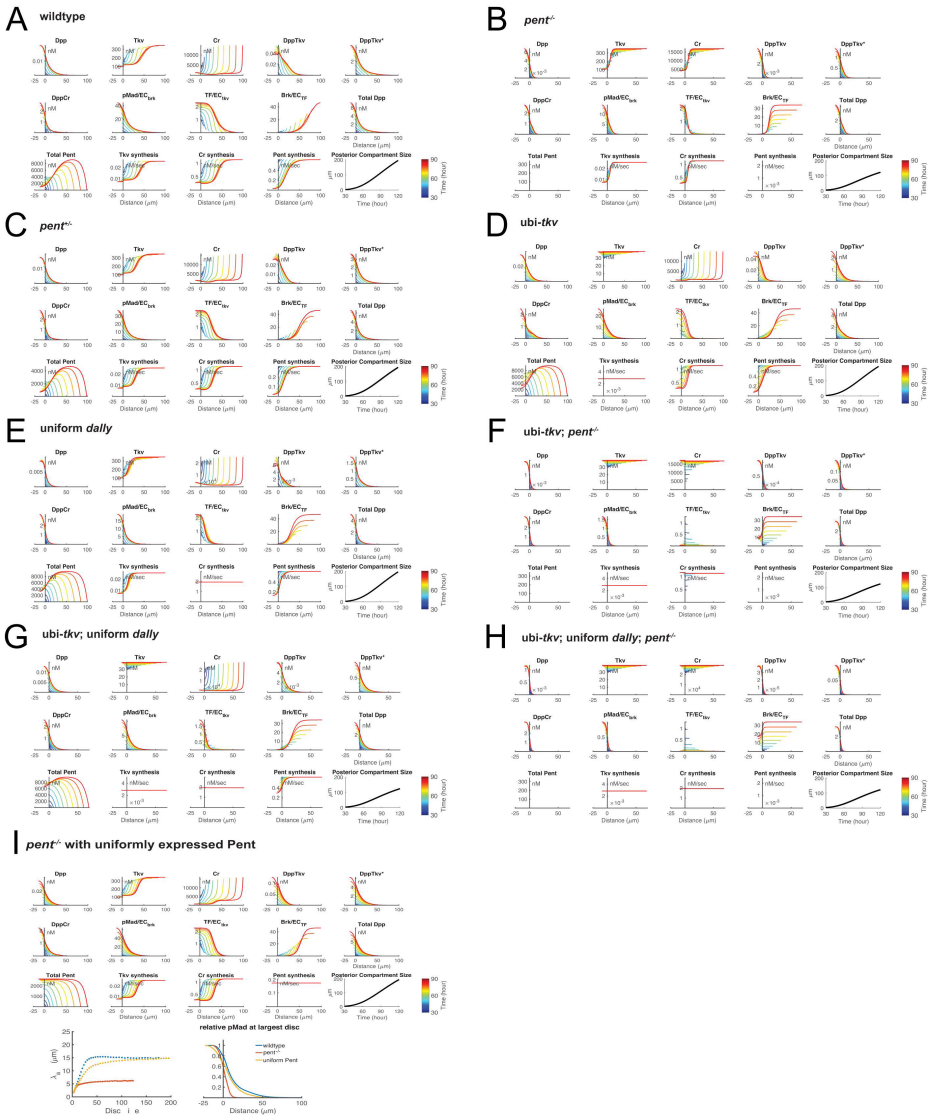

Figure 2.3: Modeling Dpp gradient scaling in the posterior compartment of the wing disc. (A-I) Time evolution of the Dpp morphogen gradient for different genotypes. Graphs show distributions of free Dpp, Dpp-receptor and -coreceptor complexes, and downstream signals and targets. $x = 0$ represents the anteroposterior compartment boundary. The final graph in the simulation shows the growth of the posterior compartment over time, and the legend shows how time is represented by color in each of the graphs. (A) wildtype; (B) $pent^{+/-}$; (C) *pent*; (D) ubi-*tkv*; (E) uniform *dally*; (F) ubi-*tkv*, *pent*; (G) ubi-*tkv*, unifrom *dally*; (H) *pent*, ubi-*tkv*, uniform *dally*; (I) *pent* with uniformly expressed Pent. In (I), the two additional graphs in the bottom compare the scaling and the pMad distribtuion at terminal time to show the uniformly expressed Pent can rescue the scaling in *pent* mutant.

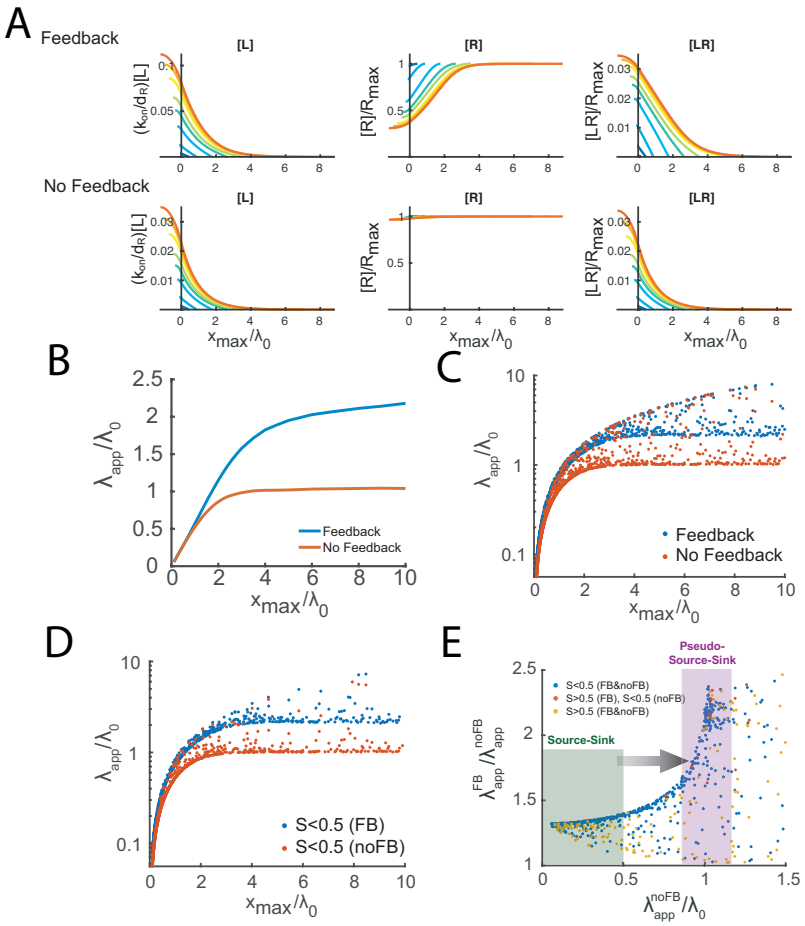

Figure 2.4: The principle of pseudo-source-sink scaling illustrated with a simplified, steady-state model, with only four free parameters, which includes only ligands, receptors and ligand-receptor complexes; irreversible capture of ligands by receptors; and downregulation of receptor synthesis. Values of LR (ligand-receptor complexes) are normalized to $R_{\max}$ (receptor concentration obtained in the absence of ligand binding or feedback), and plotted against compartment size normalized to the intrinsic decay length that would be observed in the absence of ligand binding or feedback (λ_0). (A) Distributions of ligand ([L]), receptor ([R]) and their complex ([LR]) are displayed under conditions in which feedback regulation of receptor synthesis is present ("Feedback") or ("Absent"). The parameters used for these simulations were $k = 1$, $\phi = 1$, $\xi = 1$, $\gamma = 0$ (no feedback) or 40 (feedback). The parameter ν, which was taken to be 0.05 for the no-feedback case, was adjusted to 0.15 for the feedback case in order to produce comparable [LR] amplitudes. (B) Summary of the apparent decay lengths (λ_{app}), relative to λ_0, for the curves in A. (C) Apparent decay lengths, scaled to λ_0, versus wing disc size, also scaled to λ_0. Results are for 1000 random parameter sets. Parameters ϕ, ν and ξ were sampled logarithmically between 0.01 and 100; $x_{\max}$ was sampled between 0.1 and 10. Data are as in C, except that points with high receptor saturation ($S > 0.5$) have been excluded.

Figure 2.4 *(continued)*: (E) Decay length augmentation due to feedback. The abscissa gives apparent decay lengths in the absence of feedback, λ_{app}^{noFB}, relative to the intrinsic decay length λ_0. The ordinate shows the ratio between λ_{app} for each set of parameters with and without feedback (each dot is a single parameter set). Blue denotes parameter sets where receptor saturation is below 50% at the origin for both the feedback scenario and the no-feedback scenario; red indicates that saturation is below 50% for the no-feedback case but not the no-feedback case; yellow that the saturation if above 50% in both cases (there were no parameter sets for which the feedback case was less than 50% saturated and the no-feedback case was not). The shaded bars mark the parameter regimes that produce source-sink and pseudo-source sink scaling.

2.7.3 The simiplified pseudo-source-sink model

In the section above, we show the scaling is mainly driven by the feedback regulation on receptor and co-receptor with the pseudo-source-sink mechanism. Here we illustrate the principle of pseudo-source-sink scaling using a much simpler model. In this model, shown below, only three species are considered: ligand ($[L]$), receptor ($[R]$) and the complex between ligand and receptor ($[LR]$).

$$\begin{cases} \dfrac{d[L]}{dt} = D\Delta[L] + \begin{cases} v_L - d_L[L], & \text{if } x < 0.12x_{\max} \\ -k_{on}[L][R], & \text{if } x \geq 0.12x_{\max} \end{cases} \\ \dfrac{d[R]}{dt} = \dfrac{v_R}{1+(g[LR])^2} - k_{on}[L][R] - d_R[R], \\ \dfrac{d[LR]}{dt} = k_{on}[L][R] - d_{LR}[LR]. \end{cases} \tag{2.6}$$

The spatial domain is $[0, x_{\max}]$. The effects of dilution and advection are neglected, as their impact on the full model turned out to be minimal (at least for the parameters chosen in Figure 2.3. This enabled us to solve the system at steady state on a variety of fixed domain sizes, rather than model continuous domain growth. As in the full model, ligand is produced in a localized production region that grows proportionately with the rest of the disc. The morphogen diffuses and binds receptors, but here, dissociation from receptors is neglected as

it is thought to be slow; the binding event may be understood as representing the combination of binding, uptake and destruction in a single step. Inside the morphogen production region, where we know that receptor and co-receptor levels are handled differently than elsewhere, we replace the usual receptor interaction term with a first order morphogen decay term $d_L[L]$, meant to represent the aggregate of those interactions within the production region. The production of receptor is subject to negative feedback from the amount of complex $[LR]$ (which is taken to be a proxy for "signal" from the morphogen). Parameter g is the reciprocal of an EC_{50}, and it reflects the strength of feedback. Setting $g = 0$ is equivalent to removing feedback.

We can non-dimensionalize this system to make both time and space unitless. The three species in Eq. (2.6) are thus re-named according to:

$$\begin{cases} \mu = \dfrac{k_{on}}{d_R}[L], \\ \rho = \dfrac{d_R}{v_R}[R], \\ \omega = \dfrac{d_R}{v_R}[LR]. \end{cases} \tag{2.7}$$

For receptor $[R]$ and the complex $[LR]$, this transformation is equivalent to normalization to the level of free receptor that would obtain in the absence of any feedback or ligand, $R_{\max} = v_R/d_R$. We also nondimensionalize space by defining the unit of distance to be λ_0, the intrinsic decay length that would be observed in the absence of ligand binding or feedback:

$$\lambda_0 = \sqrt{\frac{D}{k_{on}R_{\max}}} = \sqrt{\frac{Dd_R}{k_{on}v_R}}. \tag{2.8}$$

Finally, we may nondimensionalize time by scaling it to the inverse of the degradation rate of receptor d_R (although the time scale is not relevant to the steady state analysis of Eq. (2.6) it simplifies numerical solution by time-evolution). Thus, the transformation from original

coordinates (x,t) to the new coordinates (X,τ) is given by:

$$\begin{cases} X = \dfrac{x}{\lambda_0}, \\ \tau = t d_R. \end{cases} \tag{2.9}$$

The nondimensionalized equations are therefore given by

$$\begin{cases} \dfrac{d\mu(X,\tau)}{d\tau} = k\Delta\mu(X,\tau) + \begin{cases} -k\varphi\mu(X,\tau) + k\upsilon, & \text{if } X < 0.12X_{\max} \\ -k\mu(X,\tau)\rho(X,\tau), & \text{if } X \geq 0.12X_{\max} \end{cases}, \\ \dfrac{d\rho(X,\tau)}{d\tau} = \dfrac{1}{1+\left(\gamma\omega(X,\tau)\right)^2} - \mu(X,\tau)\rho(X,\tau) - \rho(X,\tau), \\ \dfrac{d\omega(X,\tau)}{d\tau} = \mu(X,\tau)\rho(X,\tau) - \xi\omega(X,\tau). \end{cases} \tag{2.10}$$

The five nondimensional free parameters in Eq. (2.10) are related to the parameters in Eq. (2.6) according to:

$$\begin{cases} k = \dfrac{k_{on} v_R}{d_R^2}, \\ \varphi = \dfrac{d_L d_R}{k_{on} v_R} \\ \upsilon = \dfrac{v_L}{v_R}, \\ \xi = \dfrac{d_{LR}}{d_R}, \\ \gamma = g\dfrac{v_R}{d_R}. \end{cases} \tag{2.11}$$

In addition, $X_{\max}$, the spatial size of the domain scaled to λ_0, enters as a sixth parameter that is required to specify the boundary condition opposite the production region. At the start of the production region we impose a no-flux boundary condition, to reflect the spatial symmetry of the system. At the end of the gradient region, $x = x_{\max}$, we impose an absorbing boundary condition.

The steady-state shapes of a series of eight gradients associated with increasing compartment sizes are shown in Figure 2.4A. Curves are color-coded to represent increasing domain sizes

(which, in this case were $X_{\max} = 1, 2, 3, 4, 5, 6, 9, \text{and } 12$). To obtain the results labeled "No Feedback", we set the feedback strength γ to zero, and adjusted the morphogen production rate to match so that the results for LR near the origin would be similar in the two cases. The third panel of each of these cases shows how feedback enables gradients to remain quasi-linear, and continue scaling, for much longer. Note also the growing suppression of receptor expression in the Feedback case.

To more thoroughly understand the behavior of the reduced model, we explored a large number of random parameters. It is clear, from Eq. (2.3) that the parameter k drops out in the steady state, so that in any exploration of parameters in which we are only interested in steady-state behavior we can simply fix k to be 1. We then randomly generated φ, υ, ξ and $X_{\max}$ using Latin hypercube sampling, initially running simulations with no feedback ($\gamma = 0$). A total simulation time of $T = 10,000$ allowed us to obtain a steady-state solution numerically. The numerical steady-state solution of ligand-receptor complex is denoted by $\omega(X)_{SS}^{noFB}$. Next, we ran simulations with feedback. Rather than choose values of γ at random, we selected them so as to exclude those that would provide only trivial amounts of feedback, as well as those that would provide so much feedback that receptors would be fully suppressed from the start. In particular, we chose γ as defined by

$$\gamma = \frac{1}{0.25 \max\limits_{X \in [0, X_{\max}]} \omega(X)_{SS}^{noFB}}. \tag{2.12}$$

We compare the results of feedback and no-feedback scenarios for 1000 randomly generated parameter sets in Figure 2.4C. Note the ability of feedback to produce values of λ_{app} much greater than observed without feedback. This effect is even more apparent if we eliminate those cases in which receptor saturation S—defined as the fraction of total receptors that are occupied (i.e. $S = [LR]/([LR]+[R])$)—exceeds 50% at the origin (the boundary between the production region and the rest of the domain), shown in Figure 2.4.

The reason for this is that morphogen decay is a function of free receptor level, and saturation amounts to lowering free receptor level. Thus, a gradient can, in principle, extend its apparent decay length simply by saturating receptors, but there are two reasons why this regime is likely to be un-biological. First, in this regime gradients adopt sigmoidal shapes, and such shapes are not observed in any known morphogen system. Second, a consequence of operating in this regime is that gradient position becomes extremely sensitive to small changes in the rate of morphogen production [90].

The plots in Figure 2.4CD do not permit individual parameter sets—considered with and without feedback—to be compared against each other. We do this in Figure 2.4E, which shows the extent to which λ_{app} is increased by feedback. Notice that, when λ_{app}^{noFB} is less than half the value of λ_0, the improvement in λ_{app} that comes from feedback is always modest. This is because, in this regime, gradient shape is close to linear even in the absence of feedback, and thus both the feedback and non-feedback case display true source-sink scaling. However, once λ_{app}^{noFB} is on the order of λ_0 or larger, the improvement in λ_{app} due to feedback is much greater for almost all parameter sets: this is the pseudo-source-sink scaling regime, in which gradients remain quasilinear and scale automatically, even though the true sink is located many values of $\lambda_{intrinsic}$ away. In highly saturated regimes (red and yellow symbols), however, some of the feedback cases perform no better than the no-feedback cases, presumably because scaling due to saturation of receptors does not require feedback.

2.8 Discussion

Morphogen gradients play a central role in animal development, tying cell behavior to spatial location. Whereas monotonic gradients of almost any sort can encode location, to encode relative location on a domain of changeable size, gradients must scale. To do so, at least one of three processes—morphogen production, transport or removal (decay)—must somehow

be coupled to the size of the morphogen field.

There have been several proposals for making such coupling automatic [11, 22, 182], an elegant example of which is the expansion-repression (ER) model. The present study began as an attempt to test whether the secreted protein Pent, which has been implicated in scaling of the *Drosophila* wing disc Dpp gradient, fits the requirements of the expander in this model. We found that Pent lacks the necessary spatial range, and that its effects can be phenocopied by disabling co-receptors in just the Pent expression domain (Figure 1-4 in [194]), suggesting that Pent need not act at a distance. We then made the observation that feedback repression of receptor and co-receptor synthesis is required for scaling (Figure 5 in [194]).

How exactly does scaling happen? Having a mathematical model that reproduces wildtype and mutant phenotypes allowed us to develop a plausible explanation. Surprisingly, the explanation does not attribute scaling to a single mechanism, but rather to a collection of passive and active processes:

First, when discs are very small—with compartment sizes up to about 10 μm, as one observes through early or mid-second larval instar—the model exhibits source-sink scaling because $\lambda_{intrinsic}$ is large enough that boundaries act as sinks. Although it is not possible to measure $\lambda_{intrinsic}$ directly, λ_{app} sets a lower bound on $\lambda_{intrinsic}$ and is well-known at later stages (for both Dpp and pMad) to be on the order of 15-20 μm [42, 55, 157, 174]. It is thus reasonable to think that, at early times, $\lambda_{intrinsic}$ could indeed exceed morphogen field size.

Later, as discs grow beyond their initial values of $\lambda_{intrinsic}$, the model predicts a "pseudo-source-sink scaling" regime (Figure 2.2), where rising morphogen levels drive down receptor and co-receptor expression, raising $\lambda_{intrinsic}$ near the morphogen source. Far from the morphogen source, however, $\lambda_{intrinsic}$ remains small, effectively creating a "pseudo-sink". As long as growth occurs in the amplitude of the morphogen gradient near the source, gradients respond by becoming shallower near the source, which makes them expand further out-

ward. Moreover, as discussed above, when gradients become shallower, that in itself drives amplitudes up, effecting something of a positive feedback.

This process occurs until receptor and co-receptor expression can be downregulated no further—their levels cannot fall to zero because their function is required to drive their repression. After that, wildtype gradients outgrow their $\lambda_{intrinsic}$ and cease scaling altogether. Not surprisingly, genotypes that compromise the ability of the morphogen to repress receptor and/or co-receptor synthesis result in gradients that cease scaling sooner.

In the output of the mathematical model, the transition from a regime in which gradients scale to one in which they do not is marked by a shift in gradient shape from linear to roughly exponential (Figure 2.3). To some extent this behavior is an artifact of using on a one-dimensional formulation. Current evidence indicates that Dpp diffuses in the basolateral space between columnar cells of the disc [56, 192]; as a result one should expect a continual "leak" of Dpp through the adjacent basement membrane (such structures are not barriers to diffusion [33]), producing, in effect, an additional sink. A more complete analysis of source-sink scaling with sinks in multiple dimensions shows that, as long as cell height and disc width increase in size proportionately (which is approximately what occurs during larval growth), gradients will still scale automatically, but may display any shape between linear and exponential. Furthermore, the necessary and sufficient condition for source-sink scaling—that $\lambda_{intrinsic}$ be larger than the anteroposterior field size—remains unchanged.

The idea that amplitude growth contributes substantially to morphogen gradient scaling is not new (reviewed by [163]). For example, selection for larger or smaller *Drosophila* embryos is accompanied by compensatory shifts in the locations at which Bicoid target genes are turned on. These shifts occur not because of a change in λ_{app} of the Bicoid gradient, but an increase in gradient amplitude alone [22]. For exponential gradients (like the Bicoid gradient), simple amplitude increase produces constant-distance shifts in threshold positions, making thresholds near the morphogen source over-scale and those far away under-scale. Thus, like

source-sink scaling, scaling due to pure-amplitude growth runs into spatial limits beyond which it is not very effective. The pseudo-source-sink mechanism partially compensates for this problem by displacing the effective sink away from the source as the amplitude near the source grows. However, it should be noted that in this case, what is truly scaling is just the relative shape of the morphogen gradient, as measured by its λ_{app}, and not the locations where absolute thresholds are crossed. At least some Dpp target genes (e.g. *dad*) do seem to scale in just this way [55, 174].

In addition to the various mechanisms—source-sink scaling, amplitude growth, pseudo-source-sink scaling—that drive Dpp gradient expansion in the model described here, other processes may matter in vivo. Growth itself tends to propel forward the molecules within a tissue—a process termed *advection*—and some growth-driven gradient expansion can occur by that process alone, although under typical conditions the effect is likely to be small [43]. Automatic scaling of certain locations within morphogen gradients can also occur if gradients operate far from steady state, i.e. if growth moves cells to new locations faster than the dynamic processes that determine gradient shape can adjust [43]. The model we present here, at least over the parameter ranges explored, operates fairly close to steady state (i.e. gradients are relatively independent of growth rate), meaning that such "dynamics"-dependent scaling is not a significant contributor.

Overall, the experiments and modeling presented here suggest a view of scaling as more "kluge" than elegant control system. Small fields with leaky boundaries contribute source-sink and amplitude-growth scaling effectively "for free", but not indefinitely, as both start to fail at large field size. Pseudo-source-sink effects prolong scaling, but only for so long, as receptor function can be suppressed only so much before signaling itself becomes too compromised.

The present study suggests that the source-sink gradients of early theorists [182], which fell strongly out of favor once it was observed that gradient shapes are quasi-exponential,

may actually have much to offer in explaining the early behaviors of morphogen gradients. Interestingly, recent work argues that source-sink behavior is also the primary determinant of BMP gradient shape in early zebrafish embryos [196]. The behavior in that system would, by our nomenclature, be more precisely termed pseudo-source sink, since the sink in that system arises from the binding of BMP to chordin, and chordin is downregulated by BMP—a feedback loop functionally analogous to the downregulation of Tkv and Dally by Dpp in the wing disc. The parallels between that system and the work described here are intriguing because the BMP gradient that patterns the early vertebrate embryo also exhibits scaling behavior (in response to embryo bisection [14, 29] as well as other kinds of manipulations [64].

The inherent limitations of pseudo-source-sink scaling that, in the model, cause scaling to stop once a certain size is reached may seem like a drawback, but may actually be a feature. Morphogens control not only pattern but also growth; in wing discs this is an essential function of Dpp [3, 106]. Wartlick argue that the key signal that maintains disc growth is a continually rising Dpp signal [174]. If gradient scaling is required to ensure that this rise occurs proportionally at all locations, as is the case in the model, failure of scaling could potentially play a causal role in terminating growth. What is intriguing about this idea is that it predicts that the size at which growth stops should correlate with the size at which scaling stops, which we in fact observe in the data: As shown in Figure 5 in [194], *pent* and ubi-*tkv*/uniform-*dally* mutant discs stop growing at a substantially smaller size than wildtype discs. These observations suggest that it may be better to view scaling and growth as one coupled system, rather than a mechanism for adjusting pattern to size.

Although the present study provides a potential explanation for Dpp gradient scaling that correctly predicts the larval phenotype of the *pent* mutant, it does not provide a satisfying explanation for why Pent is used by wing discs in the first place. In the model, *pent* discs fail to scale mainly because they start out with too small a $\lambda_{intrinsic}$, but since all Pent does

(in the model) is inhibit receptor function, it is not clear why discs don't just dispense with Pent altogether, and simply express fewer receptors and co-receptors from the outset. The situation suggests that there may be as-yet-unappreciated functions of Pent. For example, even though the model argues that Pent diffusion is not necessary for scaling, it might still be possible that Pent has a useful role as a repressible expander during very early stages, when Pent's λ_{app} is not so small, relative to disc size. It may also be worth recalling the characteristic adult phenotype displayed by *pent* mutants: loss of the fifth longitudinal vein [165]. Whereas scaling abnormalities might explain mispositioning of a vein, vein loss suggests that some Pent actions may be unrelated to Dpp gradient scaling.

2.9 Extended Information

2.9.1 Simulating rescue by compartment-wide Pent overexpression; evaluating the necessity for Pent diffusivity

The *pent* phenotype in adult wings can be rescued by overexpressing Pent uniformly throughout the wing disc [165] or throughout the posterior compartment (Figure S1 in [194])). To see whether the model and the parameters that were selected reproduce this behavior, we modified equations Eq. (2.1) to replace the equation for $[Pent]_{out}$ with

$$\frac{\partial [Pent]_{out}}{\partial t} + \frac{\partial \left(V [Pent]_{out}\right)}{\partial x} = v_{pent} + D_{pent} \Delta [Pent]_{out} - k_6 [Pent]_{out}, \tag{2.13}$$

Here v_{pent} is a uniform source term that was set to 1.71×10^{-10} M sec^{-1}. The results of numerical simulation are shown in Figure 2.3I. They show that, in the model, by the end of disc growth, posterior compartment-wide overexpression of Pent almost fully rescues the Pent phenotype.

Some of the experiments in the manuscript raise the question of whether Pent needs to diffuse at all to carry out its functions. To explore this question, we re-ran the results of the wildtype case using a value of D_{pent} of 0.01 μm^2 sec^{-1}, a factor of 2000 times smaller than had been used before. This change lowers $\lambda_{intrinsic}$ for Pent from 8 μm to 0.18 μm, i.e. it makes Pent effectively indiffusible. We compare the effect of this change on the time course of pMad apparent decay lengths in all of the above mutant scenarios. As can be seen, there is very little difference in the outcomes of these simulations whether Pent diffuses rapidly, or hardly at all (Figure 2.5).

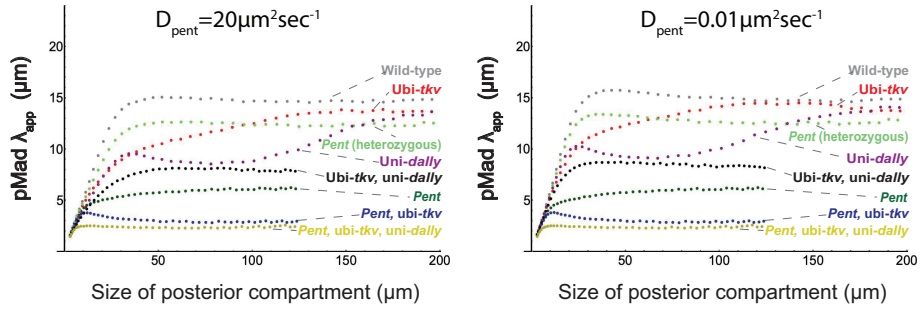

Figure 2.5: Effect of Pent diffusivity on pMad apparent decay length. The left panel reproduces Figure 2.2A and the right panel shows results when Pent diffusivity was lowered by a factor of 2000, to 0.01 μm^2 sec^{-1}.

2.9.2 Lagrangian framework for solving mathematical equations

The spatial domain of Eq. (2.1) is time-dependent, whereas PDEs solvers usually require a fixed domain. We therefore use the following linear coordinate transformation to transfer the dynamical spatial domain onto a fixed domain:

$$\begin{cases} x = r(\tau)X \\ t = \tau \end{cases}. \tag{2.14}$$

where $r(\tau) = \frac{x_{\max}(\tau)}{x_0}$. The transferred spatial domain is $X \in [0, x_0]$, where x_0 is the initial posterior compartment size shown in Eq. (2.3). Derivatives in the Lagrangian coordinate system (X, τ) have the following relationships to derivatives in the original coordinate system (x, t):

$$\begin{cases} \dfrac{\partial}{\partial X} = r\dfrac{\partial}{\partial x} \\ \dfrac{\partial^2}{\partial X^2} = r^2\dfrac{\partial^2}{\partial x^2} \\ \dfrac{\partial}{\partial \tau} = \dfrac{\partial}{\partial t} + \dfrac{\partial}{\partial x}\dfrac{\partial x}{\partial \tau} = \dfrac{\partial}{\partial t} + \dfrac{1}{r}\dfrac{dr}{d\tau}\dfrac{\partial}{\partial X} \end{cases} \tag{2.15}$$

The transformed growth velocity $\tilde{V}(X, \tau)$ has a similar relationship to Eq. (2.2).

$$\tilde{V}(X, \tau) = \frac{X}{x_0}\tilde{V}(x_0, \tau). \tag{2.16}$$

Using Eq. (2.15) and Eq. (2.16), we have

$$\frac{\partial V}{\partial x} = \frac{1}{r}\frac{\partial \tilde{V}}{\partial X} = \frac{1}{r}\frac{1}{x_0}\tilde{V}(x_0, \tau) = \frac{f(x_{\max}(\tau), \tau)}{x_{\max}(\tau)}. \tag{2.17}$$

For any equation in Eq. (2.1) with the general form

$$\frac{\partial [P]}{\partial t} + \frac{\partial \left(V[P]\right)}{\partial x} = F\left([P], x, t\right) + D\Delta[P]. \tag{2.18}$$

the transformed equation in Lagrangian coordinate is given by

$$\frac{\partial [P]}{\partial \tau} = D\left(\frac{x_0}{x_{\max}}\right)^2\frac{\partial^2 [P]}{\partial X^2} + F([P], r(\tau)X, \tau) - \frac{f(x_{\max}(\tau), \tau)}{x_{\max}(\tau)}[P]. \tag{2.19}$$

Since both boundary conditions are homogeneous, the transformed equation inherits the boundary conditions from the original condition: absorbing boundary at one side and no-flux boundary at the other. We solved the transformed equations using PDEs solver *pdepe* in MATLAB 2015b.

2.9.3 Parameter selection

There are 36 potentially free parameters in Eq. (2.1). We fixed D_{dpp} and k_1 to match values in the literature (Table 2.1). In the absence of direct measurements of Pent diffusivity, we set the value of D_{pent} to be the same as D_{dpp}, i.e. 20 μm^2 $\sec^{-1}$. To match the observed apparent decay length of Pent ($\sim$8 μm), we fixed k_6 at 0.313 $\sec^{-1}$. The remaining 32 parameters were logarithmically sampled across intervals of several orders of magnitude. Deeply sampling a 32–dimensional space at random is, of course, prohibitive (covering as few as three points in each dimension requires $> 10^{15}$ parameter sets), so an iterative procedure was used to converge on reasonable parameter values.

To begin with, parameter selection was subjected to certain constraints even prior to generating numerical solutions. These constraints reflected the requirement that values of λ_{app} for Dpp, when measured outside of the Dpp production region, should be no higher than about 30 μm for Dpp. In general, when field size $\gg \lambda_{app}$ so that boundaries play a minimal role in determining gradient shapes (e.g. toward the end of disc growth), we expect $\lambda_{app} \simeq \lambda_{intrinsic}$, where

$$\lambda_{intrinsic} = \sqrt{\frac{D}{k_{rem}}}. \tag{2.20}$$

Here D is the diffusion coefficient and k_{rem} is an effective removal rate constant. For any diffusing species, an explicit expression for k_{rem}, as a function of x and t, can be found by taking the right-hand side of the equation for that species, dropping diffusion and production terms, multiplying by -1, and dividing the remaining terms by the concentration of that species. For example, for Dpp,

$$k_{rem,Dpp}(x,t) = k_1[Tkv] + k_2[Cr] - \frac{k_{r1}[DppTkv] - k_{r2}[DppCr]}{[Dpp]} \tag{2.21}$$

the last term of which may be neglected at locations far from the Dpp source. In contrast,

for $Pent_{out}$,

$$k_{rem,Pent}(x,t) = k_6. \tag{2.22}$$

As placing a ceiling on $\lambda_{intrinsic}$ equates to placing a floor on k_{rem}, the required constraints on $\lambda_{intrinsic}$ for Pent and Dpp constrain $k_1[Tkv] + k_2[Cr]$ and k_6 respectively. As $[Tkv]$ and $[Cr]$ have maximum possible values of $tkv1/d_{tkv}$ and $cr1/d_{cr}$, the constraint that $\lambda_{intrinsic,Dpp} \leq 30$, implies $k_1 tkv1/d_{tkv} + k_2 cr1/d_{cr} \geq D_{dpp}/900$.

To find parameter sets that fit experimental data, Latin Hypercube sampling [155] was used as a high dimensional random number generator. Using a multi-step procedure (described below), we selected parameter sets based on their ability to fit dynamic data for eight genotypes: wildtype; $pent^{+/-}$; $pent^{-/-}$; ubi-*tkv*; uniform *dally*; ubi-*tkv*, uniform *dally*; ubi-*tkv*, $pent^{-/-}$; ubi-*tkv*, uniform *dally*, $pent^{-/-}$. Numerical solutions for each of these conditions were obtained by altering appropriate parameters from their wildtype values. For ubi-*tkv* (Tkv uniformly expressed in the entire disc), we took $tkv2 = tkv3 = 0$, and $tkv1$ to be an adjustable parameter. Similarly, for uniform *dally*, we took $cr2 = cr3 = 0$, and $cr1$ to be an adjustable parameter. For $pent^{+/-}$, we lowered the production rate of pent by half. To model double and triple mutants, we combined several of these alterations.

STEP 1: First, we randomly sampled all parameters in a wide range to find sets that produced roughly good decay lengths for wildtype and $pent^{-/-}$ conditions. The $k*$ parameters (k_1, k_2, k_3, k_4, k_{r1}, k_{r2}) were sampled over seven orders of magnitude $(10^{-8}, 10^{-1})$. Production rates (e.g. $tkv1$, $cr1$, v_{pent}) were sampled over two orders of magnitude $(10^{-5}, 10^{-3})$. Degradation rates (e.g. d_{dpp}, d_{tkv}) were sampled over two orders of magnitudes $(10^{-6}, 10^{-4})$. $EC50s$ (e.g. EC_{pent}) were sampled over two orders of magnitude $(10^{-3}, 10^{-1})$. 500,000 independent parameter sets were explored. Parameters were selected based on their ability to meet constraints on $\lambda_{intrinsic}$ (as discussed above), plus the following constraints on the observed λ_{app} for pMad (where λ_{app} was determined by identifying the location where pMad

declines to $1/e$ of its maximum value outside of the production region):

For wildtype:

1. $\max_{s\in(0,s_{\max})} \lambda_{app} \in [12, 20]$,
2. $\max_{s\in(0,s_{\max})} \lambda_{app} - \lambda_{app}(s_{\max}) \leq 5$.

For $pent^{-/-}$:

1. $\max_{s\in(0,s_{\max})} \lambda_{app} \leq 12$,
2. $\max_{s\in(0,s_{\max})} \lambda_{app} - \lambda_{app}(s_{\max}) \leq 5$.

Here $\lambda_{app}(s)$ is understood as the apparent decay length of pMad when the size of posterior compartment is s μm. The maximum value of s is 196 μm.

STEP 2: Starting from one selected parameter set from STEP1, we randomly perturbed 11 parameters—k_1, k_2, k_3, k_4, k_5, k_{r1}, k_{r2}, EC_{tf}, EC_{brk}, EC_{tkv}, and EC_{pent}. The $k*$ parameters were varied over two orders of magnitude, and the "EC" parameters varied between 0.25 and 4-fold (as before, random numbers were sampled logarithmically). 100,000 independent parameter sets were explored. Parameters were first tested for their ability to meet constraints on $\lambda_{intrinsic}$ (as discussed above), and results then tested for the ability to meet the following constraints on λ_{app} for pMad:

For wildtype:

1. $\max_{s\in(0,s_{\max})} \lambda_{app} \in [14, 17]$,
2. $\max_{s\in(0,s_{\max})} \lambda_{app} - \lambda_{app}(s_{\max}) \leq 2$.

For $pent^{-/-}$:

1. $\max_{s\in(0,s_{\max})} \lambda_{app} \in [3.5, 7]$,
2. $\max_{s\in(0,s_{\max})} \lambda_{app} - \lambda_{app}(s_{\max}) \leq 2$.

STEP 3: From 18 parameter sets passing the above tests, four were selected for further exploration. we perturbed all parameters over a range from 0.5-2-fold, keeping those that met the following constraints. 500,000 perturbations were carried out for each initial parameter set.

For wildtype:

1. $\max_{s\in(0,s_{\max})} \lambda_{app} \in [14.5, 16.5]$,
2. $\max_{s\in(0,s_{\max})} \lambda_{app} - \lambda_{app}(s_{\max}) \leq 2$.

For $pent^{-/-}$:

1. $\max_{s\in(0,s_{\max})} \lambda_{app} \in [4.5, 6.5]$,
2. $\max_{s\in(0,s_{\max})} \lambda_{app} - \lambda_{app}(s_{\max}) \leq 2$.

For ubi-tkv :

1. $\max_{s\in(0,s_{\max})} \lambda_{app} \leq 17$,
2. $\max_{s\in(0,s_{\max})} \lambda_{app} - \lambda_{app}(s_{\max}) \leq 1$.

For uniform $dally$:

3. $\max_{s\in(0,s_{\max})} \lambda_{app} \leq 17$,
4. $\max_{s\in(0,s_{\max})} \lambda_{app} - \lambda_{app}(s_{\max}) \leq 1$.

For ubi-tkv, uniform $dally$:

5. $\max_{s\in(0,s_{\max})} \lambda_{app} \in [5, 8]$.

Nine parameter sets passed all of the tests, and one was selected for further refinement. We examined the dynamic behavior of selected parameter sets to identify ones that fit observations reasonably well. We carefully inspected levels and distributions of all species, manually adjustng some parameters to better match prior knowledge: e.g. scaling of λ_{app} for total Dpp; Dpp and pMad gradient shapes that are close to exponential at the end of larval development; degrees of central-suppression of Tkv and Cr at the end of larval development that are consistent with observations; spatial patterns for Tkv, Cr, Brk and Pent that are consistent with observations; and levels of total Dpp inside cells that are much higher than outside [80, 192].

The final parameter set that was selected is given in Tables 2.1 and 2.2. Also shown are the parameters a, b and n that appear in growth rate equation Eq. (2.3). As shown in Figure S3 in [194], homozygous pent mutant discs grow more slowly than wild type discs, and therefore are fit with a different value of parameter b. Although we did not produce full growth curves for all genotypes, the distribution of posterior compartment sizes that we observed suggests that all of the genotypes that scale poorly (ubi-*tkv*, $pent^{-/-}$; uniform *dally*, $pent^{-/-}$; ubi-*tkv*, uniform *dally*; ubi-*tkv*, uniform *dally*, $pent^{-/-}$) grow at a rate similar to $pent^{-/-}$, whereas the others grow at a rate similar to wildtype (i.e. $pent^{+/-}$; ubi-*tkv*; uniform *dally*). The value of b used in simulation was therefore selected accordingly from the wildtype and the $pent^{-/-}$ values. The results of the numerical solutions for each genotype are shown in Figure 2.3.

2.9.4 Local sensitivity analysis

To determine whether the qualitative behaviors of the system are strongly dependent on the choice of parameters values, we systematically varied all parameters up and down 10-fold, and measured the effect on λ_{app} of pMad. Specifically, we calculated the ratio between λ_{app} at

Parameter	Value	Units	Reference
D_{dpp}	20	μm^2 $\sec^{-1}$	[192]
D_{pent}	20	μm^2 $\sec^{-1}$	
k_1	1.00×10^5	M^{-1} $\sec^{-1}$	[91]
k_2	9.69×10^5	M^{-1} $\sec^{-1}$	
k_3	1.32×10^2	M^{-1} $\sec^{-1}$	
k_4	2.39	M^{-1} $\sec^{-1}$	
k_5	4.05×10^3	M^{-1} $\sec^{-1}$	
k_6	3.13×10^{-1}	$\sec^{-1}$	
k_{r1}	2.87×10^{-5}	$\sec^{-1}$	
k_{r2}	7.37×10^{-3}	$\sec^{-1}$	
$tkv1$	4.27×10^{-12}	M $\sec^{-1}$	
$tkv2$	1.99×10^{-11}	M $\sec^{-1}$	
$tkv3$	1.42×10^{-12}	M $\sec^{-1}$	
$cr1$	8.12×10^{-11}	M $\sec^{-1}$	
$cr2$	1.06×10^{-9}	M $\sec^{-1}$	
$cr3$	3.25×10^{-11}	M $\sec^{-1}$	
v_{dpp}	8.40×10^{-12}	M $\sec^{-1}$	
v_{pmad}	6.44×10^{-11}	M $\sec^{-1}$	
v_{pent}	6.22×10^{-10}	M $\sec^{-1}$	
v_{tf}	9.46×10^{-13}	M $\sec^{-1}$	
v_{brk}	6.58×10^{-14}	M $\sec^{-1}$	
d_{tkv}	6.61×10^{-4}	$\sec^{-1}$	
d_{cr}	6.04×10^{-5}	$\sec^{-1}$	
d_{pmad}	1.00×10^{-3}	$\sec^{-1}$	
d_{pent}	5.59×10^{-5}	$\sec^{-1}$	
d_{tf}	3.38×10^{-5}	$\sec^{-1}$	
d_{brk}	$3.52x10^{-5}$	$\sec^{-1}$	
d_{dpp}	1.16×10^{-4}	$\sec^{-1}$	
d_{dpptkv}	5.59×10^{-5}	$\sec^{-1}$	
$d_{dpptkv*}$	3.95×10^{-5}	$\sec^{-1}$	
d_{dppcr}	2.57×10^{-3}	$\sec^{-1}$	
EC_{brk}	2.24×10^{-10}	M	
EC_{tkv}	9.60×10^{-9}	M	
EC_{cr}	9.60×10^{-9}	M	
EC_{tf}	3.05×10^{-10}	M	
EC_{pent}	2.24×10^{-9}	M	
p	0.12	–	
x_0	0.1	μm	
a	0.1168	$\sec^{-1}$	Figure S3 in [194]
b	4.77×10^{-6}	–	Figure S3 in [194]
n	3	–	Figure S3 in [194]

Table 2.1: Wildtype Parameters.

Parameter	Value	Units	Reference
$pent^{+/-}$			
v_{pent}	3.11×10^{-10}	M sec^{-1}	
$pent^{+/-}$			
k_3	0	M^{-1} sec^{-1}	
v_{pent}	0	M sec^{-1}	
b	6.02×10^{-6}	–	Figure S3 in [194]
ubi-tkv			
$tkv1$	3.42×10^{-12}	M sec^{-1}	
$tkv2$	0	M sec^{-1}	
$tkv3$	0	M sec^{-1}	
uniform $dally$			
$cr1$	1.95×10^{-9}	M sec^{-1}	
$cr2$	0	M sec^{-1}	
$cr3$	0	M sec^{-1}	
ubi-tkv, uniform $dally$			
$tkv1$	2.85×10^{-12}	M sec^{-1}	
$tkv2$	0	M sec^{-1}	
$tkv3$	0	M sec^{-1}	
$cr1$	1.95×10^{-9}	M sec^{-1}	
$cr2$	0	M sec^{-1}	
$cr3$	0	M sec^{-1}	
b	6.02×10^{-6}	–	Figure S3 in [194]
ubi-tkv, $pent^{-/-}$			
$tkv1$	2.85×10^{-12}	M sec^{-1}	
$tkv2$	0	M sec^{-1}	
$tkv3$	0	M sec^{-1}	
k_3	0	M^{-1} sec^{-1}	
v_{pent}	0	M sec^{-1}	
b	6.02×10^{-6}	–	Figure S3 in [194]
ubi-tkv, uniform $dally$, $pent^{-/-}$			
$tkv1$	2.85×10^{-12}	M sec^{-1}	
$tkv2$	0	M sec^{-1}	
$tkv3$	0	M sec^{-1}	
$cr1$	1.95×10^{-9}	M sec^{-1}	
$cr2$	0	M sec^{-1}	
$cr3$	0	M sec^{-1}	
k_3	0	M^{-1} sec^{-1}	
v_{pent}	0	M sec^{-1}	
b	6.02×10^{-6}	–	Figure S3 in [194]

Table 2.2: Parameter alterations in mutant genotypes.

the end of the simulation for the unperturbed case and the perturbed case. This was done for four genotypes (wildtype; $pent^{-/-}$; ubi-tkv; uniform $dally$) (Table 2.3). Most perturbations produced relatively small changes. Specifically, the system is relatively insensitive to D_{pent}, k_4, k_5, k_6, k_{r1}, k_{r3}, $tkv3$, $cr3$, d_{dpp} and d_{dpptkv}, whereas it is relatively sensitive to D_{dpp}, k_1, k_3, v_{pent}, d_{pmad}, d_{pent}, v_{dpp} and EC_{pent}. Sensitivity to D_{dpp} is to be expected, of course, because at the end of the simulation, λ_{app} for pMad mirrors $\lambda_{intrinsic}$ for Dpp which, by definition varies with the square root of D_{dpp}. By the same token, almost any change in D_{dpp} can be compensated for by a commensurate change in association rate constants k_1 or k_2 that preserves $\lambda_{intrinsic}$ for Dpp. In other words, even though parameters were selected using a model in which the value of D_{dpp} was fixed, the ability of the model to fit the data does not place constraints on the choice of D_{dpp}.

2.9.5 The influence of dimensionality on source-sink scaling

Morphogen gradients often provide positional information along a single direction; in the wing disc, for example, the Dpp gradient patterns the anterioposterior (AP) axis. Even though biology happens in three dimensions, it is common to model morphogen gradients as reaction-diffusion systems in just this one dimension. This greatly simplifies analysis, but can introduce artifacts. Here we discuss one type of artifact that arises when wing discs are small, and can affect the shapes of gradients produced by the mathematical model described above. In multiple dimensions, the steady state form of a reaction-diffusion equation within a morphogen domain in which morphogen is not produced is:

$$0 = D\nabla^2 C - f(C), \tag{2.23}$$

where C is morphogen concentration, the first term describes diffusion, and the second term stands for any intrinsic decay processes. We focus on the steady state here because, as

Ratio of perturbed λ_{app} to unperturbed λ_{app}.								
	wildtype		*pent*$^{-/-}$		ubi-*tkv*		uniform *dally*	
Fold perturbation:	×0.1	×10	×0.1	×10	×0.1	×10	×0.1	×10
D_{dpp}	0.4	3.0	0.4	2.4	0.4	2.4	0.4	3.0
D_{dpp}, k_1, k_2	1.0	1.0	1.0	1.0	1.0	1.0	1.0	1.0
D_{pent}	1.0	1.1	–	–	1.0	1.0	1.0	0.9
D_{pent}, k_6	1.0	1.0	–	–	0.98	1.0	1.0	1.0
k_1	1.4	0.6	0.5	1.0	0.8	0.8	0.7	0.5
k_2	1.6	0.5	2.8	0.3	2.2	0.3	1.2	0.3
k_3	0.6	1.5	–	–	0.4	1.9	0.4	1.2
k_4	1.0	1.0	1.0	1.1	1.0	1.0	1.0	1.0
k_5	0.9	1.0	1.0	1.0	1.0	1.0	1.0	1.0
k_6	1.1	1.0	–	–	1.0	1.0	0.9	1.0
k_{r1}	1.0	1.0	1.0	1.0	1.0	1.0	1.0	1.0
k_{r2}	0.8	1.5	0.4	2.5	0.5	2.0	0.6	1.1
$tkv1$	1.3	0.7	0.8	0.9	0.8	0.8	1.1	0.5
$tkv2$	1.1	0.7	0.5	0.9	–	–	0.7	0.5
$tkv3$	1.0	1.0	1.0	1.1	–	–	1.0	0.7
$cr1$	1.1	0.9	1.1	0.5	1.1	0.6	1.1	0.3
$cr2$	1.2	0.6	1.5	0.3	1.5	0.3	–	–
$cr3$	1.0	1.0	1.0	0.8	1.0	0.9	–	–
v_{dpp}	0.4	3.1	0.4	2.4	0.4	2.4	0.4	3.0
v_{pmad}	1.2	0.7	0.5	1.0	0.8	0.8	0.7	0.5
v_{pent}	0.6	1.5	–	–	0.4	1.9	0.4	1.2
v_{brk}	1.1	1.0	1.0	0.5	1.2	0.7	0.6	0.6
d_{tkv}	0.7	1.4	1.0	0.5	0.9	0.8	0.5	0.7
d_{cr}	1.0	1.3	0.3	2.7	1.0	1.3	1.0	0.9
d_{pmad}	0.7	1.2	1.0	0.5	0.8	0.8	0.5	0.7
d_{pent}	1.0	1.1	–	–	1.0	1.0	1.0	0.9
d_{tf}	0.7	1.0	0.6	1.1	0.8	1.0	0.6	1.0
d_{brk}	1.0	1.1	0.6	1.0	0.7	1.2	0.8	0.6
d_{dpp}	1.2	0.7	0.5	1.1	0.8	0.8	0.7	0.5
d_{dpptkv}	1.0	0.9	1.0	1.0	1.0	1.0	1.0	1.0
$d_{dpptkv*}$	1.0	1.2	1.2	0.5	1.2	0.7	0.7	0.7
d_{dppcr}	1.5	0.8	2.5	0.4	2.0	0.5	1.1	0.6
EC_{brk}	1.1	0.5	1.0	0.5	1.3	0.7	0.6	0.5
EC_{tkv}	1.1	0.8	0.8	0.9	–	–	1.1	0.5
EC_{cr}	1.3	1.0	1.6	0.6	1.6	0.7	–	–
EC_{tf}	1.0	1.1	0.5	1.0	0.7	1.2	0.6	0.6
EC_{pent}	0.7	1.4	–	–	0.5	1.5	0.5	0.8

Table 2.3: Local sensitivity analysis.

described elsewhere, the dynamic results of the model developed here are quasi-steady state (e.g. increasing or decreasing all rate constants proportionately has little effect on the model output).

If decay is linear, i.e. uniform in space and proportional to morphogen concentration, then this steady state equation becomes

$$0 = D\nabla^2 C - kC, \tag{2.24}$$

which may be written as

$$0 = \lambda^2_{\text{intrinsic}}\nabla^2 C - C, \tag{2.25}$$

where $\lambda_{intrinsic}$ has its usual definition. This may be simplified further, if k is very small, i.e. if $\lambda_{intrinsic}$ is very large, to

$$0 = \nabla^2 C, \tag{2.26}$$

which is simply Fick's second law. This approximation is a good one whenever $\lambda_{intrinsic}$ is large compared with the size of the morphogen domain, a size that we will denote as $x_{\max}$. In the model developed here, that condition applies to the very smallest disks, i.e. during the earliest simulation times.

In one dimension, Eq. (2.26) becomes $0 = C''(x)$, which solves to a straight line. If the boundary conditions are such that there is a source at one end ($x = 0$) and a sink at the other ($x = x_{\max}$), then the equation of the line is

$$C = C_0\left(1 - \frac{x}{x_{\max}}\right) \tag{2.27}$$

where C_0 means concentration at $x = 0$. We can see that such a gradient scales perfectly because the effects of multiplying $x_{\max}$ by any factor are exactly canceled by multiplying x by the same factor. This is the basis for the statement that purely "source-sink" gradients

scale "automatically".

The more general one-dimensional form, Eq. (2.25) also has an exact solution for the same boundary conditions, which is

$$C = C_0 \operatorname{csch} \frac{x_{\max}}{\lambda_{\text{intrinsic}}} \sinh \frac{x_{\max} - x}{\lambda_{\text{intrinsic}}}. \tag{2.28}$$

When $\lambda_{intrinsic} \gg x_{\max}$, Eq. (2.28) reduces to Eq. (2.27). In contrast, when $\lambda_{intrinsic} \ll x_{\max}$, Eq. (2.28) reduces to

$$C = C_0 e^{-\frac{x}{\lambda_{\text{intrinsic}}}}. \tag{2.29}$$

This form does not scale at all, because C is completely independent of $x_{\max}$. These observations tell us that, in a one-dimensional system with source-sink boundary conditions, linear shape always means automatic scaling (and vice versa), whereas exponential shape always means no scaling (and vice versa).

In the mathematical model described above, we see linear Dpp gradient shapes during the earliest stages of disc growth (until posterior compartment sizes reach about 20 μm), consistent with simple source-sink scaling due to the relatively small size of $x_{\max}$. As required by Eq. (2.27), these shapes are not only linear, but also extend all the way from source to the location of the sink ($x_{\max}$), which in the model is taken to be the edge of the posterior compartment (the justification for this will become clear shortly). The model therefore makes the prediction that Dpp gradient shapes in the posterior compartments of the very smallest discs should be linear and extend from the Dpp source to the posterior disc edge.

In practice, assessing whether pMad gradient shapes are better fit by lines or exponential is not possible when discs are small, due to the noisiness of measurements, the rather small dynamic range over which pMad can be quantified by immunofluorescence, and the need to subtract unknown amounts of background fluorescence. Consider, for example, the pMad

intensity data shown in the left panel of Figure 2.6A. Depending on the amount of background fluorescence one subtracts, one could fit the data reasonably well with a declining exponential shape (middle panel) or a straight line (right panel). However, if one does fit the data with a line, that line will not extend to the compartment edge (in the panel at right, that line intersects the background at a location only about a third of the way to the end of the domain.

On the face of it, this would appear to be an example of a strong disagreement between the model and the data: observed gradient shapes in small discs are either not linear, or do not extend far enough toward the compartment edge to fit the model. On closer examination, however, it turns out that this disagreement is most likely an artifact of the fact that the model is one dimensional, and thus ignores the dorsoventral (DV) and apicobasal (AB, i.e. cross-sectional) dimensions. Neglect of the DV direction is usually justified by the fact that the Dpp source is a long rectangle oriented parallel to the DV axis; if the rectangle is sufficiently long, and one keeps one's observations far enough away from its edges, then it is reasonable to expect that Dpp concentrations along the AP direction should be independent of DV position.

The greater problem arises with the AB dimension (for simplicity we will call this the z dimension, to contrast it with the x that we have been using to represent the AP axis). The impact of ignoring z is not widely discussed in the literature, possibly because there has been some uncertainty about the actual cell biological space in which Dpp diffuses and acts: the luminal space above columnar cells, or the basolateral space between columnar cells. If Dpp diffuses in the lumen, a thin space bounded on both sides by tight junctions, then it is probably safe to ignore z. But recent evidence strongly supports the view that, in the wing disc, Dpp's function is mediated almost exclusively by molecules diffusing in the basolateral space [56], a result also in agreement with observations that freely diffusing Dpp can be observed directly in that space by fluorescence correlation spectroscopy [192]. The

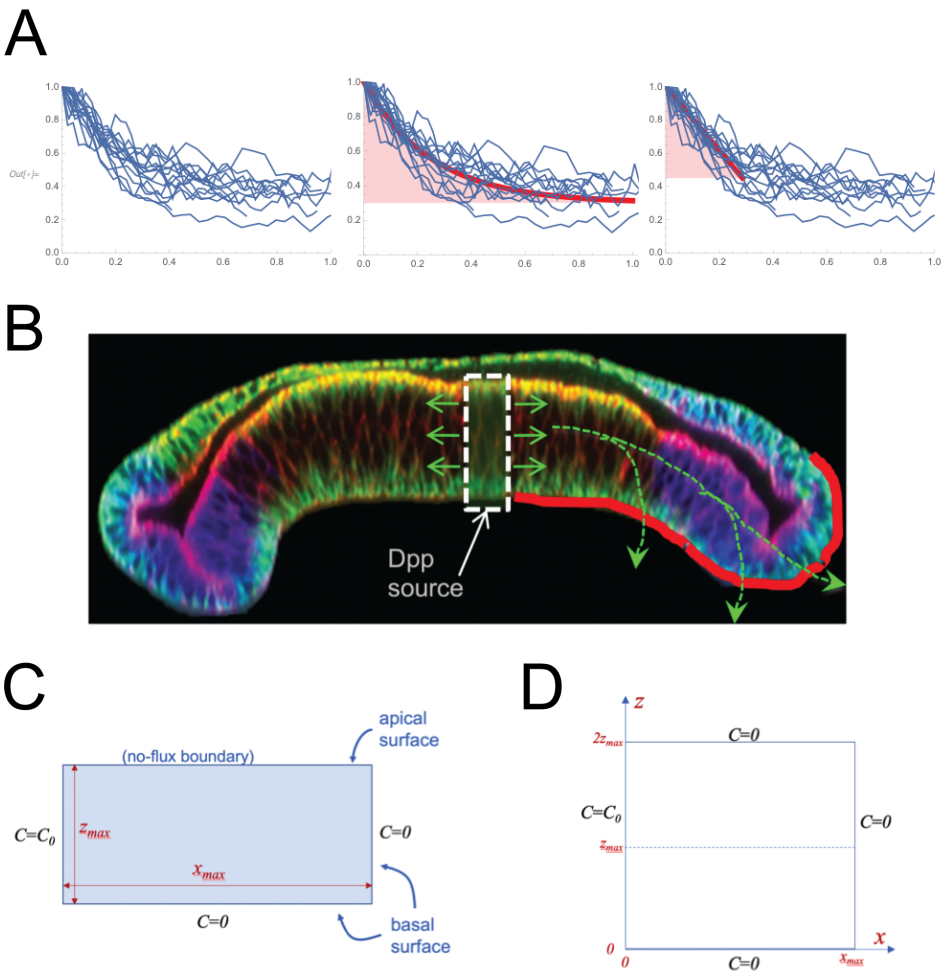

Figure 2.6: Influence of dimensionality on scaling. (A) pMad distributions observed in the posterior compartments of 16 early wildtype discs (posterior compartment sizes $< 25\mu m$). To compare relative shapes, data have been normalized to start from the same initial amplitude, and scaled so that the abscissa values of 0 and 1 represent the Dpp source and the edge of the posterior compartment. Note that the data (left) can be fit by either exponential (middle) or linear (right) forms, but the linear shapes so obtained do not extend to the free end of the compartment. (B) A cross-sectional view of the wing disc, showing the position of the Dpp source and paths for its diffusion within intercellular spaces. The diagram is adapted from a micrograph reproduced from [51]; the posterior compartment is at right, the brinker domain is in blue, and a thick red line marks the basement membrane under the columnar cells of the posterior compartment. (C) Simplified geometric formulation of the posterior compartment in panel B as a two-dimensional diffusion problem in which the dimensions are anteroposterior (x) and apicobasal (z). (D) Mathematical system that may be solved analytically, for which half the domain (from 0 to $z_{\max}$) corresponds exactly to the situation in panel C.

basolateral space is bounded by tight junctions at one end (the apical surface), but only by a basement membrane at other end. Basement membranes are structures that pose no barrier to diffusion [33]. As diagrammed in Figure 2.6B (in which the basement membrane of the posterior columnar cells is highlighted in red), a continual "leakage" of Dpp out of discs through the basement membrane into the surrounding hemolymph is to be expected. In fact, recent evidence argues that delivery of Dpp from discs, via the hemolymph, to the rest of the larva is considerable during larval development [147].

How might such leakage alter morphogen gradient shapes when measured in the AP dimension? A general treatment of this problem can be found in [86], but more useful here is a discussion of the specific case when $\lambda_{intrinsic}$ is large (the scenario that, in the model, applies to the smallest discs). In that case, steady state shapes are determined by Eq. (2.26). Because C is now a function of two dimensions, x and z, that equation no longer always solves to a straight line. As usual, the solution depends on the boundary conditions, which now must be specified in both x and z direction. In the x-direction, we choose a constant-value condition at $x = 0$ simply to represent that the morphogen domain abuts a source at that location. We choose a zero-value (sink) condition at $x = x_{\max}$, the posterior edge of the disc because, as we see in the Figure 2.6B, the basement membrane curves around at the edge of the disc, so that Dpp reaching that location is free to exit into the hemolymph (which, being a well-stirred compartment, quickly carries the Dpp away). In the z-direction, we also place a zero-value (sink) condition at $z = 0$ (the basal surface of the disc), for the same reason. At the apical surface ($z = z_{\max}$), we place a "zero-flux" boundary condition, to capture the presence of tight junctions that block the escape of molecules diffusing in basolateral space. Together, these conditions specify the two-dimensional model diagrammed in Figure 2.6C.

Due to symmetry considerations, this problem can be seen as simply the lower half of the problem in Figure 2.6D, which has only value (Dirichlet) boundary conditions, and for which a solution is well known [15]. Specifically, the steady state solution can be represented as

the infinite sum:

$$C(x,z) = C_0 \sum_{n=1}^{\infty} \left(\frac{2\left(1+(-1)^{n+1}\right)}{n\pi} \sin\left(\frac{n\pi z}{2z_{\max}}\right) \operatorname{csch}\left(\frac{n\pi x_{\max}}{2z_{\max}}\right) \sinh\left(\frac{n\pi\left(x_{\max}-x\right)}{2z_{\max}}\right)\right). \tag{2.30}$$

To see how this shape would appear to an observer focusing only on the AP plane, we may average over all z from $z = 0$ to $z = z_{\max}$, to get the following form

$$C(x) = C_0 \sum_{n=1}^{\infty} \left(\frac{\sin\left(\left(n-\frac{1}{2}\right)\frac{\pi}{2}\right)}{\left(n-\frac{1}{2}\right)\frac{\pi}{2}} \operatorname{csch}\left(\frac{\left(n-\frac{1}{2}\right)\pi x_{\max}}{z_{\max}}\right) \sinh\left(\frac{\left(n-\frac{1}{2}\right)\pi\left(x_{\max}-x\right)}{z_{\max}}\right)\right). \tag{2.31}$$

The result here is a sum of terms each of which has the form

$$\frac{1}{2\sqrt{2}a(n)} \operatorname{csch}\frac{x_{\max}}{\lambda(n)} \sinh\frac{x_{\max}-x}{\lambda(n)}. \tag{2.32}$$

With $a(n) = \pi, 3\pi, -5\pi, -7\pi, 11\pi, 13\pi, -15\pi...$ and $\lambda(n) = \frac{2z_{\max}}{\pi}, \frac{2z_{\max}}{3\pi}, \frac{2z_{\max}}{5\pi}, \frac{2z_{\max}}{7\pi}...$ Except for x near 0, the result is reasonably well approximated by the first term of the sum, i.e.

$$\frac{C_0}{2\sqrt{2}} \operatorname{csch}\frac{x_{\max}}{\frac{2}{\pi}z_{\max}} \sinh\frac{(x_{\max}-x)}{\frac{2}{\pi}z_{\max}}. \tag{2.33}$$

Except for the leading constant, this form exactly matches Eq. (2.28), with $\frac{2}{\pi}z_{\max}$ replacing $\lambda_{intrinsic}$. Thus, the shape of the morphogen gradient in the AP direction will be governed by the relationship between $\frac{2}{\pi}z_{\max}$ and $x_{\max}$. At one extreme, where $\frac{2}{\pi}z_{\max} \gg x_{\max}$, it will be a straight line from source to $x_{\max}$. At the other extreme, $\frac{2}{\pi}z_{\max} \ll x_{\max}$, it will approach a declining exponential. Strikingly, however, regardless of the shape of the gradient, it will scale automatically in response to changes in $x_{\max}$, provided that changes in $x_{\max}$ are always accompanied by proportional changes in $z_{\max}$, i.e. if disc growth is isotropic. This can be seen directly from Eq. (2.33): the effects of multiplying both $x_{\max}$ and $z_{\max}$ by any factor are exactly canceled by multiplying x by the same factor.

In summary, when morphogen gradients form under conditions of low intrinsic decay ($\frac{2}{\pi} z_{\max} \gg x_{\max}$), and the morphogen domain is growing isotropically, we should expect to observe the same kind of automatic scaling that one-dimensional models predict, but we should not expect to see linear gradient shapes, especially if $z_{\max}$ is small compared with $x_{\max}$. Measurements from confocal images indicate that, during disc growth, $z_{\max}$ is always small compared with $x_{\max}$, implying that observed gradient shapes during automatic, source-sink scaling should actually be quasi-exponential, and not linear. As can be seen from Figure 2.6, this prediction is consistent with our observations. Does this mean the one-dimensional model needs to be discarded in favor of a more complicated two (or even three)-dimensional one? Not necessarily. Although the model predicts incorrect shapes during the earliest phases of disc growth, it does capture scaling behavior correctly, including the loss of scaling that takes place when discs grow large enough that the condition $\lambda_{intrinsic} \gg x_{\max}$ starts to fail. In the two-dimensional model, the analytical solution for gradient shape under these conditions is more complicated (see [86]), but scaling eventually fails in the same way, at the same time, and for the same reasons. Moreover, it is straightforward to show that when discs grow sufficiently big that $\lambda_{intrinsic} \ll z_{\max}$, shape in the AP direction becomes effectively uncoupled from AB shape (i.e. the z-direction), meaning that the results of the one-dimensional model eventually closely approximate the two-dimensional one in all respects. Overall, then, accounting for the AB direction imposes a relatively modest correction on the one-dimensional model, which is limited to early periods of disc growth.

Chapter 3

Stochastic dynamics of cell lineage in tissue homeostasis

This chapter is a reprint of the material as it appears in Discrete and Continuous Dynamical Systems - Series B [133]. The co-authors listed in this publication directed and supervised research which forms the basis for this chapter.

3.1 Background

During epithelium tissue maintenance, lineages of cells differentiate and proliferate in a coordinated way to provide the desirable size and spatial organization of different types of cells. While mathematical models through deterministic description have been used to dissect role of feedback regulations on tissue layer size and stratification, how the stochastic effects influence tissue maintenance remains largely unknown. Here we present a stochastic continuum model for cell lineages to investigate how both layer thickness and layer stratification are affected by noise. We find that the cell-intrinsic noise often causes reduction and oscillation

of layer size whereas the cell-extrinsic noise increases the thickness, and sometimes, leads to uncontrollable growth of the tissue layer. The layer stratification usually deteriorates as the noise level increases in the cell lineage systems. Interestingly, the morphogen noise, which mixes both cell-intrinsic noise and cell-extrinsic noise, can lead to larger size of layer with little impact on the layer stratification. By investigating different combinations of the three types of noise, we find the layer thickness variability is reduced when cell-extrinsic noise level is high or morphogen noise level is low. Interestingly, there exists a tradeoff between low thickness variability and strong layer stratification due to competition among the three types of noise, suggesting robust layer homeostasis requires balanced levels of different types of noise in the cell lineage systems.

3.2 Introduction

In multicellular organisms, homeostasis is critical to tissues and organs for their functions. Multistage cell lineages, generally consisting of stem cells, transit-amplifying (TA) cells and terminally differentiated (TD) cells, serve as fundamental units for tissue and organ development, maintenance and regeneration.

Growth factors, one type of diffusive morphogen that is secreted by cells, play an important role by regulating multiple cellular processes to control the cell populations in the lineage [87]. Growth factors are often found to be important in regulating organ regeneration, as observed in liver [114], mouse olfactory epithelium [183], muscles [110], and hematopoietic system [188]. In such systems, different types of cells are located at spatial locations in the tissues for different functions. For examples, the stem cell niche, a spatial region with concentrated level of stem cells, often provides protective support for environmental variability [115, 96, 89], as seen in intestinal epithelia [185], neurons [32] and tumors [18]. In particular, the epithelium tissue is a great system to study the stratified layers of different types of cells that contain

the stem cell niche [161].

Several mathematical modeling approaches have been employed to study the tissue growth and patterning, for example, on digits of limb [136], melanoblast [102], feather [95, 97] and stripe in mammalian palate [38]. Regarding the tissue size, analysis and computation of non-spatial cell lineage models suggest that the negative feedback is critical to regulating growth in epithelium [88, 99] and blood [81, 105]. For spatial models, continuum and discrete models have been used to study formation of stratified structure and stem cell niche in tissue. A one-dimensional continuum model [24] shows that the spatial morphogen gradient contributes to the tissue stratification. Studies of two-dimensional models suggest sources for distorted tissue morphologies [125, 124]. Through studying a discrete cell model, the selective cell adhesion is found to be a key factor for layer formation and tissue stratification [35].

Recently, stochastic effects, such as noise in gene expressions [41, 109, 77, 57], stochastic gene-state switching [1, 50], noise in cell divisions [65] and cell migration [152], are found to be important in biological functions [135, 149]. In many cases, noise is detrimental to biological functions, and noise attenuation mechanisms are critical in signal transduction [10, 7, 169]. Interestingly, noise is also found to be beneficial, such as improved signal transmission facilitated by stochastic resonance [47, 111], enhanced fitness to the environmental fluctuations by gene expression noise [17, 8, 158], and sharpening patterning boundaries through gene expression noise [190, 170, 134].

While noise effect and tissue maintenance have been extensively studied individually, how noise affects tissue growth and maintenance remains elusive. Based on the one-dimensional deterministic cell lineage model for epithelium growth [24], here we develop a stochastic cell lineage model that include growth and three different types of noise. In particular, we use the multiplicative noise in the cell lineage equations to model the cell-intrinsic noise, the additive noise in the same equations for the cell-extrinsic noise, and multiplicative noise in the equation of diffusive molecules for morphogen noise. First, we study the effects of those

three types of noise individually on layer thickness and stratification. Then we look into some specific combinations according to the opposite individual effects, more particularly, the combination of cell-intrinsic noise and cell-extrinsic noise, and the combination of cell-intrinsic noise and morphogen noise. Finally we combine all three types of noise to investigate the range of noise levels under which the homeostatic thickness and stratification can be maintained.

3.3 A stochastic spatial cell lineage model and quantifications of layer thickness and stratification

3.3.1 A deterministic model

Previously a one-dimensional deterministic model was developed to study the stratification of epithelium development and maintenance [24]. In the model there are three cell stages in the main lineage consisting of stem cells, transient amplifying (TA) cells, and terminally differentiated (TD) cells, with each cell type densities represented by C_0, C_1 and C_2 (Figure 3.1), respectively. The cell lineage equations are given by:

$$\begin{aligned}
\frac{\partial C_0}{\partial t} + \frac{\partial (VC_0)}{\partial z} &= \nu_0 (2p_0 - 1) C_0, \\
\frac{\partial C_1}{\partial t} + \frac{\partial (VC_1)}{\partial z} &= \nu_0 [2 (1 - p_0) C_0] + \nu_1 (2p_1 - 1) C_1, \\
\frac{\partial C_2}{\partial t} + \frac{\partial (VC_2)}{\partial z} &= \nu_1 [2 (1 - p_1) C_1] - d_2 C2.
\end{aligned} \tag{3.1}$$

Here $V(z,t)$ is the layer growth velocity driven by cell proliferation and differentiation of cells. For i^{th} cell type, p_i denotes self-renewal probability, $1 - p_i$ is then the differentiated probability, d_i is the death rate, and ν_i is $\ln 2$ over cell cycle length. With the assumption that the total cell density remains as a constant, we then normalize the constant with

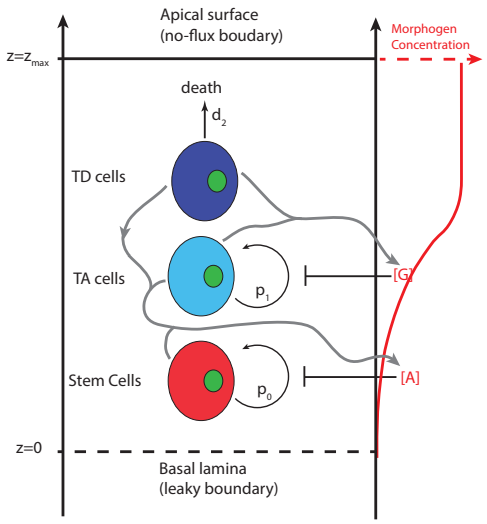

Figure 3.1: A schematic diagram of a main cell lineage in epithelium. Stem cells and TA cells proliferate with probabilities p_0 and p_1 and differentiate with probabilities $1-p_0$ and $1-p_1$. TD cells undergo cell death with rate d_2. All three types of cells can secrete molecule A that inhibits self-renewal probability p_0. TD and TA cells secrete molecule G that inhibits self-renewal probability p_1. Molecules A and G are diffusive in the epithelium. The apical surface is moving with the dynamic position $z_{\max}$ and no-flux boundary condition is imposed. On the other hand, leaky boundary condition is imposed at the basal lamina with its position fixed.

$C_0 + C_1 + C_2 = 1$. Adding all equations in Eq. (3.1) leads to

$$\frac{\partial V}{\partial z} = \nu_0 C_0 + \nu_1 C_1 - d_2 C_2. \tag{3.2}$$

The dynamic layer thickness $z_{\max}$ is governed by

$$\frac{dz_{\max}(t)}{dt} = V(z_{\max}, t). \tag{3.3}$$

The molecules secreted by cells inhibit the cell self-renewal rates (Figure 3.1). Two types of morphogen A and G are considered in this system. The proliferative probabilities p_0 and p_1 are modeled by the Hill functions:

$$\begin{aligned} p_0 &= \frac{\bar{p}_0}{1 + (\gamma_A [A])^m}, \\ p_1 &= \frac{\bar{p}_1}{1 + (\gamma_G [G])^n}, \end{aligned} \tag{3.4}$$

where $\bar{p}_0$ and $\bar{p}_1$ are the maximal self-renewal probabilities, respectively; γ_A and γ_G are the reciprocal of EC50, and m and n are the Hill coefficients.

The diffusive morphogens are modeled by the advection-diffusion equations,

$$\begin{aligned} \frac{\partial [A]}{\partial t} + \frac{\partial (V[A])}{\partial z} &= D_A \frac{\partial^2 [A]}{\partial z^2} + \sum_{i=0}^{2} \mu_i C_i - a_{\deg} [A], \\ \frac{\partial [G]}{\partial t} + \frac{\partial (V[G])}{\partial z} &= D_G \frac{\partial^2 [G]}{\partial z^2} + \sum_{i=0}^{2} \eta_i C_i - g_{\deg} [G], \end{aligned} \tag{3.5}$$

where D_A and D_G are diffusion coefficients, $a_{\deg}$ and $g_{\deg}$ are degradation rates of A and G, A and G are produced by the cell type C_i at rates μ_i and η_i, respectively. The permeable basal lamina and a closed boundary at apical surface could give rise to heterogeneous distribution of A and G, contributing to the formation of layer stratification. We take the leaky boundary conditions at $z = 0$ basal lamina and no-flux boundary conditions at $z = z_{\max}(t)$ for apical

surface:

$$\begin{aligned} \frac{\partial[A]}{\partial z}(0,t) = \alpha_A[A],\ \frac{\partial[A]}{\partial z}(z_{\max},t) = 0, \\ \frac{\partial[G]}{\partial z}(0,t) = \alpha_G[G],\ \frac{\partial[G]}{\partial z}(z_{\max},t) = 0, \end{aligned} \tag{3.6}$$

where α_A and α_G are the corresponding coefficients of permeability.

3.3.2 A stochastic model on cell lineages and morphogens

Next we add stochastic fluctuations to both equations of cell distributions and mophogens. For simplicity, we model three kinds of noise in the system: cell-intrinsic noise, cell-extrinsic noise, and morphogen noise. The cell-intrinsic noise is modeled by multiplicative noise in the cell lineage equations to mimic fluctuations on the cell density that arise due to stochastic effects associated with cell cycle, cell proliferation, or cell differentiation and so on. The cell-extrinsic noise is modeled by additive noise to mimic environmental fluctuations that may affect the overall dynamics of cell lineages, which is usually independent of the cell density level. To avoid solving stochastic differential equations for the morphogen, which is at a fast time scale, we add a multiplicative noise term to the deterministic quasi-steady state solution of the morphgens to model the noisy morphogen dynamics.

We model the cell-intrinsic and cell-extrinsic noise by adding both a term for multiplicative noise and a term for additive noise to the deterministic Eq. (3.1):

$$\begin{aligned} \frac{\partial C_0}{\partial t} + \frac{\partial (VC_0)}{\partial z} &= \nu_0 (2p_0 - 1) C_0 \\ &\quad + \left(\sigma_0 \frac{dW_0^a}{dt} + \varepsilon_0 C_0 \frac{dW_0^m}{dt} \right), \\ \frac{\partial C_1}{\partial t} + \frac{\partial (VC_1)}{\partial z} &= \nu_0 [2(1-p_0) C_0] + \nu_1 (2p_1 - 1) C_1 \\ &\quad + \left(\sigma_1 \frac{dW_1^a}{dt} + \varepsilon_1 C_1 \frac{dW_1^m}{dt} \right). \end{aligned} \tag{3.7}$$

The density C_2 is obtained by the normalized equation $C_0 + C_1 + C_2 = 1$. The multiplicative white noise, $\varepsilon_i C_i \frac{dW_i^m}{dt}$, $(i = 0,\ 1)$, mimics cell-intrinsic noise. The additive white noise, $\sigma_i \frac{dW_i^a}{dt}$, $(i = 0,\ 1)$, mimics cell-extrinsic noise.

Because the time scale of molecular diffusion is much faster than the time scale of cells divisions, we solve quasi-steady state (see Method) for Eq. (3.5) to obtain $[A]_{ss}(z,t)$ and $[G]_{ss}(z,t)$ [24]. To model the morphogen noise in the stochastic model, we add fluctuations to the quasi-steady-state at time t:

$$\begin{aligned} [A](z,t) &= [A]_{ss}(z,t) * (1 + \omega_0 \zeta_0(z,t)), \\ [G](z,t) &= [G]_{ss}(z,t) * (1 + \omega_1 \zeta_1(z,t)), \end{aligned} \tag{3.8}$$

where $\zeta_i(z,t)$ is a standard normally-distributed random variable at space z and time t, and independent of both spatial and temporal variables. Such multiplicative noise can maintain mean concentrations on morphogens.

3.3.3 Quantification of layer thickness, variability, and stratification

To systematically explore the three major properties of the tissue layer, we quantify each of them using one measurement. Due to stochastic effect, the tissue layer may not reach a constant thickness, and we define its average thickness by

$$TH = \frac{1}{T} \int_0^T z_{\max}(t)\, dt, \tag{3.9}$$

where T is the final time of the simulation. With a large T, TH will have a limiting behavior and can describe the long-term behavior of the thickness.

To measure the variability of the layer thickness, we use the coefficient of variation (CV)

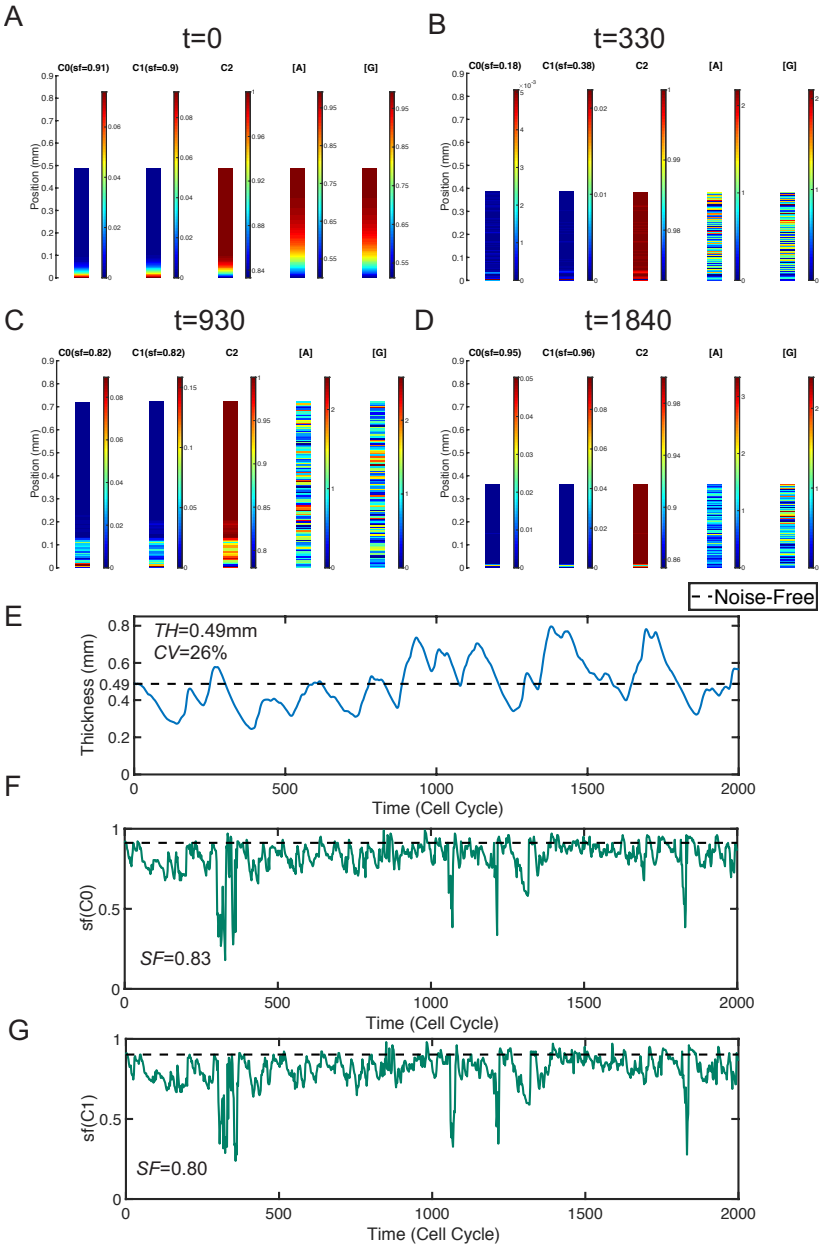

Figure 3.2: A baseline simulation for the system containing all three kinds of noise. The spatial distribution of three types of cells and different mophogens at four different time points: (A) $t = 0$; (B) $t = 330$; (C) $t = 860$; (D) $t = 1200$. (E) Layer thickness in one particular stochastic simulation. (F) Stratification factor of stem cells ($sf(C_0)$). (G) Stratification factor of TA cells ($sf(C_1)$). In (E-G), the black dash line is the steady-state value for corresponding quantities in the deterministic system. The noise levels used are $\varepsilon_0 = \varepsilon_1 = 0.6$, $\sigma_0 = \sigma_1 = 10^{-4}$, and $\omega_0 = \omega_1 = 0.58$.

relative to its mean thickness:

$$CV = \frac{\sqrt{\frac{1}{T}\int_0^T \left(z_{\max}(t) - TH\right)^2 dt}}{TH} \times 100\%. \tag{3.10}$$

A large CV can reflect either strong oscillations or rapid growth. One case with oscillations will be shown in Section 3.4.1, and the other case with rapid growth will be shown in Section 3.4.2

A stratification factor [24] was defined to measure the level of stratification for cell type i at time t:

$$sf(C_i, t) = 1 - \frac{\theta(t)}{0.8 z_{\max}(t)}, \tag{3.11}$$

where $\theta(t)$ is defined by the following equation:

$$\int_0^{\theta(t)} C_i(z,t)\, dz = 0.8 \int_0^{z_{\max}} C_i(z,t)\, dz. \tag{3.12}$$

To measure the long-time average level of the tissue stratification, we define the stratification factor for cell type i as the following:

$$SF(C_i) = \frac{1}{T}\int_0^T sf(C_i, t)\, dt. \tag{3.13}$$

The value of sf and SF are between 0 and 1. The value 0 corresponds to homogeneous distribution of cell type i and the value 1 corresponds to the extreme polarization at the basal lamina.

3.3.4 A baseline simulation

First we present a simulation for the model in which all the three types of noise are involved by setting $\varepsilon_0 = \varepsilon_1 = \varepsilon$, $\sigma_0 = \sigma_1 = \sigma$ and $\omega_0 = \omega_1 = \omega$. We show the spatial distributions of cells

and morphogens at different time points, and dynamics of layer thickness and stratification (Figure 3.2).

To study the layer maintenance, it is natural to take the steady state in the deterministic system as the initial condition for this stochastic simulation. We use the same initial condition in simulations presented in this work. To investigate the long-time behavior of the layer regarding its thickness, variability and stratification, we test different final time T in one simulation until the TH, CV and SF have no significant relative change in time. We find $T = 2000$ cell cycles allows a consistent long time behavior of the layer for all simulations presented below.

Initially, the stem cells are mainly located near the basal lamina and the morphogen concentration are higher in the region close to the apical surface, leading to a well-stratified layer which is similar to the deterministic case (Figure 3.2A). With the noise, the layer first shrinks and the morphogen gradient becomes less obvious at $t = 330$ (Figure 3.2B). As the time increases, the layer becomes thicker (Figure 3.2C) and, interestingly, later the layer shrinks again (Figure 3.2D). Clearly, by looking at the thickness as a function of time (Figure 3.2E), one observes an oscillatory behavior. The mean thickness of this layer, TH, is identical to the homeostatic thickness $SS = 0.49$mm. The variability of the layer thickness is quantified by $CV = 26\%$.

On the other hand, noise affects the stratified structure of tissues. At $t = 330$, the distribution of stem cells is nearly uniform everywhere and the extremely low stratification factor is consistent with our observation (Figure 3.2B). At $t = 930$, stem cells mainly locate in a small region next to the basal lamina (Figure 3.2C). This region with high stem cell density is slightly wider than the one at initial stage, leading to a minor reduction of stratification factor. At $t = 1840$, while the distribution of stem cells looks uniform, the stem cells highly concentrate in a very narrow region close to the basal lamina and the stratification factor is larger than the initial one (Figure 3.2D). Overall, the stratification factor is able to capture

stratified level appropriately (Figure 3.2A-D). As time increases, we observe four drops in the stratification factor and, interestingly it always returns to the average level quickly (Figure 3.2F). Overall, the layer has well-stratified stem cells in average with $SF = 0.83$ while the TA cells have an average $SF = 0.80$ (Figure 3.2G).

Together, this simulation suggests that noise affect both thickness and stratification, leading to an oscillation of the tissue thickness during tissue maintenance. To dissect the role of each type of noise, we next scrutinize each noise type one by one.

3.4 The effects of single type of noise

In the stochastic model, there are three types of noise: cell-intrinsic noise, cell-extrinsic noise and morphogen noise. In this section, we discuss the effects of each type of noise individually. For example, for the cell-intrinsic noise, we set $\sigma = \omega = 0$ and discuss the layer behaviors with different cell-intrinsic noise levels ε. We show the statistical quantities TH, CV and SF. The number of simulations has been chosen such that all these quantities become stable in the mean sense. In particular, in this study, we run 20 simulations for each scenario.

3.4.1 Cell-intrinsic noise causes reduction and oscillations of tissue layer size

For the system containing only cell-intrinsic noise ($\sigma = \omega = 0$), we first present the layer thickness as a function of time for three different noise levels (Figure 3.3A). The layer fluctuates around the homeostasis when the noise level is small such as $\varepsilon = 0.2$. As the noise level increases, such as $\varepsilon = 0.6$ or 1, the layer oscillates below its thickness at homeostasis. Especially, the oscillation exhibits a clear pattern with a period around 400 cell cycles at

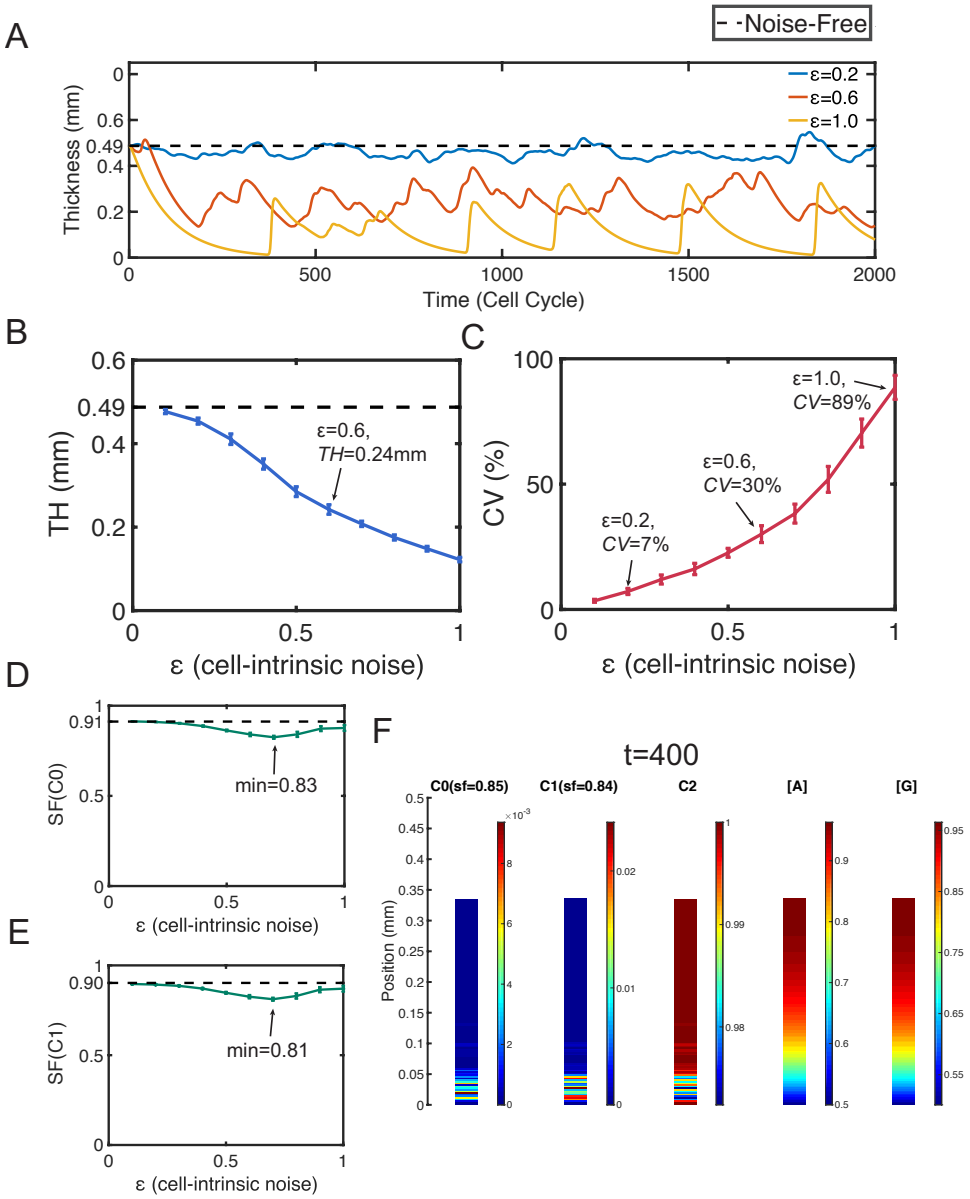

Figure 3.3: Simulations with only cell-intrinsic noise. Dash lines represent the corresponding quantities at homeostasis. (A) Layer thickness in three simulations with $\varepsilon = 0.2$, 0.6 and 1. (B) The mean TH. The error bars show the standard deviation. (C) The mean CV. The error bars show the standard deviation of CV. The mean SF of (D) stem cells and (E) TA cells. The error bars show the standard deviation. (F) Distribution of cells and morphogens in a specific simulation with $\varepsilon = 0.6$ at time $t = 400$. In (B-E), all statistical quantities are captured based on 20 simulations, and the standard deviations (error bars) are negligible compared to the means.

$\varepsilon = 1$ (Figure 3.3A).

Next we look into the statistical behaviors of the mean and variability of the layer thickness TH and CV, respectively (Figure 3.3B and 3C). As ε increases, TH decreases and a 50% reduction can be observed at $\varepsilon = 0.6$ with $TH = 0.24$mm. The thickness variability (CV) increases as ε increases. At $\varepsilon = 0.2$, $CV = 7\%$ and a 3-fold increase on CV can be observed at $\varepsilon = 0.6$. Interestingly, when the thickness variability is high, the high value quantity CV seems to reflect the oscillation amplitude of the layer. Especially, at $\varepsilon = 1$, the strongly oscillatory layer (Figure 3.3A) results in a high variability with $CV = 89\%$ (Figure 3.3C).

Then we look into the tissue stratification for both stem cells and TA cells (Figure 3.3D and 3E). Although the SFs have minor reduction when noise is induced, any SF above 0.8 still indicates a well-stratified structure for both stem cells and TA cells. One specific example of the cells distribution displays the well-stratified tissue structure (Figure 3.3F).

Therefore, the cell-intrinsic noise usually causes reduction of layer thickness and leads to oscillations on the thickness. The oscillations exhibit a periodic pattern when the noise level is high. While the noise may cause a minor reduction in stratification, the layers remain well stratified when the cell-intrinsic noise is presented only.

3.4.2 Cell-extrinsic noise causes rapid growth, and deteriorates layer stratification

For the system containing only cell-extrinsic noise ($\varepsilon = \omega = 0$), we first study the layer thickness as a function of time for three different noise levels (Figure 3.4A). All layers grow monotonically in time and their growth rates have positive correlation with the level of noise σ. The layer grows slowly at early time and then stops growing when the noise level is low such as $\sigma = 1 \times 10^{-3}$ and $\sigma = 2 \times 10^{-3}$. The unbounded growth can be observed when the

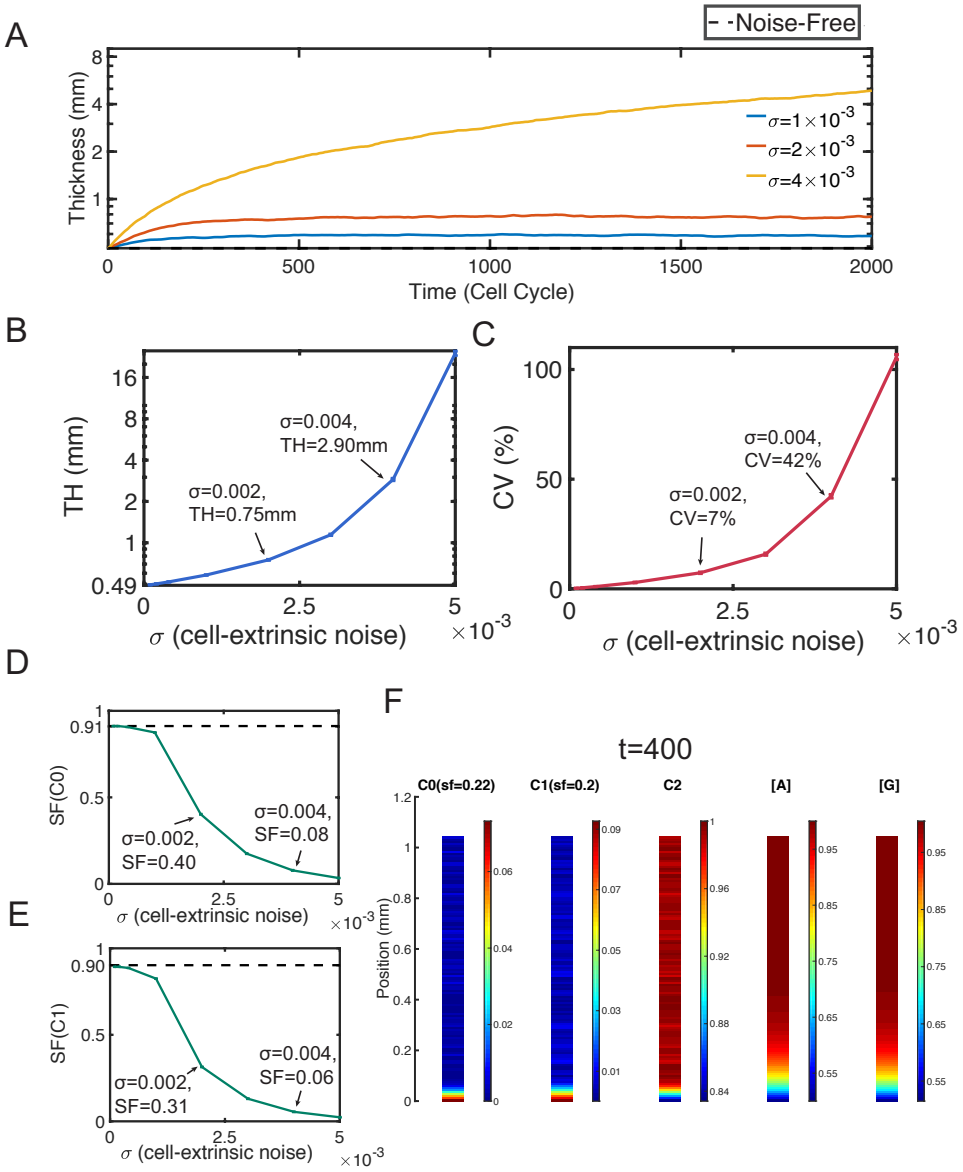

Figure 3.4: Simulations with only cell-extrinsic noise. Dash lines represent the corresponding quantities at homeostasis. (A) Layer thickness in three simulations with $\sigma = 1\times10^{-3}$, 2×10^{-3} and 4×10^{-3}. (B) The mean TH. The error bars show the standard deviation. (C) The mean CV. The error bars show the standard deviation of CV. The mean SF of (D). stem cells and (E). TA cells. The error bars show the standard deviation. (F). Distribution of cells and morphogens in a specific simulation with $\sigma = 3 \times 10^{-3}$ at time $t = 400$. In (B-E), all statistical quantities are captured based on 20 simulations, and the standard deviations (error bars) are negligible compared to the means.

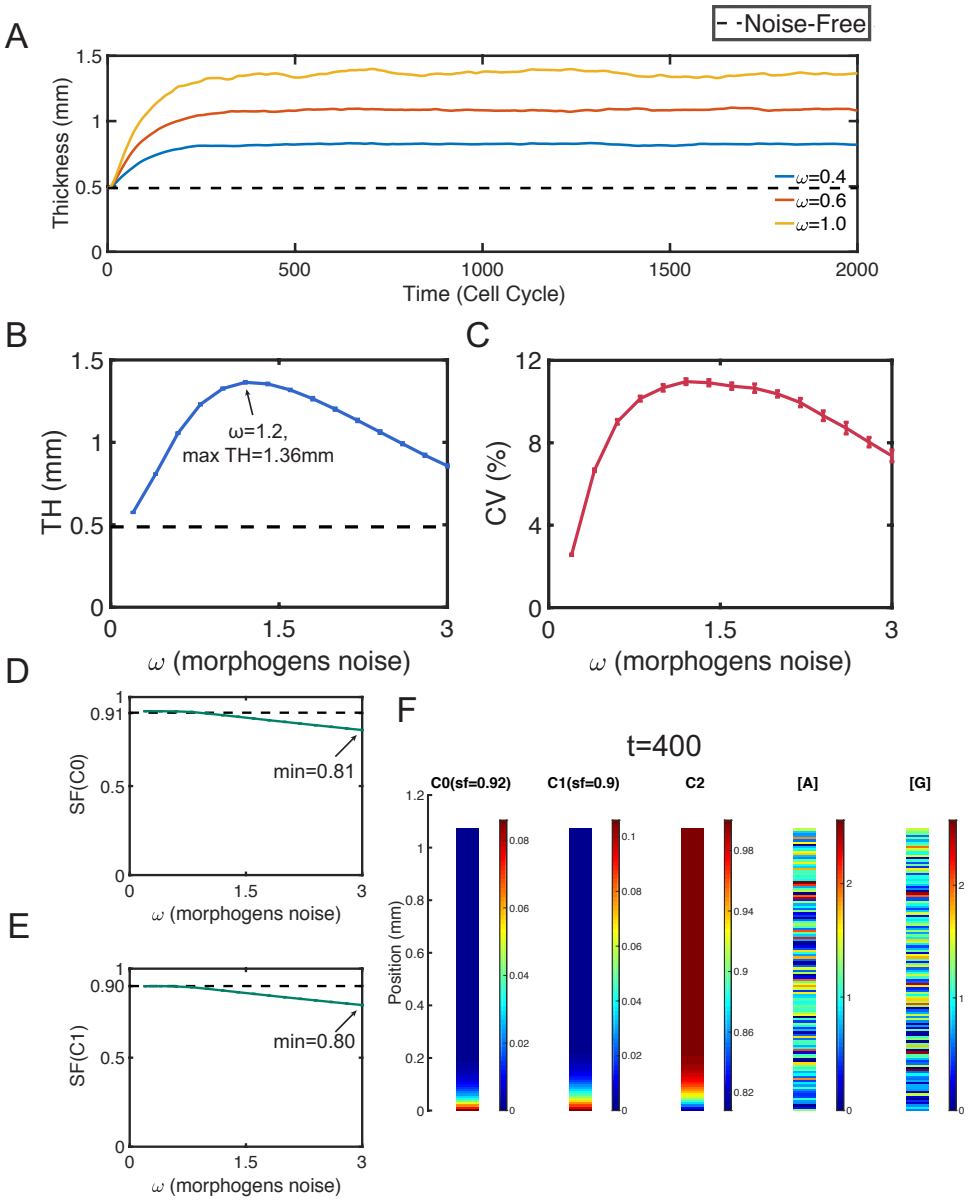

Figure 3.5: Simulations with only morphogens noise. Dash lines represent the corresponding quantities at homeostasis. (A) Layer thickness in three simulations with $\omega = 0.4$, 0.6 and 1. (B) The mean TH. The error bars show the standard deviation. (C) The mean CV. The error bars show the standard deviation of CV. The mean SF of (D) stem cells and (E) TA cells. The error bars show the standard deviation. (F). Distribution of cells and morphogens in a specific simulation with $\omega = 0.6$ at time $t = 400$. In (B-E), all statistical quantities are captured based on 20 simulations, and the standard deviations (error bars) are negligible compared to the means.

noise level is large such as $\sigma = 4 \times 10^{-3}$ (Figure 3.4A).

Next we look into statistical behaviors of the mean and variability of the layer thickness TH and CV, respectively (Figure 3.4 B and C). As σ increases, the average TH shows an exponential growth. A 6-fold increase (2.90mm) can be observed at $\sigma = 4 \times 10^{-3}$, the TH is even over 10mm at $\sigma = 5 \times 10^{-3}$ (Figure 3.4B). Also the layer thickness variability quantified by CV grows exponentially as a function of σ. When $\sigma < 3 \times 10^{-3}$, CV is still lower than 10%. At $\sigma = 4 \times 10^{-3}$, we observe $CV = 42\%$, and at $\sigma = 5 \times 10^{-3}$ CV is as high as 106% (Figure 3.4C).

On the tissue stratification (Figure 3.4D and 4E), the SFs decrease quickly as a function of σ. The stratification level of stem cells is already small at $\sigma = 2 \times 10^{-3}$ with $SF = 0.4$. The stem cells distribute nearly uniformly at $\sigma = 4 \times 10^{-3}$ with $SF = 0.08$ (Figure 3.4D). The stratification of TA cells behaves similarly as the stem cells (Figure 3.4E). As also seen in a typical simulation of the cell distribution (Figure 3.4F), the stem cells and TA cells locate in narrow regions close to the basal lamina with highest densities. Outside of those regions, the distribution of cells is nearly uniform, with a low stratification level near $SF = 0.2$.

It is clear from the simulations that the cell-extrinsic noise increases layer thickness and hinders the stratification. Such noise can lead to unbounded growth of the layer when the noise level is high.

3.4.3 Noise in morphogens increases layer size without affecting tissue stratification

For the system containing only noise on morphogen ($\varepsilon = \sigma = 0$), we first present layer thickness as a function of time for three different noise levels (Figure 3.5A). The layer thickness is increased within a short time and the layer fluctuates slightly later. As the noise level ω

increases, the layer fluctuates around a higher size.

Interestingly, the average TH has an inverted U-shape with a maximum 1.36mm at $\omega = 1.2$ (Figure 3.5B). Unlike the unbounded growth caused by cell-extrinsic noise, the morphogen noise can only induce an increase up to 3-fold (Figure 3.5B). The layer thickness variability is low with $CV < 12\%$ (Figure 3.5C), neither strong oscillation nor rapid growth is observed.

By looking at the average SF of stem cells or TA cells (Figure 3.5D and 5E), we see the average SF decreases slowly as the noise level ω increases. The minimums of SFs are larger than 0.8, indicating the layers remain well stratified. An example of the simulation shows the layer has a clear stratification despite morphogens are very noisy (Figure 3.5F).

We observe that the morphogen noise can increase the layer thickness up to a limited level and the thickness remains bounded. The tissue stratification is preserved when the morphogen noise is present only. Although such noise often causes minor reduction of stratification, the layers remain well stratified.

3.5 The effects of two different combinations of two types of noise

We have studied the effects of single noise in Section 3.4. Here we combine two types of noise that have shown opposite effects on layer thickness individually, and investigate the layer thickness and stratification under such noise combination. For convenience, from now on, the stratification factor presented below is only for stem cells as the similar stratification pattern are observed for the stem cells and TA cells.

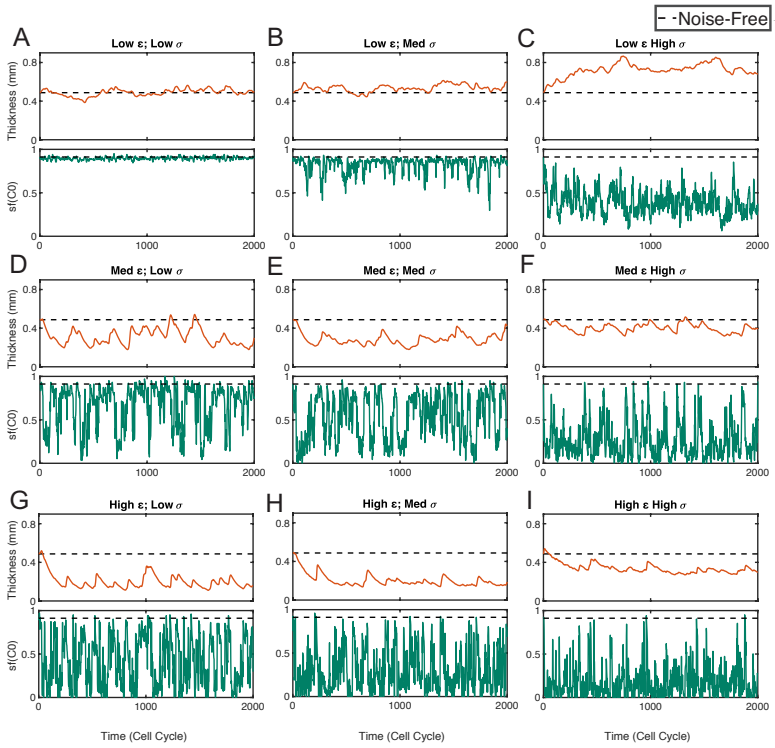

Figure 3.6: Simulations with both cell-intrinsic noise and cell-extrinsic noise. Simulations with different noise levels are shown in (A-I). In each subfigure, the panel on the top shows the dynamics of layer thickness, the panel on the bottom shows the dynamics of layer stratification of stem cells ($sf(C_0)$). The dash line represents for the corresponding quantity at homeostasis. Three different levels are chosen for each type of noise. For cell-intrinsic noise level ε: 0.2 (Low), 0.6 (Medium), 1 (High). For cell-extrinsic noise level σ: 5×10^{-4} (Low), 1×10^{-3} (Medium), 2×10^{-3} (High).

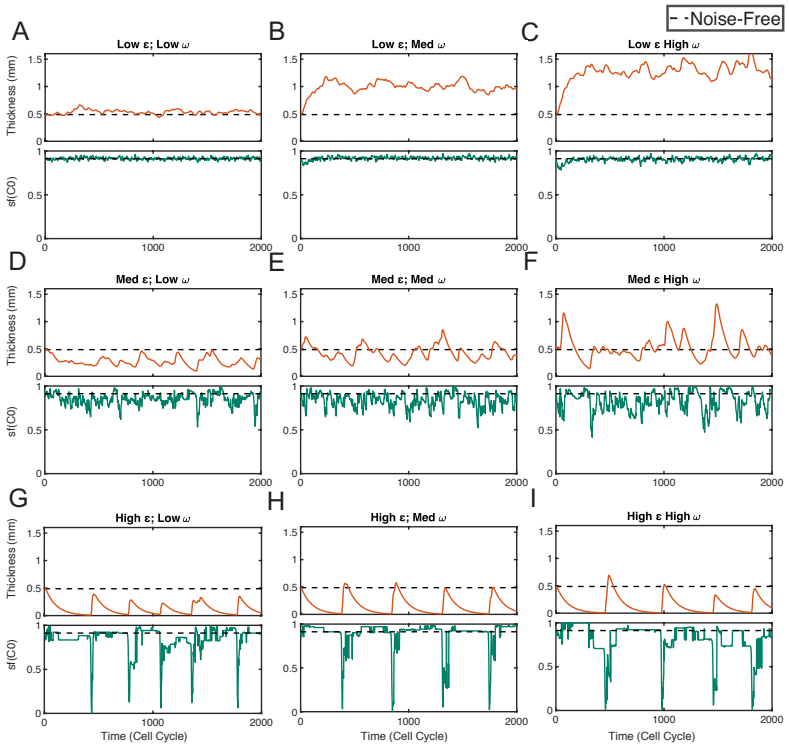

Figure 3.7: Simulations with both cell-intrinsic noise and morphogen noise. Simulations with different noise levels are shown in (A-I). In each subfigure, the panel on the top shows the dynamics of layer thickness, the panel on the bottom shows the dynamics of layer stratification of stem cells ($sf(C_0)$). The dash line represents for the corresponding quantity at homeostasis. Three different levels are chosen for each type of noise. For cell-intrinsic noise level ε: 0.2 (Low), 0.6 (Medium), 1 (High). For morphogen noise level ω: 0.2 (Low), 0.6 (Medium), 1 (High).

3.5.1 Cell-extrinsic noise reduces the variability of the layer thickness caused by cell-intrinsic noise but with less stratified layer

ε \ σ		0	5×10^{-4}	1×10^{-3}	2×10^{-3}
0	TH	0.49mm	0.53mm	0.58mm	0.75mm
	CV	0%	1%	3%	7%
	SF	0.91	0.90	0.88	0.40
0.2	TH	0.45mm	0.49mm	0.54mm	0.69mm
	CV	7%	7%	7%	8%
	SF	0.91	0.90	0.82	0.39
0.6	TH	0.24mm	0.28mm	0.30mm	0.44mm
	CV	30%	25%	23%	17%
	SF	0.84	0.69	0.52	0.27
1	TH	0.12mm	0.19mm	0.22mm	0.38mm
	CV	89%	36%	32%	19%
	SF	0.88	0.42	0.32	0.18

Table 3.1: The statistics of TH, CV and $SF(C_0)$ with combined cell-intrinsic (ε) and cell-extrinsic (σ) noise. All quantities are captured based on 20 simulations.

For the system containing both cell-intrinsic noise and cell-extrinsic noise ($\omega = 0$), we first plot layer thickness and stratification factor as functions of time in several stochastic simulations (Figure 3.6). With small noise levels, the layer thickness and stratification both fluctuates slightly around homeostasis (Figure 3.6A). As the cell-extrinsic noise level σ increases, the mean thickness increases regardless of the levels of cell-intrinsic noise ε (Figure 3.6A-C, Figure 3.6D-F, and Figure 3.6G-I). For the thickness variability, it has little changes when the cell-intrinsic noise is small, but interestingly, with a larger cell-intrinsic noise level, the thickness variability actually decreases as σ increases (Figure 3.6D-F, and Figure 3.6G-I). On the other hand, the mean thickness decreases as the cell-intrinsic noise level ε increases (Figure 3.6ADG, Figure 3.6BEH, Figure 3.6CFI). For the thickness variability, there are little changes as ε increases, except a clear increase when the noise is small (Figure 3.6AD). For the stratification, the mean of stratification factor decreases as either a function of the

ε \ ω		0	0.2	0.6	1
0	TH	0.49mm	0.58mm	1.06mm	1.33mm
	CV	0%	3%	9%	11%
	SF	0.91	0.92	0.92	0.91
0.2	TH	0.45mm	0.54mm	0.98mm	1.23mm
	CV	7%	7%	11%	13%
	SF	0.91	0.91	0.92	0.90
0.6	TH	0.24mm	0.26mm	0.43mm	0.52mm
	CV	30%	29%	30%	33%
	SF	0.84	0.83	0.84	0.81
1	TH	0.12mm	0.13mm	0.15mm	0.16mm
	CV	89%	87%	97%	108%
	SF	0.88	0.88	0.87	0.84

Table 3.2: The statistics of TH, CV and $SF(C_0)$ with combined cell-intrinsic (ε) and morphogen (ω) noise. All quantities are captured based on 20 simulations.

cell-intrinsic noise level ε or cell-extrinsic noise level σ.

The statistical quantities of TH, CV and SF (Table 3.1) show the behaviors of the layer thickness and stratification are consistent with the individual stochastic simulations (Figure 3.6). With low cell-intrinsic noise levels, such as $\varepsilon = 0.2$, CV is an increasing function of the cell-extrinsic noise level σ but the values of CV are always small ($CV < 10\%$). With high cell-intrinsic noise levels, such as $\varepsilon = 0.6$ and 1, CV is a decreasing function of σ. Especially, the decreasing rate is high when the cell-extrinsic noise is near zero. For example, CV decreases from 89% to 36% as σ increases from 0 to 5×10^{-4} at $\varepsilon = 1$. Interestingly, CV is always below 20% when $\sigma = 2 \times 10^{-3}$ regardless of the value of ε. On the other hand, as a function of ε, CV is an increasing function with small increasing rate.

In summary, with the combination of cell-intrinsic noise and cell-extrinsic noise, the cell-intrinsic noise causes reduction of layer thickness and the cell-extrinsic noise causes increase of layer thickness. These observations are similar to the observations when each of the two types of noise appears individually. For the thickness variability, we surprisingly observe that the cell-extrinsic noise can actually suppress thickness variability below a low level

($CV < 20\%$). For the stratification factor, these two types of noise have accumulative effects on reducing stratification.

3.5.2 Combination of cell-intrinsic noise and morphogen noise

For the system containing the cell-intrinsic noise and the morphogen noise ($\sigma = 0$), we first study the layer thickness and the stratification factor as functions of time in several stochastic simulations (Figure 3.7). With small noise, the layer thickness and stratification both fluctuates slightly around homeostasis (Figure 3.7A). As the morphogen noise level ω increases, both the mean thickness and the thickness variability increase regardless of the levels of cell-intrinsic noise ε (Figure 3.7A-C, Figure 3.7D-F, and Figure 3.7G-I). The mean stratification factor changes little as ω increases. On the other hand, as the cell-intrinsic noise level ε increases, the mean of the layer thickness decreases. Also oscillation becomes more obvious and the thickness variability increases as ε increases. For the stratification, as ε increases, the stratification factor ($sf(C_0)$) shows short-time corruption in its long-time dynamics but its mean seldom changes (Figure 3.7ADG, Figure 3.7BEH, and Figure 3.7CFI).

As seen through the statistical quantities of TH, CV and SF (Table 3.2), the behaviors of layer thickness, variability and stratification are all consistent with the individual stochastic simulations (Figure 3.7). In particular, CV increases as a function of both cell-intrinsic noise level ε and morphogen noise level ω. Its increasing rate with respect to ε is higher than that regarding ω. The layers always have well-stratified structure where SF is always above 0.80.

In summary, with the combination of the cell-intrinsic noise and the morphogen noise, the cell-intrinsic noise causes reduction of layer thickness and the morphogen noise causes increase of layer thickness. These observations are similar to the observations when each of the two types of noise appears individually. With a higher level of cell-intrinsic noise level, the layers show higher thickness variability. The variability becomes even higher when the

morphogen noise level increases. On the other hand, such combination of noise has little impact on the stratification.

3.6 The combination of three types of noise during homeostasis: tradeoff between low layer thickness variability and strong layer stratification

From the above study, either the cell-extrinsic noise or the morphogen noise alone results in an increase of layer size away from the homeostasis. However, by adding the cell-intrinsic noise to either one of them, the layer thickness decreases compared to the case with only cell-extrinsic noise or morphogen noise. Next we include all three types of noise to explore the conditions under which the homeostasis is maintained.

With the homeostasis maintained, the cell-extrinsic noise level σ and the morphogen noise level ω exhibit a negative correlation when the cell-intrinsic noise level ε is fixed (Figure 3.8A). The σ-ω plane is divided into stabilized (region I-IV) and non-stabilized region (region V). As long as the levels of cell-extrinsic noise and morphogen noise are located in the stabilized region, the homeostasis can be maintained with a proper cell-intrinsic noise level ε. Particularly, the curves with $\varepsilon = 0.6$, 0.8 and 1 are located in a region with narrow width at σ direction. This indicates even a small change in the cell-extrinsic noise level σ requires a large change in the cell-intrinsic noise level ε to maintain the homeostasis. Therefore, it suggests that the balance between the cell-intrinsic noise and cell-extrinsic noise plays a key role during the homeostasis maintenance regardless of the morphogen noise. On the other hand, inside non-stabilized region, the layer is unable to maintain homeostasis for any value of ε.

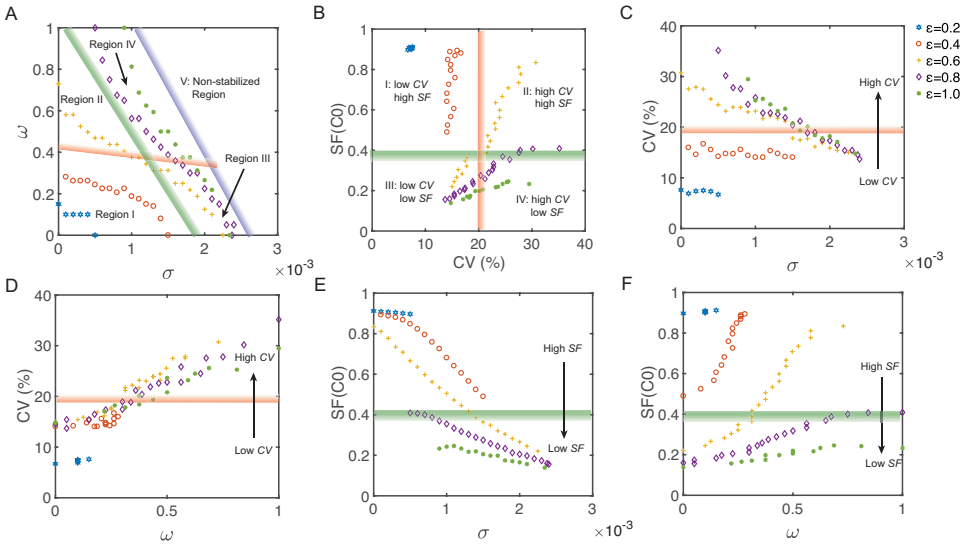

Figure 3.8: Simulations for maintaining homeostasis (SS=0.49mm) with different combinations of three types of noise. Points with the same color and the same marker represent for simulations with the same cell-intrinsic noise level ε, where $\varepsilon = 0.2$, 0.4, 0.6, 0.8 and 1 respectively. The strips, filled with color gradient, roughly divide the plane into several regions. Data points located in the region next to dark/light color of an individual strip have more/less desirable properties. (A) The relation between the cell-extrinsic noise level σ and the morphogen noise level ω. The blue strip sketches the green points with maximal cell-intrinsic noise level $\varepsilon = 1$. It divides this plane into stabilized region (region I-IV) and non-stabilized region (region V). The stabilized region is divided into four parts (region I-IV) by a red strip and a green strip. These regions will be introduced next. (B) The relation between layer thickness variability (CV) and layer stratification factor of stem cells ($SF(C_0)$). The red strip with $CV = 20\%$ divides this plane into two regions with low CV or high CV. Also the green strip with $SF(C_0) = 0.4$ divides the plane into two regions with high SF or low SF. The red and the green strips together divide the stabilized region into four regions (Region I: low CV and high SF; Region II: high CV and high SF; Region III: low CV and low SF; Region IV: high CV and low SF). (C) The relation between σ and CV. (D) The relation between ω and CV. (E) The relation between σ and $SF(C_0)$. (F) The relation between ω and $SF(C_0)$.

The stabilized region can be divided into two parts either with respect to CV by a red strip with $CV = 20\%$ (Figure 3.8A-D), or with respect to SF by a green strip with $SF = 0.4$ (Figure 3.8 A-B and E-F). Together, the stabilized region can be divided into four regions based on the thickness variability and the stratification level (Figure 3.8A-B): low-CV and high-SF region (region I); high-CV and high-SF region (region II); low-CV and low-SF region (region III) and high-CV and low-SF region (region IV).

The CV can be considered as a three-variable function in terms of noise levels $(\varepsilon, \sigma, \omega)$. With fixed cell-intrinsic noise level ε, the CV is a decreasing function of the cell-extrinsic noise level σ (Figure 3.8C) and an increasing function of the morphogen noise level ω (Figure 3.8D). It increases slowly when $\omega < 0.4$ and then increases linearly. Interestingly, as a function of ω, CV looks independent of ε and σ where all data points are located in a narrow region in the ω-CV plane (Figure 3.8D), which suggests that the layer thickness variability is mainly adjusted by morphogen noise.

The SF can also be considered as a three-variable function in terms of noise levels $(\varepsilon, \sigma, \omega)$. With fixed cell-intrinsic noise level ε, the SF is a decreasing function of σ (Figure 3.8E) and an increasing function of ω (Figure 3.8F). Its value also highly depends on ε. Therefore, all three types of noise play important roles in layer stratification.

There exists a clear tradeoff between low variability and strong stratification (Figure 3.8AB). With low cell-intrinsic noise levels ($\varepsilon \leq 0.4$), all data points are contained in region I. But a high morphogen noise level ω improves layer stratification without affecting the thickness variability. With medium cell-intrinsic noise levels ($0.6 \leq \varepsilon \leq 0.8$), data points move from region III to region II as the morphogen noise level ω increases. The layer can only have either low thickness variability or high stratification. The morphogen noise improves stratification but increases variability. In the other word, the cell-extrinsic noise improves thickness variability but deteriorate stratification. With high cell-intrinsic noise level, such as $\varepsilon = 1$, the data points move from region III to region IV as ω increases. In this case, the

low morphogen noise level ω results in low thickness variability. Although the stratification factor is still an increasing function of ω, the layer stratification is always in the undesirable range due to the high value of ε, regardless of the value of ω.

For the homeostasis maintenance, the balance between cell-intrinsic noise and cell-extrinsic noise is dominant in the combination of three types of noise. The morphogen noise can adjust the layer thickness variability, and plays a complementary role by adjusting the balance between layer thickness variability and stratification.

3.7 Method

All simulations are conducted in MATLAB 2015b. The numerical methods are described as below.

3.7.1 Solving morphogen gradient equations by using quasi-steady state

The time scale of cell cycle lengths is days, whereas the time scale of molecule interactions is hours. The morphogen system can reach the steady state quickly compared to the cell cycle. Therefore, in the deterministic system, we calculate the quasi-steady state of Eq. (3.5) at each computational time step:

$$\begin{aligned} 0 &= D_A \frac{\partial^2 [A]}{\partial z^2} + \sum_{i=0}^{2} \mu_i C_i - a_{\deg}[A], \\ 0 &= D_G \frac{\partial^2 [G]}{\partial z^2} + \sum_{i=0}^{2} \eta_i C_i - g_{\deg}[G], \end{aligned} \tag{3.14}$$

A second order central difference method is carried out to approximate Laplacian operators

in Eq. (3.14). The resulting linear systems are solved by the MATLAB's built-in backslash function "/".

In the stochastic system, we also acquire the same quasi-steady state and then add fluctuations according to Eq. (3.8).

3.7.2 Solving stochastic cell lineage equations

To solve the cell lineage equations Eq. (3.2, 3.3, 3.4, 3.7), we first transform the spatial domain $[0, z_{\max}(t)]$ to a unit domain $[0, 1]$ by a transformation [125]:

$$\begin{aligned} z &= F(X, \tau) = z_{\max}(\tau) X, \\ t &= \tau. \end{aligned} \tag{3.15}$$

By applying Eq. (3.3), we have the transformed derivatives:

$$\begin{aligned} \frac{\partial}{\partial t} &= \frac{\partial}{\partial \tau} - \frac{F_\tau}{F_X}\frac{\partial}{\partial X} = \frac{\partial}{\partial \tau} - \frac{V(z_{\max}, \tau)}{z_{\max}}\frac{\partial}{\partial X}, \\ \frac{\partial}{\partial z} &= \frac{1}{F_X}\frac{\partial}{\partial X} = \frac{1}{z_{\max}}\frac{\partial}{\partial X}, \\ \frac{\partial^2}{\partial z^2} &= \frac{1}{F_X}\frac{\partial}{\partial X}\left(\frac{1}{F_X}\frac{\partial}{\partial X}\right) = \frac{1}{z_{\max}^2}\frac{\partial}{\partial X}. \end{aligned} \tag{3.16}$$

Using Eq. (3.2), we obtain the transformed equations of Eq. (3.7) in the new coordinate system $(X,\tau) \in [0,1] \times [0,\infty)$:

$$\begin{aligned}
&\frac{\partial C_0}{\partial \tau} + \left[\frac{V(X,\tau) - V(1,\tau)}{z_{\max}}\right] \frac{\partial C_0}{\partial X} = \nu_0 (2p_0 - 1) C_0 \\
&\qquad - (\nu_0 C_0 + \nu_1 C_1 - d_2 C_2) C_0 + \left(\sigma_0 \frac{dW_0^a}{d\tau} + \varepsilon_0 C_0 \frac{dW_0^m}{d\tau}\right), \\
&\frac{\partial C_1}{\partial \tau} + \left[\frac{V(X,\tau) - V(1,\tau)}{z_{\max}}\right] \frac{\partial C_1}{\partial X} = \nu_0 [2(1-p_0) C_0] + \nu_1 (2p_1 - 1) C_1 \\
&\qquad - (\nu_0 C_0 + \nu_1 C_1 - d_2 C_2) C_1 + \left(\sigma_1 \frac{dW_1^a}{d\tau} + \varepsilon_1 C_1 \frac{dW_1^m}{d\tau}\right), \\
&C_2 = 1 - C_0 - C_1.
\end{aligned} \tag{3.17}$$

The transformed Eq. (3.2) and (3.3) are given as the following:

$$\begin{aligned}
&\frac{\partial V}{\partial X} = z_{\max} (\nu_0 C_0 + \nu_1 C_1 - d_2 C_2), \\
&\frac{dz_{\max}}{d\tau} = V(1,\tau).
\end{aligned} \tag{3.18}$$

All equations in the new coordinate are included in Eq. (3.17) and Eq. (3.18). To discretize them in space, we use a uniform grid with $N+1$ grid points $x^{(j)} = \frac{j}{N},\ j = 0, 1, \ldots, N$. In Eq. (3.17), the advection term $\frac{\partial C_i}{\partial X}$ is discretized by the second order upwind method. The infinite-dimensional noise term $\frac{dw^{(j)}}{dt}$ at $x = x^{(j)}$ [72], where $w^{(j)}$ are independent of different j. The trapezoidal rule is used to discretize $V(X,\tau)$ in Eq. (3.18).

For temporal discretization, we apply Euler-Maruyama method [82] with time step Δt. To ensure $C_i \in [0,1]$, we make the following adjustments to the numerical solution at each computational time step:

$$\begin{aligned}
&1.\ C_0 = \max\{C_0, 0\}, \quad C_1 = \max\{C_1, 0\}; \\
&2.\ C_0 = \frac{C_0}{C_0 + C_1}, \quad C_1 = \frac{C_1}{C_0 + C_1}, \quad \text{if } C_0 + C_1 > 1.
\end{aligned} \tag{3.19}$$

Parameters	Values	Units
ν_0, ν_1	1	$\ln 2*(\text{cell cycle})^{-1}$
d_2	0.01	$\ln 2*(\text{cell cycle})^{-1}$
D_A, D_G	10^{-5}	mm^2s^{-1}
μ_0, μ_1, μ_2, η_1, η_2	10^{-3}	$\text{s}^{-1}\mu M$
a_{deg}, g_{deg}	10^{-3}	s^{-1}
α_A, α_G	10	mm^{-1}
$\bar{p}_0$	0.95	–
$\bar{p}_1$	0.5	–
γ_A	1.6	μM^{-1}
γ_G	2	μM^{-1}

Table 3.3: Parameters used in Eq. (3.2) to Eq. (3.7).

	ε_0, ε_1	σ_0, σ_1	ω_0, ω_1
Figure 3.2	0.6	10^{-4}	0.58
Figure 3.3F	0.6	0	0
Figure 3.4F	0	3×10^{-3}	0
Figure 3.5F	0	0	0.6
Figure 3.6	Low; 0.2	Low: 5×10^{-4}	0
	Medium: 0.6	Medium: 1×10^{-3}	
	High: 1	High: 2×10^{-3}	
Figure 3.7	Low: 0.2	0	Low: 0.2
	Medium: 0.6		Medium: 0.6
	High: 1		High: 1

Table 3.4: Noise levels used in Eq. (3.7) and (3.8) in different figures.

3.7.3 Noise combination during tissue homeostasis

In Section 3.6, we search for the combination of all three types of noise where the homeostasis is maintained. We solve the equation $TH\,(\varepsilon, \sigma, \omega) = SS$ in the average sense for noise levels $(\varepsilon, \sigma, \omega)$. By fixed ε and σ, we solve ω by using bisection method with tolerance 3% of the homeostasis (SS). The mean TH is captured based on 20 simulations. The noise level ε and σ are chosen to satisfy $\varepsilon = 0.2k_1,\ (k_1 = 1, \ldots, 5)$ and $\sigma = 10^{-4}k_2,\ (k_2 \in \mathbb{Z}^+)$.

3.7.4 Parameters and computational setup

In this study, only noise levels ε, σ and ω are varied. The parameters used in Eq. (3.2) to Eq. (3.7) are listed in Table 3.3. The noise levels in Eq. (3.7) and (3.8) used in different figures are listed in Table 3.4.

For the initial conditions in the stochastic simulations, we take the steady state solutions of the deterministic system, with its initial thickness being $SS = 0.49$mm.

In all simulations, we choose $N = 128$ as the number of grid points and the time step $\Delta t = 0.002$. Numerical tests have been performed with different grid sizes and time steps to assure the convergence of the numerical solutions.

3.8 Discussion and Conclusions

Here we have explored noise effects on the epithelium layer maintenance on its thickness and stratification. We have found that the cell-intrinsic noise causes reduction and oscillation of layer on its thickness. The cell-extrinsic noise or the morphogen noise introduces an increase in the layer thickness. The cell-extrinsic noise can reduce the layer thickness variability introduced by the cell-intrinsic noise, but resulting in weaker stratification. To study layer homeostasis, we explore different combinations of three types of noise. The cell-extrinsic noise level and morphogen noise level display a negative correlation under a fixed cell-intrinsic noise level. With the low cell-intrinsic noise levels, the high morphogen noise levels actually improve layer stratification. With the medium cell-intrinsic noise levels, there exists a tradeoff between low layer thickness variability and strong stratification, and the high morphogen noise levels lead to better stratification whereas the low morphogen noise levels lead to lower thickness variability. However, with the high cell-intrinsic noise level, the layer stratification becomes weaker, but the layer thickness variability can be reduced

through low morphogen noise levels.

The randomness in morphogen dynamics can come from multiple biological processes with both cell-intrinsic and cell-extrinsic sources: noise in the downstream gene expression, randomness in diffusion, and stochastic bindings between morphogen and their receptors. It is not surprising that our study finds the morphogen noise has both effects similar to the cell-extrinsic noise on increasing layer thickness, and to the cell-intrinsic noise on increasing layer thickness variability without damaging stratification. Morphogen noise exhibits properties of a mixture of cell-intrinsic noise and cell-extrinsic noise.

In this study, the stochastic simulations have been performed on a very long time scale with 2000 cell cycles in order to study noise effects on homeostasis. The biological relevant span for regeneration or development is much shorter in a range of 50 cell cycles, corresponding to a few weeks in real time. During the homeostasis study, one layer oscillates with a time window shorter than 50 cell cycles (e.g. Figure 3.2E). The long time dynamics in the simulation allows us to check if the layer really approaches to a stable state or only exhibits short time transient properties.

To the best of our knowledge, our study is the first work to include noise dynamics to the cell lineage models. In stochastic gene expression modeling, the internal (or intrinsic) noise and external (or extrinsic) noise in stochastic gene expression systems are modeled in a similar way, respectively [57]. In particular, the internal noise alters the transcription rate, and is modeled by multiplicative noise, and the external noise alters the background production of gene expressions, and is then modeled by additive noise [57].

In our model, different types of noise in cell lineage equations affect the layer growth velocity through cell densities. Such stochastic effects consequently affect the layer thickness. It would be interesting to explore how other types of stochastic effects may also affect layer growth by adding noise directly to the equations for growth velocity or/and layer thickness.

Biological identities in the environment not included in our current model, such as cells in the dermal, may be modeled through the boundary conditions. Study the stochastic dynamics of those quantities requires new approaches of including noise in the boundary conditions, which is computationally challenging.

Rather than using the generic noise considered in this model, one may include more specific types of noise in the system. For example, noise on cell cycle, noise on cell death and noise on morphogen synthesis rate may be modeled in an explicit way. Complex tissue morphology in two or three dimensions may also have synergistic effect with noise. Simulations for noise in PDEs (e.g. through the two-dimensional model [124]) in two or three dimensions are usually much more challenging than the one-dimensional system studied in this work.

The morphogen is the only factor considered for regulation of stratification in our work. There are many other important factors that may also affect stratification. The selective cell-adhesion, one type of intercellular mechanical force, is another mechanism that can improve the stratification [35]. In order for the tissue to control the layer thickness variability, mechanical forces may play important role [141], for which discrete cell model may provide a convenient framework [35]. Gene regulatory networks in the downstream of the morphogens are neglected in this work. In many cases, the network structure and dynamics are critical to attenuate noise [169] and sometimes, noise in gene expression actually benefits spatial organization of cells [190, 170].

In summary, our study suggests the cell-intrinsic noise can battle the stochastic uncertainty in cell population size caused by cell-extrinsic noise. While the morphogen noise has properties of both types of noise, it can be utilized through its regulation of the downstream gene expressions to adjust the cell-intrinsic component of the stochastic effects to regulate the variability and stratification, consequently improving tissue homeostasis.

Chapter 4

Dissection of multiple morphogens and morphogenesis in zebrafish hindbrain pattern formation

This chapter is an ongoing project in collaboration with Lianna Fung, Thomas Schilling and Qing Nie.

4.1 Background

The early zebrafish hindbrain is segmented into rhombomeres (r) with distinct domains of gene expression. The boundaries between these gene expression domains are initially rough and sharpen over time by a combination of gene regulation and cell sorting. Previous computational works have revealed the synergy of gene regulation and cell sorting in contributing to the boundary sharpening process. However, it remains unclear how multiple morphogens and changes in tissue shape, morphogenesis, contribute to rhombomere formation. We de-

velop a two-dimensional stochastic multi-scale model, including gene regulation, cell sorting and tissue growth, to mimic the formation of r2-r6. We find the secondary morphogen Fibroblast Growth Factor (FGF) synthesized at r4 can significantly improve the robustness of rhombomere size. The experimental quantifications of hindbrain size during development reveal the hindbrain has a fast convergence in the left-right (LR) axis at earlier stages. We computationally compare the patterns resulting from different early convergent rates. The fast convergence rate based on experimental data was found to improve the efficiency of cell sorting during early hindbrain development. Moreover, the fast convergence rate is optimal for the synergy between gene regulation and cell sorting because cells commit their fates at the early stage and sequentially cell sorting can sharpen the boundary at the late stage without the disruption of cell identity switching. From our simulations, a trade-off between size and boundary sharpness is identified and that can be reduced through the early fast convergence rate. Altogether, The fast convergence rate provides a strategy to maintain both precise patterns along with the tight control of rhombomere sizes.

4.2 Introduction

Pattern formation is a fundamental question in developmental biology to understand how the basic architectures of tissues and organs are determined during embryogenesis. Cell fate decisions, together with tissue growth, reveal the dynamics of pattern formation [87]. Through complex gene regulation and molecular interactions, cells convert the concentration-dependent positional information from a diffusive chemical, morphogen, to coordinate their fate decisions [139]. The dynamics of pattern formation during growth have been widely studied but vary in different systems [160]. Mathematical models have successfully integrated growth and spatial signaling to reveal the patterning process in various systems including embryo segmentation [71, 70], the *Drosophila* imaginal wing disc [43, 13, 194], vertebrate

limb buds [136], vertebrate neural tube [9, 187], vertebrate hindbrain [170, 190, 19, 127], vertebrate craniofacial [112], skin [35] and hair follicles [171].

Recently, more attention has been paid to understand the stochastic effects in patterning system, raising the question of how precision is achieved in spite of the biological noise in gene expression and spatial signals. Noise attenuation mechanisms have been widely explored in diverse cellular networks [118, 131]. In morphogen gradients, the variations of spatial signaling can be reduced through many mechanisms, such as regulation on the steepness of gradient [148, 90] and self-regulated uptakes [177, 40]. The interpretation of noisy spatial signals into cell fate decisions can reduce the patterning errors through antiparallel morphogens [187] and gene regulatory networks [150, 134]. Instead of controlling the noise, the utilization of the gene expression noise to battle the noise in morphogen levels provides another strategy to achieve precise patterns [190, 133]. In addition to the strategies at the molecular levels, the precision of the pattern can also be improved through strategies at the cellular level through cell sorting driven by mechanical forces [170, 35].

The development of the embryonic zebrafish hindbrain serves as a great model system to study the role of gene regulation, stochasticity and cell sorting in pattern formation. The hindbrain is a complex coordination center of the vertebrate brain. The embryonic hindbrain is subdivided into transversal segments, called rhombomeres (r), along the anterior-posterior (A-P) axis [103]. The initial expression domains of the hindbrain have fuzzy borders and a precise pattern subsequently forms in which all cells within each region have the same identity [190, 181]. Several signaling pathways provide positional information for transcriptional networks, such as Fibroblast Growth Factor (FGF) [23, 166, 180, 84, 107] and retinoic acid (RA) [177, 143, 137, 108, 151]. Numerous transcriptional factors, including *hox* genes, *krox20*, *val*, *vhnf1* and *irx*, with specific regional expression domains are involved in complex gene regulatory networks to specify rhombomeres [5, 126, 93]. Through complex gene regulatory networks, cells commit their fates and switch their identity by interpreting the

spatial signals [2, 144]. In addition, the complementary segmental expression of Eph receptors and ephrins drives boundary sharpening by regulating the cell sorting with differential adhesion/repulsion [26, 184, 58, 130]. Despite extensive reporting of rhombomere specific gene regulation, how these gene interactions coordinate and contribute to the hindbrain patterning remains unclear. Meanwhile during embryonic development the hindbrain undergoes growth and cell migration, resulting in a morphological process called convergent extension. During convergent extension, the hindbrain narrows along the left-right (LR) axis and elongates along the anterior-posterior (AP) axis [154]. The effects of convergent extension on the boundary sharpening process remain elusive.

By considering one morphogen RA and two transcriptional factors *hoxb1a* and *krox20*, previous computational works have mimicked the boundary sharpening process in r3-r5 with mechanisms involving gene regulation and cell sorting. Here we further extend these approaches to study the hindbrain patterning process from 11 to 14 hours post fertilization (hpf) and expand our model to include r2-r6. We incorporate a second morphogen FGF and two additional transcriptional factors, *vhnf1* and *irx3* into our new model. We found the secondary morphogen FGF synthesized at r4 is able to improve the robustness of rhombomere size. Moreover, we quantify the morphological changes experimentally and adopt it to the model. The convergence is fast at the early stage then it slows down. We compare hindbrain pattern formation under different convergent rates computationally. With a fast convergence rate at early stages, we show that the cell sorting becomes more efficient at segregating cells to their territories resulting in sharper segmental boundaries. The fast convergence also forces cells to commit their fates at earlier stages allowing the cell sorting better improves the precision of the pattern at later stages. By discovering a trade-off between boundary sharpness and rhombomere sizes, we found the fast convergence rate is able to reduce this trade-off by acting on both cell sorting and cell fate commitment. The fast convergence at the early stage provides a strategy to achieve precise and accurate pattern by regulating both the boundary sharpness and rhombomere sizes.

4.3 A stochastic multi-scale model reveals rhombomere formation under growth

Rhombomere formation involves many complex processes including cell fate commitment through stochastic gene regulation, cell sorting through selective cell-cell mechanical adhesion/repulsion and growth (i.e. convergent extension). They play essential roles from pattern initiation to pattern refinement. With rough r2-r6 pattern at 11hpf, the pattern is refined over time and a precise five-segment pattern with four sharp boundaries displays at 14hpf (Figure 4.1C). To dissect the roles of each mechanism, we first build a stochastic multi-scale model to mimic the process of r2-r6 pattern formation from 11 to 14hpf.

4.3.1 Modeling stochastic gene regulations in r2-r6 with multiple morphogens

Morphogen Retinoic Acid (RA), synthesized in r7, diffuses anteriorly over the entire hindbrain for initial rhombomere formations [143, 137, 108]. RA activates *vhnf1* in r5 and r6 [108]. Through a mutual inhibition between *vhnf1* and *irx3*, the pre-rhombomeric r4/r5 boundary ($\sim$95% epiboly) is specified by the border between these two genes [93]. RA then activates *hoxb1a*, another RA-dependent transcriptional factor, at the tailbud stage. *Hoxb1a* is repressed by Vhnf1 and its expression is restricted in r4 at the 2-somites stage [108]. With Hoxb1a expression at r4, r4 becomes the secondary signaling center where Hoxb1a activates the synthesis of FGF at r4 [23, 107, 175]. The secondary morphogen FGF diffuses both anteriorly and posteriorly to induce *krox20* at r3 and r5 [166, 180, 84]. Through auto-regulation, *krox20* expression is bimodal depending on the concentration of FGF [19, 84]. The r2/r3 and r5/r6 boundaries are specified by the expression of *krox20*. The auto-regulations and mutual inhibition between *hoxb1a* and *krox20* establish a toggle switch that specifies and refines the

r3/r4 and r4/r5 boundaries [190]. When the pattern is established, *hoxb1a* marks r4, *krox20* marks r3 and r5, and low expression of both *hoxb1a* and *krox20* mark r2 and r6. We use the complex gene regulatory network discussed above to build our model, in addition, we consider the stochastic effects on the dynamics of both morphogen and downstream genes by adding the noise terms (Figure 4.1A). See Supplement for mathematical equations.

4.3.2 Modeling mechanical interactions between individual cells

We consider the cell movement driven by mechanical interactions. The subcellular element method (SCEM) is used to model the individual cells and their mechanical interactions [117]. In the zebrafish hindbrain, Eph4a receptor is expressed at odd rhombomeres (r3 and r5) and Ephrin-B2 ligand is expressed in even rhombomeres (r2, r4 and r6). This receptor-ligand binding leads to the selectivity in cell sorting where cells with same identity have attraction and cells with different identity have repulsion to each other [26]. Since *eph4a* is a direct transcriptional target of Krox20 [58], we model the selective cell sorting based on the Krox20 expression level (Figure 4.1B). The morphology of hindbrain changes along with the convergent extension. For cells in the hindbrain, we consider the chemoattractant where cells move along with the growth [146, 140].

4.3.3 Experimental quantifications of growth and the computational domains

The embryonic convergent extension drives the morphology changes of the zebrafish hindbrain. The hindbrain narrows along the LR axis and elongates along the AP axis during 11-14hpf (Figure 4.1CD). Schilling's lab perform whole mount *in situ* hybridization of zebraifsh embryos to visualize the midbrain-hindbrain boundary (MHB) by *otx2*, r3 and r5 by

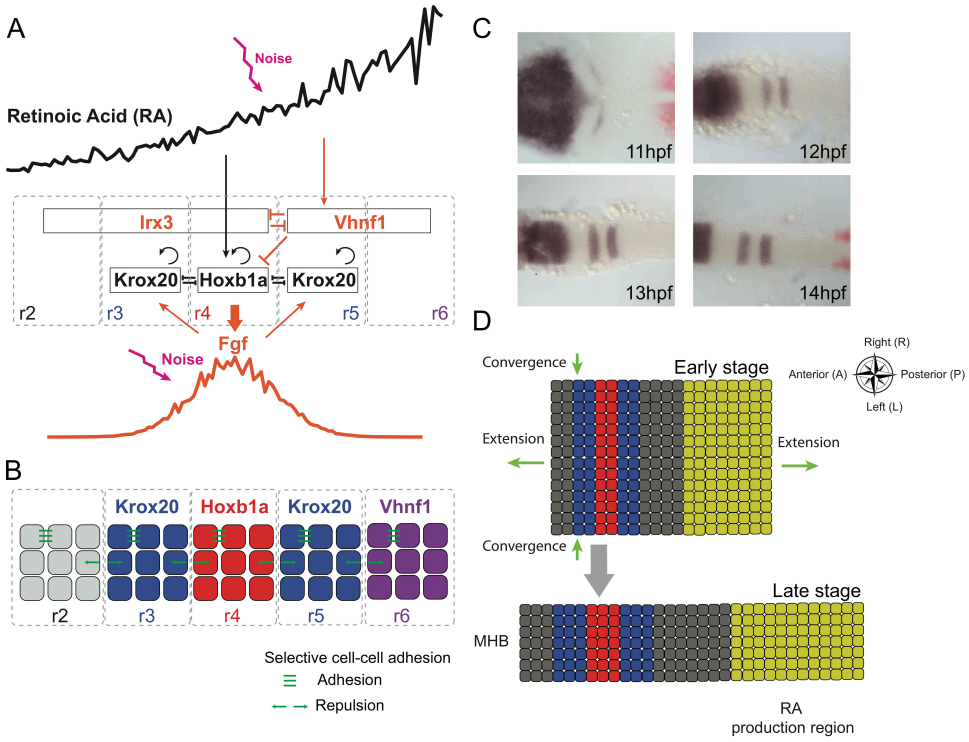

Figure 4.1: Model schematic and morphology of hindbrain. (A) Stochastic gene regulatory network for the hindbrain patterning in r2-r6. Genes and morphogens with black font were previously used for the model of r3-r5 pattern [190], genes and morphogens that are first considered in this work use orange font. Pointed arrows depict up-regulations and blunt arrows depict down-regulations. Noise causes fluctuations in morphogens distributions. The morphogen retinoic acid (RA) synthesized by posterior mesoderm and diffuses anteriorly to have a graded distribution. RA activates *hoxb1a* in r4 and *vhnf1* in r5-r6, respectively. *Vhnf1* and *irx3* mutually inhibit each other to specify the early r4/r5 boundary. Vhnf1 inhibits *hoxb1a* to constrain it in r4. Hoxb1a up-regulates the synthesis of the secondary morphogen Fibroblast Growth Factor (FGF) at r4. FGF diffuses both anteriorly and posteriorly to induce *krox20*. Krox20 is expressed in r3 and r5. The mutual inhibition also exists between *hoxb1a* and *krox20*. Both *krox20* and *hoxb1a* positively up-regulate their own expressions. (B) The illustration for r2-r6 pattern and the selective cell-cell adhesion. The expression of Hoxb1a and Krox20 determine the r3-r5 pattern, where cells in r3 and r5 express Krox20 and cells in r4 express Hoxb1a. In r2 and r6 expressions of both Hoxb1a and Krox20 are low. Cells in r6 have high Vhnf1 expression. After cells determine their identities, the selective cell-cell adhesion can improve the precision of gene expression boundary. Cells with the same identity attract each other and cells with the different identities repulse each other. (C) Whole mount *in situ* hybridization for *otx2* (purple most anterior region), *krox20* (purple segments in the center) and *aldh1a2* (red) transcripts from 11 to 14 hpf. The midbrain-hindbrain boundary (MHB) is marked by *otx2*, the r3 and r5 are marked by *krox20* and the RA production region is marked by *aldh1a2*. Embryos are flat-mounted with anterior to the left. (D) The illustration of the convergent extension (i.e. growth) of the hindbrain. The hindbrain shrinks in LR direction and elongates in AP direction.

krox20 and RA production region by *aldh1a2*. At each hour, we measure the LR width of hindbrain at the location of r4, the AP length of hindbrain and production region at the center of LR axis. Total n=9 samples are taken for each time point and the statistics of the hindbrain dimensions are shown in Figure 4.2AB.

In the model, we simply take the hindbrain shape as a rectangle by utilizing the dimensions from the experimental quantifications (Figure 4.1D). We consider two domains in the computational framework: morphogen domain and tissue domain. In morphogen domain, we model the morphogens in a continuum description. In tissue domain, we model the discrete cells along with the intracellular gene expressions in a discrete description. The hindbrain (r1-r7) and RA production region are taken as the morphogen domain to model dynamics of morphogens. Two morphogens, RA and FGF, are modeled by stochastic reaction-diffusion equations and the morphogen domain with regular rectangular mesh is used for their spatial domain with the finite difference spatial discretization. One part of the morphogen domain, r2-r6 region, is taken as the tissue domain to model the dynamics of individual cells. In tissue domain, the sub-cellular element method (SCEM) is used to describe the morphology, mechanical interactions and movement of cells. All discrete cells considered by the model are contained in the tissue domain and a group of elements (nodes) is used to represent the cell. The gene regulation of all intracellular genes, including *krox20*, *val*, *vhnf1* and *irx3*, are defined within each individual cell. The morphogens diffuse in extracellular environment (morphogen domain) and associate with the individual cells (tissue domain). The exchanges between extracellular environment and individual cells are carried out by interpolation methods (Supplement).

4.3.4 A stochastic simulation captures the r2-r6 pattern formation

With the consideration of the multiple mechanisms discussed above, the stochastic multi-scale model successfully mimics the dynamics of r2-r6 formation. In this section, we show one stochastic simulation with spatial distributions of multiple genes.

First, we show the spatial distributions of morphogens. Both RA and FGF signals have noisy distributions over the space (Figure 4.2CD). The RA gradient is decreasing from posterior to anterior while FGF level is high at r4 and decreases in both anterior and posterior directions.

Next, we show a time series of the spatial patterns of the intracellular genes (Figure 4.2E-G). The expression patterns of *hoxb1a* and *krox20* provide a good description of the boundary sharpening process. The distinct cell identities present in r2-r6 can be observed via the expressions of these two genes, where *hoxb1a* is expressed at r4, *krox20* is expressed at r3 and r5, and low expressions of both *hoxb1a* and *krox20* is observed at r2 and r6 (Figure 4.2E). Initially at 11hpf, *hoxb1a* is observed at r4 alongside weak *krox20* expression in r3 and r5. Notably, *krox20* expression is stronger in r3 than r5 (Figure 4.2C). At 12hpf, *krox20* expression is clear at both r3 and r5 but boundaries of these two rhombomeres are still rough. One cell with *hoxb1a* identity intermingles with r3 cells. A few cells close to the r4/r5 boundary are undergoing identity switching as they co-express low levels of *krox20* and *hoxb1a*. At 13hpf, the intermingling *hoxb1a* cell segregates closer to the r3/r4 boundary and most of the *krox20* and *hoxb1a* co-expressing cells commit to a specific cell identity. Boundaries at this stage are also sharper compared to 12hpf. At 14hpf, all cells segregate to their territories and the boundaries are fully sharpened. A precise five-segments pattern can be observed.

The time series of *vhnf1* and *irx3* expression is shown in Figure 4.2FG. At 11hpf, the boarder between *vhnf1* and *irx3* determines the position of the pre-rhombomeric r4/r5 boundary. At later stages, the border between *vhnf1* and *irx3* shifts posteriorly and is located in r5

[93]. Unlike *hoxb1a* and *krox20*, there is no auto-regulation for *vhnf1*. *Vhnf1* is not able to maintain its own expression without RA signals. Consequently, the decreasing level of RA over time (Figure 4.11C) leads to the posterior shift of *vhnf1* expression.

To quantitatively study the size and boundary sharpness of the system, we define three quantities for the simulation result: the rhombomeres size, boundary sharpness index (SI) and number of dislocated cells (DC). The SI describes the sharpness level of each boundary where a lower value indicates a sharper boundary. For a cell located too far away from its region, we identify it as the dislocated cells and DC gives the counts of all dislocated cells in the simulation. The SI and DC can describe the precision of the pattern. See Supplement for details.

The stochastic simulations are repeated (n=100) independently under different random seeds and the statistics of the quantities are shown in Figure 4.2K. The results at the end of the simulations show a good fit with experimental measurements of the rhombomere sizes at 14hpf. From 11-12hpf, identity switching affects the sharpness of boundaries and we observe DC and SI(r5/r6) increase in this period. From 12-14hpf, the boundary sharpness process can also be observed by the quantifications, DC and SIs, where they gradually fall down to the minimum.

4.4 The cooperation between RA and FGF contributes to the robust segmental pattern

Since two morphogens are involved in this model, here we discuss how these two morphogens cooperate and contribute to the pattern. A previous work took RA as the only morphogen and it successfully simulated the formation of r2-r5 pattern [190]. For simplification, *hoxb1a* and *krox20* were taken as the direct downstream targets of RA, despite *krox20* indirectly

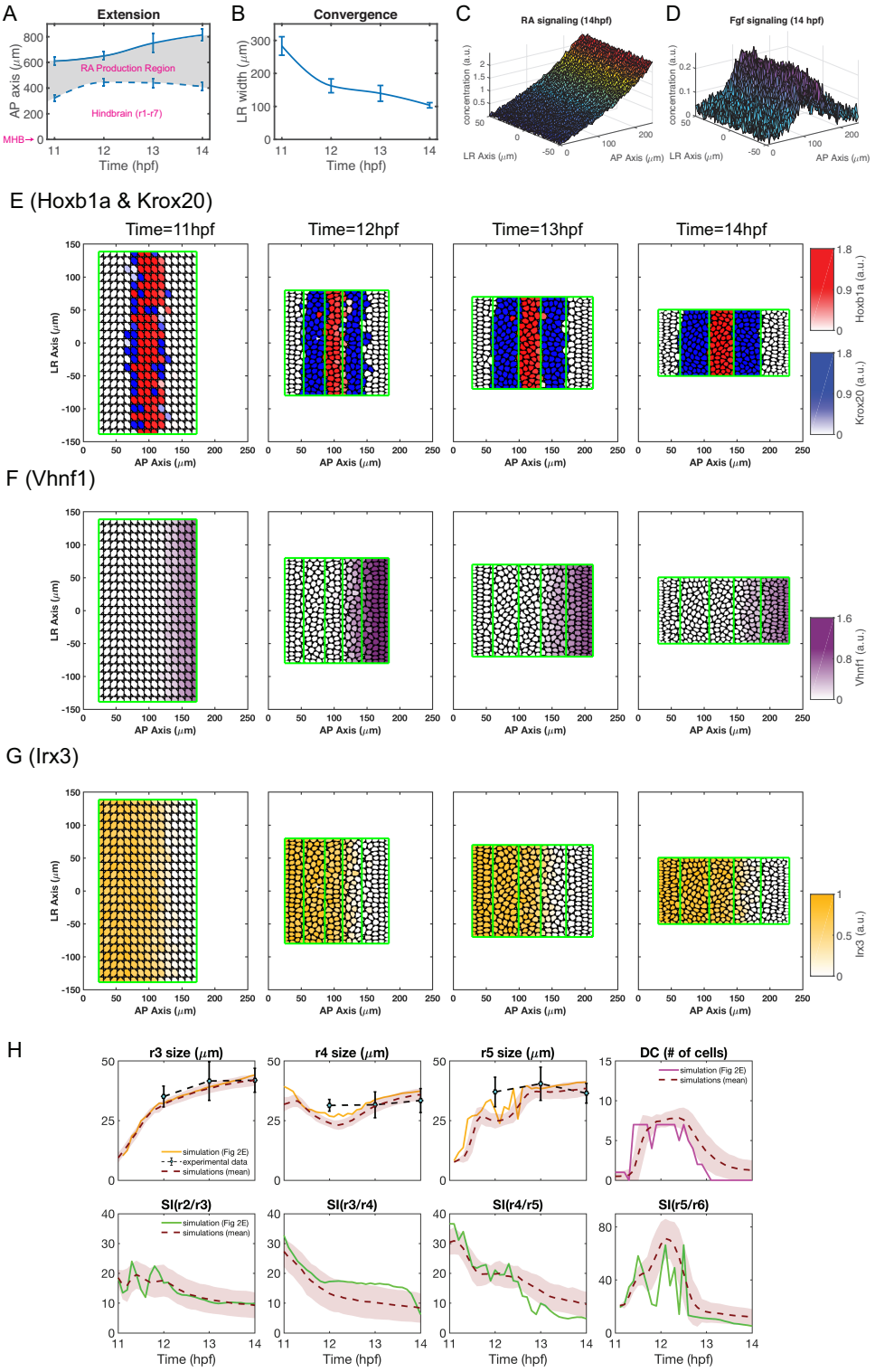

Figure 4.2: A baseline simulation mimics the boundary sharpening process during zebrafish hindbrain patterning (11-14hpf).

Figure 4.2 *(continued)*: Dimensions of hindbrain in (A) AP and (B) LR axes. Experimental quantifications (n=9) provide data points at 11, 12, 13 and 14hpf. The error bars represent the standard deviation. Cubic interpolation is used to obtain the smooth curves and the growth curves are used in the model. (A) AP length of the hindbrain is measured from the posterior end of MHB to the anterior end of the RA production region. The AP length of the RA production region is measured for the AP length of aldh1a2 region. (B) The LR width of the hindbrain is measured at the position of r4 at AP axis. The hindbrain is taken as a rectangle in the model for simplification. (C) The noisy distribution of RA signaling ($[RA]_{in}$) at 14hpf. (D) The noisy distributions of FGF signaling ($[FGF]_{in}$) at 14hpf. (E-G) Time series of gene expressions: (E) Hoxb1a (red) and Krox20 (blue) expressions, (F) Vhnf1 (purple), (G) Irx3 (yellow). (H) Quantifications of rhombomere sizes, number of dislocated cells and sharpness index versus time. solid line: the quantities for the simulation shown in (E). The statistics of rhombomere sizes (r3, r4 and r5), sharpness index for four boundaries (SI(r2/r3), SI(r3/r4), SI(r4/r5), SI(r5/r6)) and the number of dislocated cells (DC) (n=100) are displayed: brown dash line for the average and brown shade for the standard deviation. dash black line represents for the rhombomere sizes from experimental measurement and the error bars represent for the standard deviation (n=9).

induced by RA through Hoxb1a and FGF. Here we compare our model with the previous model to discuss the significance of the secondary morphogen FGF on the pattern formation. To focus on the effects of gene regulation on the final pattern, we only look into steady state solutions of the gene regulation model in a one-dimensional fixed spatial domain with deterministic description.

Distributions of genes and morphogens for the two-morphogen model and one-morphogen model are shown in Figure 4.3A and 4.3D, respectively. In both models, the borders between *hoxb1a* and *krox20* specify the r3/r4 and r4/r5 boundaries. The border between *vhnf1* and *irx3* locates posterior to the r4/r5 boundary. With the auto-regulation, *krox20* behaves as a bi-stable switch to the morphogen level (either RA or FGF). In the two-morphogen model, FGF has high expression level at r4 and decreases at both anterior and posterior directions. FGF can reach the threshold of *krox20* expression at two positions located anterior and posterior to r4. Indeed, the two-morphogen model is able to specify the r2/r3 and r5/r6 boundary. However, in the one-morphogen model, the RA gradient decreases monotonically from posterior to anterior. RA can reach the threshold of *krox20* expression at only one

position that located anterior to r4. The one-morphogen model fails to specify the r5/r6 boundary.

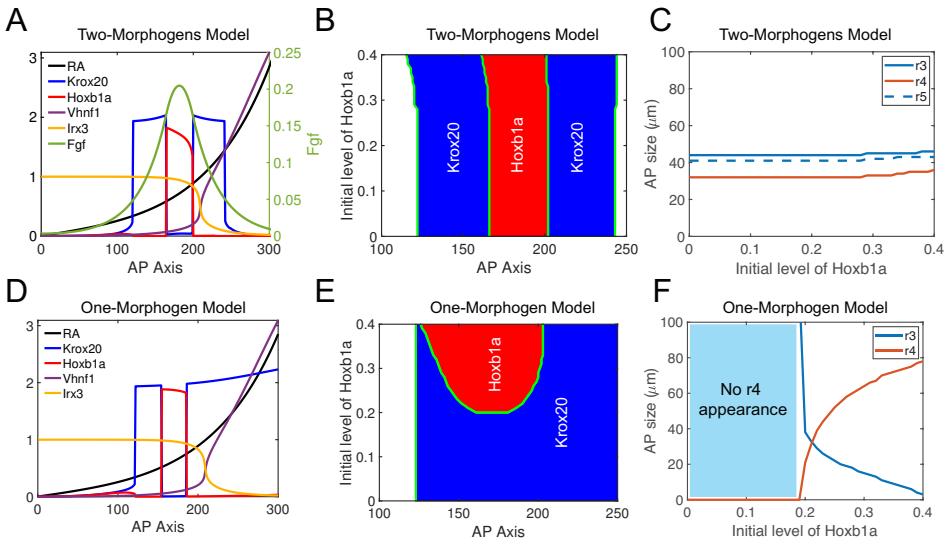

Figure 4.3: Comparisons between two-morphogens (RA and FGF) model and one-morphogen (RA) model. (A-C) One dimensional simulations for the two-morphogens model: (A) spatial distributions of RA, Krox20, Hoxb1a, Vhnf1, Irx3 and FGF. (B) Phase diagram of Hoxb1a and Krox20 under different initial level of Hoxb1a. (C) Rhombomere sizes under different initial level of Hoxb1a. (D-F) One dimensional simulations for the one-morphogen model: (D) Spatial distributions of RA, Krox20, Hoxba1, Vhnf1 and Irx3. (E) Phase diagram of Hoxb1a and Krox20 under different initial level of Hoxb1a. (F) Rhombomere sizes under different initial level of Hoxb1a.

Next, we test the robustness of the systems in terms of their initial *hoxb1a* levels. Because RA, *vhnf1* and *irx3* expression appear before rhombomere formation, we pick their steady state as the initial conditions. We use an initial condition of zero for both *krox20* and FGF since they emerge later after *hoxb1a*. The initial condition of Hoxb1a is picked as a constant over the space since *hoxb1a* has low expression level at the early stage. Then we compute this system until all species reach steady states. By varying the initial Hoxb1a level, we obtain the phase diagrams and the rhombomeres AP sizes for both two-morphogen and one-morphogen model (Figure 4.3BCEF). For the two-morphogen model, locations of all gene expression boundaries and sizes of three rhombomeres are relatively fixed for different initial

Hoxb1a levels. Only a slight expansion is observed when the initial hoxb1a exceedes 0.3. For the one-morphogen model, its rhombomere sizes are more sensitive to initial Hoxb1a levels. In simulations with low initial Hoxb1a levels (< 0.2), no Hoxb1a expression is observed. The r4 region expands and r3 region reduces quickly as initial Hoxb1a level increases from 0.2 to 0.4. A 15% increase of initial Hoxb1a level (0.2-0.23) simply leads to an over two-folds expansion of r4 (21-44 μm). The r3 even vanishes when initial Hoxb1a level is close to 0.4. The two-morphogen model outperforms the one-morphogen model in robustness of rhombomere size. Indeed, the secondary FGF signaling can reduce the variation caused by the initial gene expression.

In the morphogen-mediated patterning system, the steepness of the gradient leads to a trade-off between accuracy of pattern positioning and precision of boundary [87, 90]. A shallow gradient more accurately locates the position of pattern under perturbation on its synthesis, but becomes less noise resistant to allow cells to specify the precise location information. A steeper gradient transmits less noisy location signals to cells but is less robust to perturbations on synthesis. Since RA is responsible for initial patterning, its accuracy in specifying pattern location is more important. The shallow distribution of RA [151] and its self-enhanced degradation [177] are beneficial for achieving better accuracy. For RA synthesis, the expression region of Aldh1a2 which converts retinaldehyde to RA, has high variability and the intensity of *aldh1a2* is highly fluctuated. But the synthesis of FGF has less variation since its upstream regulator Hoxb1a is tightly controlled by a complex network and the bi-stability of hoxb1a can reduce the fluctuations on its intensity. Indeed, the robustness to synthesis is less desirable for FGF. Synthesized at the stage where initial pattern has already been established, a steep FGF gradient is helpful in improving the precision of boundaries adjacent to its source.

Overall, the cooperation between the long-range shallow RA and the short-range steep FGF provides a strategy for achieving both accurate and precise rhombomere pattern.

4.5 Boundary sharpness and size of rhombomeres under growth

In this section, we explore the effects of growth on boundary sharpness and rhombomere size. From 11 to 14hpf, the morphology of the hindbrain changes in both LR and AP axis. The AP length changes slowly during this period, but the LR width shrinks dramatically from 280 μm to 160 μm at the first hour (11-12hpf) and shrinks slowly to 103 μm during the last two hours (12-14hpf). We aim to figure out why it is necessary to have a fast convergence rate at the early hindbrain development. We modeled two additional types of convergence rates, called medium and slow convergence based on their rate relative to the experimental convergent rate, to compare with the fast convergence from our measurement. All three types of convergence have the same initial and terminal LR width. The curve of the medium convergence is taken as a linear function. The curve of the slow convergence and the curve of the fast convergence are symmetric to the linear curve (Figure 4.4A).

4.5.1 Fast convergence makes cell sorting more effective in achieving sharper boundaries

First, we look into the effects of cell sorting alone by excluding the gene regulation from the model. We only consider three cell identities in the five segments (r2-r6). Cells with the same identities are assigned the same level of gene expression of *hoxb1a* and *krox20*: white cells have zeros expression of *hoxb1a* and *krox20*, blue cells have zero expression of *hoxb1a* and maximum level of *krox20* and red cells have maximum level of *hoxb1a* and zero expression of *krox20*. The initial "salt-and-pepper" cell distribution (Figure 4.4B) is sampled by mixture Gaussian distribution based on cell AP position (Supplement).

Starting from the same "salt-and-pepper" cell distribution, we run the simulations with

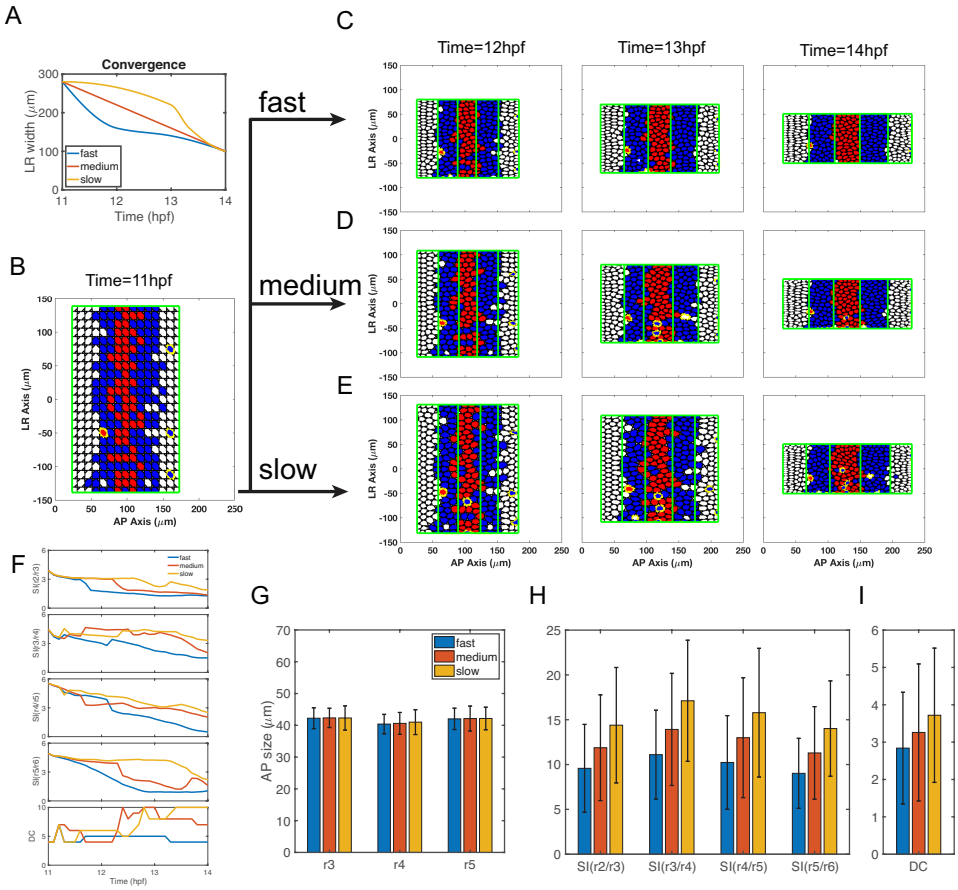

Figure 4.4: Simulations with only selective cell-cell adhesion under different types of convergence. (A) Three types of convergence considered in the model start and terminate with the same LR width. We call them fast convergence, medium convergence and slow convergence based on their convergence rates at the early stage. The fast convergence is measured from experimental measurement (adopted from Figure 2B). The curve of slow convergence is symmetric to the curve of fast convergence with respect to the curve of linear function. The curve of medium convergence is taken as a linear function. (B-E) The time series of cell distributions under different types of convergence from 11 to 14hpf. Cell identities are denoted by the expression of Hoxb1a (red) and Krox20 (blue). The dislocated cells are highlighted by yellow edges. (B) Three simulations start with the same initial cell distribution (11hpf). The initial cell distribution is generated by a Gaussian mixture distribution. Cell distributions with (C) fast, (D) medium and (E) slow convergence from 12 to 14hpf. (F) The sharpness index for four boundaries (SI(r2/r3), SI(r3/r4), SI(r4/r5) and SI(r5/r6)) and number of dislocated cells (DC) versus time. Statistics of three types of convergence for their (G) rhombomere sizes of r3, r4 and r5, (H) SI and (I) DC. Total 100 independent stochastic simulations for each type of convergence are computed under the same parameters set. Error bars represent the standard deviation.

only cell sorting under different types of convergence. The boundary sharpening process can be observed for all three types of convergence (Figure 4C-E). Most of the intermingling cells segregate to their correct corresponding territories and the final patterns display sharp boundaries between rhombomeres. By comparing different types of convergence, the case with fast convergence achieves the sharpest boundaries and the fewest number of dislocated cells while the case with slow convergence results in the roughest boundaries and the greatest number of dislocated cells (Figure 4.4F). The statistics of sharpness index and number of dislocated cells at the final time in over 100 independent simulations show the consistent conclusions as we observed in the single simulation (Figure 4.4H and 4.4I). For the final rhombomere sizes, different types of convergence have minor effects on it (Figure 4.4G).

In this cell-sorting model, an early fast convergence results in better precision in the final patterns. Intuitively, a faster convergence squeezes the hindbrain to have smaller LR width resulting in shorter distances between cells. Since the cell sorting acts through the cell-cell contact, with the shorter distances between cells, the intercellular mechanical forces can be stronger. Consequently, the faster convergence makes the cell sorting more effective leading to the more precise pattern.

4.5.2 Fast convergence regulates boundary sharpness and rhombomere sizes

Now, we turn our attention to the full model including both gene regulation and cell sorting. Similar to the observations above, the faster convergence results in more precise patterns with sharper boundaries and fewer dislocated cells in almost all boundaries examined. The exception is that the fast convergence and the medium convergence have similar sharpness level and the number of dislocated cells at the r5/r6 boundary (Figure 4.5A-E and G). For the rhombomere sizes, they vary greatly under different types of convergence (Figure 4.5F).

The simulations with slow convergence reach the largest sizes for all rhombomeres (r3, r4 and r5). The simulations with the fast convergence have similar r3 size, but smaller r4 size and larger r5 size compared to the simulations with the medium convergence. Based on the experimental measurement of the hindbrain at 14hpf, all three rhombomeres should be roughly similar in size. With a small r5 size, the medium convergence fails to produce balanced rhombomeres of similar size. Taken together, the fast convergence is optimal in achieving both sharp boundaries and balanced rhombomere sizes.

Next, we investigate how the convergence influences the pattern at the gene expression level. We look into the spatio-temporal dynamics of cell fate commitment and morphogens. For the fast convergence, RA signal increases quickly at the early stage from 11-12 hpf, then it falls down gradually. Vhnf1 displays a similar behavior as RA (Figure 4.6AB). Near the r4/r5 boundary, *hoxb1a* is repressed by the increasing Vhnf1. FGF then activates *krox20* leading to identity switching for cells near the r4/r5 boundary with low Hoxb1a expression. The identity switching leads to a smaller r4 (Figure 4.5B). Similar to RA, FGF increases and hits its maximum levels at an early stage ($\sim$12hpf). The majority of cells commit their fates before 12hpf since they have received the maximum spatial signals during this period (Figure 4.5D). For the slow convergence, both RA and FGF levels increase at later stages and reach maximum at 14hpf. Indeed, besides cells that commit their fates before 11hpf, most cells make their fate decisions at later stages (Figure 4.6G). For the medium convergence, both RA and FGF levels are relatively unchanged and increase slowly comparing to other cases. Indeed, comparing to other cases, we observe more cells commit their fates before 11hpf, especially, for cells in r5 (Figure 4.6D). In fast convergence, cells switch from r4 to r5 identities due to the increasing RA and Vhnf1, and in slow convergence, cells switch from r6 to r5 identities due to the increasing FGF. Unlike these two cases, the medium convergence has less cells committing to r5 identities leading to the smaller r5 size (Figure 4.5G).

In the hindbrain pattern formation, gene regulation and cell sorting synergize where gene

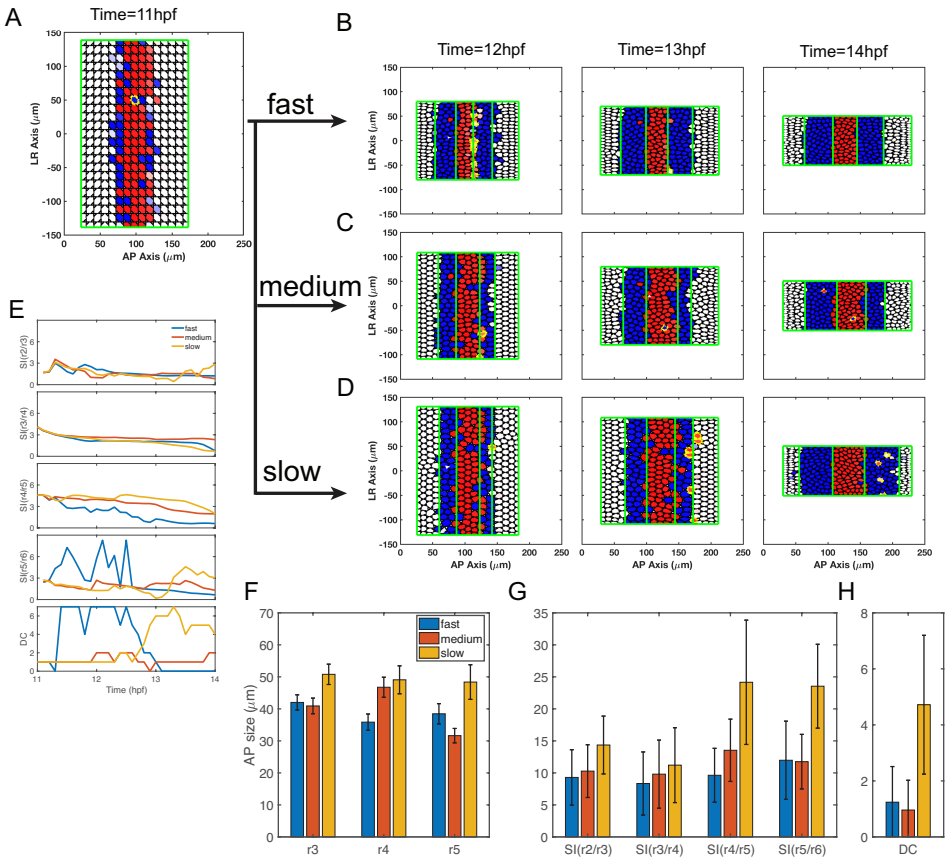

Figure 4.5: Simulations for the full model combining gene regulation and cell sorting under different types of convergence. (A-D) The time series of cell distributions under different types of convergence from 11 to 14hpf. Cell identities are denoted by the expressions of Hoxb1a (red) and Krox20 (blue). The dislocated cells are highlighted by yellow edges. (A) Three simulations start with the same initial cell distribution (11hpf). The initial is generated by gene expression model (see supplement). Cell distributions with (B) fast, (C) medium and (D) slow convergence from 12 to 14hpf. (E) The sharpness index for four boundaries (SI(r2/r3), SI(r3/r4), SI(r4/r5) and SI(r5/r6)) and number of dislocated cells (DC) versus time. Statistics of three types of convergence for their (F) rhombomere sizes of r3, r4 and r5, (G) SI and (H) DC. Total of 100 independent stochastic simulations for each type of convergence are computed under the same parameters set. Error bars represent the standard deviation.

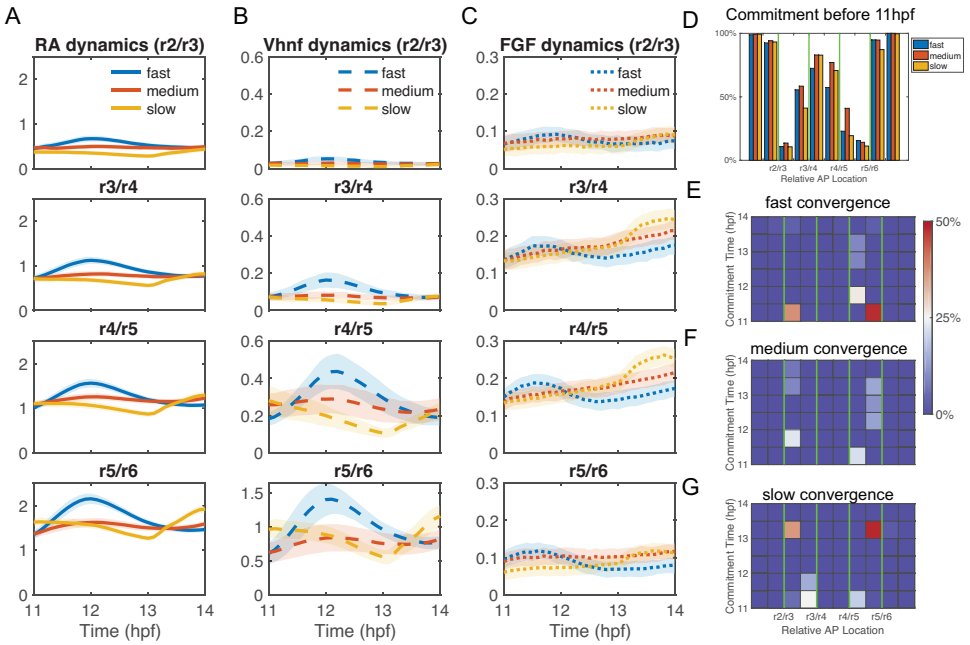

Figure 4.6: Dynamics of morphogens and cell commitment time under different types of convergence. The statistics of the dynamics of (A) RA signaling ($[RA]_{in}$), (B) FGF signaling ($[Fgf]_{in}$) and (C) Vhnf1 near r2/r3, r3/r4, r4/r5 and r5/r6 boundaries. For each boundary, 500 cells are used to calculate the statistics where five cells that are closest to this boundary are pick in each simulation and total n=100 simulations are used. The lines represent the average values and the width of the shades represent the standard deviation. (D-G) Statistics of cell commitment time in different spatial regions. (D) Percentage of cells that make their commitment before 11hpf (initial) at different locations from r2 to r6. Percentage of cells that make their commitment from 11 to 14hpf under (E) fast convergence, (F) medium convergence and (G) slow convergence. The data is the same with the data used in Figure 4.5.

regulation is responsible for the pattern initialization at earlier stages and cell sorting is responsible for the pattern refinement at later stages [170]. We verify this conclusion in our model by perturbing the periods of gene regulation and the selectivity in cell sorting. When gene regulation is turned off at later stages, there are only minor effects on boundary sharpness in the pattern (Figure 4.8). We also turn on the selectivity in cell sorting for only one hour, letting cells sort each other equally in the rest of the time. The worse patterns were observed when the selectivity is turned on at the early stage (11-12hpf) (Figure 4.9).

Taken together, the fast convergence is optimal for regulating both precise patterning and balanced rhombomere size by acting on both cell sorting and gene regulation. With the small r5 size, the medium convergence fails to maintain the balanced rhombomere size, and the boundaries are slightly rougher than that in the fast convergence. In the slow convergence, more cells commit at the late stage which disrupts the synergy between cell sorting and gene expressions resulting in the rough boundaries (Figure 4.5GH).

4.5.3 Fast convergence regulates the trade-off between size and boundary sharpness

The fast convergence provides advantages in regulating both rhombomere size and boundary sharpness. Here we look into the relationship between size and boundary sharpness by showing simulations (n=1000) with random parameters (Figure 4.7 and 4.10). The size and boundary sharpness exhibit a trade-off where smaller size usually results in rougher boundaries. With smaller rhombomere size, the cell sorting is less effective since fewer cells with the same identity are able to sort for each other. Consequently, the boundary is more difficult to sharpen. We observe that the fast convergence can significantly reduce the trade-off for the posterior rhombomeres (r4 and r5) (Figure 4.7). For r3, the fast convergence reduces the trade-off slightly (Figure 4.10).

We also count the number of simulations with balanced rhombomere sizes. From the experimental measurement, the average and the standard deviation of r3, r4 and r5 sizes at 14hpf are 42±5 μm, 35±5 μm and 37±4 μm, respectively (Figure 4.2H). We search for the simulations where the sizes of all rhombomeres are inside the ranges given by the experimental quantifications. In total, we find 15, 5 and 5 out of 1000 simulations for fast, medium and slow convergence, respectively. The fast convergence generates more easily patterns with balanced rhombomere sizes.

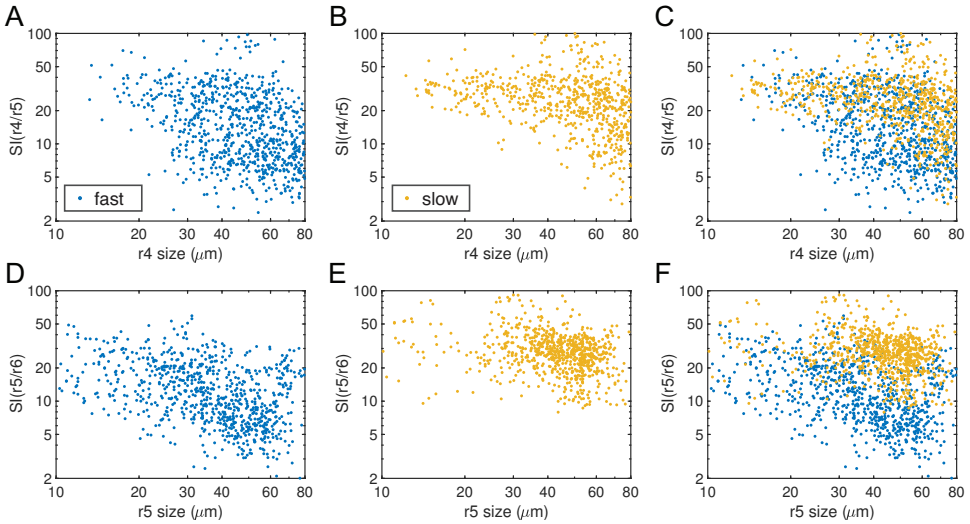

Figure 4.7: The relationship between rhombomere size and the level of boundary sharpness (SI). Simulations are generated with randomly perturbed parameters. A total of 513 and 452 simulations out of 1000 simulations under fast convergence and slow convergence successfully generated the r2-r6 pattern. Each dot represent the corresponding quantities of each simulation. (A-C) Size of r4 versus sharpness index of r4/r5 boundary: (A) fast convergence, (B) slow convergence and (C) the comparison between fast and slow convergence. (D-F) Size of r5 versus sharpness index of r5/r6 boundary: (D) fast convergence, (E) slow convergence and (F) the comparison between fast and slow convergence

The actual size of each rhombomere is in the order of 3-5 cell-diameters which is relatively small. It is challenging to sharpen the boundaries of small segments, and even more so to regulate all rhombomeres to be similarly sized. Surprisingly, we find that the fast convergence rate during the hindbrain development coordinates both size and boundary sharpness to facilitate the patterning process.

4.6 Discussion

Our modeling results show that the robustness of segment size in the hindbrain pattern can be significantly improved by adding a short-range morphogen to the system alongside a long-range morphogen. This cooperation between two morphogens may be a strategy for maintaining both accuracy and precision in pattern formation. Despite the elongation in AP axis possibly hindering the boundary sharpening process [190], fast convergence in the LR axis can improve regulation of the rhombomere size and boundary sharpness leading to a precise pattern.

RA level increases during early stages of hindbrain development due to its synthesis and accumulation [108], then decreases due to the source of RA associated with axial elongation and the addition of new somites [5, 126]. The abnormal pattern appears if the RA synthesis is knocked down before 6hpf and the normal pattern can be observed if RA synthesis is knocked down after 6hpf. This indicates the degradation of RA is slow and its signal remains in cells for a while. This slow degradation is necessary for our model to have different morphogen dynamics under different types of convergence. In particular, in the current parameters set, the time scale of RA degradation is slower than the convergence: the half-life of RA is about 1.7 hour and the LR width is almost halved in 1 hour.

In the simulations, intermingling cells are found in r2 and r6 due to randomness in gene expression. Especially, sometimes, *hoxb1a* cells can be observed in r2 because RA is increasing at the early time and it is possible to induce the *hoxb1a* at r2. The model can't predict how those intermingling cells switch to the correct identities. The "community effect" may cause intermingling cells to switch to the identity of its surrounding cells although the underlying mechanisms havent been fully identified [2, 144]. Other inhibitors of *hoxb1a* or *krox20* may exist to prevent the intermingling cells.

During the developemnt of hindbrain, cells are dividing and migrating along the dorsal-

ventral (DV) axis. Cells are also migrating from r5 to the neural crest which may cause the reduction of r5 size observed in the experimental measurements (Figure 4.2K). Our simplified two-dimensional model omits the DV axis and the complicated dynamics of cell migrations and divisions. Indeed, the simulated dynamics of rhombomere sizes cannot fit perfectly to the experimental quantifications, but those factors won't affect the behaviors of morphogens predicted in this work. Indeed, this simplification can still provide the insight for the impacts of growth on the pattern formations.

4.7 Supplement

4.7.1 Modeling the growing domains

The morphogen domain describes the region for the entire hindbrain for modeling the diffusive morphogens. In the two-dimensional model, we consider AP and LR axes. In AP direction, we take the posterior end of the midbrain-hindbrain boundary (MHB) as $x_1 = 0$ and the posterior end of RA production region as $x_1 = L_1(t)$. We assume the LR length of the hindbrain, $L_2(t)$, is a constant in AP direction for simplification. Then, the morphogen domain has a rectangular structure with dynamical sizes:

$$M(t) = \left\{ \left(x^{(1)}, x^{(2)}\right) \in H : H = [0, L_1(t)] \times \left[-\frac{1}{2}L_2(t), \frac{1}{2}L_2(t) \right] \right\}. \tag{4.1}$$

The RA production region is taken as:

$$P(t) = \left\{ \left(x^{(1)}, x^{(2)}\right) : \left(x^{(1)}, x^{(2)}\right) \in [p(t), L_1(t)] \times \left[-\frac{1}{2}L_2(t), \frac{1}{2}L_2(t) \right] \right\}. \tag{4.2}$$

The data of $L_1(t)$, $L_2(t)$ and $p(t)$ are from the experimental quantifications at 11, 12, 13 and 14hpf. We use the cubic interpolation to obtain the smooth curves in Figure 4.2AB.

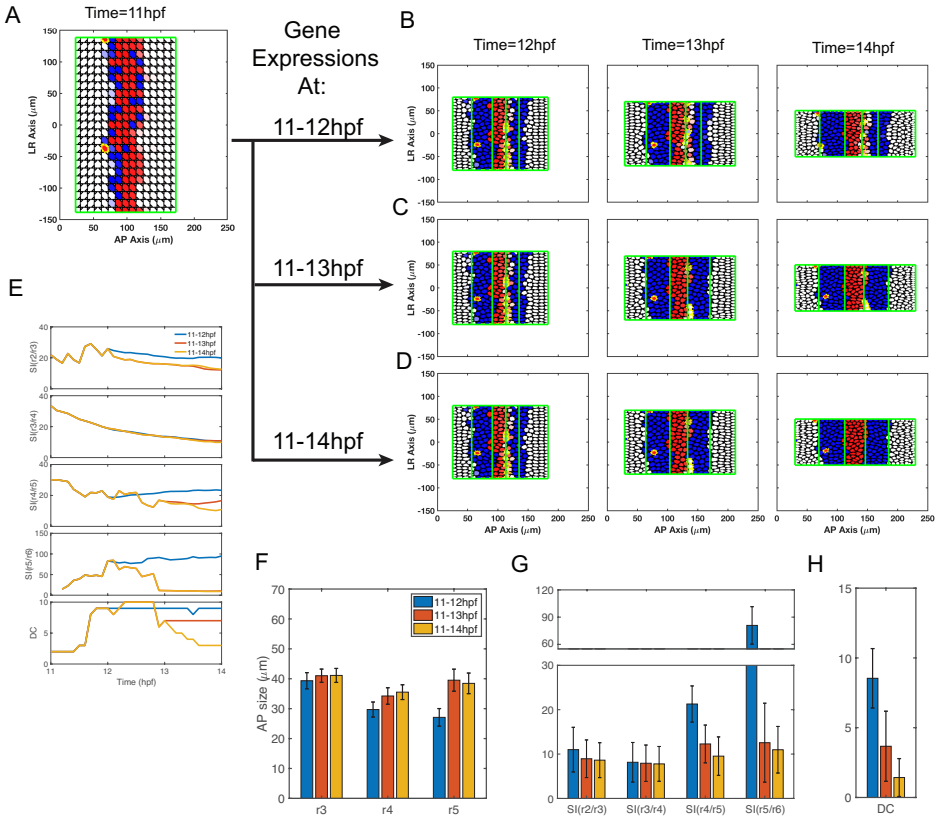

Figure 4.8: Simulations with gene regulation turned on at different periods. (A-D) The time series of cell distribution with gene regulation turned on at different periods. Cell identities are denoted by the expression of Hoxb1a (red) and Krox20 (blue). The dislocated cells are highlighted by yellow edges. (A) Three simulations start with the same initial cell distribution (11hpf). The initial condition is generated by gene expression model. The gene regulation is turned on for different length of periods: (B) 11-12hpf, (C) 11-13hpf and (D) 11-14hpf. (F) The sharpness index for four boundaries (SI(r2/r3), SI(r3/r4), SI(r4/r5) and SI(r5/r6)) and number of dislocated cells (DC) versus time. Statistics of three cases for their (G) rhombomere sizes of r3, r4 and r5, (H) SI and (I) DC. Total 100 independent stochastic simulations for each type of convergence are computed under the same parameters set. Error bars represent the standard deviation.

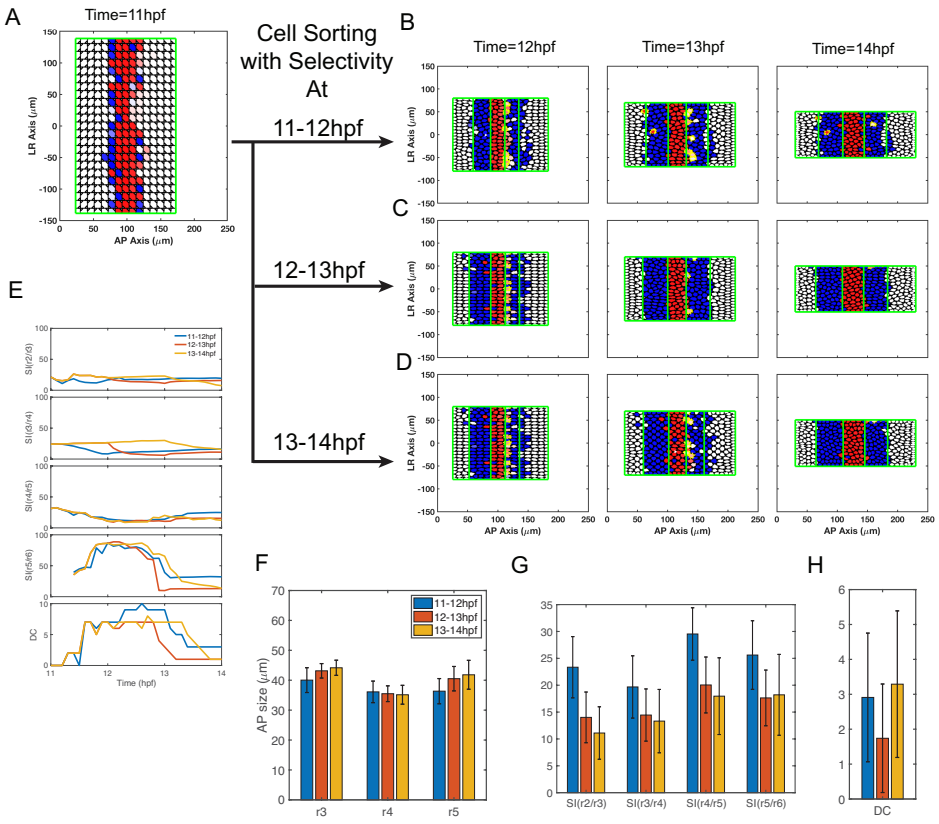

Figure 4.9: Simulations with selectivity in cell sorting in different periods. To turn off the selectivity in cell sorting, we set the similarity function as a constant $\mathcal{F} = 0.5$ where cells sort equally. (A-D) The time series of cell distribution with selectivity during different periods. Cell identities are denoted by the expression of Hoxb1a (red) and Krox20 (blue). The dislocated cells are highlighted by yellow edges. (A) Three simulations start with the same initial cell distribution (11hpf). The initial is generated by gene expression model. The cells sort for each other all the time, but the selectivity is only turned on at one hour in each case: (B) 11-12hpf, (C) 12-13hpf and (D) 13-14hpf. (F) The sharpness index for four boundaries (SI(r2/r3), SI(r3/r4), SI(r4/r5) and SI(r5/r6)) and number of dislocated cells (DC) versus time. Statistics of three types of convergence for their (G) rhombomere sizes of r3, r4 and r5, (H) SI and (I) DC. A total of 100 independent stochastic simulations for each type of convergence are computed under the same parameters set. Error bars represent the standard deviation.

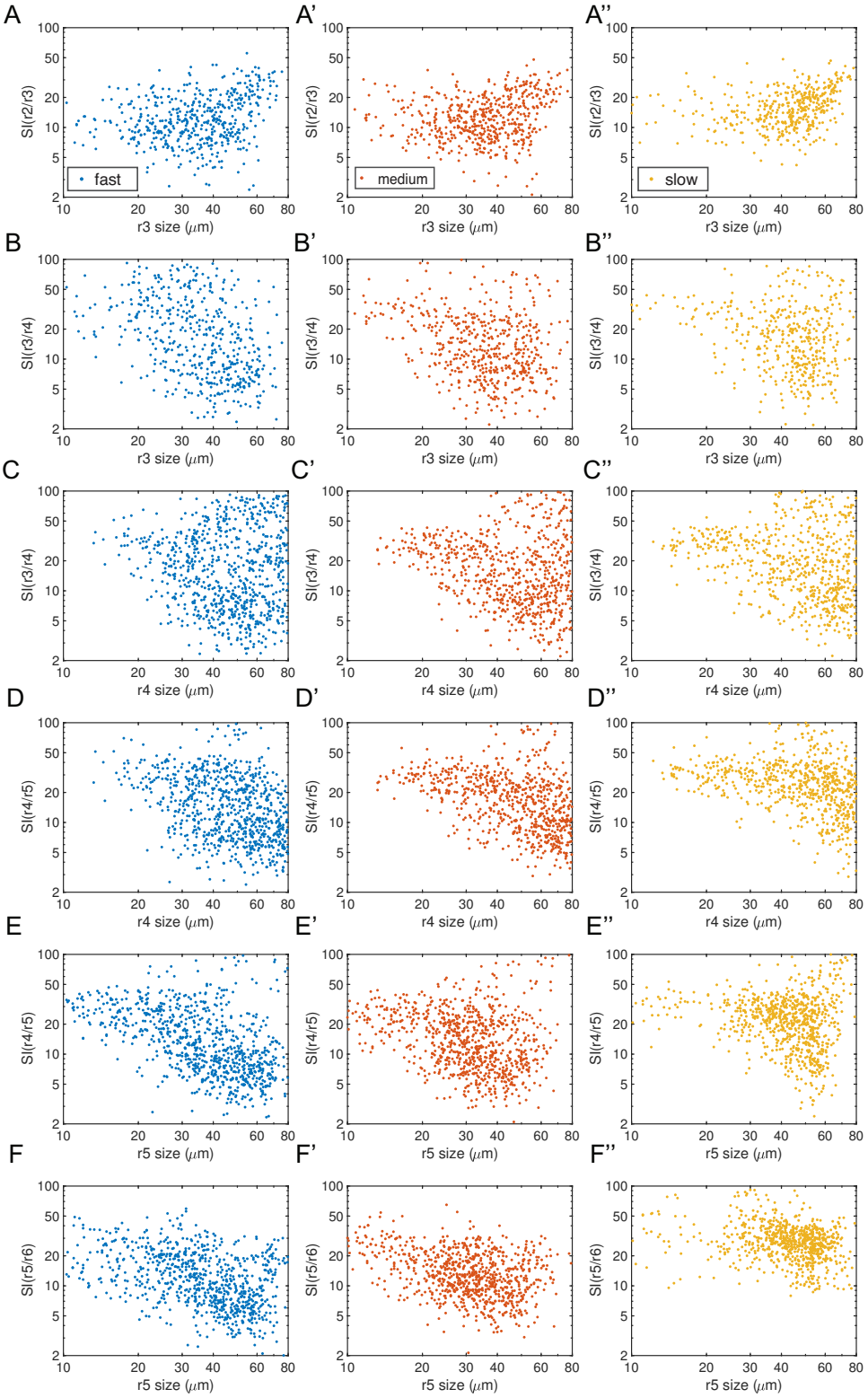

Figure 4.10: The relations between rhombomere size and the level of boundary sharpness (SI).

Figure 4.10 *(continued)*: In each plot, one dot represents for a simulation that generated from the stochastic simulation with a random parameters set. A total of 513, 562 and 452 simulations out of 1000 simulations under fast, medium and slow convergence successfully generated the r2-r6 pattern and they are displayed in the plots. (A-A) Size of r3 versus SI(r2/r3) under (A) fast, (A) linear and (A) slow convergence. (B-B) Size of r3 versus SI(r3/r4) under (B) fast, (B) linear and (B) slow convergence. (C-C) Size of r4 versus SI(r3/r4) under (C) fast, (C) linear and (C) slow convergence. (D-D) Size of r4 versus SI(r4/r5) under (D) fast, (D) linear and (D) slow convergence. (E-E) Size of r5 versus SI(r4/r5) under (E) fast, (E) linear and (E) slow convergence. (F-F) Size of r5 versus SI(r5/r6) under (F) fast, (F) linear and (F) slow convergence.

Since we mainly focus on the pattern in the region r2-r6, we only consider discrete cells in one part of the hindbrain, called tissue domain, to save the computational cost. We assume the growth is isotropic and the tissue domain scales proportionally with the morphogen domain:

$$T(t) = \left\{ \left(x^{(1)}, x^{(2)}\right) : \left(x^{(1)}, x^{(2)}\right) \in [r_1 L_1(t), r_2 L_1(t)] \times \left[-\frac{1}{2} L_2(t), \frac{1}{2} L_2(t) \right] \right\} \tag{4.3}$$

where r_1 and r_2 are constants given in the Table 4.2.

With the isotropic growth, at $\mathbf{x} = (x_1, x_2)$, the growth velocity of the tissue is given by

$$\mathbf{V}(\mathbf{x}, t) = \left({L_1}'(t) \frac{x^{(1)}}{L_1(t)}, {L_2}'(t) \frac{x^{(2)}}{L_2(t)} \right). \tag{4.4}$$

4.7.2 Stochastic dynamics of morphogens and intracellular gene expressions

morphogen

To model dynamics of morphogen in the growing hindbrain, the stochastic convection-reaction-diffusion equations are used. We assume the hindbrain growth is isotropic. The

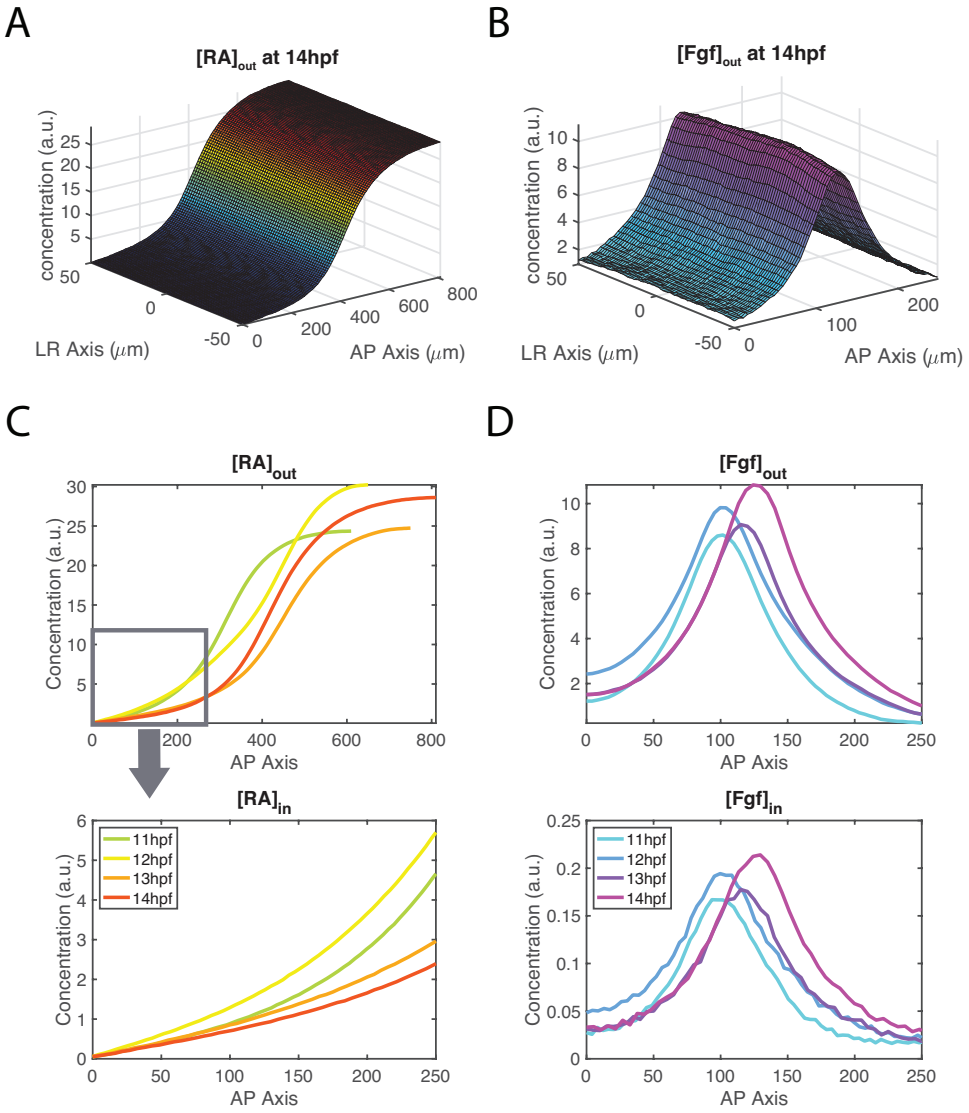

Figure 4.11: Morphogens distributions. (A) The distribution of [RA]out at 14hpf. (B) The distribution of [Fgf]out at 14hpf. (C) The AP distribution of $[RA]_{out}$ in the morphogen domain and the zoomed-in AP distribution of $[RA]_{in}$ for the AP range present in the tissue domain. The curves show the average morphogen level over LR axis. (D) The AP distribution of $[Fgf]_{out}$ and $[Fgf]_{in}$. The curves show the average morphogen level over LR axis.

equations of RA are given by

$$\begin{aligned}
\frac{\partial [RA]_{out}}{\partial t} + \overbrace{\nabla \cdot (\mathbf{V}[RA]_{out})}^{\text{convection}} &= \overbrace{D_r \Delta [RA]_{out}}^{\text{diffusion}} + \overbrace{A(\mathbf{x},t)}^{\text{production}} \\
&\quad + \overbrace{k_r[RA]_{in} - (1+\beta_r)k_r[RA]_{out}}^{f_1} + \overbrace{\mu_{r1}\frac{dw_{r1}(t)}{dt}}^{\text{noise}}, \\
\frac{\partial [RA]_{in}}{\partial t} + \nabla \cdot (\mathbf{V}[RA]_{in}) &= \overbrace{k_r[RA]_{out} - k_r[RA]_{in} - d_r(x_1)[RA]_{in}}^{f_2} \\
&\quad + \mu_{r2}\frac{dw_{r2}(t)}{dt},
\end{aligned} \tag{4.5}$$

where $[RA]_{out}$ and $[RA]_{in}$ are extracellular and intracellular forms of RA, respectively. The convection term describes the dilution and advection of RA caused by growth. $\mathbf{V}(\mathbf{x},t)$ is the growth velocity of tissue at location $\mathbf{x}$ and time t. The production rate is confined at the RA production region and modeled by a hill function of AP position $x^{(1)}$ with a large hill coefficient:

$$A(\mathbf{x},t) = \frac{v_r}{1 + \left(\frac{x^{(1)}}{p(t)}\right)^{-20}}. \tag{4.6}$$

In f_1 and f_2, k_f is the rate of exchange of morphogen between intracellular and extracellular forms. The degradation of extracellular morphogen rate is taken as a constant $\beta_r k_r$ and the degradation of intracellular morphogen rate d_r is a piecewise function for AP axis

$$d_r(\mathbf{x}) = \begin{cases} k_{\max}, & \text{if } x^{(1)} > p(t), \\ k_0, & \text{otherwise.} \end{cases} \tag{4.7}$$

The degradation rate in the RA production region takes a large value $k_{\max}$, since the RA degrading enzymes cyp26s highly expressed in the RA production region [177]. We take absorbed boundary condition at $x^{(1)} = 0$ since cyp26s is highly expressed in MHB that provides a sink for RA. No-flux boundary conditions are taken on the other three boundaries.

Similarly, we model both intracellular and extracellular FGF as the following:

$$\begin{aligned}\frac{\partial [Fgf]_{out}}{\partial t} + \nabla \cdot (V[Fgf]_{out}) &= D_f \Delta [Fgf]_{out} + A_f([H], x) + k_f [Fgf]_{in} \\ &\quad - (1+\beta_f)\, k_f [Fgf]_{out} + \mu_{f1} \frac{dw_{f1}(t)}{dt}, \\ \frac{\partial [Fgf]_{in}}{\partial t} + \nabla \cdot (V[Fgf]_{in}) &= k_f [Fgf]_{out} - k_f [Fgf]_{in} \\ &\quad - d_f [Fgf]_{in} + \mu_{f2} \frac{dw_{f2}(t)}{dt},\end{aligned} \tag{4.8}$$

The production of FGF is upregulated by hoxb1a and the production rate is given by a hill function of $[H]$:

$$A_f([H], \mathbf{x}) = v_f \frac{[H](\mathbf{x})^2}{1 + a_{hf}[H](\mathbf{x})^2}. \tag{4.9}$$

The intracellular gene $[H]$ is defined on the locations of cell centers. The term $[H](\mathbf{x})$ is obtained by interpolating $[H]$ values with locations in cell centers (see "Signaling exchange between continuum domain and discrete cell" for details).

Intracellular genes

The intracellular genes expression levels determine the cell fate of each individual cell. The gene regulatory network has been discussed in Section 4.3.1. We model the dynamics of gene expressions by a system of stochastic differential equations. The expressions of intracellular genes are defined on the individual cell in the tissue domain. For the i-th cell centered at $\mathbf{c}_i$, the equations are given by

$$\begin{aligned}\frac{d[H]_i}{dt} &= v_h \frac{a_{hh}[H]_i^2 + a_{rh}[RA]_{in}^2}{1 + a_{hh}[H]_i^2 + a_{rh}[RA]_{in}^2 + b_{kh}[K]_i^2 + b_{vh}[V]_i^2} - d_h [H]_i + \mu_h \frac{dw_h}{dt}, \\ \frac{d[K]_i}{dt} &= v_k \frac{a_{kk}[K]_i^2 + a_{fk}[Fgf]_{in}^2}{1 + a_{kk}[K]_i^2 + a_{fk}[Fgf]_{in}^2 + b_{hk}[H]_i^2} - d_k [K]_i + \mu_k \frac{dw_k}{dt}, \\ \frac{d[V]_i}{dt} &= v_v \frac{a_{rv}[RA]_{in}^2}{1 + a_{rv}[RA]_{in}^2 + b_{iv}[I]_i^2} - d_v [V]_i + \mu_v \frac{dw_v}{dt}, \\ \frac{d[I]_i}{dt} &= v_i \frac{1}{1 + b_{vi}[V]_i^2} - d_i [I]_i + \mu_i \frac{dw_i}{dt},\end{aligned} \tag{4.10}$$

where $[H]$, $[K]$, $[V]$ and $[I]$ are concentrations of *hoxb1a*, *krox20*, *vhnf1* and *irx3*, respectively. $[RA]_{in} = [RA]_{in}|_{\mathbf{x}=\mathbf{c}_i}$ and $[Fgf]_{in} = [Fgf]_{in}|_{\mathbf{x}=\mathbf{c}_i}$ are intracellular form of RA and Fgf at location $\mathbf{c}_i$ that provide spatial signal for the cell. To generate the initial gene expressions at 11hpf, we run the stochastic gene expressions for two hours without the consideration of cell movement. In the first hour, we start with the equilibrium of RA and zero expression of *vhnf1* and *irx3*, and we only run the stochastic simulations of $[RA]_{out}$, $[RA]_{in}$, $[V]$ and $[I]$ for one hour since RA gradients are established before 6hpf and *vhnf1* and *irx3* expressions are earlier than *hoxb1a*, *krox20* and FGF. For the second hour, we run the stochastic simulations for all morphogens and genes. The *hoxb1a* starts with uniform expression level 0.1 and *krox20* and FGF start with zeros expression.

Signaling exchange between continuum domain and discrete cell

In morphogen domain and tissue domain, the signals exchange between each other. In the computational framework, the morphogen domain uses regular rectangular mesh and the tissue domain has irregular mesh where grids are the centers of moving cells. Morphogens need to give signal to individual cell and cells need to provide information for FGF synthesis. We use interpolations to conduct the signaling exchange from two domains.

From morphogen domain to tissue domain, we use a constant interpolation. For i-th cell, it receives the signals of intracellular morphogen at the grid point that is closest to the cell location:

$$\begin{cases} [M]_{in}|_{\mathbf{x}=\mathbf{c}_i} \approx [M]_{in}\Big|_{\mathbf{x}=\left(x_{i_0}^{(1)},x_{j_0}^{(2)}\right)}, \\ (i_0,j_0) = \arg\min\limits_{i,j} \left|\left(x_i^{(1)},x_j^{(2)}\right) - \mathbf{c}_i\right|. \end{cases} \tag{4.11}$$

From tissue domain to morphogen domain, we use the build-in function *"griddata"* in MATLAB to interpolate the function ($[H]$) defined on scatter points to the regular mesh in mor-

phogen domain:

$$[H](\mathbf{x}) = griddata([H]_i \Big|_{i=1}^{N_{cell}}, \mathbf{c}_i \Big|_{i=1}^{N_{cell}}, \mathbf{x}). \tag{4.12}$$

4.7.3 Modeling discrete cells and their mechanical interactions

In tissue domain, we model the individual cells and their movement driven by mechanical interactions. Following the previous work [170], we use the subcellular element method (SCEM) to model those individual cells [117]. Each cell consists of sub-cellular elements (nodes) and interacts according to a prescribed intercellular force potential. A cell consist of $2N_{node}$ ($N_{node} = 6$) nodes and those nodes form two hexagon layers as shown in Figure 4.12A. The radius of the outer layer is R_{out} and the radius of the inner layer is R_{in}. And we generate the initial distribution of cells uniformly in the tissue domain as shown in Figure 4.2H. For a system with N_{cell} cells and each cell has $2N_{node}$ nodes, the location of i-th node in n-th cell $\mathbf{x}_{n,j}$ is determined by the equation

$$\frac{d}{dt}\mathbf{x}_{n,i} = \mathbf{v}_{n,i}^{\text{chemo}} + \mathbf{v}_{n,i}^{\text{inter}} + \mathbf{v}_{n,i}^{\text{inner}}. \tag{4.13}$$

On the right hand side, the first term is the chemoattractant that drive cell migration along with the convergent extension [146, 140]. It is given by

$$\begin{cases} \mathbf{v}_{n,j}^{\text{chemo}} = \mathbf{V}(\mathbf{c}_n, t), \\ \mathbf{c}_n = \dfrac{1}{2N_{node}} \displaystyle\sum_{i=1}^{2N_{node}} \mathbf{x}_{n,i}. \end{cases} \tag{4.14}$$

The second term represents the forces between nodes given by Morse potential, and the last term is an additional term for the forces from the nodes in the same cell to maintain stable cell morphology.

For two nodes, their forces are determined by Morse potential:

$$\Phi(r) = \begin{cases} U\exp(-\frac{r}{\xi}) - V\exp(-\frac{r}{\zeta}), & \text{if } r \leq d; \\ 0, & \text{otherwise;} \end{cases} \tag{4.15}$$

where r is the distance between these two nodes and d is the constant cut-off distance taken as two times of the cell diameters ($4R_0 = 16\ \mu m$). The short-range repulsion $U\exp(-\frac{r}{\xi})$ maintains a minimum distance between nodes and the long-range attraction $-V\exp(-\frac{r}{\zeta})$ makes nodes moving closer.

For nodes in the same cell, the non-zeros intra-cellular forces are determined by:

$$\Phi_{\text{intra}}(|\mathbf{x}_{n,i} - \mathbf{x}_{n,j}|) = U_{\text{intra}}\exp\left(-\frac{|\mathbf{x}_{n,i} - \mathbf{x}_{n,j}|}{\xi_{\text{intra}}}\right) - V_{\text{intra}}\exp\left(-\frac{|\mathbf{x}_{n,i} - \mathbf{x}_{n,j}|}{\zeta_{\text{intra}}}\right). \tag{4.16}$$

Nodes in two cells are subject to inter-cellular forces and the magnitude of inter-cellular forces depend on cell-identity of these two cells. For the extreme case, two nodes are subject to an attractive force with a short-range repulsion if two cells they have same identity; two nodes are subject to a repulsive force if two cells they belong to have different identities:

$$\Phi_{\text{inter}}(r) = \begin{cases} U_{\text{inter}}^{\text{Atr}}\exp(-\frac{r}{\xi_{\text{inter}}}) - V_{\text{inter}}^{\text{Atr}}\exp(-\frac{r}{\zeta_{\text{inter}}}), & \text{same identity;} \\ U_{\text{inter}}^{\text{Rep}}\exp(-\frac{r}{\xi_{\text{inter}}}), & \text{different identities.} \end{cases} \tag{4.17}$$

The selective cell-cell adhesion depends on the *krox20* expression in a pair of cells. A similarity function between m-th and n-th cell is defined by the following:

$$\mathcal{F}(m,n) = \frac{1}{2}(\delta^m\delta^n + 1) \in [0,1], \tag{4.18}$$

where δ^i is a linear function of $[K]$ normalized by the maximum expression *krox20* in i-th cell. $\delta^i = 1$ indicates the cell expresses maximum level of *krox20* and $\delta^i = -1$ indicates the

cell has no expression of *krox20*. The force is attractive when two cells have similar *krox20* level ($\mathcal{F} = 1$ if $\delta^m = \delta^n = \pm 1$) and is repulsive when two cells have different *krox20* level ($\mathcal{F} = 0$ if $\delta^m = -\delta^n = \pm 1$).

The Morse potentials between a pair of nodes in two different cells with locations at $\mathbf{x}_{m,j}$ and $\mathbf{x}_{n,j}$ are defined by

$$\begin{aligned}\Phi_{\text{inter}}(|\mathbf{x}_{n,i} - \mathbf{x}_{m,j}|) = &\left[(1-\mathcal{F})\, U_{\text{inter}}^{\text{Rep}} + \mathcal{F} U_{\text{inter}}^{\text{Atr}}\right] \exp\left(-\frac{|\mathbf{x}_{n,i} - \mathbf{x}_{m,j}|}{\xi_{\text{inter}}}\right) \\ &- \mathcal{F} \mathrm{V}_{\text{inter}}^{\text{Atr}} \exp\left(-\frac{|\mathbf{x}_{n,i} - \mathbf{x}_{m,j}|}{\zeta_{\text{inter}}}\right).\end{aligned} \tag{4.19}$$

Taken together, the first term in Eq. (4.13) given by

$$\mathbf{v}_{n,i}^{\text{inter}} = \eta_{n,i} - \nabla_{\mathbf{x}_{n,i}} \left[\sum_{j \neq i}^{2N_{node}} \Phi_{\text{intra}}(|\mathbf{x}_{n,i} - \mathbf{x}_{n,j}|) + \sum_{m \neq n}^{N_{cell}} \sum_{j}^{2N_{node}} \Phi_{\text{inter}}(|\mathbf{x}_{n,i} - \mathbf{x}_{m,j}|)\right], \tag{4.20}$$

where $\eta_{n,i} \sim \mathcal{N}(0, 10)$ is the Gaussian-distributed noise.

The canonical SCEM only consider Morse potentials discussed above. To avoid squashed or explode cell, we add another spring-type pair-wise forces to nodes within the same cell [170]. In i-th cell, we evenly divide nodes into two layers, where each layer initially has a structure of regular polygon. This pair-wise forces act on neighboring nodes between the same layer $\mathbf{x}_{n,i} \sim \mathbf{x}_{n,i+1}$ and the nodes between different layers with the same index $\mathbf{x}_{n,i} \sim \mathbf{x}_{n,i \pm N_{node}}$. The force is given by

$$\Psi(\mathbf{x}_{n,i}, \mathbf{x}_{n,j}) = \mu \frac{|\mathbf{x}_{n,i} - \mathbf{x}_{n,j}| - l_{i,j}^n}{|\mathbf{x}_{n,i} - \mathbf{x}_{n,j}|} (\mathbf{x}_{n,i} - \mathbf{x}_{n,j}), \tag{4.21}$$

where $l_{i,j}^n$ is the constant length between node $\mathbf{x}_{n,i}$ and $\mathbf{x}_{n,j}$ at initial time and it has three possible values, l_{out}, l_{in}, l_{inter}, depending on the types of two nodes (Figure 4.12A). Then for

i-th node in the n-th cell, the motion from this force is

$$\mathbf{v}_{n,i}^{\text{inner}} = \Psi(\mathbf{x}_{n,i}, \mathbf{x}_{n,i+1}) + \Psi(\mathbf{x}_{n,i}, \mathbf{x}_{n,i-1}) + \Psi(\mathbf{x}_{n,i}, \mathbf{x}_{n,i\pm N_{node}}). \tag{4.22}$$

To prevent cells running out the tissue domain, we add two layers of "ghost cells" located outside the boundary tissue domain to provide extra forces to keep cells staying inside the tissue domain.

4.7.4 Quantifications of boundary location (m), sharpness index (SI) and number of dislocated cells (DC) in model

In this study, we aim to study rhombomere size and boundary sharpness. We need to quantify the location of the boundary and its sharpness level. Here we introduce three quantifications allowing a systematic way to study the sharpness and size.

Taken r3/r4 boundary as an example, it is a straight line vertical to the AP axis with AP location denoted by $m(r3/r4)$ and its sharpness index is denoted by $SI(r3/r4)$. We identity a cell as a dislocated cell if its shortest distance to the region it belongs to is over 3 cell-diameters ($6R_0$). The total number of dislocated cells is counted and denoted by DC.

In a region with AP range (a, b), we split the index set of all cells into two sets S_L and S_R. We define the distance function from the i-th cell centered at $\mathbf{c}_i$ to an arbitrary straight line with AP position k:

$$\text{dis}(\mathbf{c}_i, k) = \begin{cases} \text{ReLU}(\mathbf{c}_i^{(1)} + R_0 - k), \text{ if } i \in S_L, \\ \text{ReLU}(-\mathbf{c}_i^{(1)} + R_0 + k), \text{ if } i \in S_R, \end{cases} \tag{4.23}$$

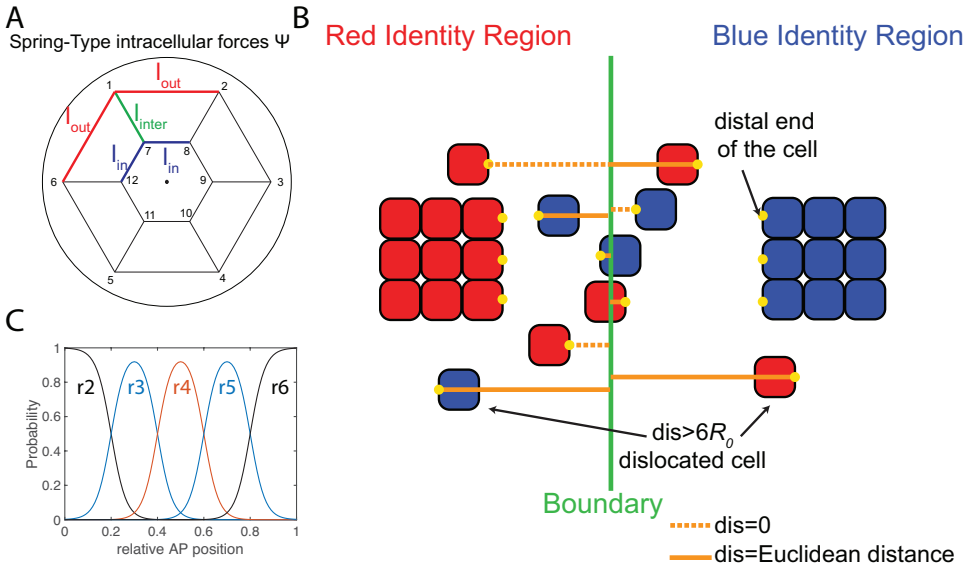

Figure 4.12: Additional information for the model. (A). Cell representation in SCEM: Each cell is represented by two layers of nodes and each layer has $N_{node} = 6$ nodes with a hexagon structure. The pairwise lengths used in Eq. (4.21) have three possible constant values, lout, lin, linter. The length between two neighbor nodes in the outer layer is lout. The length between two neighbor nodes in the inner layer is lin. For two nodes in different layers with same angle, the length is linter. (B). An illustration of the distance function between cell and the boundary. For cell with identity belonging to the left side of the boundary (red cells), the distal end is taken as the most right side of the cell. The distance is the Euclidean distance from the distal end to the boundary if the distal end is on the right of the boundary. Otherwise the distance is zero. Similarly, for the cell with identity belonging to the right side of the boundary (blue cells), the distal end is taken as the most left side of the cell. The distance is the Euclidean distance from the distal end to the boundary if the distal end is on the left of the boundary. Otherwise the distance is zero. For the distance greater than $6 * r$, (r is the radius of the cell), the cell is identified as a dislocated cell. (C) The probability distribution for generating the initial distribution of cells in Figure 4.4B. There are five cell identities and each of them is a Gaussian with respect to the AP position.

where r is the radius of the cell, and

$$\mathrm{ReLU}(x) = \begin{cases} x, \text{ if } x > 0, \\ 0, \text{ if } x \leq 0, \end{cases} \tag{4.24}$$

is the rectified linear unit function. For a cell in S_L or S_R with non-zero distance, this distance function calculates the Euclidean distance between the right or left distal end of this cell to the boundary m. An illustration for this distance function is shown in Figure 4.12B.

We quantify the boundary location (m), sharpness index (SI) and number of dislocated cells (DC) in this region, called K, by solving an optimization problem:

$$\begin{aligned} m_K &= \underset{k\in(a,b)}{\arg\min} \left(\sum_{\mathrm{dis}(\mathbf{c}_i,k)\leq 6R_0} \left(\mathrm{dis}(\mathbf{c}_i,k)\right)^2 \right)^{\frac{1}{2}}, \\ SI_K &= \min_{k\in(a,b)} \left(\sum_{\mathrm{dis}(\mathbf{c}_i,k)\leq 6R_0} \left(\mathrm{dis}(\mathbf{c}_i,k)\right)^2 \right)^{\frac{1}{2}}, \\ DC_K &= \#\left\{k : \mathrm{dis}(\mathbf{c}_i, m_R) > 6R_0\right\}. \end{aligned} \tag{4.25}$$

Next, we split all cells in tissue domain with index set S into three sets with distinct cell types at time t. There are *hoxb1a* cells (S_h), *krox20* cells (S_k) and none expressing cells (S_n) based on their expression level of hoxb1a and krox20:

$$\begin{aligned} S_h &= \left\{i \in S : [H]_i(t) \geq 1.2\right\}, \\ S_k &= \left\{i \in S : [K]_i(t) \geq 1.2\right\}, \\ S_n &= \left\{i \in S : i \notin S_h \bigcup S_k\right\}. \end{aligned} \tag{4.26}$$

Now, we calculate those quantities for four boundaries in the tissue domain one by one by

utilizing Eq. (4.25) and Eq. (4.26) in the flow shown in Table 4.1.

STEP 1	$C = \underset{i \in S_h}{\text{mean}} (\mathbf{c}_i^{(1)})$	Find a point to split the tissue domain
STEP 2	$K_1 = [r_1 L_1(t), C]$, $S_L = \left\{ i \in S : i \in S_k \bigcup S_n \text{ and } \mathbf{c}_i^{(1)} \in K_1 \right\}$, $S_R = \left\{ i \in S : i \in S_h \text{ and } \mathbf{c}_i^{(1)} \in K_1 \right\}$, $m(r3/r4\ ) = m_{K_1}$, $SI(r3/r4\ ) = SI_{K_1}$, $DC(r3/r4\ ) = DC_{K_1}$.	Quantify r3/r4 boundary: hoxb1a cells are on the right and other cells are on the left.
STEP 3	$K_2 = [C, r_2 L_1(t)]$, $S_L = \left\{ i \in S : i \in S_h \text{ and } \mathbf{c}_i^{(1)} \in K_2 \right\}$, $S_R = \left\{ i \in S : i \in S_k \bigcup S_n \text{ and } \mathbf{c}_i^{(1)} \in K_2 \right\}$, $m(r4/r5\ ) = m_{K_2}$, $SI(r4/r5\ ) = SI_{K_2}$, $DC(r4/r5\ ) = DC_{K_2}$.	Quantify r4/r5 boundary
STEP 4	$K_3 = [r_1 L_1(t), m(r3/r4\ )]$, $S_L = \left\{ i \in S : i \in S_n \text{ and } \mathbf{c}_i^{(1)} \in K_3 \right\}$, $S_R = \left\{ i \in S : i \in S_k \text{ and } \mathbf{c}_i^{(1)} \in K_3 \right\}$, $m(r2/r3\ ) = m_{K_3}$, $SI(r2/r3\ ) = SI_{K_3}$, $DC(r2/r3\ ) = DC_{K_3}$.	Quantify r2/r3 boundary
STEP 5	$K_4 = [m(r4/r5\ ), r_2 L_1(t)]$, $S_L = \left\{ i \in S : i \in S_k \text{ and } \mathbf{c}_i^{(1)} \in K_4 \right\}$, $S_R = \left\{ i \in S : i \in S_n \text{ and } \mathbf{c}_i^{(1)} \in K_4 \right\}$, $m(r5/r6\ ) = m_{K_4}$, $SI(r5/r6\ ) = SI_{K_4}$, $DC(r5/r6\ ) = DC_{K_4}$.	Quantify r5/r6 boundary
STEP 6	$DC = DC(r2/r3\ ) + DC(r3/r4\ )$ $+ DC(r4/r5\ ) + DC(r5/r6\ )$.	Calculate the number of dislocated cells

Table 4.1: Calculate m, SI and DC for cells in domain with AP range $[r_1 L_1(t), r_2 L_1(t)]$.

4.7.5 One-morphogen model

In Section 4.4, we present two models, the two-morphogens model and the one-morphogen model. The equations for the two-morphogens model are followed by Eq. (4.5), (4.8) and (4.10) in the one-dimensional space without the noise terms. For the one-morphogen model, RA induces both *hoxb1a* and *krox20*. There is no FGF and the equation of *krox20* is modified:

$$\frac{d[K]}{dt} = v_k \frac{a_{kk}[K]^2 + a_{rk}[RA]_{in}^2}{1 + a_{kk}[K]^2 + a_{rk}[RA]_{in}^2 + b_{hk}[H]^2} - d_k[K]. \tag{4.27}$$

4.7.6 Initial cell distribution for the model with only selective cell-cell adhesion.

In Figure 4.4B, we use mixture Gaussian distribution to generate the "salt-and-pepper" initial cell distribution. We label the cells with r2, r3, r4, r5 and r6 identity as 1, 2, 3, 4 and 5. For a cell with AP position x, we normalized its AP position $\tilde{x} = \frac{x - x_{\min}}{x_{\max} - x_{\min}}$ in the range of $[0, 1]$ where $x_{\min} = r_1 L_1(0)$ and $x_{\max} = r_2 L_1(0)$ are AP positions of boundaries of the tissue domain. The probability for this cell being i-th type of cell is given by

$$p_i(\tilde{x}) = \frac{\phi_i \mathcal{N}(\tilde{x} | \mu_i, \sigma_i)}{\sum_{i=1}^{5} \phi_i \mathcal{N}(\tilde{x} | \mu_i, \sigma_i)}. \tag{4.28}$$

We take the weights and the variance as $\phi_i = 1/5$ and $\sigma_i = 0.08$ for all i. The means $\vec{\mu} = \frac{1}{10}(1, 3, 5, 7, 9)$ denote the average AP positions of each type of cells. The probability distributions of different cell types are shown in Figure 4.12C.

4.7.7 Determination of cell type

In Section 4.5.2, we talk about the cell commitment time. The commitment time is defined by the latest time that a cell changes its fate. To determine the cell type numerically, we set thresholds for *hoxb1a* and *krox20* expression, respectively. There is a total of three types of cells in the r2-r6 pattern. The cells in r2 and r6 are identified by low expressions of both *hoxb1a* and *krox20*. The cells in r3 and r5 are identified by low expression of *hoxb1a* and high expression of *krox20*. The cells in r4 are identified by high expression of *hoxb1a* and low expression of *krox20*. The expression thresholds are selected to specify the "high" and "low" expression levels. Under those thresholds, there is no cell being identified with high expressions of *hoxb1a* and *krox20*. The expression thresholds are picked up as 1.2 as the following:

$$\begin{aligned} &\text{none expressing identity: } [H] < 1.2,\ [K] < 1.2; \\ &\textit{hoxb1a} \text{ identity: } [H] < 1.2,\ [K] \geq 1.2; \\ &\textit{krox20} \text{ identity: } [H] \geq 1.2,\ [K] < 1.2. \end{aligned} \tag{4.29}$$

4.7.8 Numerical solvers

Solving PDEs (morphogens) in moving boundary

For morphogens RA and FGF, their two-dimensional spatial domains have moving boundaries. A general form of the equation is given by

$$\begin{aligned} &\frac{\partial [M]}{\partial t} + \nabla \cdot (\mathbf{V}[M]) = D\Delta[M] + f, \\ &\mathbf{x} = (x^{(1)}, x^{(2)}) \in [0, L_1(t)] \times [-\frac{1}{2}L_2(t), \frac{1}{2}L_2(t)]. \end{aligned} \tag{4.30}$$

To handle those PDEs, we first transform the dynamical domain to the unit square by using a coordinate transformation:

$$\begin{cases} \mathbf{X} = (X^{(1)}, X^{(2)}) = \left(\dfrac{1}{L_1(t)} x^{(1)}, \dfrac{1}{L_2(t)} x^{(2)} + \dfrac{1}{2} \right) \in [0,1] \times [0,1], \\ \tau = t. \end{cases} \tag{4.31}$$

The partial derivatives in transformed coordinate are given by

$$\begin{aligned} \nabla_{\mathbf{X}} &= \left(\frac{\partial}{\partial X^{(1)}}, \frac{\partial}{\partial X^{(2)}} \right) = \left(L_1(t) \frac{\partial}{\partial x^{(1)}}, L_2(t) \frac{\partial}{\partial x^{(2)}} \right), \\ \frac{\partial^2}{\partial (X^{(1)})^2} &= (L_1(t))^2 \frac{\partial^2}{\partial (x^{(1)})^2}, \\ \frac{\partial^2}{\partial (X^{(2)})^2} &= (L_2(t))^2 \frac{\partial^2}{\partial (x^{(2)})^2}, \\ \frac{\partial}{\partial \tau} &= \frac{\partial}{\partial t} + L_1'(t) X^{(1)} \frac{\partial}{\partial x^{(1)}} + L_2'(t) \left(X^{(2)} - \frac{1}{2} \right) \frac{\partial}{\partial x^{(2)}}. \end{aligned} \tag{4.32}$$

Then the equation in the new coordinate systems are given by:

$$\frac{\partial [M]}{\partial \tau} = \frac{1}{(L_1(t))^2} \frac{\partial^2 [M]}{\partial (X^{(1)})^2} + \frac{1}{(L_2(t))^2} \frac{\partial^2 [M]}{\partial (X^{(2)})^2} + \frac{L_1'(t)}{L_1(t)} [M] + \frac{L_2'(t)}{L_2(t)} [M] + f. \tag{4.33}$$

For spatial discretization, we use the uniform rectangular grids with 151 and 71 grid points in AP and LR axis, respectively. The central difference method is used for the discretization of the diffusion term. For temporal discretization, we use the Euler-Maruyama method with fixed time step. The time step for morphogens and gene expression model is $\Delta t_{gene} = 1.8$ seconds.

Solving discrete cells dynamics

We use Euler-Maruyama method to solve Eq. (4.13) with fixed time step $\Delta t_{gene} = 3.6$ seconds. For the pairwise interactions between nodes in Eq. (4.20), we use GPUs algorithm

Parameters	Value	Unit
R_0 (Cell radius)	4	μm
R_{out}	3.60	μm
R_{in}	1.80	μm
l_{out}	3.60	μm
l_{in}	1.80	μm
l_{inter}	1.80	μm
μ	1.11	$\sec^{-1}$
U_{intra}	1.33×10^{-1}	$\mu m^2\ \sec^{-1}$
ξ_{intra}	2.4	μm
V_{intra}	5.56×10^{-2}	$\mu m^2\ \sec^{-1}$
ζ_{intra}	3.6	μm
$U_{\text{inter}}^{\text{Atr}}$	1.04×10^{-1}	$\mu m^2\ \sec^{-1}$
$U_{\text{inter}}^{\text{Rep}}$	2.50×10^{-2}	$\mu m^2\ \sec^{-1}$
ξ_{inter}	5.0	μm
$V_{\text{inter}}^{\text{Atr}}$	6.67×10^{-2}	$\mu m^2\ \sec^{-1}$
ζ_{inter}	11.00	μm
r_1	0.038	–
r_2	0.28	–

Table 4.2: Parameters for the discrete cell model.

to accelerate the computation where *gpuArray* function in MATLAB is used.

4.7.9 Parameters

Here, we list the parameters we used for the simulations shown in this work. The parameters for discrete cells (Table 4.2) are adopted from [170] and take the same values in the entire work.

In Figure 4.7 and 4.10, we generated the simulations with random parameters on the equations of *hoxb1a* and *krox20*. We use the Latin hypercube sampling to generate a high dimension random numbers and each sample is written as $(\omega_1, ..., \omega_N)$. We list the parameters that are perturbed by using the random number. If not listed, those parameters are taken as the same with that in Table 4.4.

Parameters	**Value**	**Unit**
D_r	2.83	μm^2 $\sec^{-1}$
v_r	$1.11\times^{-2}$	$\sec^{-1}$
k_r	2.22×10^{-4}	$\sec^{-1}$
β_r	1	–
$k_{\max}$	5.56×10^{-1}	$\sec^{-1}$
k_0	1.11×10^{-4}	$\sec^{-1}$
D_f	0.85	μm^2 $\sec^{-1}$
v_f	5.56×10^{-2}	$\sec^{-1}$
a_{hf}	2	–
k_f	2.67×10^{-4}	$\sec^{-1}$
β_f	1	–
d_f	0.013	$\sec^{-1}$
μ_{r1}	0.1	–
μ_{r2}	0.003	–
μ_{f1}	0.1	–
μ_{f2}	0.01	–
v_h	0.056	$\sec^{-1}$
v_k	0.056	$\sec^{-1}$
v_v	0.11	$\sec^{-1}$
v_i	3.33×10^{-4}	$\sec^{-1}$
a_{hh}	0.85	–
a_{rh}	0.13	–
a_{kk}	0.9	–
a_{fk}	6	–
a_{rv}	0.1	–
b_{kh}	40	–
b_{vh}	5	–
b_{hk}	20	–
b_{iv}	3.5	–
b_{vi}	5	–
d_h	0.022	$\sec^{-1}$
d_k	0.022	$\sec^{-1}$
d_v	0.022	$\sec^{-1}$
d_i	3.33×10^{-4}	$\sec^{-1}$
μ_h	0.01	–
μ_k	0.01	–
μ_v	0.005	–
μ_i	0.005	–

Table 4.3: Parameters for the equations of morphogens and intracellular genes.

Parameters	**Value**	**Unit**
a_{hh}	$0.85 \times 2^{-0.4+0.8\omega_1}$	–
a_{kk}	$0.9 \times 2^{-0.4+0.8\omega_2}$	–
a_{rh}	$0.13 \times 2^{-1+2\omega_3}$	–
a_{fk}	$6 \times 2^{-1+2\omega_4}$	–
b_{kh}	$40 \times 2^{-1+2\omega_5}$	–
b_{vh}	$5 \times 2^{-1+2\omega_6}$	–
b_{hk}	$20 \times 2^{-1+2\omega_7}$	–
d_h	$0.022 \times 2^{-1+2\omega_8}$	sec^{-1}
d_k	$0.022 \times 2^{-1+2\omega_9}$	sec^{-1}
b_{iv}	4	–
v_h	$2.5d_h$	sec^{-1}
v_k	$2.5d_k$	sec^{-1}

Table 4.4: Parameters for Figure 4.7 and 4.10. If not specified, they are the same as that in Table 4.3.

Chapter 5

A hybrid method for stiff reaction-diffusion equations

This chapter is a reprint of the material as it appears in Discrete and Continuous Dynamical Systems - Series B [132]. The co-authors listed in this publication directed and supervised research which forms the basis for this chapter.

5.1 Background

The second-order implicit integration factor method (IIF2) is effective at solving stiff reaction–diffusion equations owing to its nice stability condition. IIF has previously been applied primarily to systems in which the reaction contained no explicitly time-dependent terms and the boundary conditions were homogeneous. If applied to a system with explicitly time-dependent reaction terms, we find that IIF2 requires prohibitively small time-steps, that are relative to the square of spatial grid sizes, to attain its theoretical second-order temporal accuracy. Although the second-order implicit exponential time differencing (iETD2) method

can accurately handle explicitly time-dependent reactions, it is more computationally expensive than IIF2. In this work, we develop a hybrid approach that combines the advantages of both methods, applying IIF2 to reaction terms that are not explicitly time-dependent and applying iETD2 to those which are. The second-order hybrid IIF-ETD method (hIFE2) inherits the lower complexity of IIF2 and the ability to remain second-order accurate in time for large time-steps from iETD2. Also, it inherits the unconditional stability from IIF2 and iETD2 methods for dealing with the stiffness in reaction–diffusion systems. Through a transformation, hIFE2 can handle nonhomogeneous boundary conditions accurately and efficiently. In addition, this approach can be naturally combined with the compact and array representations of IIF and ETD for systems in higher spatial dimensions. Various numerical simulations containing linear and nonlinear reactions are presented to demonstrate the superior stability, accuracy, and efficiency of the new hIFE method.

5.2 Introduction

Consider a reaction–diffusion system

$$\mathbf{u}_t = D\Delta\mathbf{u} + \mathbf{f}(\mathbf{u}, \mathbf{x}, t), \quad \mathbf{x} \in \Omega \subset \mathbb{R}^k, \ t \in [0, T], \tag{5.1}$$

where $\mathbf{u} = \mathbf{u}(\mathbf{x}, t) \in \mathbb{R}^m$, $D \in \mathbb{R}^{m\times m}$ is the diffusion coefficient matrix, and $\mathbf{f}(\mathbf{u}, \mathbf{x}, t)$ describes the reactions. In biology, reaction–diffusion equations have been used to model predator–prey interactions [128, 48, 49], the formation of Turing patterns in organs or tissues [162, 52], stochastic dynamics in gene networks [138], and fetal and adult dermal wound healing [28]. In ecology, they have been applied to study population dynamics [63, 129, 6]. In finance, the estimation of option prices under several risk factors can be represented by reaction–diffusion systems as well [195]. While the reaction terms in these applications are often autonomous, i.e. $\mathbf{f}(\mathbf{u}, \mathbf{x}, t) = \mathbf{h}(\mathbf{u})$, in morphogen gradients systems in biology [39, 186, 173, 80, 91, 189],

the reactions contain explicitly time-dependent terms.

Many numerical methods have been developed to solve (5.1). Typically, finite difference or finite element methods are used to approximate the equation in space, equipped with some time integration method. To ensure stability, classic explicit methods require a time step $\Delta t \sim \Delta x^2$ [92, 113, 159]. To relax this severe stability restriction, many other schemes have been developed, such as exponential time differencing (ETD) and semi-implicit integration factor (IIF) methods. In both ETD and IIF methods, (5.1) is written into a system of ordinary differential equations (ODEs) by applying the spatial discretization,

$$U_t = AU + F(U, t), \tag{5.2}$$

where $U = U(t)$ is the spatially discretized form of $\mathbf{u}$, and AU is the finite difference approximation of the diffusion term $D\Delta\mathbf{u}$. By using the integration factor e^{-At} to integrate (5.2) from t_n to t_{n+1} exactly, i.e.,

$$\begin{aligned} U(t_{n+1}) &= e^{A\Delta t}U(t_n) + e^{A\Delta t}\int_0^{\Delta t} e^{-A\tau}F\big(U(t_n+\tau), t_n+\tau\big)\,d\tau, \\ &\triangleq e^{A\Delta t}U(t_n) + \tilde{F}_n, \end{aligned} \tag{5.3}$$

the stability constraint due to the diffusion is removed, and the problem becomes one of approximating the integral $\tilde{F}_n$.

In ETD, $\tilde{F}_n$ is approximated by integrating the product of $e^{-A\tau}$ and the interpolated $F(U, t_n+\tau)$ [16, 62]. All explicit ETD (eETD) methods are not unconditionally linearly stable; they require prohibitively small time steps to solve stiff systems [85]. To help improve stability, Runge–Kutta-type methods are sometimes employed [27, 60, 61, 79], and several methods have been developed through splitting of the linear diffusion operator [36, 37, 76, 193]. An unconditionally linearly stable (A-stable) method is the implicit second-order ETD method (iETD2). Although iETD2 is A-stable, it has the drawback of high computational cost to

solve the implicit equations at each step [120].

In IIF, instead of only interpolating $F(U, t_n+\tau)$, the approximation of $\tilde{F}_n$ is obtained by interpolating $e^{-A\tau}F(U, t_n+\tau)$ [120]. The second-order IIF method (IIF2) is A-stable like iETD2, but it has the advantage that the nonlinear equations at each step are much cheaper to solve. Owing to its good stability and reduced computational complexity compared with iETD2, IIF2 is more suitable for solving stiff reaction–diffusion equations. For high-dimensional systems, compact and array representations of IIF [119, 168] are effective in reducing the storage and computational cost associated with the exponential matrix, along with the flexibility to handle non-constant diffusion coefficients or cross-derivatives. Furthermore, by incorporating the sparse grids technique [167, 100], the IIF method can be applied to multi-dimensional systems with better efficiency. IIF has also been extended to treat fourth-order parabolic equations [75, 104], reaction–diffusion–advection equations [191], and stochastic differential equations [153], and it has been combined with adaptive meshes [98].

In both ETD and IIF methods, the high cost of computing exponential matrices is challenging. To speed up the computation, the discrete fast Fourier transformation (FFT)-based algorithms were adopted in both ETD and IIF methods [164, 179, 76]. For non-constant diffusion coefficients, Krylov-ETD and Krylov-IIF methods [145, 21, 73, 74, 101] were developed to reduce the computational cost and storage associated with exponential matrices by utilizing Krylov subspace approximation [142, 46, 59].

Although the IIF2 method is theoretically second order in time [120], when it is applied to explicitly time-dependent reactions, extremely small time steps compared to spatial grid sizes, $\Delta t \leq \mathcal{O}(\Delta x^2)$, are required to observe second-order temporal error. Above some critical threshold for Δt, the observed error in IIF2 is only first order. In contrast, iETD2 remains second order in time for larger Δt, especially for finer spatial discretization. When applied to nonhomogeneous boundary conditions, IIF2 also requires small Δt to retain second-order accuracy because the nonhomogeneous boundary conditions can be interpreted as introduc-

ing a large time-dependent reaction to the semi-discrete form in (5.2) [76]. In an attempt to construct a method that can deal with both explicitly time-dependent reactions and nonhomogeneous boundary conditions efficiently, the fast explicit integration factor (fEIF) method [76] can retain its theoretical order of accuracy under large Δt like iETD2 and has low computational cost like IIF2. One of the drawbacks of fEIF is that, as a conditionally stable method, it has strict time step constraint when reactions are stiff.

In this work, we introduce a new hybrid method which combines the IIF and iETD methods. The hybrid IIF-ETD method (hIFE) is composed in such a way as to inherit the advantages of both methods simultaneously: that is, to retain second-order accuracy for large time steps with time-dependent reactions like iETD and to reduce computational complexity in each iteration like IIF. In addition, in contrast to fEIF2, the second-order hIFE method (hIFE2) inherits A-stability from its constituents. We also introduce a procedure to more easily accommodate nonhomogeneous boundary conditions by transforming the system into one with homogeneous boundary conditions, using hIFE on the transformed system. Combining the transformation with hIFE2 provides a framework for an A-stable, efficient numerical method that remains effectively second-order accurate in time in the presence of time-dependent terms and nonhomogeneous boundary conditions.

The rest of the chapter is organized as follows. In Section 5.3, we introduce the IIF2, iETD2, and new hIFE2 methods and explore and compare the order of accuracy of hIFE2 with that of IIF2 and iETD2 for explicitly time-dependent, autonomous, and mixed reactions in both scalar and semi-discrete form. In Section 5.4, we apply hIFE2 to systems with nonhomogeneous boundary conditions and introduce a transformation to better treat these boundary conditions. In Section 5.5, we demonstrate an extension of the hIFE2 method to high-dimensional problems. In Section 5.6, we provide multiple numerical tests to demonstrate the accuracy, efficiency, and stability of hIFE. In Section 5.7, we prove that IIF2 displays first order when the time step is large. In Section 5.8, we provide the complexity analysis. In

Section 5.9, we introduce the exponential-like matrices formation. In Section 5.10, we give some concluding remarks.

5.3 Temporal error analysis

The defining feature of each of the methods discussed in this work is how the integral $\tilde{F}_n$ in (5.3) is approximated. Both ETD and IIF approximate $\tilde{F}_n$ using Lagrange interpolation [67]. In ETD, only the reaction $F(U, t_n + \tau)$ is interpolated, yielding a polynomial $p(\tau)$. Then the product $e^{-A\tau}p(\tau)$ is integrated exactly [16, 62]. The approximation for iETD2 is thus given by

$$\tilde{F}_n \approx \frac{I + (-I + A\Delta t)e^{A\Delta t}}{A^2\Delta t}F_n + \frac{(-I - A\Delta t) + e^{A\Delta t}}{A^2\Delta t}F_{n+1}, \tag{5.4}$$

where $F_n \triangleq F(U(t_n), t_n)$. In IIF, instead of only interpolating $F(U, t_n + \tau)$, the approximation of $\tilde{F}_n$ is obtained by interpolating the entire integrand, $e^{-A\tau}F(U, t_n + \tau) \approx q(\tau)$, and integrating $q(\tau)$ exactly [120]. IIF2 approximates

$$\tilde{F}_n \approx \frac{\Delta t}{2}\big(e^{A\Delta t}F_n + F_{n+1}\big). \tag{5.5}$$

We show in Section 5.3.1 that, when applied to time-dependent reactions, IIF2 requires extremely small Δt to exhibit second-order behavior while iETD2 remains second order for large time steps. Motivated by this analysis, we define for our hIFE method a splitting of the reaction term

$$F(U, t) = [F(U, t) - F(0, t)] + [F(0, t)] \triangleq F_1(U, t) + F_2(t) \tag{5.6}$$

in (5.3) and apply IIF on $F_1(U,t)$ and iETD on $F_2(t)$. The second-order hybrid method (**hIFE2**) thus approximates

$$\begin{aligned}\tilde{F}_n &= e^{A\Delta t}\int_0^{\Delta t} e^{-A\tau}F_1\big(U(t_n+\tau),t_n+\tau\big)\,d\tau + e^{A\Delta t}\int_0^{\Delta t} e^{-A\tau}F_2\big(t_n+\tau\big)\,d\tau \\ &\approx \frac{\Delta t}{2}\big(e^{A\Delta t}(F_1)_n + (F_1)_{n+1}\big) + \frac{I+(-I+A\Delta t)e^{A\Delta t}}{A^2\Delta t}(F_2)_n + \frac{(-I-A\Delta t)+e^{A\Delta t}}{A^2\Delta t}(F_2)_{n+1}.\end{aligned} \tag{5.7}$$

In Section 5.3.1, we perform an analysis of the temporal error in using each method to solve (5.2) with the operator A replaced by a scalar α for explicitly time-dependent, autonomous, and mixed reactions. Then in Section 5.3.2, we investigate the differences between the scalar and semi-discrete form, showing that iETD2 and hIFE2 remain effectively second order for large Δt while IIF2 does not.

5.3.1 Accuracy in scalar form

To compare the error associated with each method above, we first consider the scalar form of (5.2), where A is replaced by the scalar α:

$$\begin{cases} u_t = \alpha u + f(u,t), \quad t\in[0,T], \\ u(0) = v. \end{cases} \tag{5.8}$$

By making use of the Taylor expansions

$$\begin{aligned} \frac{1+(-1+\alpha\Delta t)e^{\alpha\Delta t}}{\alpha^2\Delta t} &= \Delta t\sum_{k=0}^{\infty}\frac{1}{(k+2)k!}(\alpha\Delta t)^k, \quad f(t_{n+1}) = \sum_{k=0}^{\infty}\frac{1}{k!}\Delta t^k\frac{d^k}{dt^k}f_n, \\ \frac{(-1-\alpha\Delta t)+e^{\alpha\Delta t}}{\alpha^2\Delta t} &= \Delta t\sum_{k=0}^{\infty}\frac{1}{(k+2)!}(\alpha\Delta t)^k, \quad u(t_{n+1}) = \sum_{k=0}^{\infty}\frac{1}{k!}\Delta t^k\frac{d^k}{dt^k}u_n, \end{aligned} \tag{5.9}$$

and, from (5.8),

$$\frac{d^k}{dt^k}u = \alpha^k u + \sum_{j=0}^{k-1} \alpha^{k-1-j}\frac{d^j}{dt^j}f, \tag{5.10}$$

we derive the local truncation errors, T_n, of iETD2 and IIF2 for a general $f(u,t)$ to be

$$\begin{aligned} T_n^{iETD2} &= \frac{1}{\Delta t}\left(u(t_{n+1}) - e^{\alpha\Delta t}u_n - \frac{1+(-1+\alpha\Delta t)e^{\alpha\Delta t}}{\alpha^2\Delta t}f_n - \frac{(-1-\alpha\Delta t)+e^{\alpha\Delta t}}{\alpha^2\Delta t}f_{n+1}\right) \\ &= \sum_{j=2}^{\infty}\Delta t^j\frac{d^j}{dt^j}f_n\left[\sum_{k=0}^{\infty}\left(\frac{1}{(k+j+1)!}-\frac{1}{j!(k+2)!}\right)(\alpha\Delta t)^k\right] \\ &= \sum_{j=2}^{\infty}\Delta t^j\frac{d^j}{dt^j}f_n\left(Q_{j+1}(\alpha\Delta t)-\frac{1}{j!}Q_2(\alpha\Delta t)\right), \end{aligned} \tag{5.11}$$

$$\begin{aligned} T_n^{IIF2} &= \frac{1}{\Delta t}\left(u(t_{n+1}) - e^{\alpha\Delta t}u_n - \frac{\Delta t}{2}\left(e^{\alpha\Delta t}f_n + f_{n+1}\right)\right) \\ &= \alpha^2\Delta t^2 f_n\sum_{k=0}^{\infty}\left(\frac{1}{(k+3)!}-\frac{1}{2(k+2)!}\right)(\alpha\Delta t)^k \\ &\qquad + \sum_{j=1}^{\infty}\Delta t^j\frac{d^j}{dt^j}f_n\left(\sum_{k=0}^{\infty}\frac{1}{(k+j+1)!}(\alpha\Delta t)^k - \frac{1}{2j!}\right) \\ &= \alpha^2\Delta t^2 f_n\left(Q_3(\alpha\Delta t)-\frac{1}{2}Q_2(\alpha\Delta t)\right) + \alpha\Delta t^2\frac{d}{dt}f_n Q_3(\alpha\Delta t) \\ &\qquad + \sum_{j=2}^{\infty}\Delta t^j\frac{d^j}{dt^j}f_n\left(Q_{j+1}(\alpha\Delta t)-\frac{1}{2j!}\right), \end{aligned} \tag{5.12}$$

where we have made use of the function

$$Q_j(x) = \frac{e^x - \sum_{k=0}^{j-1}\frac{1}{k!}x^k}{x^j} = \sum_{k=0}^{\infty}\frac{1}{(k+j)!}x^k \tag{5.13}$$

from [16] to simplify the expressions.

The truncation error for hIFE is a more complicated expression, and its general form is omitted in favor of more specific cases below. We now investigate the properties of each of these for three different possible $f(u,t)$: (I) explicitly time-dependent reactions,

$f(u,t) = g(t)$; (II) autonomous reactions, $f(u,t) = h(u)$; and (III) mixed reactions of the form $f(u,t) = h(u) + g(t)$. The first few terms of each of these expressions is included in explicit form up to $\mathcal{O}(\Delta t^4)$ for each of these cases in Table 5.1.

Case I: explicitly time-dependent reactions

Here we consider explicitly time-dependent reactions of the form $f(u,t) = g(t)$. We assume $g \in C^\infty$ and g and its derivatives of any order are bounded and $\mathcal{O}(1)$. We only compare IIF2 and iETD2 here, since hIFE2 is equivalent to iETD2 in this case ($F_1(u,t) \equiv 0$ in (5.6)). Since $f(u,t) = g(t)$ is dependent only on t, the time derivatives $\frac{d^j}{dt^j} f$ in (5.11) and (5.12) are just the single-variable derivatives $g^{(j)}(t)$, so the truncation error takes the same general form as those expressions in this case.

Although both methods have second-order truncation errors $\mathcal{O}(\Delta t^2)$ and thus should exhibit second-order behavior in the limit $\Delta t \to 0$, for a fixed nonzero Δt, we are only guaranteed to observe second-order behavior if the higher-order terms are much smaller in magnitude than the terms involving Δt^2. By comparing the Δt^2 and Δt^3 terms (given explicitly in Table 5.1), we see in both IIF2 and iETD2 that if $\Delta t > \mathcal{O}(1/|\alpha|)$, the Δt^3 terms have a larger magnitude than the Δt^2 terms. If we want to observe second-order behavior, then it must satisfy $\Delta t < \mathcal{O}(1/|\alpha|)$; the behavior of the error above this threshold is unpredictable. We demonstrate this claim by means of an example, taking $g(t) = t^2$. The numerical errors from applying IIF2 and iETD2 (and, thus, hIFE2) to (5.8) with $f(u,t) = t^2$ are plotted in Figure 5.1A as a function of Δt for various $-\alpha$. We see that for a fixed $-\alpha$, the thresholds at which both IIF2 and iETD2 "switch" to second order are similar to each other, and both are near $\Delta t \approx 1/|\alpha|$, consistent with our claim.

On the other hand, another interesting feature of the plot is that for a fixed Δt, the error in IIF2 *increases* as $-\alpha$ increases while that of iETD2/hIFE2 *decreases*. Indeed, to demonstrate

why the error for each method behaves differently as $-\alpha$ increases for general $g(t)$, we explore the magnitudes of truncation errors when $\alpha \to 0$ and $\alpha \to -\infty$. We first note that for a fixed Δt, as $\alpha \to 0$, the truncation errors in (5.11) and (5.12) for both methods take the form of the Crank–Nicholson method, with truncation error

$$T_n = \sum_{j=2}^{\infty} \Delta t^j g_n^{(j)} \left(\frac{1}{(j+1)!} - \frac{1}{2j!} \right) = \mathcal{O}(\Delta t^2).$$

Then as $\alpha \to -\infty$, the truncation error for iETD2 in (5.11) tends to zero while that for IIF2 in (5.12) tends to $-\frac{1}{2} g_{n+1}$, which is $\mathcal{O}(1)$. When $-\alpha$ varies from 0 to ∞, the truncation errors of iETD2 are generally decreasing, changing from $\mathcal{O}(\Delta t^2)$ to 0. In contrast, the truncation errors of IIF2 are generally increasing, changing from $\mathcal{O}(\Delta t^2)$ to $\mathcal{O}(1)$. Thus, we expect, for a fixed Δt, the global error for iETD2 to decrease for larger $-\alpha$ while the global error in IIF2 should increase.

Remark. We have shown in the scalar case that the threshold at which IIF2 and iETD2 "switch" to second-order temporal error for time-dependent reactions is similar in both methods, and this seems to invalidate our entire motivation for developing hIFE2 in the first place. It is, however, the preceding observation concerning the behavior of the errors for large $-\alpha$ that will prove crucial to why iETD2 remains second order for larger Δt than IIF2 when applied to a semi-discrete system with time-dependent reactions. We examine that form in Section 5.3.2.

Remark. In Figure 5.1A, for Δt above the threshold, the temporal error of IIF2 has *first*-order behavior instead of second. For some remarks on why that might be the case, see Section 5.7.

Case II: autonomous reactions

We now consider reactions of the form $f(u,t) = h(u)$ satisfying $h(0) = 0$, which do not have explicitly time-dependent terms. In this case, hIFE2 is equivalent to IIF2 since $F_2(t) \equiv 0$ in (5.6), so again we only compare IIF2 and iETD2 here. Further, we only consider $h(u) = ru$ ($r \in \mathbb{R}$) since this form is easily extendable to the semi-discrete case.

Here, the total time derivatives in (5.11) and (5.12) take the form

$$\frac{d^j}{dt^j} f_n = r(\alpha + r)^j u_n = r(\alpha + r)^j e^{(\alpha+r)t_n} u_0, \tag{5.14}$$

where we have made use of the exact solution $u_n = u_0 e^{(\alpha+r)t_n}$. The full truncation error up to $\mathcal{O}(\Delta t^4)$ is given for both methods in Table 5.1. Similar to Case I, we note that the Δt^3 coefficients are $\mathcal{O}(\alpha)$ larger than the coefficients of Δt^2 in both iETD2 and IIF2/hIFE2 so that it must also satisfy $\Delta t < \mathcal{O}(1/|\alpha|)$ to observe second-order behavior of the error.

The most important difference between this case and Case I, though, is that the error in both IIF2 and iETD2 now includes, through the derivatives, a factor of $u_n = u_0 e^{(\alpha+r)t_n}$ in every term, and thus as $-\alpha$ increases, u_n exponentially suppresses the truncation error to zero in *both* methods, not just in iETD2.

Again, we demonstrate the validity of our claims with an example. The error in applying iETD2 and IIF2/hIFE2 to (5.8) with $f(u,t) = -u$ (so $r = -1$) is shown as a function of Δt for various $-\alpha$ in Figure 5.1B. We note that, consistent with the above analysis, the error decreases dramatically with $-\alpha$ for both iETD2 and IIF2/hIFE, and both demonstrate second-order accuracy for $\Delta t < \mathcal{O}(1/|\alpha|)$ while the error (particularly in iETD2) remains unpredictable above this threshold.

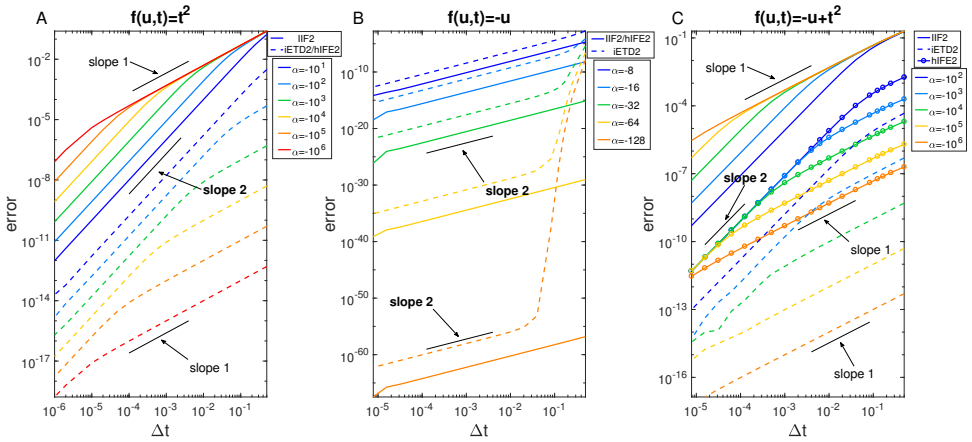

Figure 5.1: Plots of the numerical error at $T = 1$ after applying IIF2, iETD2, and hIFE2 to the scalar equation in (5.8) with $u(0) = 1$ for various Δt. Plots are shown for (A) $f(u,t) = t^2$ with $\alpha = -10^1,\ -10^2,\ -10^3,\ -10^4,\ -10^5$, and -10^6; (B) $f(u,t) = -u$ with $\alpha = -8,\ -16,\ -32,\ -64$, and -128; and (C) $f(u,t) = -u+t^2$ with $\alpha = -10^2,\ -10^3,\ -10^4,\ -10^5$, and -10^6. The curves for iETD2 and hIFE2 are identical in (A), and those for IIF2 and hIFE2 are identical in (B). We see that for the time-dependent reactions (A,C), the error in IIF2 increases as $-\alpha$ increases while the error in iETD2 and hIFE2 decreases.

Case III: mixed reactions

Finally, we consider mixed reactions of the form $f(u,t) = ru + g(t)$, where, as in Case I, we assume $g \in C^\infty$ and g and all its derivatives are bounded and $\mathcal{O}(1)$. Again, we only consider ru for the u-dependent term so that the extension of the analysis to system case in the next section is straightforward. In this case, the derivatives in (5.11) and (5.12) are given by

$$\frac{d^j}{dt^j} f_n = r(\alpha + r)^j u_n + g_n^{(j)} + r \sum_{l=0}^{j-1} (\alpha + r)^{j-1-l} g_n^{(l)}. \tag{5.15}$$

The expressions for the truncation errors of IIF2, iETD2, and hIFE2 up to $\mathcal{O}(\Delta t^4)$ are given in Table 5.1. This is the first (and only) case we examine where the hIFE2 method differs from both IIF2 and iETD2.

As in Cases I and II, we observe that the Δt^3 terms are $\mathcal{O}(\alpha)$ times larger than the Δt^2 terms, so the threshold $\Delta t < \mathcal{O}(1/|\alpha|)$ also applies here. The main feature we point out for

the errors in this case is that, owing to the form of the derivatives in (5.15), after substituting this expression into the truncation errors in (5.11) and (5.12) and multiplying everything out, the truncation error in this case will contain terms that involve just the derivatives $g_n^{(j)}$, exactly replicating the error in Case I. Then, regardless of how the other terms behave, there will be a part of the error that behaves in the same manner as the time-dependent Case I. That is, as $-\alpha$ grows, some part of the error will increase under IIF2 whereas that same part of the error will decrease under iETD2. The error should also decrease under hIFE2 since this method treats those time-dependent terms with iETD2. Thus, in this case we expect to observe similar behavior as in Case I: increasing error in IIF2 and decreasing error in iETD2 and hIFE2 as $-\alpha$ increases.

We demonstrate this claim with yet another example, this time taking $f(u,t) = -u + t^2$, the results of which are shown in Figure 5.1C as a function of Δt. We see that indeed the error for all three methods behaves similarly to Case I, increasing as $-\alpha$ increases under IIF2 while decreasing under iETD2 and hIFE2. The plot also verifies our prediction that the threshold at which second-order behavior is seen is around $\Delta t \approx 1/|\alpha|$.

5.3.2 Accuracy in semi-discrete form

Having examined each of the three cases for the scalar equation (5.8), we now turn our attention to the differences between the scalar form and the semi-discrete form,

$$U_t = AU + F(U,t). \tag{5.16}$$

Method	Reaction f	Truncation error
IIF2	$g(t)$	$-\frac{1}{12}\Delta t^2(\alpha^2 g_n - 2\alpha g_n' + g_n'')$ $-\frac{1}{24}\Delta t^3(\alpha^3 g_n - \alpha^2 g_n' - \alpha g_n'' + g_n''') + \mathcal{O}(\Delta t^4)$
	ru	$-\frac{1}{12}\Delta t^2 r^3 u_n$ $-\frac{1}{24}\Delta t^3(2\alpha r^3 + r^4)u_n + \mathcal{O}(\Delta t^4)$
	$ru + g(t)$	$-\frac{1}{12}\Delta t^2\big[\alpha^2 g_n + \alpha(-r g_n - 2g_n') + (r^3 u_n + r^2 g_n + r g_n' + g_n'')\big]$ $-\frac{1}{24}\Delta t^3\big[\alpha^3 g_n + \alpha^2(-r g_n - g_n') + \alpha(2r^3 u_n + r^2 g_n - g_n'')$ $+(r^4 u_n + r^3 g_n + r^2 g_n' + r g_n'' + g_n''')\big] + \mathcal{O}(\Delta t^4)$
iETD2	$g(t)$	$-\frac{1}{12}\Delta t^2 g_n''$ $-\frac{1}{24}\Delta t^3(\alpha g_n'' + g_n''') + \mathcal{O}(\Delta t^4)$
	ru	$-\frac{1}{12}\Delta t^2(\alpha^2 r + 2\alpha r^2 + r^3)u_n$ $-\frac{1}{24}\Delta t^3(2\alpha^3 r + 5\alpha^2 r^2 + 4\alpha r^3 + r^4)u_n + \mathcal{O}(\Delta t^4)$
	$ru + g(t)$	$-\frac{1}{12}\Delta t^2\big[\alpha^2 r u_n + \alpha(2r^2 u_n + r g_n) + (r^3 u_n + r^2 g_n + r g_n' + g_n'')\big]$ $-\frac{1}{24}\Delta t^3\big[2\alpha^3 r u_n - \alpha^2(5r^2 u_n + 2r g_n) + \alpha(4r^3 u_n + 3r^2 g_n + 2r g_n' + g_n'')$ $+(r^4 u_n + r^3 g_n + r^2 g_n' + r g_n'' + g_n''')\big] + \mathcal{O}(\Delta t^4)$
hIFE2	$g(t)$	equivalent to iETD2
	ru	equivalent to IIF2
	$ru + g(t)$	$-\frac{1}{12}\Delta t^2\big[-\alpha r g_n + (r^3 u_n + r^2 g_n + r g_n' + g_n'')\big]$ $-\frac{1}{24}\Delta t^3\big[-\alpha^2 r g_n + \alpha(2r^3 u_n + r^2 g_n + g_n'')$ $+(r^4 u_n + r^3 g_n + r^2 g_n' + r g_n'' + g_n''')\big] + \mathcal{O}(\Delta t^4)$

Table 5.1: The truncation errors of IIF2, iETD2, and hIFE2 when applied to (5.8) with different reactions.

A motivating one-dimensional problem that can be written in the form (5.16) is

$$\begin{cases} u_t = d u_{xx} + f(u, x, t), \quad x \in [a, b],\ t \in [0, T], \\ u_x|_{x=a} = u|_{x=b} = 0, \\ u(x, 0) = v(x), \end{cases} \tag{5.17}$$

where $u = u(x, t)$, $d > 0$, and we require $v(x)$ to satisfy the given boundary conditions. Note that the boundary conditions here are mixed homogeneous; we discuss different types of boundary conditions in Section 5.4.

We can put the partial differential equation (PDE) (5.17) into the form (5.16) by using finite

difference discretization of the operator $d\frac{\partial^2}{\partial x^2}$. Let $\Delta x = (b-a)/N$ be the mesh size and N be the number of grid points in the spatial discretization. We can write A as the diagonalizable $N \times N$ matrix,

$$A = \frac{d}{\Delta x^2} \begin{bmatrix} -2 & 2 & & & & & \\ 1 & -2 & 1 & & & & \\ & 1 & -2 & 1 & & & \\ & & \ddots & \ddots & \ddots & & \\ & & & 1 & -2 & 1 & \\ & & & & 1 & -2 & \end{bmatrix}_{N\times N}, \tag{5.18}$$

and we form the vectors

$$\begin{aligned} U(t) &= \left(u^0(t), u^1(t), \ldots, u^{N-1}(t)\right)^T \\ F(U,t) &= \left(f(u^0(t), x^0, t), f(u^1(t), x^1, t), \ldots, f(u^{N-1}(t), x^{N-1}, t)\right)^T \end{aligned} \tag{5.19}$$

where $x^i = a + i\Delta x$, $i = 0, \ldots, N-1$, are the grid points in the discretization (we identify $x_N = b$), and $u^i(t) \triangleq u(x^i, t)$. This spatial discretization completely removes x-dependence from the equation and introduces an error from the exact solution of $\mathcal{O}(\Delta x^2)$; we assume this level of spatial error in the remaining calculations and only discuss temporal error for the remainder of the analysis.

The matrix A has N distinct eigenvalues, $\lambda_j \triangleq d\sigma_j/\Delta x^2$, $j = 1, \ldots, N$, where σ_j are listed in descending order:

$$\sigma_j = -2 + 2\cos\frac{(2j-1)\pi}{2N}, \quad j = 1, \ldots, N. \tag{5.20}$$

The eigenvalues are all negative, and in the limit $N \to \infty$,

$$\lambda_1 \to -d\left(\frac{\pi/2}{b-a}\right)^2 = \mathcal{O}(d), \quad \lambda_N \approx -\frac{4d}{\Delta x^2} \to -\infty. \tag{5.21}$$

For convenience, we henceforth set $a = 0$, $b = \pi/2$ so that $\lambda_1 \to -d$. The least negative possible eigenvalue occurs at $N = j = 1$, where $\lambda_1 = -\frac{8d}{\pi^2}$. For small Δx (i.e. large N), the range of eigenvalues is large, as listed in Table 5.2. Though we have only discussed mixed boundary conditions here, the eigenvalues of the matrices corresponding to Neumann and Dirichlet conditions have similar properties, which are all negative and differ in a large range [159].

j \ N	32	64	128	256	512	1024
1	−1.00	−1.00	−1.00	−1.00	−1.00	−1.00
5	−7.97e+1	−8.07e+1	−8.09e+1	−8.09e+1	−8.10e+1	−8.10e+1
$N/2$	−7.89e+2	−3.23e+03	−1.31e+04	−5.28e+04	−2.12e+05	−8.49e+05
N	−1.66e+03	−6.64e+03	−2.66e+04	−1.06e+05	−4.25e+05	−1.70e+06

Table 5.2: Eigenvalues of A, λ_j, under different spatial resolutions, where $d = 1$, $a = 0$, $b = \pi/2$, $j = 1,\ 5,\ N/2,\ N$.

Relating the error in semi-discrete form to that of the scalar form

In each of the three cases in Section 5.3.1, we have considered reactions that were easily extendable to the semi-discrete form. Since the matrix A in (5.18) is diagonalizable, we thus set $A = H\Lambda H^{-1}$, where Λ is the diagonal matrix consisting of the eigenvalues λ_j, $j = 1, \ldots, N$. Then for an explicitly time-dependent reaction $F(U,t) = G(t)$, we can multiply (5.16) on the left by H^{-1} to obtain

$$\frac{d}{dt}\left(H^{-1}U\right) = \Lambda\left(H^{-1}U\right) + H^{-1}G(t), \tag{5.22}$$

where $H^{-1}U$ and $H^{-1}G(t)$ are N-vectors. Then since Λ is diagonal, the jth component of this system takes the form

$$\frac{d}{dt}\left(H^{-1}U\right)_j = \lambda_j\left(H^{-1}U\right)_j + \left(H^{-1}G\right)_j(t), \tag{5.23}$$

which matches the scalar form (5.8) with the new variable $u = (H^{-1}U)_j$, $\alpha = \lambda_j$, and $f(u,t) = (H^{-1}G)_j(t)$, independent of u. We can thus solve this system by solving each of the components individually.

Similarly, if $F(U,t) = rU$, we can also diagonalize the system, writing

$$\frac{d}{dt}\left(H^{-1}U\right) = \Lambda\left(H^{-1}U\right) + r\left(H^{-1}U\right), \tag{5.24}$$

so that we obtain a system of scalar equations with $\alpha = \lambda_j$, $f(u,t) = r(H^{-1}U)_j$ (cf. $u_t = \alpha u + ru$). For the mixed reaction, $F(U,t) = rU + G(t)$, a similar form can be obtained. For general nonlinear reactions, the conclusions in scalar form cannot be directly extended to semi-discrete form since the system may not be diagonalizable. We do not analyze the nonlinear reactions in this work, only numerical tests are carried out in Section 5.6.

From the above, we see that solving an equation in the semi-discrete form is equivalent to solving N separate scalar equations, each with different α. We showed in Sections 5.3.1 and 5.3.1 that for scalar equations with time-dependent or mixed reactions, as $-\alpha$ increases, the error in IIF2 increases while the error in iETD2 and hIFE2 decreases. Thus, if we apply each method to the entire system (5.22) and measure error with the maximum norm, the component we expect to have the largest error under IIF2 is the one with the largest (i.e. most negative) eigenvalue, λ_N, whereas we expect the component with the largest error under iETD2 and hIFE2 to be the one with the smallest eigenvalue, λ_1. Since each scalar equation requires $\Delta t < \mathcal{O}(1/|\alpha|) = \mathcal{O}(1/|\lambda_j|)$ to observe second-order temporal error (Section 5.3.1), we expect iETD2 and hIFE2 to display second-order behavior for any $\Delta t < \mathcal{O}(1/|\lambda_1|) = \mathcal{O}(1/d)$ while IIF2 requires $\Delta t < \mathcal{O}(1/|\lambda_N|) = \mathcal{O}(\Delta x^2/d)$. For large N, the magnitudes of λ_1 and λ_N differ in large range as shown in (5.21), then IIF2 requires a much smaller Δt to exhibit second-order temporal error than iETD2 and hIFE2. Meanwhile, for autonomous reactions, we showed in Section 5.3.1 that the error for the scalar

equation in all three methods decreases with larger $-\alpha$. Thus, in this case, the error in all three methods is dictated by the smallest eigenvalue, λ_1, so that all three methods exhibit second-order temporal error for large $\Delta t < \mathcal{O}(1/d)$.

We demonstrate the above claims in Figure 5.2 by comparing the behavior of IIF2, iETD2, and hIFE2 on the three reactions $F(U,t) = t^2$, $F(U,t) = -U$, and $F(U,t) = -U + t^2$ with various N as a function of Δt. We see that indeed for IIF2, as N increases, progressively smaller Δt are required to observe second-order temporal error. In contrast, iETD2 and hIFE2 always maintain second-order temporal accuracy for different N, consistent with our analysis.

Remark. When the explicitly time-dependent terms appear in the reactions, the difference in performance of the IIF2 and iETD2 methods makes intuitive sense. In IIF2, the product of the exponential integration factor and the reaction is interpolated together, whereas in iETD2, only the reaction is interpolated, not the exponential. For large $-\alpha$, IIF2 has to interpolate an exponentially increasing function, $e^{-\alpha t}g(t)$, with a polynomial, thus likely introducing a lot of error. In contrast, iETD2 interpolates only the reaction, $g(t)$, which is independent of $-\alpha$ and likely varies less over time. Therefore, the approximation by iETD2 is likely to be more accurate than IIF2 in this case.

Remark. In previous work, the absolute stability analysis was carried out on ETD [16] and IIF [120] methods. Both iETD2 and IIF2 are unconditionally linearly stable (A-stable), while eETD2 is conditionally linearly stable. The absolute stability analysis only considers equations with autonomous reactions and homogeneous boundary conditions. The hIFE2 has the same absolute stability with IIF2. The fEIF2 method [76] has the same absolute stability with eETD2. Therefore, the hIFE2 method is A-stable, and fEIF2 is conditionally linearly stable. For solving stiff systems, a large time step size is allowed if the method is A-stable. We show the advantage of hIFE2 over fEIF2 in stability in Section 5.6.2.

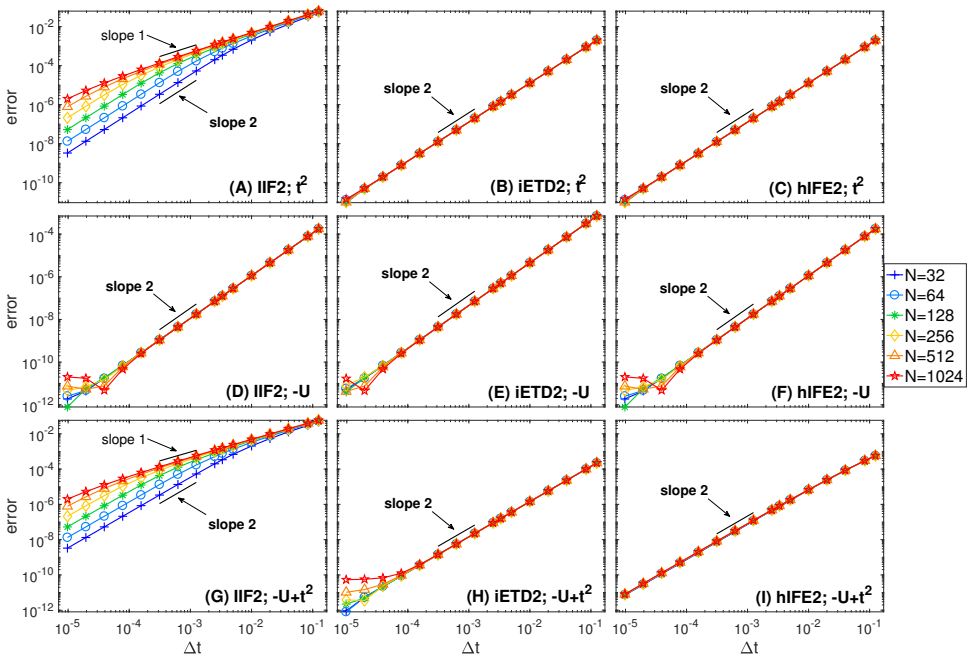

Figure 5.2: The temporal errors at $T = 1$ in the maximum norm when solving the semi-discrete form (5.16) of (5.27) for different reactions with the IIF, iETD2, and hIFE2 methods. In all simulations, the reaction coefficient $d = 1$. (A) IIF2 for $F(U,t) = t^2$; (B) iETD2 for $F(U,t) = t^2$; (C) hIFE2 for $F(U,t) = t^2$; (D) IIF2 for $F(U,t) = -U$; (E) iETD2 for $F(U,t) = -U$; (F) hIFE2 for $F(U,t) = -U$; (G) IIF2 for $F(U,t) = -U + t^2$; (H) iETD2 for $F(U,t) = -U + t^2$; (I) hIFE2 for $F(U,t) = -U + t^2$. Different colors represent the number of points, N, in the spatial discretization, where $N = 32$, 64, 128, 256, 512, and 1024. Subfigures in same row share the same y-axis while subfigures in same column share the same x-axis. Panels (B) and (C) are identical because hIFE2 treats time-dependent terms with iETD2, and panels (D) and (F) are identical since hIFE2 treats autonomous terms with IIF2.

5.4 The hybrid method hIFE for systems with nonhomogeneous boundary conditions

We showed that hIFE2 is more accurate than IIF2 in Section 5.3 and has lower computational cost than iETD2 in Section 5.8. In this section, we discuss the extension of hIFE2 to equations with nonhomogeneous boundary conditions through a transformation.

5.4.1 Direct treatment of nonhomogeneous boundary conditions

In all of the analysis in Section 5.3, we assumed that the explicitly time-dependent terms were $\mathcal{O}(1)$. When considering a one-dimensional reaction–diffusion equation of the form

$$u_t = du_{xx} + f(u, x, t). \tag{5.25}$$

with nonhomogeneous boundary conditions, however, the system can be written in the modified semi-discrete form (cf. (5.16)),

$$U_t = AU + B(t) + F(U, t), \tag{5.26}$$

where $B(t)$ is a time-dependent term of $\mathcal{O}(1/\Delta x)$ or $\mathcal{O}(1/\Delta x^2)$ for Neumann- or Dirichlet-type conditions, respectively [159]. Then hIFE2 may not remain second-order under large Δt.

For example, we consider a specific one-dimensional reaction–diffusion equation,

$$\begin{cases} u_t = u_{xx} - u, \quad x \in \left[0, \dfrac{\pi}{2}\right], \\ u(x, 0) = \sin(x + \dfrac{\pi}{6}), \end{cases} \tag{5.27}$$

a solution of which is

$$u(x, t) = e^{-2t} \sin(x + \frac{\pi}{6}). \tag{5.28}$$

We now consider three different variations of this problem with different nonhomogeneous boundary conditions dictated by the exact solution (5.28): (a) the Neumann boundary conditions; (b) the Dirichlet boundary conditions; (c) mixed boundary conditions, Neumann at $x = 0$ and Dirichlet at $x = \frac{\pi}{2}$. We list the boundary conditions and the corresponding A and $B(t)$ in the semi-discrete form (5.26) in Table 5.3. Note that Neumann conditions cause

$B(t)$ to be $\mathcal{O}(1/\Delta x)$, and Dirichlet and mixed conditions cause $B(t)$ to be $\mathcal{O}(1/\Delta x^2)$.

	Neumann	Dirichlet	Mixed
BCs	$u_x\|_{x=0} = e^{-2t}\cos\frac{\pi}{6}$ $u_x\|_{x=\frac{\pi}{2}} = e^{-2t}\cos\frac{2\pi}{3}$	$u\|_{x=0} = e^{-2t}\sin\frac{\pi}{6}$, $u\|_{x=\frac{\pi}{2}} = e^{-2t}\sin\frac{2\pi}{3}$	$u_x\|_{x=0} = e^{-2t}\cos\frac{\pi}{6}$ $u\|_{x=\frac{\pi}{2}} = e^{-2t}\sin\frac{2\pi}{3}$
$B(t)$	$e^{-2t}\begin{bmatrix} -\frac{2\cos\frac{\pi}{6}}{\Delta x} \\ 0 \\ \vdots \\ 0 \\ \frac{2\cos\frac{2\pi}{3}}{\Delta x} \end{bmatrix}_{N+1}$	$e^{-2t}\begin{bmatrix} \frac{\sin\frac{\pi}{6}}{\Delta x^2} \\ 0 \\ \vdots \\ 0 \\ \frac{\sin\frac{2\pi}{3}}{\Delta x^2} \end{bmatrix}_{N-1}$	$e^{-2t}\begin{bmatrix} -\frac{2\cos\frac{\pi}{6}}{\Delta x} \\ 0 \\ \vdots \\ 0 \\ \frac{\sin\frac{2\pi}{3}}{\Delta x^2} \end{bmatrix}_{N}$
A	$\frac{1}{\Delta x^2}\begin{bmatrix} -2 & 2 & & & \\ 1 & -2 & 1 & & \\ & \ddots & \ddots & \ddots & \\ & & 1 & -2 & 1 \\ & & & 2 & -2 \end{bmatrix}_{(N+1)^2}$	$\frac{1}{\Delta x^2}\begin{bmatrix} -2 & 1 & & & \\ 1 & -2 & 1 & & \\ & \ddots & \ddots & \ddots & \\ & & 1 & -2 & 1 \\ & & & 1 & -2 \end{bmatrix}_{(N-1)^2}$	$\frac{1}{\Delta x^2}\begin{bmatrix} -2 & 2 & & & \\ 1 & -2 & 1 & & \\ & \ddots & \ddots & \ddots & \\ & & 1 & -2 & 1 \\ & & & 1 & -2 \end{bmatrix}_{N^2}$

Table 5.3: Different boundary conditions in (5.27), and their corresponding A and $B(t)$ in the semi-discrete form (5.26).

We directly apply hIFE2 to (5.27) with these three kinds of boundary conditions and plot the error at $T = 1$ in Figure 5.3A–C. In hIFE2, the explicitly time-dependent term $B(t)$ is treated by iETD2, and the autonomous term $-U$ is treated by IIF2. In each of the cases, we refine Δt until the error is dominated by spatial error introduced in the discretization. We see that hIFE2 exhibits second-order accuracy only for the $\mathcal{O}(1/\Delta x)$ Neumann boundary conditions. The hIFE2 method does not retain second-order accuracy for large Δt with the $\mathcal{O}(1/\Delta x^2)$ Dirichlet or mixed boundary conditions, presumably because $B(t)$ is too large.

5.4.2 A transformation for nonhomogeneous boundary conditions

To observe second-order behavior for hIFE2 under large time step when dealing with non-homogeneous boundary conditions, we construct an auxiliary function u_B that satisfies the same boundary conditions as u and form a new system in terms of the variable $\tilde{u} = u - u_B$ that satisfies *homogeneous* boundary conditions [176]. We then solve the new system using hIFE2 for $\tilde{u}$ and add the auxiliary function u_B back into the obtained solution to recover

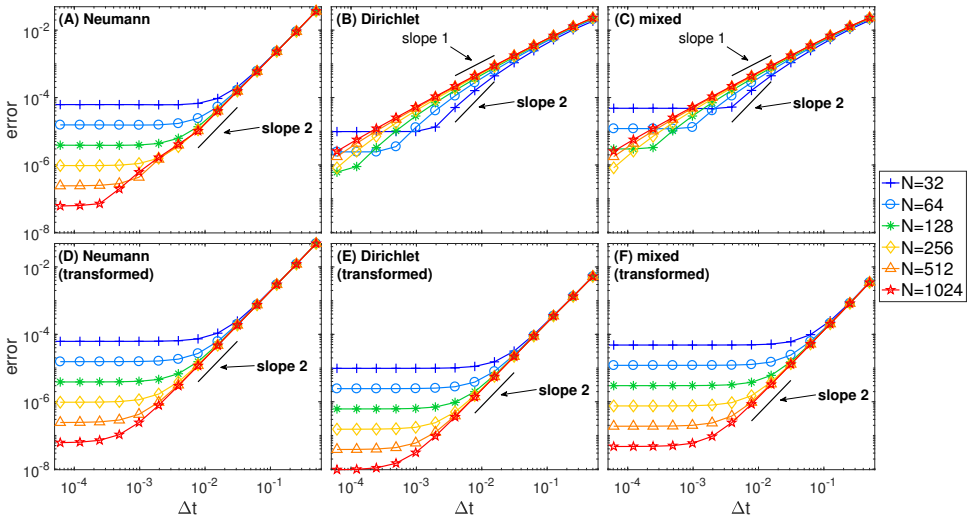

Figure 5.3: Plots of the numerical error at $T = 1$ in maximum norm after applying hIFE2 to (5.27) with Neumann, Dirichlet, and mixed boundary conditions for various Δt and fixed N. The hIFE2 is applied to both original and transformed (Section 5.4.2) equations. Plots are shown for hIFE2 on: (A) the original equation with Neumann boundary; (B) the original equation with Dirichlet boundary; (C) the original equation with mixed boundary; (D) the transformed equation with Neumann boundary; (E) the transformed equation with Dirichlet boundary; (F) the transformed equation with mixed boundary. Different colors represent different spatial mesh sizes N, where $N = 32,\ 64,\ 128,\ 256,\ 512$, and 1024.

u. Since $\tilde{u}$ satisfies homogeneous boundary conditions, hIFE2 can obtain a solution with second-order accuracy even when u itself satisfies Dirichlet conditions.

One-dimensional system

Let $u(x,t)$ satisfy (5.25) with the following general nonhomogeneous boundary conditions on a one-dimensional domain $[x_1, x_2]$:

$$\begin{cases} \mathcal{B}_1 u(x_1,t) = (\alpha_1 u + \beta_1 u_x)|_{x=x_1} = f_1(t), \\ \mathcal{B}_2 u(x_2,t) = (\alpha_2 u + \beta_2 u_x)|_{x=x_2} = f_2(t). \end{cases} \tag{5.29}$$

To construct the auxiliary function u_B, we define two basis functions,

$$\begin{aligned} C_1(x) &= \frac{(x-x_2)^2}{\alpha_1(x_1-x_2)^2 + 2\beta_1(x_1-x_2)}, \\ C_2(x) &= \frac{(x-x_1)^2}{\alpha_2(x_2-x_1)^2 + 2\beta_2(x_2-x_1)}, \end{aligned} \tag{5.30}$$

so that

$$\mathcal{B}_1 C_1(x_1) = 1,\ \mathcal{B}_1 C_2(x_1) = 0,$$

$$\mathcal{B}_2 C_1(x_2) = 0,\ \mathcal{B}_2 C_2(x_2) = 1.$$

Then we construct u_B as a linear combination of the basis functions

$$u_B(x,t) = C_1(x) f_1(t) + C_2(x) f_2(t), \tag{5.31}$$

so that u_B satisfies the same nonhomogeneous boundary conditions (5.29) as u. Hence, $\tilde{u} = u - u_B$ will satisfy homogeneous boundary conditions in the modified equation

$$\tilde{u}_t = d\tilde{u}_{xx} + f(\tilde{u} + u_B, x, t) - (u_B)_t + d(u_B)_{xx}. \tag{5.32}$$

This modified equation can thus be solved by hIFE2 and the original solution u of (5.25) can be found by adding u_B back into the numerically obtained solution $\tilde{u}$ of (5.32). Note that the function u_B is known, so u_B and its derivatives can be computed analytically. The modified equation includes nonzero explicitly time-dependent terms with magnitude $\mathcal{O}(1)$. Indeed, hIFE2 can exhibit second order in time for large Δt while IIF2 cannot exhibit that. The effect of the transformation can be thought of as "spreading out" the two large nonzero components in the untransformed $B(t)$ over the entire domain to dampen their magnitude.

We include plots of the numerical results of applying hIFE2 to the transformed versions of the model problem (5.27) from the previous section in Figure 5.3D–F, noting that indeed hIFE2 remains second order for the transformed equations when it failed to do so for the untransformed ones.

Higher-dimensional systems

Suppose a solution $u(x, y, t)$ is desired on the two-dimensional domain $[x_1, x_2] \times [y_1, y_2]$, with nonhomogeneous boundary conditions,

$$\begin{cases} \mathcal{B}_{11}u(x_1, y, t) = (\alpha_{11}u + \beta_{11}u_x)|_{x=x_1} = f_1(y, t), \\ \mathcal{B}_{12}u(x_2, y, t) = (\alpha_{12}u + \beta_{12}u_x)|_{x=x_2} = f_2(y, t), \\ \mathcal{B}_{21}u(x, y_1, t) = (\alpha_{21}u + \beta_{21}u_y)|_{y=y_1} = g_1(x, t), \\ \mathcal{B}_{22}u(x, y_2, t) = (\alpha_{22}u + \beta_{22}u_y)|_{y=y_2} = g_2(x, t). \end{cases} \tag{5.33}$$

Using a similar technique as in the one-dimensional case (5.30), we define the basis functions $C_{11}(x)$, $C_{12}(x)$, $C_{21}(y)$, $C_{22}(y)$ satisfying

$$\begin{aligned}
\mathcal{B}_{11}C_{11}(x_1) = 1,\ \mathcal{B}_{11}C_{12}(x_1) = 0,\\
\mathcal{B}_{12}C_{11}(x_2) = 0,\ \mathcal{B}_{12}C_{12}(x_2) = 1,\\
\mathcal{B}_{21}C_{21}(y_1) = 1,\ \mathcal{B}_{21}C_{22}(y_1) = 0,\\
\mathcal{B}_{22}C_{21}(y_2) = 0,\ \mathcal{B}_{22}C_{22}(y_2) = 1.
\end{aligned}$$

To construct the auxiliary function u_B, we first transform the boundary conditions at $x = x_1, x_2$, letting

$$u_{B_1}(x,y,t) = C_{11}(x)f_1(y,t) + C_{12}(x)f_2(y,t). \tag{5.34}$$

Then $u - u_{B_1}$ satisfies the boundary conditions

$$\begin{aligned}
&\mathcal{B}_{11}(u - u_{B_1})(x_1,y,t) = 0,\\
&\mathcal{B}_{12}(u - u_{B_1})(x_2,y,t) = 0,\\
&\mathcal{B}_{21}(u - u_{B_1})(x,y_1,t) = g_1(x,t) - [C_{11}(x)\mathcal{B}_{21}f_1(y_1,t) + C_{12}(x)\mathcal{B}_{21}f_2(y_1,t)] \triangleq \tilde{g}_1(x,t),\\
&\mathcal{B}_{22}(u - u_{B_1})(x,y_2,t) = g_2(x,t) - [C_{11}(x)\mathcal{B}_{22}f_1(y_2,t) + C_{12}(x)\mathcal{B}_{22}f_2(y_2,t)] \triangleq \tilde{g}_2(x,t),
\end{aligned}$$

which is homogeneous with respect to x. Then we transform the boundary conditions at $y = y_1, y_2$, letting

$$u_{B_2}(x,y,t) = C_{21}(y)\tilde{g}_1(x,t) + C_{22}(y)\tilde{g}_2(x,t).$$

Then $u_B = u_{B_1} + u_{B_2}$ satisfies the same boundary conditions (5.33) as u so that $\tilde{u} = u - u_{B_1} - u_{B_2} = u - u_B$ satisfies homogeneous boundary conditions. Altogether, then, we have

$$\begin{aligned}
u_B = {} & C_{11}(x)f_1(y,t) + C_{12}(x)f_2(y,t) + C_{21}(y)g_1(x,t) + C_{22}(y)g_2(x,t)\\
& - C_{11}(x)C_{21}(y)\mathcal{B}_{21}f_1(y_1,t) - C_{12}(x)C_{21}(y)\mathcal{B}_{21}f_2(y_1,t)\\
& - C_{11}(x)C_{22}(y)\mathcal{B}_{22}f_1(y_2,t) - C_{12}(x)C_{22}(y)\mathcal{B}_{22}f_2(y_2,t).
\end{aligned} \tag{5.35}$$

Remark. Such an approach of constructing u_B can be extended to higher dimensions in a straightforward manner.

5.5 The hIFE method in higher dimensions

We now introduce a higher-dimensional version of the hIFE method that utilizes the compact versions of iETD [76] and IIF [119] to reduce the size of the system compared with a naïve discretization of the Laplacian operator. We only introduce the three-dimensional version since the procedure generalizes trivially to other dimensions.

The main drawback of higher-dimensional IIF and iETD methods is the large size of the system. For example, in three dimensions, if N_x, N_y, and N_z correspond to the number of grid points in the x, y, and z, directions, respectively, the matrix A in the semi-discrete form (5.2) has dimension $N_xN_yN_Z \times N_xN_yN_z$ (or $N^3 \times N^3$ if $N_x = N_y = N_z = N$). Since the number of computations per iteration for IIF is proportional to the square of the size of the system, each iteration requires $\mathcal{O}(N_x^2N_y^2N_z^2)$ operations (or $\mathcal{O}(N^6)$ if all are equal). The number of operations for iETD is proportional to the *cube* of the size of the system—$\mathcal{O}(N^9)$ operations per iteration for equal spacing in all directions.

In contrast, the compact representation reduces the storage requirement on A to $\mathcal{O}(N_x^2+N_y^2+N_z^2) = \mathcal{O}(3N^2)$ and the number of operations in each iteration to $\mathcal{O}(N_x^2N_yN_z + N_xN_y^2N_z + N_xN_yN_z^2) = \mathcal{O}(3N^4)$. When applied to hIFE, this approach leads to a significant improvement in its efficiency for higher-dimensional systems.

To illustrate the compact representation approach, we consider (5.1) in three dimensions. As in the one-dimensional hIFE, we split the reaction term $f(u,x,y,z,t) = f_1(u,x,y,z,t) + f_2(x,y,z,t)$, where $f_1(u,x,y,z,t) \triangleq f(u,x,y,z,t) - f(0,x,y,z,t)$ and $f_2(x,y,z,t) \triangleq f(0,x,y,z,t)$. Let N_x, N_y, and N_z be the number of grid points in each dimension, and h_x, h_y, and h_z be

the corresponding mesh sizes. The spatial discretization is $\{(x_i, y_j, z_k) : 1 \le i \le N_x, 1 \le j \le N_y, 1 \le k \le N_z\}$. Denote the discretized u by $U_{N_x \times N_y \times N_z} = (U_{i,j,k})_{N_x \times N_y \times N_z}$. Here $F_1(U,t)$ and $F_2(t)$ are the discretized forms of f_1 and f_2, respectively. We define the linear operators ⓧ, ⓨ, and ⓩ as

$$\begin{aligned}(A \circledcirc{x} U)_{i,j,k} &= \sum_{l=1}^{N_x} A_{i,l} U_{l,j,k} \\ (B \circledcirc{y} U)_{i,j,k} &= \sum_{l=1}^{N_y} B_{j,l} U_{i,l,k} \\ (C \circledcirc{z} U)_{i,j,k} &= \sum_{l=1}^{N_z} C_{k,l} U_{i,j,l},\end{aligned} \tag{5.36}$$

and define the matrices $\mathcal{L}_x, \mathcal{L}_y, \mathcal{L}_z$ to approximate the one-dimensional diffusion operators $D\frac{\partial^2}{\partial x^2}, D\frac{\partial^2}{\partial y^2}, D\frac{\partial^2}{\partial z^2}$ by the same second-order central difference in the one-dimensional method. The compact representation for the diffusion approximation is

$$U_t = \mathcal{L}_x \circledcirc{x} U + \mathcal{L}_y \circledcirc{y} U + \mathcal{L}_z \circledcirc{z} U + F_1(U,t) + F_2(t). \tag{5.37}$$

The matrices $\mathcal{L}_x$, $\mathcal{L}_y$, and $\mathcal{L}_z$ are diagonalizable, i.e.,

$$\mathcal{L}_x = P_x \Lambda_x P_x^{-1}, \quad \mathcal{L}_y = P_y \Lambda_y P_y^{-1}, \quad \mathcal{L}_z = P_z \Lambda_z P_z^{-1},$$

where Λ_x, Λ_y, and Λ_z are diagonal matrices,

$$\begin{aligned}\Lambda_x &= \mathrm{diag}[\alpha_1, \alpha_2, \ldots, \alpha_{N_x}], \\ \Lambda_y &= \mathrm{diag}[\beta_1, \beta_2, \ldots, \beta_{N_y}], \\ \Lambda_z &= \mathrm{diag}[\gamma_1, \gamma_2, \ldots, \gamma_{N_z}].\end{aligned}$$

We define $H = (h_{i,j,k})_{N_x \times N_y \times N_z}$ such that

$$h_{i,j,k} = \alpha_i + \beta_j + \gamma_k,$$

the operator (e^*) as taking exponential of an array element by element,

$$(e^*)^H = (e^{h_{i,j,k}})_{N_x \times N_y \times N_z},$$

and the operator $\odot$ as componentwise matrix multiplication,

$$A \odot B = (a_{i,j,k} b_{i,j,k})_{N_x \times N_y \times N_z}.$$

Then we define the operator $\mathcal{L}(t)$ applied to U as

$$\begin{aligned}
\mathcal{L}(t)U &= e^{-\mathcal{L}_z t} \textcircled{z} e^{-\mathcal{L}_y t} \textcircled{y} e^{-\mathcal{L}_x t} \textcircled{x} U \\
&= (P_z \textcircled{z} P_y \textcircled{y} P_x \textcircled{x}) e^{-\Lambda_z t} \textcircled{z} e^{-\Lambda_y t} \textcircled{y} e^{-\Lambda_x t} \textcircled{x} (P_z^{-1} \textcircled{z} P_y^{-1} \textcircled{y} P_x^{-1} \textcircled{x} U) \\
&= (P_z \textcircled{z} P_y \textcircled{y} P_x \textcircled{x})(e^*)^{-Ht} \odot (P_z^{-1} \textcircled{z} P_y^{-1} \textcircled{y} P_x^{-1} \textcircled{x} U).
\end{aligned}$$

Using $\mathcal{L}(t)$ as an integration factor in (5.37) and integrating over $[t_n,\ t_{n+1}]$, we obtain

$$\begin{aligned}
U_{n+1} = \mathcal{L}(-\Delta t) U_n + \mathcal{L}(-\Delta t) \int_0^{\Delta t} \mathcal{L}(\tau) F_1(U(t_n + \tau), t_n + \tau)\, d\tau \\
+ \mathcal{L}(-\Delta t) \int_0^{\Delta t} \mathcal{L}(\tau) F_2(t_n + \tau)\, d\tau \qquad (5.38) \\
\triangleq \mathcal{L}(-\Delta t) U_n + (\tilde{F}_1)_n + (\tilde{F}_2)_n,
\end{aligned}$$

which takes a similar form to (5.3) in the one-dimensional method. Motivated by the one-dimensional method, then, in the compact hIFE we approximate $(\tilde{F}_1)_n$ using the compact IIF and $(\tilde{F}_2)_n$ using the compact iETD. As in one dimension, the compact iETD approximates $F_2 \approx p(\tau)$ using Lagrange interpolation, and $\mathcal{L}(\tau)p(\tau)$ is integrated exactly. The compact IIF interpolates $\mathcal{L}(\tau)F_1 \approx q(\tau)$, and $q(\tau)$ is integrated exactly. The compact hIFE2 thus

approximates

$$(\tilde{F}_1)_n \approx \frac{\Delta t}{2}\Big(F_1(U_{n+1}) + e^{\mathcal{L}_z\Delta t}\textcircled{z}e^{\mathcal{L}_y\Delta t}\textcircled{y}e^{\mathcal{L}_x\Delta t}\textcircled{x}F_1(U_n)\Big), \tag{5.39}$$

$$\begin{aligned}(\tilde{F}_2)_n \approx P_z\textcircled{z}P_y\textcircled{y}P_x\textcircled{x}\Bigg(&\Big(\frac{1+(-1+h_{i,j,k}\Delta t)e^{h_{i,j,k}\Delta t}}{h_{i,j,k}^2\Delta t}\Big)_{i,j,k}\odot(\mathbf{F}_2)_n\\ &+\Big(\frac{(-1-h_{i,j,k}\Delta t)+e^{h_{i,j,k}\Delta t}}{h_{i,j,k}^2\Delta t}\Big)_{i,j,k}\odot(\mathbf{F}_2)_{n+1}\Bigg).\end{aligned} \tag{5.40}$$

Note that these expressions are very similar to expression (5.7) for hIFE2 in one dimension.

5.6 Application of hIFE to more complex systems

In this section, we present several numerical simulations, demonstrating the advantages of hIFE2 in accuracy, complexity, and stability compared with the other methods. In Section 5.6.1, we apply IIF2, iETD2, fEIF2, and hIFE2 to a nonlinear reaction to demonstrate the advantages of hIFE2 over IIF2 and iETD2 in accuracy and complexity. Then, in Section 5.6.2, we apply all of the methods to a stiff system of coupled PDEs to demonstrate the stability advantage of hIFE2 over fEIF2. In both examples we choose systems with nonhomogeneous boundary conditions to highlight how hIFE2 can handle these (with the aid of the transformation from Section 5.4.2). In Section 5.6.3, we provide examples justifying the choice of F_1, F_2 in (5.6) compared with the more "obvious" choice. Finally, in Section 5.6.4, we provide an example of the compact hIFE2 in three dimensions.

5.6.1 Reaction–diffusion equation with a nonlinear reaction term

All the reactions we have considered in the analysis so far have been linear in u. We now consider an equation with a nonlinear reaction term and, just for good measure, a space-

dependent term as well. We compare the obtained solutions using IIF2, iETD2, fEIF2, and hIFE2 in terms of accuracy and complexity. We start with the equation

$$\begin{cases} u_t = du_{xx} + u^2 - e^{-2dt}\sin^2 x, \quad 0 \le x \le \dfrac{\pi}{2}, \\ u_x|_{x=0} = e^{-dt}, \quad u|_{x=\frac{\pi}{2}} = e^{-dt}, \\ u(x,0) = \sin x, \end{cases} \tag{5.41}$$

which has the exact solution

$$u = e^{-dt}\sin x. \tag{5.42}$$

Since the boundary conditions are nonhomogeneous, we apply the transformation introduced in Section 5.4.2 to the equation, setting

$$u_B = e^{-dt}\left(\frac{-(x-\frac{\pi}{2})^2}{\pi} + \frac{4x^2}{\pi^2}\right)$$

so that we obtain a transformed equation for $\tilde{u} = u - u_B$,

$$\tilde{u}_t = d\tilde{u}_{xx} + \tilde{u}^2 + 2u_B\tilde{u} + u_B^2 + du_B + de^{-dt}\left(-\frac{2}{\pi} + \frac{8}{\pi^2}\right) - e^{-2dt}\sin^2 x, \tag{5.43}$$

with homogeneous boundary conditions. Since fEIF2 is supposed to work without transforming the boundary conditions, we apply it to the untransformed equation (5.41), and we apply IIF2, iETD2, and hIFE2 to the transformed equation (5.43). In both cases, we choose a uniform spatial grid with $\Delta x = \pi/2N$ and set the time step to vary proportional to the spatial grid, $\Delta t = 0.1\Delta x$. We further set the diffusion constant $d = 2$ and approximate the solution through time $T = 1$. Since fEIF2 is a second-order explicit method, we require knowledge of the discretized U at two time steps to begin the approximation when we are only given the initial condition. To determine the second time step, $U_1 = U(\Delta t)$, we modify fEIF2 to use the first-order eETD1 on the reaction terms and iETD2 on the boundary terms. Then we proceed with the usual fEIF2 for later time steps. For solving the nonlinear

equations in the implicit methods, IIF2, iETD2, and hIFE2, we use Newton's method [67] with a tolerance of 10^{-8} and a maximum of 15 iterations.

We compare the results of the four methods for various N in terms of the L^∞ error at $T = 1$ and CPU time for the computation in Table 5.4. We include both the CPU time ("CPU time 1") for forming the exponential-like matrices (Section 5.9) and ("CPU time 2") for the actual iterations. The total CPU time is listed in a separate column. We see that, consistent with Section 5.3, IIF2 does not attain second-order accuracy, especially for large N, while the other methods do. In addition, consistent with Section 5.8, the ratio of CPU time among IIF2:hIFE2:fEIF2 is around 1:3:5, and the computation time of iETD2 is much higher than the others.

In this example, hIFE2 and fEIF2 perform similarly and exhibit a major advantage in accuracy compared with IIF2 and computational speed compared with iETD2. Despite being implicit, hIFE2 even has a minor advantage in computational time over fEIF2.

5.6.2 Stiff system of coupled reaction–diffusion equations

In the previous example, hIFE2 and fEIF2 performed similarly in terms of accuracy and complexity. We note, however, that the IIF2, iETD2, and hIFE2 methods are A-stable whereas fEIF2 is not. This advantage in stability will be significant for systems with stiff

	N	L^∞ error	Order	CPU time (s)	CPU time 1 (s)	CPU time 2 (s)
IIF2	8	0.00228	-	0.09	0.05	0.04
	16	0.000591	1.95	0.04	0.02	0.02
	32	0.000198	1.58	0.07	0.03	0.04
	64	7.81e-05	1.34	0.13	0.04	0.09
	128	0.000108	−0.46	0.54	0.07	0.47
	256	5.18e-05	1.06	1.26	0.23	1.03
	512	1.83e-05	1.50	4.00	1.39	2.61
	1024	2.07e-05	−0.18	28.30	7.75	20.55
	2048	1.07e-05	0.96	168.12	42.10	126.02
	4096	5.35e-06	1.00	1148.42	265.35	883.07
	N	L^∞ error	Order	CPU time (s)	CPU time 1 (s)	CPU time 2 (s)
iETD2	8	0.00216	-	0.07	0.04	0.03
	16	0.000539	2.00	0.07	0.04	0.03
	32	0.000135	2.00	0.12	0.06	0.06
	64	3.37e-05	2.00	0.80	0.07	0.73
	128	8.41e-06	2.00	3.78	0.16	3.62
	256	2.1e-06	2.00	22.99	0.54	22.45
	512	5.26e-07	2.00	289.66	2.70	286.96
	1024	1.32e-07	2.00	2841.66	14.65	2827.01
	2048	3.31e-08	1.99	35348.32	91.84	35256.48
	4096	-	-	too long	-	-
	N	L^∞ error	Order	CPU time (s)	CPU time 1 (s)	CPU time 2 (s)
hIFE2	8	0.00217	-	0.12	0.09	0.03
	16	0.000544	1.99	0.06	0.04	0.02
	32	0.000137	1.99	0.08	0.05	0.03
	64	3.42e-05	2.00	0.16	0.08	0.08
	128	8.75e-06	1.97	0.76	0.17	0.59
	256	2.21e-06	1.99	1.85	0.54	1.31
	512	5.53e-07	2.00	9.17	2.61	6.56
	1024	1.49e-07	1.89	61.82	14.20	47.62
	2048	3.93e-08	1.93	419.24	89.49	329.75
	4096	1.12e-08	1.81	3096.23	603.04	2493.19
	N	L^∞ error	Order	CPU time (s)	CPU time 1 (s)	CPU time 2 (s)
fEIF2	8	0.00216	-	0.37	0.37	0.00
	16	0.00054	2.00	0.04	0.04	0.00
	32	0.000135	2.00	0.07	0.07	0.00
	64	3.38e-05	2.00	0.09	0.08	0.01
	128	8.44e-06	2.00	0.54	0.18	0.36
	256	2.11e-06	2.00	1.41	0.69	0.72
	512	5.28e-07	2.00	11.62	3.01	8.61
	1024	1.32e-07	2.00	84.11	16.11	68.00
	2048	3.31e-08	1.99	613.91	101.12	512.79
	4096	8.89e-09	1.90	4700.11	707.64	3992.47

Table 5.4: Numerical errors in terms of the maximum norm and CPU time for the various methods on the example in Section 5.6.1 at $T = 1$ with diffusion coefficient $d = 2$. Here N is the number of grid points in the spatial discretization ($\Delta x = \pi/2N$), and the time step $\Delta t = 0.1\Delta x$. "CPU time 1" is the CPU time for initializing the matrices (Section 5.9), "CPU time 2" is the CPU time for the iterations, and "CPU time" is the sum of the two.

reactions, which we now investigate. In the system of PDEs,

$$\begin{cases} u_t = du_{xx} - au + v, \\ v_t = dv_{xx} - bv, \\ u_x|_{x=0} = e^{-(a+d)t} + e^{-(b+d)t}, \quad v_x|_{x=0} = (a-b)e^{-(b+d)t}, \\ u|_{x=\frac{\pi}{2}} = e^{-(a+d)t} + e^{-(b+d)t}, \quad v|_{x=\frac{\pi}{2}} = (a-b)e^{-(b+d)t}, \\ u(x,0) = 2\sin x, \\ v(x,0) = (a-b)\sin x, \end{cases} \tag{5.44}$$

whose exact solution is

$$\begin{aligned} u(x,t) &= (e^{-(a+d)t} + e^{-(b+d)t})\sin(x), \\ v(x,t) &= (a-b)e^{-(b+d)t}\sin(x), \end{aligned} \tag{5.45}$$

if a and b have very different magnitudes, the resulting system will be stiff. As such, we compare the performance of IIF2, iETD2, fEIF2, and hIFE2 on this system of PDEs.

We transform the equation to make the boundary conditions homogeneous and apply IIF2, iETD2, and hIFE2 to the transformed system whereas we apply fEIF2 to the untransformed system. The corresponding auxiliary functions are

$$\begin{cases} u_B = (e^{-(a+d)t} + e^{-(b+d)t})\left(\dfrac{-(x-\frac{\pi}{2})^2}{\pi} + \dfrac{4x^2}{\pi^2}\right), \\ v_B = (a-b)e^{-(b+d)t}\left(\dfrac{-(x-\frac{\pi}{2})^2}{\pi} + \dfrac{4x^2}{\pi^2}\right). \end{cases}$$

In each of the simulations, we fix the spatial mesh size $\Delta x = \pi/2N$ with $N = 1024$ and run each method through K time steps to a final time T (so $\Delta t = T/K$). We set $a = 500$, $b = -2$, $d = 0.1$, $T = 1$, and include the results for various K in Table 5.5. As the magnitude of the solutions is large, we also include the relative error in this table.

In this example, hIFE2 is still more accurate than IIF2 and faster than iETD2. The fEIF2

method, however, suffers from stability issues. The numerical solution obtained with fEIF2 blows up when the time step size is not small enough. Meanwhile, the other three methods never suffer from this blow-up issue since they are all A-stable. When $K = 320$ (so $\Delta t = 1/320 = 3.125 \times 10^{-3}$), the error in the numerical solution of fEIF2 is still huge while the relative error of hIFE2 is already very small. A-stability in solving stiff equations is thus a significant advantage of hIFE2 over fEIF2, cementing its position as the most versatile of the four methods examined in this work.

	K	L^∞ error	Relative error	Order	CPU time (s)	CPU time 1 (s)	CPU time 2 (s)
IIF2	20	10	0.00381	-	5.32	5.25	0.07
	40	4.81	0.00182	1.06	5.07	4.91	0.16
	80	2.32	0.000881	1.05	5.09	4.78	0.31
	160	1.12	0.000425	1.05	5.07	4.44	0.63
	320	0.534	0.000203	1.07	5.24	3.90	1.34
	640	0.251	9.51e-05	1.09	5.92	3.40	2.52
	1280	0.115	4.34e-05	1.13	7.90	2.92	4.98
	2560	0.0503	1.91e-05	1.19	12.84	2.55	10.29
	K	L^∞ error	Relative error	Order	CPU time (s)	CPU time 1 (s)	CPU time 2 (s)
iETD2	20	3.99	0.00151	-	19.63	10.88	8.75
	40	0.994	0.000377	2.00	28.60	10.80	17.80
	80	0.248	9.41e-05	2.00	46.92	10.76	36.16
	160	0.0617	2.34e-05	2.01	80.10	10.41	69.69
	320	0.0152	5.76e-06	2.02	148.60	9.80	138.80
	640	0.00366	1.39e-06	2.05	285.20	9.27	275.93
	1280	0.000872	3.31e-07	2.07	567.11	8.94	558.17
	2560	0.000227	8.61e-08	1.94	1140.59	8.49	1132.10
	K	L^∞ error	Relative error	Order	CPU time (s)	CPU time 1 (s)	CPU time 2 (s)
hIFE2	20	4.19	0.000397	-	11.11	0.00	0.28
	40	1.05	0.000397	2.00	11.96	11.39	0.57
	80	0.261	9.91e-05	2.00	11.61	10.70	0.91
	160	0.0652	2.47e-05	2.00	12.36	10.37	1.99
	320	0.0162	6.14e-06	2.01	13.90	9.84	4.06
	640	0.00397	1.51e-06	2.03	17.65	9.43	8.22
	1280	0.000971	3.68e-07	2.03	25.08	8.88	16.20
	2560	0.000256	9.72e-08	1.92	40.83	8.45	32.38
	K	L^∞ error	Relative error	Order	CPU time (s)	CPU time 1 (s)	CPU time 2 (s)
fEIF2	20	1.49e+29	4.43e+25	-	12.42	11.96	0.46
	40	2.9e+48	8.65e+44	−64.08	12.61	11.78	0.83
	80	6.04e+73	1.8e+70	−84.11	13.07	11.46	1.61
	160	2.27e+96	6.77e+92	−74.99	14.43	11.20	3.23
	320	1.92e+79	5.71e+75	56.72	17.20	10.59	6.61
	640	0.251	7.48e-05	265.37	23.47	9.93	13.54
	1280	0.119	3.54e-05	1.08	35.96	9.57	26.39
	2560	0.0603	1.8e-05	0.98	62.05	9.08	52.97

Table 5.5: Numerical errors and CPU time for the test in Section 5.6.2 at time $T = 1$. We set the diffusion coefficient $d = 0.1$ and the coefficients of the reactions $a = 500$ and $b = -2$. For each simulation, we fix the number of grid points $N = 1024$ ($\Delta x = \pi/2N$), and run the simulation for K time steps ($\Delta t = T/K$). The error e is measured in the maximum norm, and the relative error is defined by $e/\max\{\|U_K\|_\infty, \|V_K\|_\infty\}$, where U_K and V_K are the numerical solutions after K time steps. "CPU time 1" is the CPU time for initialization (Section 5.9), "CPU time 2" is the CPU time for the iterations, and "CPU time" is the sum of the two.

5.6.3 Justification of the chosen splitting of the reaction terms

Recall that the motivation for the hIFE2 method was that IIF2 could not handle time-dependent reaction terms with second-order temporal accuracy while iETD2 could. For the hIFE2 method, we then defined a splitting of the reaction term in (5.6) that might at first glance seem more complicated than necessary. At the level of the undiscretized PDEs, the method splits the reaction $f(u,x,t) = f_1(u,x,t) + f_2(x,t)$, where

$$f_1(u,x,t) = f(u,x,t) - f(0,x,t), \quad f_2(x,t) = f(0,x,t). \tag{5.46}$$

In this section we demonstrate by means of two examples why we suggest this decomposition over what one may consider a more "obvious" one.

Consider a general reaction–diffusion equation in one dimension with homogeneous boundary conditions,

$$\begin{cases} u_t = u_{xx} + f(u,x,t), & 0 \le x \le \dfrac{\pi}{2}, \\ u_x|_{x=0} = 0, \quad u|_{x=\frac{\pi}{2}} = 0, \\ u(x,0) = \cos x. \end{cases}$$

Straightforward decomposition

First consider the reaction

$$f(u,x,t) = \cos u + t. \tag{5.47}$$

Since hIFE2 aims to treat time-dependent terms with iETD2 and autonomous terms with IIF2, one might be led to choose the straightforward decomposition of the reaction

$$f_1(u,x,t) = \cos(u), \quad f_2(x,t) = t. \tag{5.48}$$

The decomposition in (5.46), however, would lead to the splitting

$$f_1(u,x,t) = \cos(u) - 1, \quad f_2(x,t) = 1 + t. \tag{5.49}$$

We include the numerical results of each of the decompositions (5.48) and (5.49) for various spatial mesh sizes, N, fixing $\Delta t = 0.1\Delta x$ in Table 5.6(A). We see that indeed the decomposition (5.49) outperforms the naïve decomposition (5.48) for each value of N since it remains second order while the naïve decomposition does not.

Numerical results aside, however, there are other problems with naïvely splitting the reaction into time-dependent and autonomous terms. Namely, what does one do with a term such as ut, $\cos(t)u^2$, or e^{tu}? Should they be included in f_1 or f_2? The decomposition (5.46) provides a framework for even these more complicated reactions and so is more desirable than the naïve decomposition, especially since it seems to give more accurate results anyway.

More complicated reactions

In this section, we provide an example of a more complicated reaction. We construct a reaction that contains x and t, and is unable to be fully decomposed into an autonomous term and an explicitly time-dependent term:

$$f(u,x,t) = (t+1)\cos(xu) + xe^t. \tag{5.50}$$

The naïve decomposition is

$$f_1(u,x,t) = (t+1)\cos(xu), \quad f_2(x,t) = xe^t, \tag{5.51}$$

and the decomposition followed by (5.46) is

$$f_1(u,x,t) = (t+1)\cos(xu) - (t+1), \quad f_2(x,t) = t + 1 + xe^t. \tag{5.52}$$

The numerical errors for various N, similar to the previous example, are shown in Table 5.6(B). Again, we see that the decomposition (5.52) outperforms the naïve decomposition (5.51) for each value of N since it remains second order while the naïve decomposition does not. The hIFE2 method is thus able to accurately handle even complicated equations with temporal and spatial variables present in both of the decomposed terms.

Remark. Despite the appearance of explicitly time-dependent term in f_1, the hIFE2 method can achieve second–order accuracy with large time step as long as $f_1(0,x,t) = 0$ is held. This example shows that hIFE2 is also able to handle complicated reactions efficiently.

5.6.4 Reaction–diffusion system with nonhomogeneous boundary conditions in three dimensions

Finally, we include an example of the compact hIFE2 applied to a three-dimensional system with nonhomogeneous boundary conditions,

$$\begin{cases} u_t = d_1 u_{xx} + d_2 u_{yy} + d_3 u_{zz} + ru, \quad (x,y,z) \in \left[0, \dfrac{\pi}{2}\right]^3 \\ u_x|_{x=0} = u|_{x=\frac{\pi}{2}} = E\sin y \sin z, \\ u_y|_{y=0} = u|_{y=\frac{\pi}{2}} = E\sin x \sin z, \\ u_z|_{z=0} = u|_{z=\frac{\pi}{2}} = E\sin x \sin y, \end{cases}$$

		Decomposition (5.48)		Decomposition (5.49)	
	N	A priori error	Order	A priori error	Order
	16	0.00103	-	0.00102	-
	32	0.000532	0.95	0.000255	2.00
	64	0.000328	0.70	6.37e-05	2.00
(A)	128	8.21e-05	2.00	1.59e-05	2.00
	256	0.000196	−1.25	3.98e-06	2.00
	512	0.000106	0.88	9.95e-07	2.00
	1024	8.69e-06	3.61	2.49e-07	2.00
	2048	3.37e-05	−1.96	6.19e-08	2.01
	4096	1.75e-05	0.95	1.42e-08	2.12

		Decomposition (5.51)		Decomposition (5.52)	
	N	A priori error	Order	A priori error	Order
	16	0.00979	-	0.00977	-
	32	0.00245	2.00	0.00245	1.99
	64	6.67e-04	1.88	0.000614	2.00
(B)	128	1.67e-04	2.00	0.000153	2.00
	256	3.94e-04	-1.24	3.83e-05	2.00
	512	2.13e-04	0.89	9.59e-06	2.00
	1024	1.76e-05	3.60	2.4e-06	2.00
	2048	6.75e-05	-1.94	5.99e-07	2.00
	4096	3.50e-05	0.95	1.48e-07	2.02

Table 5.6: Numerical a priori error in applying hIFE2 to a one-dimensional reaction–diffusion system with (A) $f(u,x,t) = \cos u + t$ for the decomposition (5.48) and (5.49) and (B) $f(u,x,t) = (t+1)\cos(xu) + xe^t$ for the decomposition (5.51) and (5.52). The a priori error is defined by $\|u^N - u^{N/2}\|_\infty$, where N is the number of grid points in the spatial discretization. The simulations are run through time $T = 1$ with $\Delta x = \frac{\pi}{2N}$ and $\Delta t = 0.1\Delta x$.

where $E = e^{(-d_1-d_2-d_3+r)t}$. The exact solution is

$$u(x,y,z,t) = e^{(-d_1-d_2-d_3+r)t}\sin x \sin y \sin z.$$

As usual, we transform the boundary conditions to be homogeneous, yielding the auxiliary function

$$\begin{aligned} u_B =& E\left[C(x)\sin y\sin z + C(y)\sin x\sin z + C(z)\sin x\sin y\right. \\ &- C(x)C(y)\sin z - C(x)C(z)\sin y - C(y)C(z)\sin x \\ &\left.+C(x)C(y)C(z)\right], \end{aligned}$$

where $C(x) = \frac{-(x-\frac{\pi}{2})^2}{\pi} + \frac{4x^2}{\pi^2}$. We use a uniform mesh with $N_x = N_y = N_z = N$, and set $\Delta x = \pi/2N$ and time step $\Delta t = 0.1\Delta x$. We choose parameters $d_1 = d_2 = d_3 = 1$, $r = -1$,

and $T = 1$. Applying compact hIFE2 to the transformed equation for $\tilde{u} = u - u_B$ with homogeneous boundary conditions, the numerical errors are listed in Table 5.7 for various N. We verify that indeed the method attains second-order temporal error as expected.

$N \times N \times N$	L^∞ error	Order
$4 \times 4 \times 4$	1.33e-03	-
$8 \times 8 \times 8$	3.28e-04	2.02
$16 \times 16 \times 16$	8.17e-05	2.01
$32 \times 32 \times 32$	2.04e-05	2.00
$64 \times 64 \times 64$	5.10e-05	2.00
$128 \times 128 \times 128$	1.27e-06	2.00

Table 5.7: Numerical errors in the maximum norm for hIFE2 applied to the example in Section 5.6.4. The spatial resolution is $\Delta x = \frac{\pi}{2N}$ in all three dimensions, the time step is $\Delta t = 0.1\Delta x$, the ending time is $T = 1$, and the coefficients are $d_1 = d_2 = d_3 = 1$ and $r = -1$.

5.7 The first-order exhibition of IIF2

In Section 5.3, when dealing with explicitly time-dependent reactions, we conclude that IIF2 requires $\Delta t < \mathcal{O}(1/|\alpha|)$ in the scalar equation (5.8) or $\Delta t < \mathcal{O}(\Delta x^2/d)$ in semi-discrete form (5.16) to ensure second-order temporal accuracy, but we did not address the accuracy of IIF2 for Δt above this threshold. In Figures 5.1A and 5.2(A), however, we observe IIF2 exhibits first-order behavior when Δt is large. Motivated by this observation, we attempt to provide an explanation for the first-order behavior in this section.

First, we investigate the scalar equation (5.8), only considering explicitly time-dependent reactions, $f(u,t) = g(t)$, with $g \in C^\infty$ having an upper bound $M > 0$. We consider the global error at time $0 < T < \infty$, with a fixed $\Delta t = T/K$ (so K time steps) and various $\alpha < 0$ satisfying $\Delta t > \mathcal{O}(1/|\alpha|)$.

The one-step iteration of IIF2 at arbitrary time step t_n only depends on the value of u_{n-1} multiplied by an exponential factor $e^{\alpha\Delta t}$. Then since $\Delta t > \mathcal{O}(1/|\alpha|) \implies |\alpha\Delta t| > \mathcal{O}(1) \implies$

$e^{\alpha\Delta t} \ll 1$. Indeed even for $\alpha\Delta t = -100$, $e^{\alpha\Delta t} \approx 10^{-44}$. Then for large $-\alpha$, the approximation u_n becomes essentially independent of previous iterates,

$$u_n = e^{\alpha\Delta t}u_{n-1} + \frac{\Delta t}{2}e^{\alpha\Delta t}g_{n-1} + \frac{\Delta t}{2}g_n \longrightarrow \frac{\Delta t}{2}g_n \quad (\alpha \to -\infty), \tag{5.53}$$

so that, in particular,

$$u_K \to \frac{\Delta t}{2}g_K = \frac{\Delta t}{2}g(T) \quad (\alpha \to -\infty). \tag{5.54}$$

Now the exact solution $u(T)$ can be written in integral form, which we can bound using the assumption $|g(t)| \leq M$:

$$|u(T)| = \left| e^{\alpha T}u(0) + e^{\alpha T}\int_0^T e^{-\alpha t}g(t)\,dt \right| \leq e^{\alpha T}|u(0)| + \left|\frac{e^{\alpha T}-1}{\alpha}\right| M. \tag{5.55}$$

Then as $\alpha \to -\infty$, $|u(T)| \to 0$. Indeed, even for finite but large $-\alpha$, we have $|u(T)| \lesssim M/|\alpha|$. We thus have as a rough estimate of the global error $e(T,K) \triangleq |u(T) - u_K|$ in IIF2 for large $-\alpha$,

$$e(T,K) \lesssim \frac{\Delta t}{2}|g(T)| + \frac{1}{|\alpha|}M. \tag{5.56}$$

Since we are working under the assumption $\Delta t > \mathcal{O}(1/|\alpha|)$, $\frac{1}{|\alpha|} \ll \frac{\Delta t}{2}$, so that we have $e(T,K) = \mathcal{O}(\Delta t)$, first-order temporal error.

The same argument applies to IIF2 on the semi-discrete equation (5.16) with an explicitly time-dependent reaction. As demonstrated in Section 5.3.2, if we apply IIF2 to the diagonal system (5.22) and measure error with the maximum norm, the component that has the largest error is that with the most negative eigenvalue. This then requires $\Delta t < \mathcal{O}(1/|\lambda_N|) = \mathcal{O}(\Delta x^2/d)$ to observe second-order temporal error. Repeating the above procedure with $\Delta t > \mathcal{O}(\Delta x^2/d)$, the error of IIF2 in that component will be first order, causing the overall error to be first order as well.

5.8 Complexity

In this section, we compare the computational cost per iteration of iETD2, IIF2, hIFE2, and fEIF2, showing hIFE2 requires far fewer operations than iETD2 and a number of operations similar to that of the less-costly IIF2 method.

We remind the reader of the form of the iteration in each of the methods below for convenience:

$$\begin{aligned} U_{n+1}^{iETD2} &= e^{A\Delta t}U_n + \frac{I + (-I + A\Delta t)e^{A\Delta t}}{A^2\Delta t}F_n + \frac{(-I - A\Delta t) + e^{A\Delta t}}{A^2\Delta t}F_{n+1} \\ &\triangleq e^{A\Delta t}U_n + \Delta t\Big[L_1(A\Delta t)F_n + L_2(A\Delta t)F_{n+1}\Big], \end{aligned} \tag{5.57}$$

$$U_{n+1}^{IIF2} = e^{A\Delta t}U_n + \frac{\Delta t}{2}\big(e^{A\Delta t}F_n + F_{n+1}\big), \tag{5.58}$$

$$U_{n+1}^{hIFE2} = e^{A\Delta t}U_n + \frac{\Delta t}{2}\big(e^{A\Delta t}(F_1)_n + (F_1)_{n+1}\big) + \Delta t\Big[L_1(A\Delta t)(F_2)_n + L_2(A\Delta t)(F_2)_{n+1}\Big], \tag{5.59}$$

$$U_{n+1}^{fEIF2} = e^{A\Delta t}U_n + \Delta t\Big[L_3(A\Delta t)F_{n-1} + L_4(A\Delta t)F_n + L_1(A\Delta t)B_n + L_2(A\Delta t)B_{n+1}\Big], \tag{5.60}$$

where $F_1(U,t)$ and $F_2(t)$ were defined in (5.6), $L_3(A\Delta t)$ and $L_4(A\Delta t)$ are $N \times N$ matrices of similar form to L_1 and L_2 (i.e., including factors of $e^{A\Delta t}$) whose exact forms are tangential to this discussion but given in full in [76], and B is a vector related to nonhomogeneous boundary conditions that does not depend on U (see Section 5.4 for details). The formation of the exponential-like matrices, $L_i(A\Delta t),\ i = 1, 2, 3, 4$, can be found in Section 5.9. Assuming the exponential-like matrices have already been formed, the two main sources of computational cost are matrix–vector multiplication and solving implicit equations.

At the beginning of each iteration in iETD2, the vectors U_n and F_n are known from the previous iteration, and the matrices $e^{A\Delta t}$, $L_1(A\Delta t)$, and $L_2(A\Delta t)$ are assumed to have already been computed and stored. Then after performing two matrix–vector multiplications,

requiring $\mathcal{O}(2N^2)$ operations, the system takes the form

$$U_{n+1} = \Delta t L_2(A\Delta t)F(U_{n+1}, t_{n+1}) + \text{known} \triangleq \mathcal{F}_1(U_{n+1}).$$

This is a nonlinear system of N equations for the components of U_{n+1} that can be solved, e.g., by Newton's method. During each step of Newton's method, however, the $N \times N$ Jacobian matrix $J_{\mathcal{F}_1}$ of $\mathcal{F}_1$ needs to be inverted, requiring $\mathcal{O}(N^3)$ operations since the matrix L_2 is not in general diagonal. This computation then dominates the cost of the method, pushing it up to $\mathcal{O}(kN^3)$ operations if Newton's method converges in k steps.

In IIF2, the vectors U_n and F_n are known, and we can form the vector $U_n + \frac{\Delta t}{2}F_n$ in just $\mathcal{O}(N)$ operations, so that only one matrix–vector multiplication is required for a total of $\mathcal{O}(N^2)$ operations. Then the system takes the form

$$U_{n+1} = \frac{\Delta t}{2}F(U_{n+1}, t_{n+1}) + \text{known} \triangleq, \mathcal{F}_2(U_{n+1})$$

which is again a nonlinear system. Since $\frac{\Delta t}{2}$ is just a number, though, we can decouple this system into N individual scalar equations, one for each component, eliminating the need to invert the Jacobian so that the total number of computations required to find a solution is reduced to $\mathcal{O}(kN)$ for convergence in k iterations. The initial multiplication then dominates the cost of this method, making its total complexity $\mathcal{O}(N^2)$, an entire order of magnitude smaller than iETD2.

Recall that the hIFE2 method splits $F(U, t)$ into two parts: $F_1(U, t)$ and $F_2(t)$. Since F_2 is only time-dependent, it is easy to calculate at each step, so in addition to the pre-determined vectors U_n, $(F_1)_n$, and $(F_2)_n$, $(F_2)_{n+1}$ can be calculated in $\mathcal{O}(N)$ operations at the beginning of the iteration. Similar to IIF2, we can form the vector $U_n + \frac{\Delta t}{2}(F_1)_n$ in only $\mathcal{O}(N)$ operations, so we only require three matrix–vector multiplications, a total of $\mathcal{O}(3N^2)$ operations. Since only F_2 is treated with iETD2 while F_1 is treated with IIF2, the nonlinear

system obtained after these multiplications takes the same form as IIF2 and so can also be decoupled into N separate scalar equations and solved in $\mathcal{O}(kN)$ operations. Thus, the total complexity of this method is $\mathcal{O}(3N^2)$, slightly more than IIF2 but still an order of magnitude better than iETD2.

Finally, fEIF2 is a completely explicit method, so all vectors are known at the beginning of the iteration, and no nonlinear equations need to be solved. Each term involves a different matrix, and there are five in total, so this method requires $\mathcal{O}(5N^2)$ operations. Even though fEIF2 is an explicit method, the implicit hIFE2 requires fewer operations per iteration due to the ease with which the nonlinear equations are solved.

We summarize the complexity of these four methods in Table 5.8. The iETD2 method has the largest computational complexity of all the examined methods, a full order of magnitude larger than any of the others. The fEIF2 method has a higher computational complexity than hIFE2, and hIFE2 has a higher computational complexity than IIF2, which scores the best among the methods. We conclude that since both hIFE2 and iETD2 were shown to remain second-order accurate in time (Section 5.3) for larger Δt than IIF2, since hIFE2 requires fewer computations per iteration than iETD2, it is the more desirable method, especially for large systems.

	Operations per iteration	Total complexity (ratio)
IIF2	$\mathcal{O}(N^2)$	1
iETD2	$\mathcal{O}(kN^3)$	$\mathcal{O}(kN)$
hIFE2	$\mathcal{O}(3N^2)$	3
fEIF2	$\mathcal{O}(5N^2)$	5

Table 5.8: A comparison of the computational complexity between the IIF2, iETD2, hIFE2, and fEIF2 methods.

5.9 Exponential-like matrices formation

When iETD2, IIF2, and hIFE2 are applied, those matrices involved in an exponential matrix only need to be formed once if the time step Δt is fixed. In our work, the matrix $e^{A\Delta t}$ in (5.3) and (5.5) is approximated by the `expm()` function in MATLAB, and the two exponential-like matrices, $L_1(A\Delta t) = \frac{I+(-I+A\Delta t)e^{A\Delta t}}{A^2\Delta t^2}$ and $L_2(A\Delta t) = \frac{(-I-A\Delta t)+e^{A\Delta t}}{A^2\Delta t^2}$, in the iETD2 iteration (5.4) are obtained via a cutoff of Taylor series [27] to avoid cancellation errors related to inverting the matrix A.

We see that since A is diagonalizable, so are $L_1(A\Delta t)$ and $L_2(A\Delta t)$. We can thus build the matrices by operating on the eigenvalues one by one rather than performing many matrix multiplications. We only need to evaluate $L_1(\lambda\Delta t)$ and $L_2(\lambda\Delta t)$ for arbitrary eigenvalue λ of A. If $|\lambda\Delta t|$ is small, $L_1(\lambda\Delta t)$ and $L_2(\lambda\Delta t)$ are "$\frac{0}{0}$"-type fractions in their analytic forms, we will encounter a large cancellation error. We set a threshold $bd = 10$, where if $|\lambda_j\Delta t| < bd$, we use a cutoff of the Taylor series

$$\begin{aligned} L_1(\lambda\Delta t) &= \sum_{n=0}^{\infty} \frac{1}{(n+2)n!}(\lambda\Delta t)^n \\ L_2(\lambda\Delta t) &= \Delta t \sum_{n=0}^{\infty} \frac{1}{(n+2)!}(\lambda\Delta t)^n \end{aligned} \tag{5.61}$$

up to a chosen tolerance $TOL = 10^{-8}$, and otherwise use the direct expression in the fractional form. We provide the algorithm of $L_1(A\Delta t)$ for an instance, the formation of $L_2(A\Delta t)$ follows the same procedure.

5.10 Conclusions and discussion

IIF and iETD methods are two existing methods designed for dealing with stiffness in reaction–diffusion equations. When solving systems that have explicitly time-dependent

Algorithm 1 Generate $L_1(A\Delta t)$

procedure
  $\Lambda = \text{diag}(\lambda_1, \lambda_2, \ldots, \lambda_N) \leftarrow$ *diagonalization* : $[V, \Lambda] = eig(A)$ where $A = V\Lambda V^{-1}$
  for $j = 1 : N$ **do**
    if $|\lambda_j \Delta t| < bd$ **then**
      $m = 1,\ n = 0,\ \mu_j = 0,$
      while $m < TOL$ **do**
        $m = \frac{1}{(n+2)n!}(\lambda_j \Delta t)^n$ ▷ Use Taylor expansion
        $n \leftarrow n + 1$
        $\mu_j \leftarrow \mu_j + m$
      end while
    else
      $\mu_j = \frac{1+(-1+\lambda_j \Delta t)e^{\lambda_j \Delta t}}{(\lambda_j \Delta t)^2}$ ▷ Direct implementation
    end if
  end for
  $L_1(A\Delta t) \leftarrow V\text{diag}(\mu_1, \mu_2, \ldots, \mu_N)V^{-1}$
end procedure

reactions, these two methods behave differently in accuracy and efficiency. In particular, IIF2 requires extremely small time steps to exhibit the theoretical second-order temporal accuracy in practice, whereas the iETD2 method maintains the second order with relatively large time steps. On the other hand, the IIF2 method has the advantage of being more efficient than iETD2 when solving systems with nonlinear reactions owing to the lower computational cost per time step. The hybrid (hIFE) method intends to take advantage of the strength in both methods. In hIFE method, the key step is to split the reaction term into two parts by using (5.6), and to treat F_1 by IIF and F_2 by iETD. For complicated reactions, as long as the condition $F_1|_{t=0} = 0$ is held (i.e. a more general form than autonomous), the hIFE method exhibits theoretical order of accuracy with large time step sizes compared to spatial grid size. We have applied this hybrid method to reaction–diffusion systems containing explicitly time-dependent reactions, as well as systems with nonhomogeneous boundary conditions through a transformation. To reduce the cost associated with both the storage and computation of large matrices in high dimensions, we have incorporated the compact representation previously developed for IIF and ETD methods into the high-dimensional hIFE method. Based on various numerical simulations and comparisons with other schemes,

the hIFE method is found to be more advantageous with respect to stability, efficiency, and accuracy in solving reaction–diffusion systems with more complicated reactions or nonhomogeneous boundary conditions. The stability and restriction on the time step Δt to exhibit second order for all methods presented in this work are provided in Table 5.9.

Method	A-stability	Δt to exhibit second-order accuracy	
		Time-dependent reactions	Nonhomogeneous BCs
IIF2	Yes	$\mathcal{O}(\Delta x^2)$	$\leq \mathcal{O}(\Delta x^2)$
iETD2	Yes	$\mathcal{O}(1)$	-
fEIF2	No	$\mathcal{O}(1)$	$\mathcal{O}(1)$
hIFE2	Yes	$\mathcal{O}(1)$	$< \mathcal{O}(1)$
hIFE2 (transformed)	Yes	$\mathcal{O}(1)$	$\mathcal{O}(1)$

Table 5.9: A summary of the four methods: for their A-stability, and the restriction on Δt to exhibit second order, with explicitly time-dependent reactions or nonhomogeneous boundary conditions.

The computational complexity (Section 5.8) of our method is based on a simple implementation in this work. There are other techniques to reduce the computational cost. For example, the discrete fast Fourier transformation [164, 179, 76] and Krylov method [145, 21, 73, 74, 101] are two effective ways to reduce the computational cost for matrix-vector multiplications. While the Newton's method has been used to solve the nonlinear equations in hIFE, the fixed–point method could be used to reduce the cost in each iteration whereas the number of iterations may increase. Because IIF2 and hIFE2 do not involve solving large nonlinear systems, its associated cost for the Newton's methods is significantly lower than the iETD2 method [120]. Together, hIFE2 will cost less computationally than iETD2 but slightly more than IIF2, as long as similar matrix-vector multiplication techniques and nonlinear solvers are used.

In high dimensions, the current compact hIFE method can only deal with systems on fixed rectangular domains and equally distributed meshes in spatial discretization. For more complicated geometry or unstructured meshes, hIFE method needs to be further improved, potentially coupled with Krylov method [21, 101], to reduce the computational cost. For

systems in higher dimension (> 3), other techniques, such as the sparse grid technique, can be incorporated into this hybrid scheme to further improve the efficiency. In addition, the hybrid approach can potentially be applied to convection–reaction–diffusion equations with explicitly time-dependent reactions, nonhomogeneous boundary conditions or domains moving with time. It will be also interesting to generalize this hybrid method to reaction–diffusion equations with anisotropic diffusion or to PDEs with high-order spatial differential operators, such as Cahn–Hilliard equations with dynamic boundary conditions.

Bibliography

[1] M. Acar, J. T. Mettetal, and A. Van Oudenaarden. Stochastic switching as a survival strategy in fluctuating environments. *Nature Genetics*, 40(4):471, 2008.

[2] M. Addison, Q. Xu, J. Cayuso, and D. G. Wilkinson. Cell identity switching regulated by retinoic acid signaling maintains homogeneous segments in the hindbrain. *Developmental Cell*, 45(5):606–620, 2018.

[3] M. Affolter and K. Basler. The decapentaplegic morphogen gradient: from pattern formation to growth regulation. *Nature Reviews Genetics*, 8(9):663–674, 2007.

[4] T. Akiyama, K. Kamimura, C. Firkus, S. Takeo, O. Shimmi, and H. Nakato. Dally regulates Dpp morphogen gradient formation by stabilizing Dpp on the cell surface. *Developmental Biology*, 313(1):408–419, 2008.

[5] T. Alexander, C. Nolte, and R. Krumlauf. Hox genes and segmentation of the hindbrain and axial skeleton. *Annual Review of Cell and Developmental*, 25:431–456, 2009.

[6] D. Alonso, F. Bartumeus, and J. Catalan. Mutual interference between predators can give rise to Turing spatial patterns. *Ecology*, 83(1):28–34, 2002.

[7] D. Austin, M. Allen, J. McCollum, R. Dar, J. Wilgus, G. Sayler, N. Samatova, C. Cox, and M. Simpson. Gene network shaping of inherent noise spectra. *Nature*, 439(7076):608–611, 2006.

[8] S. V. Avery. Microbial cell individuality and the underlying sources of heterogeneity. *Nature Reviews Microbiology*, 4(8):577–587, 2006.

[9] N. Balaskas, A. Ribeiro, J. Panovska, E. Dessaud, N. Sasai, K. M. Page, J. Briscoe, and V. Ribes. Gene regulatory logic for reading the sonic hedgehog signaling gradient in the vertebrate neural tube. *Cell*, 148(1-2):273–284, 2012.

[10] A. Becskei and L. Serrano. Engineering stability in gene networks by autoregulation. *Nature*, 405(6786):590–593, 2000.

[11] D. Ben-Zvi and N. Barkai. Scaling of morphogen gradients by an expansion-repression integral feedback control. *Proceedings of the National Academy of Sciences*, 107(15):6924–6929, 2010.

[12] D. Ben-Zvi, G. Pyrowolakis, N. Barkai, and B.-Z. Shilo. Expansion-repression mechanism for scaling the Dpp activation gradient in *Drosophila* wing imaginal discs. *Current Biology*, 21(16):1391–1396, 2011.

[13] D. Ben-Zvi, B.-Z. Shilo, and N. Barkai. Scaling of morphogen gradients. *Current Opinion in Genetics & Development*, 21(6):704–710, 2011.

[14] D. Ben-Zvi, B.-Z. Shilo, A. Fainsod, and N. Barkai. Scaling of the BMP activation gradient in Xenopus embryos. *Nature*, 453(7199):1205–1211, 2008.

[15] T. L. Bergman, F. P. Incropera, D. P. DeWitt, and A. S. Lavine. *Fundamentals of heat and mass transfer*. John Wiley & Sons, 2011.

[16] G. Beylkin, J. M. Keiser, and L. Vozovoi. A new class of time discretization schemes for the solution of nonlinear PDEs. *Journal of Computational Physics*, 147(2):362–387, 1998.

[17] W. J. Blake, G. Balázsi, M. A. Kohanski, F. J. Isaacs, K. F. Murphy, Y. Kuang, C. R. Cantor, D. R. Walt, and J. J. Collins. Phenotypic consequences of promoter-mediated transcriptional noise. *Molecular Cell*, 24(6):853–865, 2006.

[18] T. Borovski, E. M. Felipe De Sousa, L. Vermeulen, and J. P. Medema. Cancer stem cell niche: the place to be. *Cancer Research*, 71(3):634–639, 2011.

[19] Y. X. Bouchoucha, J. Reingruber, C. Labalette, M. A. Wassef, E. Thierion, C. D.-T. Dinh, D. Holcman, P. Gilardi-Hebenstreit, and P. Charnay. Dissection of a Krox20 positive feedback loop driving cell fate choices in hindbrain patterning. *Molecular Systems Biology*, 9(1), 2013.

[20] K. M. Cadigan, M. P. Fish, E. J. Rulifson, and R. Nusse. Wingless repression of *Drosophila* frizzled 2 expression shapes the wingless morphogen gradient in the wing. *Cell*, 93(5):767–777, 1998.

[21] S. Chen and Y.-T. Zhang. Krylov implicit integration factor methods for spatial discretization on high dimensional unstructured meshes: application to discontinuous Galerkin methods. *Journal of Computational Physics*, 230(11):4336–4352, 2011.

[22] D. Cheung, C. Miles, M. Kreitman, and J. Ma. Scaling of the bicoid morphogen gradient by a volume-dependent production rate. *Development*, 138(13):2741–2749, 2011.

[23] S.-K. Choe, X. Zhang, N. Hirsch, J. Straubhaar, and C. G. Sagerström. A screen for hoxb1-regulated genes identifies ppp1r14al as a regulator of the rhombomere 4 Fgf-signaling center. *Developmental Biology*, 358(2):356–367, 2011.

[24] C.-S. Chou, W.-C. Lo, K. K. Gokoffski, Y.-T. Zhang, F. Y. Wan, A. D. Lander, A. L. Calof, and Q. Nie. Spatial dynamics of multistage cell lineages in tissue stratification. *Biophysical Journal*, 99(10):3145–3154, 2010.

[25] J. Cooke. Scale of body pattern adjusts to available cell number in amphibian embryos. *Nature*, 290(5809):775–778, 1981.

[26] J. E. Cooke, H. A. Kemp, and C. B. Moens. Epha4 is required for cell adhesion and rhombomere-boundary formation in the zebrafish. *Current Biology*, 15(6):536–542, 2005.

[27] S. M. Cox and P. C. Matthews. Exponential time differencing for stiff systems. *Journal of Computational Physics*, 176(2):430–455, 2002.

[28] P. D. Dale, J. A. Sherratt, and P. K. Maini. Role of fibroblast migration in collagen fiber formation during fetal and adult dermal wound healing. *Bulletin of Mathematical Biology*, 59(6):1077–1100, 1997.

[29] E. M. De Robertis. Spemann's organizer and self-regulation in amphibian embryos. *Nature Reviews Molecular Cell Biology*, 7(4):296–302, 2006.

[30] D. del Álamo Rodrıguez, J. T. Felix, and F. J. Dıaz-Benjumea. The role of the t-box gene optomotor-blind in patterning the *Drosophila* wing. *Developmental Biology*, 268(2):481–492, 2004.

[31] E. Dessaud, L. L. Yang, K. Hill, B. Cox, F. Ulloa, A. Ribeiro, A. Mynett, B. G. Novitch, and J. Briscoe. Interpretation of the sonic hedgehog morphogen gradient by a temporal adaptation mechanism. *Nature*, 450(7170):717–720, 2007.

[32] F. Doetsch. A niche for adult neural stem cells. *Current Opinion in Genetics & Development*, 13(5):543–550, 2003.

[33] C. J. Dowd, C. L. Cooney, and M. A. Nugent. Heparan sulfate mediates bFGF transport through basement membrane by diffusion with rapid reversible binding. *Journal of Biological Chemistry*, 274(8):5236–5244, 1999.

[34] H. Driesch. Entwicklungsmechanische studien i-ii. *Z. wiss. Zool.*, 53:160–184, 1891.

[35] H. Du, Y. Wang, D. Haensel, B. Lee, X. Dai, and Q. Nie. Multiscale modeling of layer formation in epidermis. *PLoS Computational Biology*, 14(2):e1006006, 2018.

[36] Q. Du and W. Zhu. Stability analysis and application of the exponential time differencing schemes. *Journal of Computational Mathematics*, pages 200–209, 2004.

[37] Q. Du and W. Zhu. Analysis and applications of the exponential time differencing schemes and their contour integration modifications. *BIT Numerical Mathematics*, 45(2):307–328, 2005.

[38] A. D. Economou, A. Ohazama, T. Porntaveetus, P. T. Sharpe, S. Kondo, M. A. Basson, A. Gritli-Linde, M. T. Cobourne, and J. B. Green. Periodic stripe formation by a Turing mechanism operating at growth zones in the mammalian palate. *Nature Genetics*, 44(3):348, 2012.

[39] A. Eldar, R. Dorfman, D. Weiss, H. Ashe, B.-Z. Shilo, and N. Barkai. Robustness of the BMP morphogen gradient in *Drosophila* embryonic patterning. *Nature*, 419(6904):304–308, 2002.

[40] A. Eldar, D. Rosin, B.-Z. Shilo, and N. Barkai. Self-enhanced ligand degradation underlies robustness of morphogen gradients. *Developmental Cell*, 5(4):635–646, 2003.

[41] M. B. Elowitz, A. J. Levine, E. D. Siggia, and P. S. Swain. Stochastic gene expression in a single cell. *Science*, 297(5584):1183–1186, 2002.

[42] E. V. Entchev, A. Schwabedissen, and M. González-Gaitán. Gradient formation of the TGF-β homolog Dpp. *Cell*, 103(6):981–992, 2000.

[43] P. Fried and D. Iber. Dynamic scaling of morphogen gradients on growing domains. *Nature Communications*, 5(1):1–12, 2014.

[44] M. Fujise, S. Izumi, S. B. Selleck, and H. Nakato. Regulation of dally, an integral membrane proteoglycan, and its function during adult sensory organ formation of *Drosophila*. *Developmental Biology*, 235(2):433–448, 2001.

[45] M. Fujise, S. Takeo, K. Kamimura, T. Matsuo, T. Aigaki, S. Izumi, and H. Nakato. Dally regulates Dpp morphogen gradient formation in the *Drosophila* wing. *Development*, 130(8):1515–1522, 2003.

[46] E. Gallopoulos and Y. Saad. Efficient solution of parabolic equations by Krylov approximation methods. *SIAM Journal on Scientific and Statistical Computing*, 13(5):1236–1264, 1992.

[47] L. Gammaitoni, P. Hänggi, P. Jung, and F. Marchesoni. Stochastic resonance. *Reviews of Modern Physics*, 70(1):223, 1998.

[48] M. Garvie and C. Trenchea. Analysis of two generic spatially extended predator-prey models. *Nonlinear Anal. Real World Appl.*, 2005.

[49] M. R. Garvie. Finite-difference schemes for reaction–diffusion equations modeling predator–prey interactions in MATLAB. *Bulletin of Mathematical Biology*, 69(3):931–956, 2007.

[50] H. Ge, H. Qian, and X. S. Xie. Stochastic phenotype transition of a single cell in an intermediate region of gene state switching. *Physical Review Letters*, 114(7):078101, 2015.

[51] M. C. Gibson and N. Perrimon. Extrusion and death of DPP/BMP-compromised epithelial cells in the developing *Drosophila* wing. *Science*, 307(5716):1785–1789, 2005.

[52] A. Gierer and H. Meinhardt. A theory of biological pattern formation. *Biological Cybernetics*, 12(1):30–39, 1972.

[53] T. Gregor, W. Bialek, R. R. D. R. Van Steveninck, D. W. Tank, and E. F. Wieschaus. Diffusion and scaling during early embryonic pattern formation. *Proceedings of the National Academy of Sciences*, 102(51):18403–18407, 2005.

[54] T. Gregor, E. F. Wieschaus, A. P. McGregor, W. Bialek, and D. W. Tank. Stability and nuclear dynamics of the bicoid morphogen gradient. *Cell*, 130(1):141–152, 2007.

[55] F. Hamaratoglu, A. M. de Lachapelle, G. Pyrowolakis, S. Bergmann, and M. Affolter. Dpp signaling activity requires pentagone to scale with tissue size in the growing *Drosophila* wing imaginal disc. *PLoS Biology*, 9(10), 2011.

[56] S. Harmansa, I. Alborelli, D. Bieli, E. Caussinus, and M. Affolter. A nanobody-based toolset to investigate the role of protein localization and dispersal in *Drosophila*. *Elife*, 6:e22549, 2017.

[57] J. Hasty, J. Pradines, M. Dolnik, and J. J. Collins. Noise-based switches and amplifiers for gene expression. *Proceedings of the National Academy of Sciences*, 97(5):2075–2080, 2000.

[58] R. E. Hernandez, H. A. Rikhof, R. Bachmann, and C. B. Moens. vhnf1 integrates global RA patterning and local FGF signals to direct posterior hindbrain development in zebrafish. *Development*, 131(18):4511–4520, 2004.

[59] M. Hochbruck and C. Lubich. On Krylov subspace approximations to the matrix exponential operator. *SIAM Journal on Numerical Analysis*, 34(5):1911–1925, 1997.

[60] M. Hochbruck and A. Ostermann. Explicit exponential Runge–Kutta methods for semilinear parabolic problems. *SIAM Journal on Numerical Analysis*, 43(3):1069–1090, 2005.

[61] M. Hochbruck and A. Ostermann. Exponential Runge–Kutta methods for parabolic problems. *Applied Numerical Mathematics*, 53(2):323–339, 2005.

[62] M. Hochbruck and A. Ostermann. Exponential integrators. *Acta Numerica*, 19:209–286, 2010.

[63] E. E. Holmes, M. A. Lewis, J. Banks, and R. Veit. Partial differential equations in ecology: spatial interactions and population dynamics. *Ecology*, 75(1):17–29, 1994.

[64] Y. Huang and D. M. Umulis. Scale invariance of BMP signaling gradients in zebrafish. *Scientific Reports*, 9(1):1–9, 2019.

[65] D. Huh and J. Paulsson. Non-genetic heterogeneity from stochastic partitioning at cell division. *Nature Genetics*, 43(2):95, 2011.

[66] H. Inomata. Scaling of pattern formations and morphogen gradients. *Development, Growth & Differentiation*, 59(1):41–51, 2017.

[67] E. Isaacson and H. B. Keller. *Analysis of numerical methods*. Courier Corporation, 1994.

[68] K. Ishimatsu, T. W. Hiscock, Z. M. Collins, D. W. K. Sari, K. Lischer, D. L. Richmond, Y. Bessho, T. Matsui, and S. G. Megason. Size-reduced embryos reveal a gradient scaling-based mechanism for zebrafish somite formation. *Development*, 145(11):dev161257, 2018.

[69] S. Jackson, H. Nakato, M. Sugiura, A. Jannuzi, R. Oakes, V. Kaluza, C. Golden, and S. Selleck. division abnormally delayed, a *Drosophila* glypican, controls cellular responses to the TGF-ß-related morphogen, Dpp. *Development*, 124:4113–4120, 1997.

[70] J. Jaeger. Modelling the drosophila embryo. *Molecular BioSystems*, 5(12):1549–1568, 2009.

[71] J. Jaeger, S. Surkova, M. Blagov, H. Janssens, D. Kosman, K. N. Kozlov, E. Myasnikova, C. E. Vanario-Alonso, M. Samsonova, D. H. Sharp, et al. Dynamic control of positional information in the early *Drosophila* embryo. *Nature*, 430(6997):368–371, 2004.

[72] A. Jentzen and P. E. Kloeden. *Taylor approximations for stochastic partial differential equations*, volume 83. SIAM, 2011.

[73] T. Jiang and Y.-T. Zhang. Krylov implicit integration factor WENO methods for semilinear and fully nonlinear advection–diffusion–reaction equations. *Journal of Computational Physics*, 253:368–388, 2013.

[74] T. Jiang and Y.-T. Zhang. Krylov single-step implicit integration factor WENO methods for advection–diffusion–reaction equations. *Journal of Computational Physics*, 311:22–44, 2016.

[75] L. Ju, X. Liu, and W. Leng. Compact implicit integration factor methods for a family of semilinear fourth-order parabolic equations. *Discrete & Continuous Dynamical Systems-Series B*, 19(6), 2014.

[76] L. Ju, J. Zhang, L. Zhu, and Q. Du. Fast explicit integration factor methods for semilinear parabolic equations. *Journal of Scientific Computing*, 62(2):431–455, 2015.

[77] M. Kaern, T. C. Elston, W. J. Blake, and J. J. Collins. Stochasticity in gene expression: from theories to phenotypes. *Nature Reviews Genetics*, 6(6):451–464, 2005.

[78] T. Kähkönen, K. Ivaska, M. Jiang, K. Büki, H. Väänänen, and P. Härkönen. Role of fibroblast growth factor receptors (FGFR) and FGFR like-1 (FGFRL1) in mesenchymal stromal cell differentiation to osteoblasts and adipocytes. *Molecular and Cellular Endocrinology*, 461:194–204, 2018.

[79] A.-K. Kassam and L. N. Trefethen. Fourth-order time-stepping for stiff PDEs. *SIAM Journal on Scientific Computing*, 26(4):1214–1233, 2005.

[80] A. Kicheva, P. Pantazis, T. Bollenbach, Y. Kalaidzidis, T. Bittig, F. Jülicher, and M. Gonzalez-Gaitan. Kinetics of morphogen gradient formation. *Science*, 315(5811):521–525, 2007.

[81] D. C. Kirouac, G. J. Madlambayan, M. Yu, E. A. Sykes, C. Ito, and P. W. Zandstra. Cell–cell interaction networks regulate blood stem and progenitor cell fate. *Molecular Systems Biology*, 5(1), 2009.

[82] P. E. Kloeden and E. Platen. Numerical solution of stochastic differential equations.

[83] W.-J. Kuo, M. A. Digman, and A. D. Lander. Heparan sulfate acts as a bone morphogenetic protein coreceptor by facilitating ligand-induced receptor hetero-oligomerization. *Molecular Biology of the Cell*, 21(22):4028–4041, 2010.

[84] C. Labalette, M. A. Wassef, C. D.-T. Dinh, Y. X. Bouchoucha, J. Le Men, P. Charnay, and P. Gilardi-Hebenstreit. Molecular dissection of segment formation in the developing hindbrain. *Development*, 142(1):185–195, 2015.

[85] J. D. Lambert. *Numerical methods for ordinary differential systems: the initial value problem*. John Wiley & Sons, Inc., 1991.

[86] A. Lander, Q. Nie, B. Vargas, and F. Wan. Size-normalized robustness of Dpp gradient in *Drosophila* wing imaginal disc. *Journal of Mechanics of Materials and Structures*, 6(1):321–350, 2011.

[87] A. D. Lander. Pattern, growth, and control. *Cell*, 144(6):955–969, 2011.

[88] A. D. Lander, K. K. Gokoffski, F. Y. Wan, Q. Nie, and A. L. Calof. Cell lineages and the logic of proliferative control. *PLoS Biology*, 7(1), 2009.

[89] A. D. Lander, J. Kimble, H. Clevers, E. Fuchs, D. Montarras, M. Buckingham, A. L. Calof, A. Trumpp, and T. Oskarsson. What does the concept of the stem cell niche really mean today? *BMC Biology*, 10(1):19, 2012.

[90] A. D. Lander, W.-C. Lo, Q. Nie, and F. Y. Wan. The measure of success: constraints, objectives, and tradeoffs in morphogen-mediated patterning. *Cold Spring Harbor Perspectives in Biology*, 1(1):a002022, 2009.

[91] A. D. Lander, Q. Nie, and F. Y. Wan. Do morphogen gradients arise by diffusion? *Developmental Cell*, 2(6):785–796, 2002.

[92] S. Larsson and V. Thomée. *Partial differential equations with numerical methods*, volume 45. Springer Science & Business Media, 2008.

[93] V. Lecaudey, I. Anselme, F. Rosa, and S. Schneider-Maunoury. The zebrafish Iroquois gene iro7 positions the r4/r5 boundary and controls neurogenesis in the rostral hindbrain. *Development*, 131(13):3121–3131, 2004.

[94] T. Lecuit and S. M. Cohen. Dpp receptor levels contribute to shaping the Dpp morphogen gradient in the *Drosophila* wing imaginal disc. *Development*, 125(24):4901–4907, 1998.

[95] A. Li, S. Figueroa, T.-X. Jiang, P. Wu, R. Widelitz, Q. Nie, and C.-M. Chuong. Diverse feather shape evolution enabled by coupling anisotropic signalling modules with self-organizing branching programme. *Nature Communications*, 8(1):1–13, 2017.

[96] L. Li and T. Xie. Stem cell niche: structure and function. *Annu. Rev. Cell Dev. Biol.*, 21:605–631, 2005.

[97] C.-M. Lin, T. X. Jiang, R. E. Baker, P. K. Maini, R. B. Widelitz, and C.-M. Chuong. Spots and stripes: pleomorphic patterning of stem cells via p-ERK-dependent cell chemotaxis shown by feather morphogenesis and mathematical simulation. *Developmental Biology*, 334(2):369–382, 2009.

[98] X. Liu and Q. Nie. Compact integration factor methods for complex domains and adaptive mesh refinement. *Journal of Computational Physics*, 229(16):5692–5706, 2010.

[99] W.-C. Lo, C.-S. Chou, K. K. Gokoffski, F. Y.-M. Wan, A. D. Lander, A. L. Calof, and Q. Nie. Feedback regulation in multistage cell lineages. *Mathematical Biosciences and Engineering: MBE*, 6(1):59, 2009.

[100] D. Lu and Y.-T. Zhang. Krylov integration factor method on sparse grids for high spatial dimension convection–diffusion equations. *Journal of Scientific Computing*, 69(2):736–763, 2016.

[101] D. Lu and Y.-T. Zhang. Computational complexity study on Krylov integration factor WENO method for high spatial dimension convection–diffusion problems. *Journal of Scientific Computing*, 73(2-3):980–1027, 2017.

[102] F. Luciani, D. Champeval, A. Herbette, L. Denat, B. Aylaj, S. Martinozzi, R. Ballotti, R. Kemler, C. R. Goding, F. De Vuyst, et al. Biological and mathematical modeling of melanocyte development. *Development*, 138(18):3943–3954, 2011.

[103] A. Lumsden and R. Krumlauf. Patterning the vertebrate neuraxis. *Science*, 274(5290):1109–1115, 1996.

[104] M. Machen and Y.-T. Zhang. Krylov implicit integration factor methods for semilinear fourth-order equations. *Mathematics*, 5(4):63, 2017.

[105] A. Marciniak-Czochra, T. Stiehl, A. D. Ho, W. Jäger, and W. Wagner. Modeling of asymmetric cell division in hematopoietic stem cellsregulation of self-renewal is essential for efficient repopulation. *Stem Cells and Development*, 18(3):377–386, 2009.

[106] C. Martín-Castellanos and B. A. Edgar. A characterization of the effects of Dpp signaling on cell growth and proliferation in the *Drosophila* wing. *Development*, 129(4):1003–1013, 2002.

[107] L. Maves, W. Jackman, and C. B. Kimmel. FGF3 and FGF8 mediate a rhombomere 4 signaling activity in the zebrafish hindbrain. *Development*, 129(16):3825–3837, 2002.

[108] L. Maves and C. B. Kimmel. Dynamic and sequential patterning of the zebrafish posterior hindbrain by retinoic acid. *Developmental Biology*, 285(2):593–605, 2005.

[109] H. H. McAdams and A. Arkin. Stochastic mechanisms in gene expression. *Proceedings of the National Academy of Sciences*, 94(3):814–819, 1997.

[110] S. McCroskery, M. Thomas, L. Maxwell, M. Sharma, and R. Kambadur. Myostatin negatively regulates satellite cell activation and self-renewal. *The Journal of Cell Biology*, 162(6):1135–1147, 2003.

[111] M. D. McDonnell and D. Abbott. What is stochastic resonance? Definitions, misconceptions, debates, and its relevance to biology. *PLoS Computational Biology*, 5(5), 2009.

[112] L. Meinecke, P. P. Sharma, H. Du, L. Zhang, Q. Nie, and T. F. Schilling. Modeling craniofacial development reveals spatiotemporal constraints on robust patterning of the mandibular arch. *PLoS Computational Biology*, 14(11), 2018.

[113] R. E. Mickens. Nonstandard finite difference schemes for reaction-diffusion equations. *Numerical Methods for Partial Differential Equations*, 15(2):201–214, 1999.

[114] F. L. Moolten and N. L. Bucher. Regeneration of rat liver: transfer of humoral agent by cross circulation. *Science*, 158(3798):272–274, 1967.

[115] K. A. Moore and I. R. Lemischka. Stem cells and their niches. *Science*, 311(5769):1880–1885, 2006.

[116] M. Nahmad and A. Stathopoulos. Dynamic interpretation of hedgehog signaling in the *Drosophila* wing disc. *PLoS Biology*, 7(9), 2009.

[117] T. J. Newman. Modeling multi-cellular systems using sub-cellular elements. *arXiv preprint q-bio/0504028*, 2005.

[118] Q. Nie, L. Qiao, Y. Qiu, L. Zhang, and W. Zhao. Noise control and utility: From regulatory network to spatial patterning. *Science China Mathematics*, pages 1–16, 2020.

[119] Q. Nie, F. Y. Wan, Y.-T. Zhang, and X. Liu. Compact integration factor methods in high spatial dimensions. *Journal of Computational Physics*, 227(10):5238–5255, 2008.

[120] Q. Nie, Y.-T. Zhang, and R. Zhao. Efficient semi-implicit schemes for stiff systems. *Journal of Computational Physics*, 214(2):521–537, 2006.

[121] M. Norman, R. Vuilleumier, A. Springhorn, J. Gawlik, and G. Pyrowolakis. Pentagone internalises glypicans to fine-tune multiple signalling pathways. *Elife*, 5:e13301, 2016.

[122] Y. Ogiso, K. Tsuneizumi, N. Masuda, M. Sato, and T. Tabata. Robustness of the Dpp morphogen activity gradient depends on negative feedback regulation by the inhibitory Smad, Dad. *Development, Growth & Differentiation*, 53(5):668–678, 2011.

[123] M. M. Oliveira, A. W. Shingleton, and C. K. Mirth. Coordination of wing and whole-body development at developmental milestones ensures robustness against environmental and physiological perturbations. *PLoS Genetics*, 10(6), 2014.

[124] J. Ovadia and Q. Nie. Stem cell niche structure as an inherent cause of undulating epithelial morphologies. *Biophysical Journal*, 104(1):237–246, 2013.

[125] J. Ovadia and Q. Nie. Numerical methods for two-dimensional stem cell tissue growth. *Journal of Scientific Computing*, 58(1):149–175, 2014.

[126] H. J. Parker and R. Krumlauf. Segmental arithmetic: summing up the hox gene regulatory network for hindbrain development in chordates. *Wiley Interdisciplinary Reviews: Developmental Biology*, 6(6):e286, 2017.

[127] R. Perez-Carrasco, P. Guerrero, J. Briscoe, and K. M. Page. Intrinsic noise profoundly alters the dynamics and steady state of morphogen-controlled bistable genetic switches. *PLoS Computational Biology*, 12(10), 2016.

[128] S. V. Petrovskii and H. Malchow. A minimal model of pattern formation in a prey-predator system. *Mathematical and Computer Modelling*, 29(8):49–63, 1999.

[129] S. V. Petrovskii and H. Malchow. Wave of chaos: new mechanism of pattern formation in spatio-temporal population dynamics. *Theoretical Population Biology*, 59(2):157–174, 2001.

[130] M. E. Pitulescu and R. H. Adams. Eph/ephrin molecules—A hub for signaling and endocytosis. *Genes & Development*, 24(22):2480–2492, 2010.

[131] L. Qiao, W. Zhao, C. Tang, Q. Nie, and L. Zhang. Network topologies that can achieve dual function of adaptation and noise attenuation. *Cell Systems*, 9(3):271–285, 2019.

[132] Y. Qiu, W. Chen, and Q. Nie. A hybrid method for stiff reaction–diffusion equations. *Discrete & Continuous Dynamical Systems-B*, 24(12):6387, 2019.

[133] Y. Qiu, W. Chen, and Q. Nie. Stochastic dynamics of cell lineage in tissue homeostasis. *Discrete & Continuous Dynamical Systems-B*, 24(8):3971, 2019.

[134] C. Rackauckas, T. Schilling, and Q. Nie. Mean-independent noise control of cell fates via intermediate states. *iScience*, 3:11–20, 2018.

[135] C. V. Rao, D. M. Wolf, and A. P. Arkin. Control, exploitation and tolerance of intracellular noise. *Nature*, 420(6912):231–237, 2002.

[136] J. Raspopovic, L. Marcon, L. Russo, and J. Sharpe. Digit patterning is controlled by a Bmp-Sox9-Wnt Turing network modulated by morphogen gradients. *Science*, 345(6196):566–570, 2014.

[137] M. Rhinn and P. Dollé. Retinoic acid signalling during development. *Development*, 139(5):843–858, 2012.

[138] H. Risken. The Fokker-Planck equation. Methods of Solution and Applications, vol. 18 of. *Springer Series in Synergetics*, 1989.

[139] K. W. Rogers and A. F. Schier. Morphogen gradients: from generation to interpretation. *Annual Review of Cell and Developmental Biology*, 27:377–407, 2011.

[140] P. Rørth. Fellow travellers: emergent properties of collective cell migration. *EMBO Reports*, 13(11):984–991, 2012.

[141] T. Ruiz-Herrero, K. Alessandri, B. V. Gurchenkov, P. Nassoy, and L. Mahadevan. Organ size control via hydraulically gated oscillations. *Development*, 144(23):4422–4427, 2017.

[142] Y. Saad. Analysis of some Krylov subspace approximations to the matrix exponential operator. *SIAM Journal on Numerical Analysis*, 29(1):209–228, 1992.

[143] T. F. Schilling, Q. Nie, and A. D. Lander. Dynamics and precision in retinoic acid morphogen gradients. *Current Opinion in Genetics & Development*, 22(6):562–569, 2012.

[144] T. F. Schilling, V. Prince, and P. W. Ingham. Plasticity in zebrafish hox expression in the hindbrain and cranial neural crest. *Developmental Biology*, 231(1):201–216, 2001.

[145] J. C. Schulze, P. J. Schmid, and J. L. Sesterhenn. Exponential time integration using Krylov subspaces. *International Journal for Numerical Methods in Fluids*, 60(6):591–609, 2009.

[146] L. J. Schumacher, P. M. Kulesa, R. McLennan, R. E. Baker, and P. K. Maini. Multidisciplinary approaches to understanding collective cell migration in developmental biology. *Open Biology*, 6(6):160056, 2016.

[147] L. Setiawan, X. Pan, A. L. Woods, M. B. O'Connor, and I. K. Hariharan. The BMP2/4 ortholog Dpp can function as an inter-organ signal that regulates developmental timing. *Life Science Alliance*, 1(6), 2018.

[148] B.-Z. Shilo, M. Haskel-Ittah, D. Ben-Zvi, E. D. Schejter, and N. Barkai. Creating gradients by morphogen shuttling. *Trends in Genetics*, 29(6):339–347, 2013.

[149] M. L. Simpson, C. D. Cox, M. S. Allen, J. M. McCollum, R. D. Dar, D. K. Karig, and J. F. Cooke. Noise in biological circuits. *Wiley Interdisciplinary Reviews: Nanomedicine and Nanobiotechnology*, 1(2):214–225, 2009.

[150] T. R. Sokolowski, T. Erdmann, and P. R. Ten Wolde. Mutual repression enhances the steepness and precision of gene expression boundaries. *PLoS Computational Biology*, 8(8), 2012.

[151] J. Sosnik, L. Zheng, C. V. Rackauckas, M. Digman, E. Gratton, Q. Nie, and T. F. Schilling. Noise modulation in retinoic acid signaling sharpens segmental boundaries of gene expression in the embryonic zebrafish hindbrain. *Elife*, 5:e14034, 2016.

[152] C. L. Stokes, D. A. Lauffenburger, and S. K. Williams. Migration of individual microvessel endothelial cells: stochastic model and parameter measurement. *Journal of Cell Science*, 99(2):419–430, 1991.

[153] C. Ta, D. Wang, and Q. Nie. An integration factor method for stochastic and stiff reaction–diffusion systems. *Journal of Computational Physics*, 295:505–522, 2015.

[154] M. Tada and C.-P. Heisenberg. Convergent extension: using collective cell migration and cell intercalation to shape embryos. *Development*, 139(21):3897–3904, 2012.

[155] B. Tang. Orthogonal array-based latin hypercubes. *Journal of the American Statistical Association*, 88(424):1392–1397, 1993.

[156] H. Tanimoto, S. Itoh, P. ten Dijke, and T. Tabata. Hedgehog creates a gradient of Dpp activity in *Drosophila* wing imaginal discs. *Molecular Cell*, 5(1):59–71, 2000.

[157] A. A. Teleman and S. M. Cohen. Dpp gradient formation in the *Drosophila* wing imaginal disc. *Cell*, 103(6):971–980, 2000.

[158] M. Thattai and A. Van Oudenaarden. Stochastic gene expression in fluctuating environments. *Genetics*, 167(1):523–530, 2004.

[159] J. W. Thomas. *Numerical partial differential equations: finite difference methods*, volume 22. Springer Science & Business Media, 2013.

[160] M. Towers and C. Tickle. Growing models of vertebrate limb development. *Development*, 136(2):179–190, 2009.

[161] T. Tumbar, G. Guasch, V. Greco, C. Blanpain, W. E. Lowry, M. Rendl, and E. Fuchs. Defining the epithelial stem cell niche in skin. *Science*, 303(5656):359–363, 2004.

[162] A. M. Turing. The chemical basis of morphogenesis. *Bulletin of Mathematical Biology*, 52(1-2):153–197, 1990.

[163] D. M. Umulis and H. G. Othmer. Mechanisms of scaling in pattern formation. *Development*, 140(24):4830–4843, 2013.

[164] C. Van Loan. *Computational frameworks for the fast Fourier transform*, volume 10. SIAM, 1992.

[165] R. Vuilleumier, A. Springhorn, L. Patterson, S. Koidl, M. Hammerschmidt, M. Affolter, and G. Pyrowolakis. Control of Dpp morphogen signalling by a secreted feedback regulator. *Nature Cell Biology*, 12(6):611–617, 2010.

[166] J. Walshe, H. Maroon, I. M. McGonnell, C. Dickson, and I. Mason. Establishment of hindbrain segmental identity requires signaling by fgf3 and fgf8. *Current Biology*, 12(13):1117–1123, 2002.

[167] D. Wang, W. Chen, and Q. Nie. Semi-implicit integration factor methods on sparse grids for high-dimensional systems. *Journal of Computational Physics*, 292:43–55, 2015.

[168] D. Wang, L. Zhang, and Q. Nie. Array-representation integration factor method for high-dimensional systems. *Journal of Computational Physics*, 258:585–600, 2014.

[169] L. Wang, J. Xin, and Q. Nie. A critical quantity for noise attenuation in feedback systems. *PLoS Computational Biology*, 6(4), 2010.

[170] Q. Wang, W. R. Holmes, J. Sosnik, T. Schilling, and Q. Nie. Cell sorting and noise-induced cell plasticity coordinate to sharpen boundaries between gene expression domains. *PLoS Computational Biology*, 13(1), 2017.

[171] Q. Wang, J. W. Oh, H.-L. Lee, A. Dhar, T. Peng, R. Ramos, C. F. Guerrero-Juarez, X. Wang, R. Zhao, X. Cao, et al. A multi-scale model for hair follicles reveals heterogeneous domains driving rapid spatiotemporal hair growth patterning. *Elife*, 6, 2017.

[172] Y. Wang, C. F. Guerrero-Juarez, Y. Qiu, H. Du, W. Chen, S. Figueroa, M. V. Plikus, and Q. Nie. A multiscale hybrid mathematical model of epidermal-dermal interactions during skin wound healing. *Experimental dermatology*, 28(4):493–502, 2019.

[173] O. Wartlick, A. Kicheva, and M. González-Gaitán. Morphogen gradient formation. *Cold Spring Harbor Perspectives in Biology*, 1(3):a001255, 2009.

[174] O. Wartlick, P. Mumcu, A. Kicheva, T. Bittig, C. Seum, F. Jülicher, and M. Gonzalez-Gaitan. Dynamics of Dpp signaling and proliferation control. *Science*, 331(6021):1154–1159, 2011.

[175] A. J. Waskiewicz, H. A. Rikhof, and C. B. Moens. Eliminating zebrafish pbx proteins reveals a hindbrain ground state. *Developmental Cell*, 3(5):723–733, 2002.

[176] A.-M. Wazwaz. *Partial differential equations*. CRC Press, 2002.

[177] R. J. White, Q. Nie, A. D. Lander, and T. F. Schilling. Complex regulation of cyp26a1 creates a robust retinoic acid gradient in the zebrafish embryo. *PLoS Biology*, 5(11), 2007.

[178] T. J. Widmann and C. Dahmann. Dpp signaling promotes the cuboidal-to-columnar shape transition of drosophila wing disc epithelia by regulating Rho1. *J Cell Sci*, 122(9):1362–1373, 2009.

[179] A. Wiegmann. Fast Poisson, fast Helmholtz and fast linear elastostatic solvers on rectangular parallelepipeds. *Lawrence Berkeley National Laboratory*, 2010.

[180] E. L. Wiellette and H. Sive. vhnf1 and Fgf signals synergize to specify rhombomere identity in the zebrafish hindbrain. *Development*, 130(16):3821–3829, 2003.

[181] D. G. Wilkinson. Establishing sharp and homogeneous segments in the hindbrain. *F1000Research*, 7, 2018.

[182] L. Wolpert. Positional information and the spatial pattern of cellular differentiation. *Journal of Theoretical Biology*, 25(1):1–47, 1969.

[183] H.-H. Wu, S. Ivkovic, R. C. Murray, S. Jaramillo, K. M. Lyons, J. E. Johnson, and A. L. Calof. Autoregulation of neurogenesis by gdf11. *Neuron*, 37(2):197–207, 2003.

[184] Q. Xu, G. Mellitzer, V. Robinson, and D. G. Wilkinson. In vivo cell sorting in complementary segmental domains mediated by Eph receptors and ephrins. *Nature*, 399(6733):267–271, 1999.

[185] T.-H. Yen and N. A. Wright. The gastrointestinal tract stem cell niche. *Stem Cell Reviews*, 2(3):203–212, 2006.

[186] S. R. Yu, M. Burkhardt, M. Nowak, J. Ries, Z. Petrášek, S. Scholpp, P. Schwille, and M. Brand. Fgf8 morphogen gradient forms by a source-sink mechanism with freely diffusing molecules. *Nature*, 461(7263):533–536, 2009.

[187] M. Zagorski, Y. Tabata, N. Brandenberg, M. P. Lutolf, G. Tkačik, T. Bollenbach, J. Briscoe, and A. Kicheva. Decoding of position in the developing neural tube from antiparallel morphogen gradients. *Science*, 356(6345):1379–1383, 2017.

[188] J. Zhang, C. Niu, L. Ye, H. Huang, X. He, W.-G. Tong, J. Ross, J. Haug, T. Johnson, J. Q. Feng, et al. Identification of the haematopoietic stem cell niche and control of the niche size. *Nature*, 425(6960):836–841, 2003.

[189] L. Zhang, A. D. Lander, and Q. Nie. A reaction–diffusion mechanism influences cell lineage progression as a basis for formation, regeneration, and stability of intestinal crypts. *BMC Systems Biology*, 6(1):1, 2012.

[190] L. Zhang, K. Radtke, L. Zheng, A. Q. Cai, T. F. Schilling, and Q. Nie. Noise drives sharpening of gene expression boundaries in the zebrafish hindbrain. *Molecular Systems Biology*, 8(1), 2012.

[191] S. Zhao, J. Ovadia, X. Liu, Y.-T. Zhang, and Q. Nie. Operator splitting implicit integration factor methods for stiff reaction–diffusion–advection systems. *Journal of Computational Physics*, 230(15):5996–6009, 2011.

[192] S. Zhou, W.-C. Lo, J. L. Suhalim, M. A. Digman, E. Gratton, Q. Nie, and A. D. Lander. Free extracellular diffusion creates the Dpp morphogen gradient of the *Drosophila* wing disc. *Current Biology*, 22(8):668–675, 2012.

[193] L. Zhu, L. Ju, and W. Zhao. Fast high-order compact exponential time differencing Runge–Kutta methods for second-order semilinear parabolic equations. *Journal of Scientific Computing*, 67(3):1043–1065, 2016.

[194] Y. Zhu, Y. Qiu, W. Chen, Q. Nie, and A. Lander. Scaling a Dpp morphogen gradient through feedback control of receptors and co-receptors. *Developmental Cell*, 53(6):724–739, 2020.

[195] Y.-L. Zhu, X. Wu, I.-L. Chern, and Z.-Z. Sun. *Derivative Securities and Difference Methods*. Springer, 2004.

[196] J. Zinski, Y. Bu, X. Wang, W. Dou, D. Umulis, and M. C. Mullins. Systems biology derived source-sink mechanism of BMP gradient formation. *Elife*, 6:e22199, 2017.